University of Brighton

Developing protein-based bio-inks for FDM 3D printed microfluidic and millifluidic biosensor applications

ELAHEH SIRJANI

A thesis submitted in partial fulfilment of the requirements of the University of Brighton for the degree of Doctor of Philosophy in Pharmacy and Biomolecular Science

2019

ABSTRACT

Protein-based bio-inks for fused deposition modelling (FDM) 3D printers were developed along with protocols for printing these bio-inks on the surface of the 3D-prints in such a way that they retain their biological activity.

Firstly, physical characterisation of a range of novel FDM filaments was performed in the printed state, to provide a set of criteria to determine an optimum filament for the fabrication of a microfluidic or millifluidic (biosensor) device containing the developed bio-inks.

Secondly, a custom-built syringe extruder for the MakerBot Replicator 2X experimental 3D printer was constructed and characterised. The syringe extruder was prepared to establish methodological approaches so that bio-inks could be decanted directly onto 3D prints during production.

Thirdly a series of approaches were trialled to develop bio-inks for FDM 3D printed microfluidic or millifluidic biosensor application. Protein-based bio-inks were made by covalently coupling glucose oxidase and horseradish peroxidase proteins to 20 nm and 50 nm AuNPs, gold-coated magnetic nanoparticles (Nitmagold50nm) and magnetic Dynabeads. Suitability of developed bio-inks for FDM 3D printing applications was evaluated by assessing immobilisation and inhibition of bio-inks enzymatic activity in 3D printed devices using an optimised protocol.

A set of functional bio-inks were successfully prepared using glucose oxidase and horseradish peroxidase protein coupled to Dynabeads, decanted into 3D printed devices using the FDM 3D printer syringe extruder, to make a simple glucose detection system.

Finally, using transparent filaments 3D-printed inserts for a UV/vis spectrometer were developed and loaded with bio-inks to enable a colorimetric enzymatic cascade reaction capable of quantifying lactose in solution to be carried out.

The findings of this research are a step toward creating inexpensive and rapidly produced 3D printed biosensor devices for colorimetric enzymatic assays by open source methods.

Content Page

List of Tables

List of Figures

ABBREVIATION

ABS	:	Acrylonitrile butadiene styrene
AM	:	Additive manufacturing
AuNPs	:	Gold nanoparticles
BSA	:	Bovine serum albumin
CAD	:	Computer-aided design
DNA	:	Deoxyribonucleic acid
FDM	:	Fused deposition modelling
FFF	:	Fused filament fabrication
LOM	:	Laminated object manufacturing
PET	:	Polyethylene terephthalate
PLA	:	Poly lactic acid
RD	:	Robotic deposition
RP	:	Rapid prototyping
SFF	:	Solid free-form technology
SLA	:	Stereolithography
SLS	:	Selective laser sintering
STL	:	Standard tessellation language
TPE	:	Thermoplastic elastomer
3D	:	Three-dimensional
β-Gal	:	β-Galactosidase
GOD	:	Glucose oxidase
HRP	:	Horseradish peroxidase

Acknowledgements

The research work presented in this thesis was carried out during the years of 2015-2018. The project was funded by University of Brighton Doctoral college. Undertaking this doctoral degree has been a truly life changing experience for me and it would not have been possible without the support and guidance that I received from many people.

First and foremost, I would like to express my deepest gratitude to my supervisors Dr. M Dymond, and Dr. P Cragg for their valuable guidance and support throughout my research work. Your feedback and encouragement contributed a lot to my research and your advice were priceless. Especially Dr. M Dymond who has been my major source of inspiration and motivation during the whole process.

I owe special thanks to the people who mean a lot to me; my parents (Hossein Sirjani and Azam Zafari), brother (Aryan Sirjani) and siblings for their consistent, unconditional love and support throughout my entire life. A special mention of thanks to the love of my life Hossein Khakbazi and, loved one Sahar Zafari and Aidin Hassanzade, for there great emotional support, endless encouragement and affection during the writing of this dissertation.

CHAPTER 1

LITERATURE REVIEW

1.1 Introduction

Three-dimensional (3D) printing or additive manufacturing (AM) is a versatile prototyping technology with many applications in the fields of biomedical engineering, translational medicine (Jose *et al.*, 2016) and the food industry (Holland *et al.*, 2018)(Godoi, Prakash and Bhandari, 2016). The increasing availability of fused deposition model (FDM) 3D printers and the modular nature of some models make this an attractive research area for applied and fundamental biochemistry research as it overlaps with biotechnology.

Improved fabrication speed (Chiulan *et al.*, 2017)(Gordeev, Galushko and Ananikov, 2018), portability, increases in the availability of a broader range of printable materials (Chapiro, 2016) and the growth of online innovation design communities, such as Thingiverse, (Baichtal, 2008) have driven many recent innovations. Examples include customised medical and biological devices (Shankles *et al.*, 2018) such as microfluidic, lab on a chip (LOC) and point of care (POC) diagnostics (He *et al.*, 2016)(Patrick *et al.*, 2015)(Zhou, 2017) .

Recent applications of FDM 3D printers in the fabrication of millifluidic and microfluidic reactionware include;

- Development of a configurable 3D millifluidic and microfluidic lab on a chip reaction ware device, which can be used to perform organic/inorganic and material synthesis (Kitson *et al.*, 2012).
- 3D-printed photo-spectroelectrochemical devices for in situ and in operando X-ray absorption spectroscopy investigation (Achilli *et al.*, 2016).
- Fabrication of 3D printed flow plate devices for distribution of liquid reagents and gaseous products in an electrochemical cell (Chisholm *et al.*, 2014).

- Fabrication of 3D-printing platforms as solid-and liquid-handling reactionware for chemical synthesis with reagents, catalysts and purification apparatus integrated into monolithic devices (Kitson *et al.*, 2013).
- Fabrication of a 3D printed composite microfluidic pump for wearable biomedical applications (Thomas, Tehrani and Redfearn, 2016).
- Fabrication of 3D printed cell holder for rapid, low volume spectroelectrochemistry assays (Brisendine *et al.*, 2013).
- The fabrication of a 3D printed chip that performs DNA isolation, PCR, bacterial cultivation and detection of an amplified gene, using gold nanoparticle (AuNP) probes to detect methicillin-resistant Staphylococcus aureus (MRSA) bacteria (Chudobova *et al.*, 2015).
- A 3D printed supercapacitor powered electrochemiluminescent protein immunoarray which can deliver sensitive onsite cancer diagnostic tests in resource-limited settings (Kadimisetty *et al.*, 2016).

In spite of recent progress, a key challenge in FDM 3D printing is the ability to print or decant functional biomolecules such as DNA and protein directly onto the 3D print during construction. Advances in this approach could facilitate the fabrication of reactionware containing active functional biomolecules, which has many potential applications. Recent work shows the viability of this approach using a customised FDM 3D printer to print with a nucleic acid adhesive. The DNA 'adhesive' was extruded as a suspension via a programmable syringe pump (Allen *et al.*, 2015). A similar experimental setup was used for 3D printing of complex biological structures by the freeform reversible embedding of suspended hydrogels (Hinton *et al.*, 2015).

In principle, bio-inks for 3D-printers could be developed that enable functional proteins, peptides, siRNAs, RNA, DNA or aptamers to be integrated within 3D-printed biomedical devices and biosensors.

This thesis aims to evaluate protein-based biomolecular inks for 3D printing applications using FDM. To achieve this goal, protocols are needed to enable printing of these bio-inks to the surface of the 3D-prints in such a way that they retain their biological activity. Overall this thesis aims to show a proof of concept of protein-based bioinks that will enable inexpensive 3D-printed millifluidic or microfluidic biosensor devices to be produced.

1.2 Overview of 3D-printing

Three-dimensional printing is the process by which manufactured goods derived from computer-aided design (CAD) are constructed in a layer-by-layer manner (Chae *et al.*, 2015). Three-dimensional printing is often referred to as rapid prototyping (RP) or solid freeform technology (SFF) (Ventola, 2014) based, initially, on equipment and materials developed in the 1980s . Early 3D printing techniques were invented and patented in 1986 by Hull (Hull and Arcadia, 1986) and termed as stereolithography (SLA). Later Deckard developed the selective laser sintering (SLS) 3D printing process (Deckard, Beaman and Darrah, 1992). In 1999, a moulding technique was used to produce a synthetic human bladder (Oberpenning *et al.*, 1999). Following this, the first patent for a bioprinting technique was filed by Boland in 2003, which was based on inkjet printer technology (Wilson and Boland, 2003). Over the following years, the extrusion-based bioprinting (EBB) method became a novel direction in biomedical engineering, biotechnology, tissue engineering and regenerative medicine (Jose *et al.*, 2016).

To date 3D printing techniques have been used for wide range of biomedical applications such as cell-based cytotoxicity assays, flow cytometry analysis, cell sorting and manipulation, and cell imaging (O'Neill *et al.*, 2014). 3D Printers have also been used for medical applications, producing complex biomedical devices such as implants, diagnostic platforms, scaffolds for tissue engineering (Armstrong et al., 2016) and drug

delivery systems for pre-surgical visualization models and tooling moulds (Horowitz, Awschalom and Pennathur, 2008)(Qiu, Haghiashtiani and McAlpine, 2018)(Shafiee and Atala, 2016). The 3D printer has also been used to develop lab on a chip devices for blood sampling and analysis (Lee and Lee, 2013). Blood, being a fluid containing a rich amount of information on the physiological and pathological state of the human body, is an excellent target for micro-devices designed to diagnose major diseases including cancer, heart disorders, and diabetes mellitus (Pinto *et al.*, 2015). 3D Printing technology has also been used by surgeons (Rengier *et al.*, 2010)(Chae *et al.*, 2015) for educational proposes, surgical planning and prosthetic device design (Gerstle *et al.*, 2014).

3D Bioprinting has been used to produce and transplant human/animal tissues, including multilayered skin, ear, bone, tracheal splints and heart tissue (Schubert, Van Langeveld and Donoso, 2014)(Monti, 2015)(Murphy and Atala, 2014), (Shieh and Jennings, 2017)(Wang *et al.*, 2018). The bioprinted tissue models have been used for research, toxicology and drug discovery.

1.2.1 3D-printing methods

The 3D printing field has evolved a variety of methods for creating 3D items. 3D Printing processes are divided into seven categoriesas shown in Table 1.1 and Figure 1.1. The utility of each of the methods varies depending on the aim, the material used, cross-linking mechanism and extrusion or jetting technique used.

Of the seven categories of 3D printing techniques (Table 2.1), material extrusion and material jetting are the most used in research laboratories whereas the other 3D printing methods are mostly used in industry, since they are very specialized and costly (Gross *et al.*, 2014).

The resolution of the 3D models printed by material extrusion is lower when compared to material jetting 3D printing, but the low cost and printing speed of material extrusion 3D printing (Sood, Ohdar and Mahapatra, 2010) is a major advantage for use in research and development purposes.

There are two types of material extrusion 3D printing techniques EBB and FDM. Of these two different 3D printing techniques the FDM 3D method is cheaper, customisable and it allows construction of devices with high mechanical strength where it is not achievable by EBB. It is anticipated that, depending on the target goals of the research, the combination of these two types of material extrusion 3D printing techniques and the exploration of their features combined with the application of specific (ink/material) formulations could form a basic requirement for fabricating customised material and devices.

Table 1.1| **A summary of 3D printing techniques.** Described by (Jose et al., 2016), (Ngo et al., 2018) and (Lee, Ann and Chua, 2017).

3D printing processes categories	Materials	3D printing Methods	Benefits	Limitations	Unique features	References
Material jetting: Liquid droplets of the material are jetted down onto the working platform where they solidify into an object.	More commonly Photopolymers, photoresins,	Inkjet printing	2D resolution	Limited Z resolution	Cell compatible Small amount of material used Touchless handling Particles (50-100 μm in diameter)	(Cui et al., 2010) (Cui et al., 2014) (Xu et al., 2005) (Dawes et al., 2016)
Binder jetting: Use binding agent droplets, to link powder particles together into the desired shape.	Metal, sand and ceramics	Acoustic ejection droplet	Fast, Low cost, High precision, Ultra high throughput	Limited Z resolution, inverted substrates, low viscosity		
Direct energy deposition: Heats up the material such as metal powder by a source of energy, usually a powerful laser, and melts them onto the substrate.	Plaster powder	Inkjet head printing and power bed	The bioactive component can be integrated	Appropriate only for powdered thermos responsive materials	High mechanical strength	(Lee, An and Chua, 2017)
VAT Photopolymerisation: Is a process in which photocurable materials such as photopolymers, undergo solidification when exposed to UV radiation	Acrylate-based resin with proprietary photoinitiators, the support material, is mix of polyethylene glycols, glycerin	Stereo Lithography (SLA)	High 3D resolution	Cell photo persuaded damage	Cell compatible Well-suited for most photo-polymerisable materials	(Chia and Wu, 2015) (Käpylä et al., 2014)
Powder bed fusion: Works by a laser or an electron beam as a source of thermal energy to melt and full fusion the material powder to form a layer, use a roller to balance the surface, followed by application of the next layer to form the 3D model.	Powdered polycarbonate, ABS, nylon resin, metal, ceramic powder, polyester	Selective laser sintering (SLS)	High mechanical strength, faster and higher resolution when compared with other powder methods	Appropriate for powdered thermos responsive materials	FDA approved product (based on OsteoFab product)	(Duan et al., 2010) (Jose et al., 2016)
Material extrusion: Heats up material at their melting state, push material through a nozzle or syringe for bioprinting at a set speed and thickness on building platform. Deposit material layer by layer to form 3D object.	Polycarbonate, ABS, nylon, wax blends, metal, ceramics (with binder),	Fused deposition modelling (FDM)	High accuracy and reproducibility (well-established methods)	Thermoplastic material only, photosensitive materials, modified devices are only cell compatible when processed at biological temperatures	Commercially available (affordable product based on price when compared to other 3D methods)	(Jose et al., 2016) (Zein et al., 2002) (Thomas and Adam, 2016) (Ozbolat and Hospodiuk, 2016)
	Hydrogel, chitosan, gelatin, agarose,	EBB (Bioprinting) or Direct write (DW)	Variety of material (Bioinks)	Low mechanical strength, mostly personalised for desire need, The commercially available bioprinters are costly.	Complex 3D structure, cell compatible Freeform structures possible	
Sheet lamination: Materials are drawn across a build platform by a system of feed rollers, cut out using a laser and joined together using an adhesive or by ultrasound.	Paper, plastic and some sheet metals	Laminated object manufacturing (LOM)	Low cost Ease of material handling	Poor surface finish Difficult in creating hollow parts	Speed	(Bhushan and Caspers, 2017)

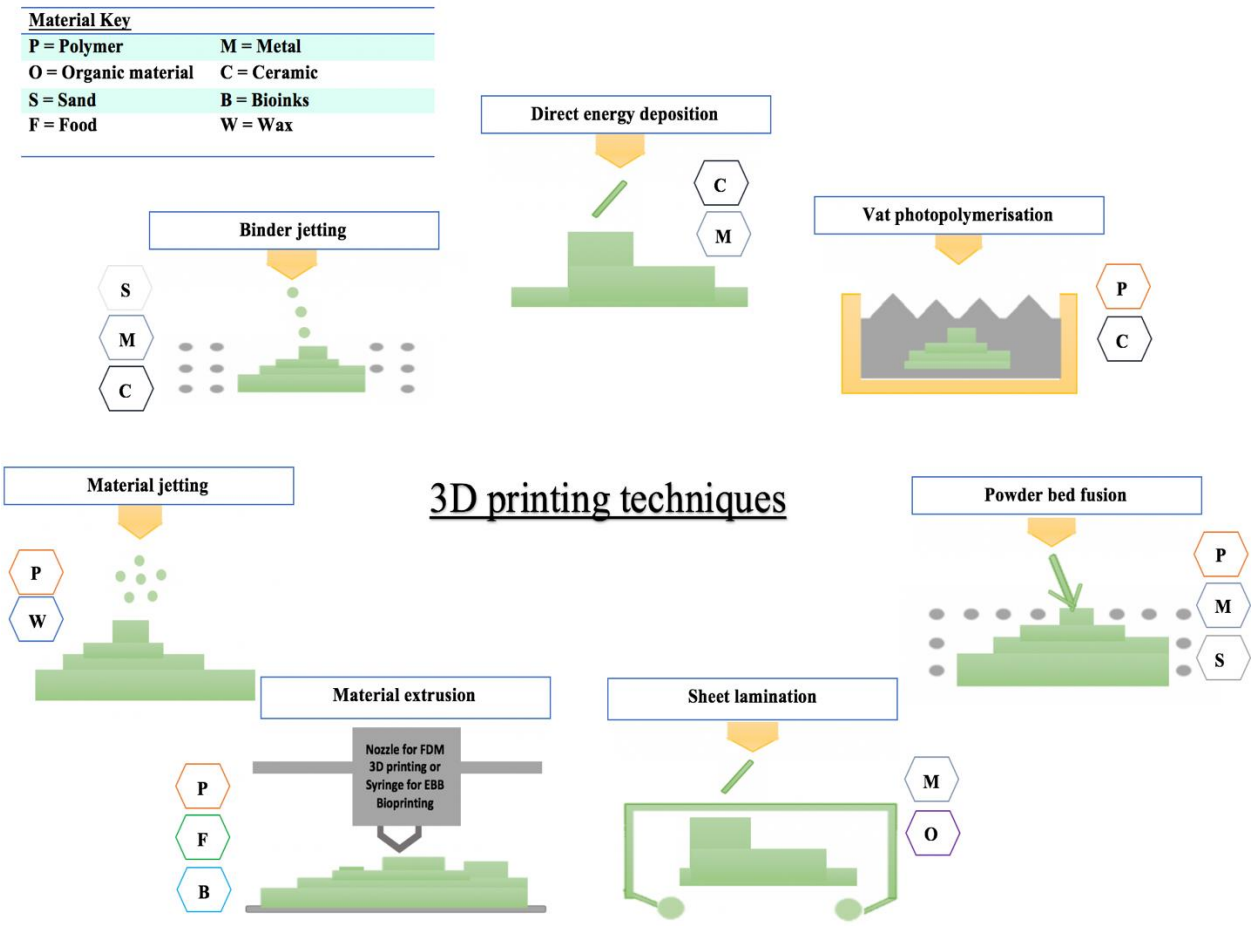

Figure 1.1| **3D Printing techniques.** Adapted from (Desai, 2017).

1.2.1.1 An overview of bioprinting techniques

Bioprinting is a type of 3D printing method that uses cells and other biological molecules or biomaterial as a bio-ink to fabricate biological structures and biomedical parts that imitate natural biomolecular characteristics. Examples of bioprinting applications are cell tissue, tissue constructs, organ modules, biomaterials, drugs and microfluidic devices (Jose *et al.*, 2016). Many bio-printers are not available commercially and are made in-house, which limits the advancement of 3D bioprinting research (Hong *et al.*, 2017). The bioprinting processes are divided into three categories which are presented in Figure 1.2.

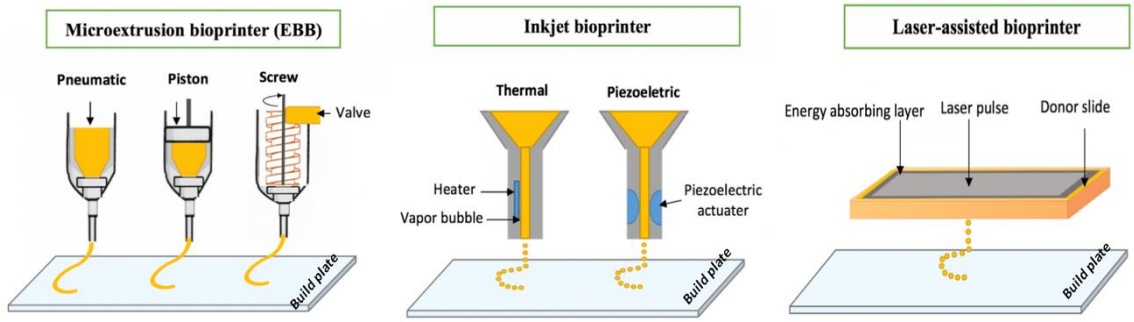

Figure 1.2| **Bioprinting techniques:** Inkjet and laser-assisted bio-printer works by decanting or printing biological molecules/material as a form of liquid droplets onto the working platform. Microextrusion bio-printer or EBB push material (usually gel types) through a syringe for bioprinting at a set speed and thickness on building platform where it can deposit material layer by layer to form 3D object. Adapted from (Murphy and Atala, 2014).

Extrusion-based bio-printers are available commercially but their application is limited to cell plotting, tissue and organ fabrication (Ozbolat and Hospodiuk, 2016). EBB is a layer-by-layer manufacturing procedure similar to FDM 3D printing that uses a robotic system to push the biomaterial or bio-inks placed in a syringe onto any substrate at the command of a stepper motor or a pump. EBB 3D printers are not commonly used for fabrication of reactionware and biological devices due to cost and lack of suitable bio-inks with desired characteristics (Chimene *et al.*, 2016). Lack of bio-inks with high structural fidelity, high mechanical strength, bioactivity and biodegradability (Chimene *et al.*, 2016) to construct a 3D model is the commonly reported issue.

1.2.1.2 FDM 3D printing

FDM or fused filament fabrication (FFF) 3D printers contain robotic deposition (RD) hardware with temperature controllers and heated build plates. As shown in Table 1.1 the FDM 3D printers work by heating the thermoplastic filaments to the semi-molten state before extrusion. Next, the softened material is pushed through extruder nozzle moving in X, Y plane on a building platform. The material solidifies upon deposition on a heated build plate (building platform). The 3D object is formed layer by layer by careful positioning and movement of extruder nozzle (in the Z direction) from the bottom to the top of the 3D-print (Figure 1.3).

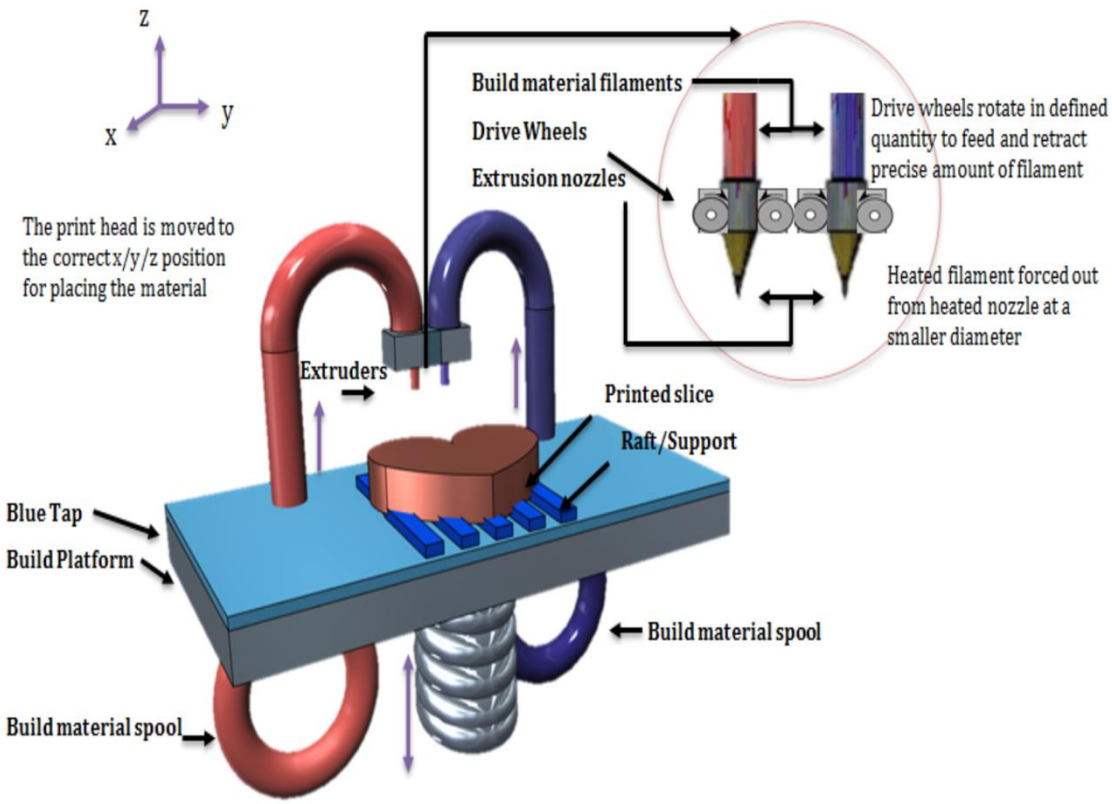

Figure 1.3| **Representation of the FDM 3D printing process**: the FDM 3D printing process enclosing two extruders.

To print a 3D model, the 3D design software (CAD) model is first constructed. Typical programs that are used are; Sketch Up, 123D Catch and Autodesk 123D design. After drawing, the design is then exported as an STL (Standard Tessellation language) file. Information for the 3D design is stored in the STL file in the form of triangulated sections, where the vertices are coordinates listed in a text file. Next, the STL file is exported into a (X3G) G-file using slicing software. The X3G G-file can then be loaded on to an SD card to provide instructions for the 3D printing process. The G-file is a compact format containing information that divides the 3D STL file into sequences of 2D dimensional horizontal cross-sections. This allows the 3D object to be printed starting at the base, layer by layer, fabricating the 3D model from the sequences of 2D layers. Figure 1.4 represents the FDM 3D printing process.

Figure 1.4| **The 3D printing process, from CAD model to a 3D object.**

1.2.2.1 MakerBot Replicator 2X Experimental 3D printer

In this project, a MakerBot Replicator 2X experimental 3D printer (Figure 1.5), a traditional thermoplastic FDM printer equipped with two extruders, was used. The MakerBot Replicator 2X contains super-flat heated build platform fabricated of 356 aluminium which is covered with Kapton polyimide tape, blue tape and build Tak, to help with thermoplastic adherence, avoiding upward wrapping and curling when printing.

MakerBot Replicator 2X experimental works by feeding the filaments into the extruders of the 3D printer, where material is heated to its melting point and pushed out through the nozzle layer by layer on heated platform to create the print.

The dual extruders of the MakerBot Replicator 2X allow two materials, different coloured filaments or complex models that use a dissolvable filament, often print optimally at different temperature and resolution settings.

The two extruders of the MakerBot replicator 2X are fitted separately on the 3D printer and can be modified and controlled individually. These outputs attract the use of this printer in different areas of research. One example is the modification of the MakerBot replicator 2X 3D printer into a liquid dispensing 3D printer to fabricate patient-specific liquid capsules (Okwuosa et al., 2018). The 3D printing device was modified by replacing a right extruder/head with a syringe-based liquid dispenser obtained from an open source design. The parts assembled to make syringe-based extruding head were produced by 3D printing using an M2 Makergear FDM 3D printer and ABS filament (Okwuosa et al., 2018).

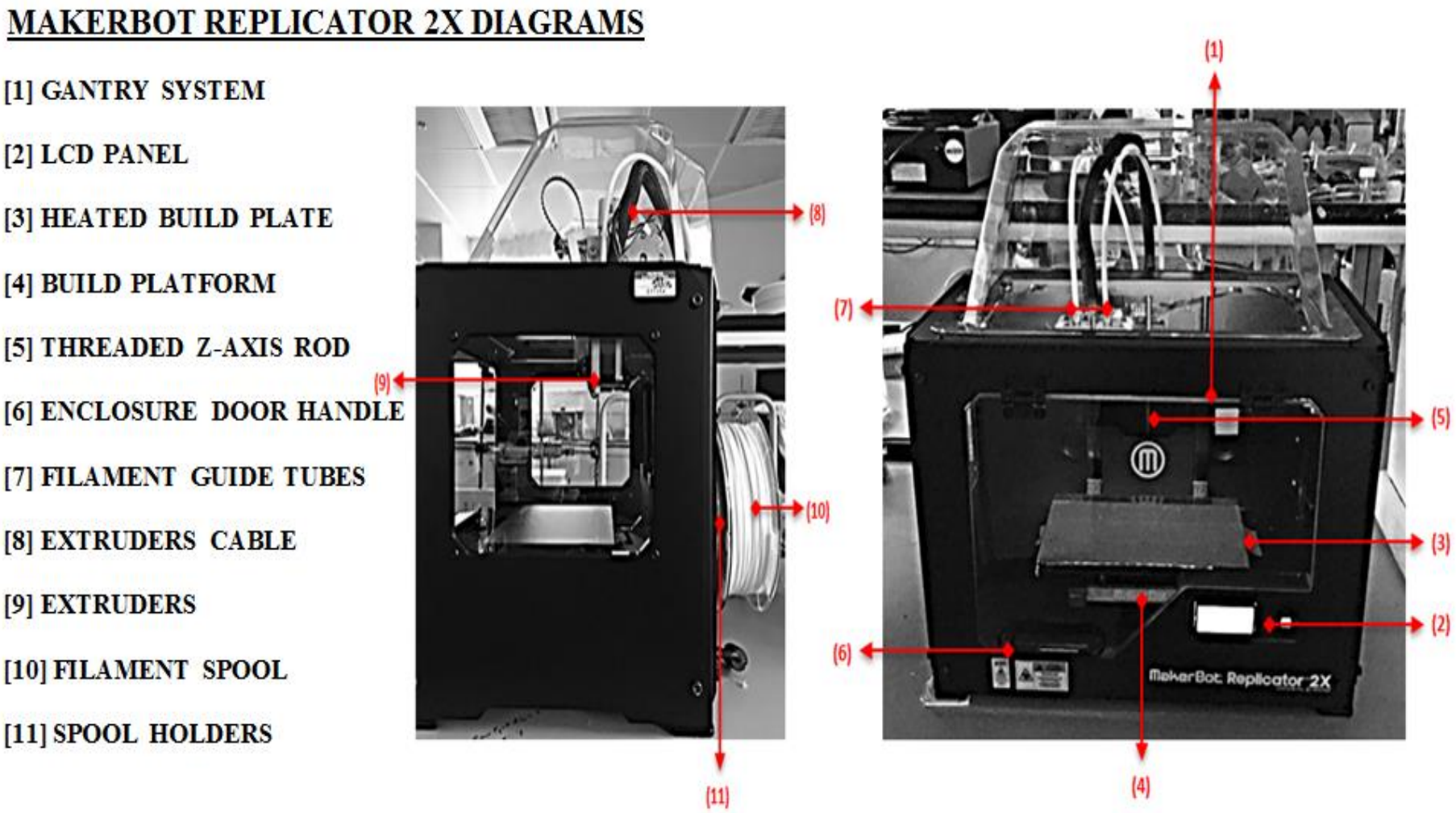

Figure 1.5| **Photograph of MakerBot Replicator 2X experimental 3D printer**: Build volume: 24.6 cm (W) x 16.3 cm (L) x 15.5 cm (H). Filament diameter: 1.75mm. Nozzle diameter: 0.4 mm. Physical dimensions (with spools): 49 cm (W) x 42 cm (L) x 38 cm (H). Software bundle: MakerBot MakerWare TM. File Type: STL, OBJ, Thing. Connectivity: SD card [FATI6, max 2GB].

Models can be printed using the MakerBot Desktop software at different print settings (extrusion and platform temperatures), extrusion speed, infill percentage, model properties, rafts, supports and bridging for each extruder. Controlling these features enables makes laboratories to quickly prototype a wide range of applications, using a range of filaments. Also, it has been reported that the optimisation of these printing features, especially for new filaments, is a crucial factor in FDM 3D printing to achieve an object with desired properties (Villalpando, Eiliat and Urbanic, 2014). Parameters such as layer height (or layer thickness), the speed of printing, extrusion temperature, and infill density were reported as most significant features that could directly influence the quality of the final product (Anitha *et al.*, 2001) (Elsholtz and Harper, 2015).

Table 1.2 defines the key parameters that can be customised with the MakerBot Replicator 2X experimental printer.

Table 1.2| **Outlines MakerBot desktop software printer terminology**

	Print settings	Definition
Device Settings	Extruder Temperature Right (℃)	Sets the temperature of the extruder for the filament to extrude out of the nozzle.
	Platform Temperature (℃)	Sets the temperature of the heated build plate for a 3D printed object to be printed at.
	Travel Speed (mm/s)	Travel speed is for setting the extruder speed for travel move when it is not extruding any plastic.
	Z- axis Travel speed (mm/s)	Z-axis Travel speed is for setting the speed of the build plate movement between layers.
	Minimum Layer Duration (s)	Minimum Layer Duration is for setting the time taken for plastic to cool before applying the next layer.
Extrusion Speeds	(Bridges, first layer, first layer raft, floor surface fills, infill, insets, outlines, raft, sparse roof surface fill) in (mm/s)	Extrusion Speed is for controlling the speeds level when printing different section of the object. Each layer can be set to print at a minimum of 10mm/s and maximum of 160mm/s.
Infill	Infill density	Infill density is to set the compactness of object interior. The minimum infill density is 10% and can be increased up to 100%.
	Infill pattern	Is the pattern used spontaneously for building the interior part of 3D printed object; pattern available by MakerBot 3D printer are Hexagonal linear, diamond, moroccanstar, catfill and sharkfil. Refer to figure 1.3
Model Properties	Layer Height (mm)	Layer Height is for setting the thickness of printed object individual layers.
	Number of Shells (mm)	Is for setting the number of outlines that extruder print on before printing the infill
	Roof/ Floor Thickness (mm)	Sets the height, of a group of solid layers at highest and lowest part of the 3D printed object.
	Coarseness (mm^2)	Is for simplifying the outlines of each layer of the print before the toolpath is shaped. Vertices that produce features smaller than coarseness area are collapsed.
Multi-Material Printing	Support Material Extruder	Multi-Material Printing is used for dual extrusion when printing with two different filaments. Support material extruder is used to control how extruders are used on different parts of the printing object. In setting 0 point to the right extruder and 1 point to the left extruder.
	Purge Wall	Purge wall is an extraneous wall or structure that is printed on the side of the printed object. Purge wall helps to reduce the mixing of material thru dual extrusion prints. Use of purge wall will increase the print time and it can be turned on and off if needed.
Raft	Raft to model spacing, margin, [(base, interface, surface) layers]	The raft is a printing base that keeps the object stable through the printing process. Raft to model spacing, margin and each layer of raft can be controlled in raft setting. Is good to be used for printing large objects. The raft is mostly recommended to be used for 5^{th} generation MakerBot 3D printers (MakerBot, 2015).
Supports and Bridging	Support density, margin,	Support and Bridging are used to enhance printing quality when printing models with overhangs and long bridges. Support density and margin and other extra setting related to support and bridging can be controlled using this setting.
Right or Left Extruder	Filament diameter (mm)	Right or left extruder setting give user controls over each extruder separately. Filament diameter reflects the diameter of the filament that is used. If the value is higher than actual filament diameter, the extruder may not put out enough plastic during you print or oppose.
	Retraction distance (mm)	Is to control the length of filament/material retracted before a travel move.
	Retraction speed (mm)	Is to set how fast the filament/material pushed back into nozzle after a travel move.
	Extra restart distance (mm)	Is to set the extruder to push out more or less plastic after a retraction.
	Extra restart speed (mm)	Is to set a different extrusion rate for the amount of filament that was set in Extra restart distance.

Infill patterns supported by MakerBot Desktop software are hexagonal, linear, diamond, moroccanstar, catfill and sharkfil (Figure 1.6). Hexagonal infill is the most frequent pattern that is used by operators since it provides optimal strength without adding weight. Diamond is designed to print quickly and to be strong however it can increase the complexity of the toolpath. Linear infill is made up of parallel straight lines followed by a perpendicular line to the previous layer. It is fast to print for simple toolpath. The other patterns such as moroccanstar, catfill , and sharkfil are meant to be decorative and fun.

Figure 1.6| **Photograph of MakerBot Replicator 2X infill patterns.**

The compactness of the 3D printed object infill patterns is linked to infill density. Increasing the printing setting infill density to 100% will remove the gap within the patterns and potentially increase water tightness of the final print.

1.2.2.2 Filaments used in FDM 3D Printing

Filaments are plastic materials utilized in FDM printing techniques to make 3D prints (Au *et al.*, 2016). The filaments that are most frequently used in FDM 3D printers are ABS (Ahn *et al.*, 2002)(Lee, Abdullah, and Khan, 2016), PLA (Drummer, Cifuentes-Cuéllar and Rietzel, 2012) and nylon (Masood and Song, 2004). However novel composite filaments of ABS and PLA materials possessing certain novel features such as a colour change with temperature, antimicrobial, fluorescence, magnetic and metallic filaments are available. Moreover, the range of novel filaments is rapidly expanding, for

example, biocompatible, chemically resistant, conductive, biodegradable, flexible, optically transparent and food safe filaments are now available. Biofila Linen, HIPS, XT-Copolyester, T-Glase, HD Glass, Nylon, SemiFlex, and Makerbot Flexible are the examples of these filaments. The increase in availability of some of these materials for FDM printing is an excellent opportunity to explore the use of these filaments for biological application to fabricate biomedical devices with good supportability, optical transparency, excellent inertness, high strength and mechanical properties (Nge, Rogers and Woolley, 2013).

1.3 Use of AM in making reactionware in biochemistry

Reactionware devices are classified as nano-fluidic (1-100 nm), microfluidic (100 nm to 1 mm) and millifluidic (1-10 mm) devices according to the dimension of reactors (Zhou, 2017) (Illg, Löb and Hessel, 2010). AM is continuously used to fabricate millifluidic and microfluidic reactionware. Microfluidic reactionware typically allow precise control of small (10^{-3} to 10^{-12} microliter) volumes of fluids over short distances. Millifluidic devices contain internal structures sized from sub-micrometre to the sub-millimetre range where biological or chemical reactions are conducted (Zhou, 2017). Millifluidic and microfluidic reactionware compatible with a wide range of reagents have been prepared using AM with glass, silicon, metal, ceramic and Teflon (Capel *et al.*, 2013).

The 3D printing methods of stereolithography (SL) and laminated object manufacturing (LOM) allow the reproducible fabrication of complex microfluidic channels. FDM 3D printing has also been used for the fabrication of millifluidic and microfluidic devices, but currently, the applications of this technology are limited (Kitson *et al.*, 2012)(Zhou, 2017).

1.3.1 Use of FDM 3D printers for making millifluidic and microfluidic devices and their limitation

To date, few millifluidic and microfluidic devices have been printed using fused deposition modeling (FDM) of thermoplastic (Bhattacharjee *et al.*, 2016) because the technology applied in constructing reactionware using FDM 3D printers is relatively unexplored and challenging. FDM 3D printing has repeatedly been discounted as a reliable method to produce fluid manipulation devices due to leakage between the extruded layers of the printed object and perceived lack of accuracy and lower resolution (Ho *et al.*, 2015a). However, recent papers report the production of reliable fluid manipulating FDM 3D printed devices (Morgan *et al.*, 2016) (Tsuda *et al.*, 2015). A good example is presented by Pisaruka and Dymond where they fabricated a leak-free temperature-controlled cuvette by tweaking the 3D printing setting and immersing the final print in acetone (Pisaruka and Dymond, 2016). A leak-free, optically transparent FDM 3D printed microfluidic device printed with PLA filament was also recently reported (Tothill *et al.*, 2017). These studies show that to achieve water-tightness, suitable surface treatments, optimum printing setting parameters (dependent on the material used) and optimal 3D-designs need to be found.

Some new filaments may possess properties that make them better suited to fluid applications such as hydrophobicity (Zhou, 2017). Reports suggest for microfluidic applications, using hydrophobic polymers to construct channels allows easy movement of liquid in the device (Lee, Zhang and Yeong, 2016). Factors such as shrinkage, layer bonding, surface roughness, hydrophobicity, and biocompatibility are an important aspect to ensure optimum fluidic devices with no/minimum leakage are fabricated (Lee, Zhang and Yeong, 2016).

1.4 Bio-inks for 3D printing

Bio-inks are biomaterials or biomolecular that can be extruded through a printing nozzle/needle, directly into a substrate or onto a surface by a 3D printer (Prendergast, Solorzano and Cabrera, 2016). Printing or decanting bio-inks in reactionware can enable the rapid production of a combinatorial array for high throughput screening (Jose *et al.*, 2016).

Bio-inks are either low viscosity liquids, for deposition by an inkjet printer, bio-ink filaments or gels that are often deposited by EBB under mild conditions to preserve bio-ink printability (Chimene *et al.*, 2016). Some bio-inks for inkjet and laser 3D printers are composites of living cells (typically 10,000 to 30,000 cells per 10–50 μL droplet) suspended in a medium or pre-gel solution by polymer cross linkers that are activated by enzymatic, photo or thermal processes (Xu *et al.*, 2005).

Bio-inks containing drugs (Cui *et al.*, 2010), DNA (Okamoto, Suzuki and Yamamoto, 2000), mammalian cells (Parsa *et al.*, 2010), lipid vesicles (Stachowiak *et al.*, 2009), proteins and enzymes (Cook, Wang and Derby, 2010) are typically printed/decanted via inkjet 3D printers with minimal impact on the viability of printed biologicals molecules. However, the low viscosity ink used in inkjet printing does not facilitate the rapid generation of the 3D structure.

A wide selection of bio-inks generating 3D structures, including 3D hydrogels (Stanton, *et al.*, 2015), cellulose hydrogel (Mulakkal et al., 2018), cell pellets (Owens *et al.*, 2013), alginate/nanocellulose (Levato *et al.*, 2014), polycaprolactone/pluronic (Yu *et al.*, 2016), agarose (Mehesz *et al.*, 2011) and decellularized matrix components (Pati *et al.*, 2014) for tissue construct are typically printed by EBB.

To date, EBB is the most promising bioprinting technique due to its versatility in printing various bio-ink types, with acceptable mechanical and biological properties which cannot be achieved with using inkjet and laser bioprinting method (Ozbolat and

Hospodiuk, 2016). However, there are currently no reports on the fabrication of protein/enzyme/DNA bio-inks for EBB and FDM 3D printing.

1.5 Immobilization of proteins-based bio-ink for millifluidic and microfluidic applications

Physical and chemical immobilization procedures are commonly used to achieve bio-ink immobilized on surfaces. In 3D printed reactionware bio-ink immobilization is fundamental to facilitate the rapid production of micro/millifluidic (biosensor) devices such as arrays for high throughput screening (Jose *et al.*, 2016). To date, there have been several reports dealing with proteins (Delamarche, 1997), cells (Khademhosseini and Bong, 2006) and planar lipid bilayers (Yang *et al.*, 2001) for patterning and immobilizing surfaces at micrometer scale resolution for the microfluidic application. Most of the studies are restricted to immobilization of biological molecules or material to the PDMS microfluidic channels or on a glass surface (Mao, Yang and Cremer, 2002). Currently, no techniques for immobilization of enzymatic bio-inks to the surface of FDM 3D printed polymer material, during printing, have been reported.

The major advantages of using enzymatic bio-ink in FDM 3D printed micro/millifluidic systems are their high specificity and efficiency. Enzymes act as biocatalysts to speed up a chemical reaction (Mateo *et al.*, 2007). Enzymes have high stereoselectivity and can work under green chemistry conditions of ambient temperature and mild pH. Immobilization of enzymatic bio-inks in FDM 3D printed micro/millifluidic devices would also potentially decrease the cost of an enzymatic reaction since a lower enzyme concentration would be required for the same number of catalytic processes, over a longer period of time. The main methods used for enzyme immobilization, shown in Figure 1.7, are: (a) cross-linking of enzymes, (b) enzymes entrapment into a polymeric

gel, capsule, membrane and channel, (c) covalent attachment (enzyme immobilization on a substrate (solid surface)), (d) physical adsorption (Mohamad *et al.*, 2015)(Hartmann and Jung, 2010).

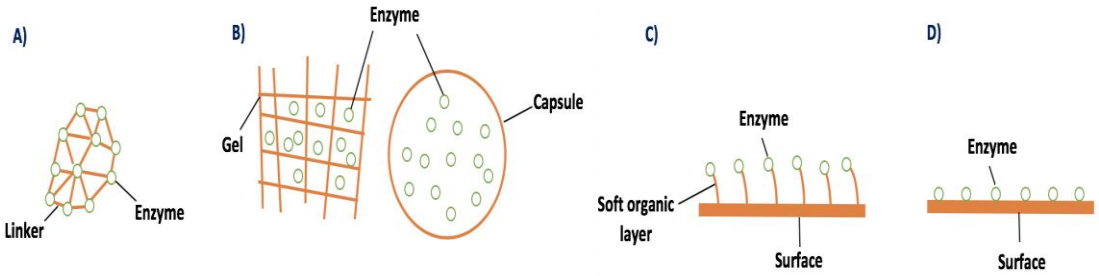

Figure 1.7| **Enzyme immobilisation:** A) Enzyme cross-linking, B) Enzyme entrapment in gel or capsule, C+D) enzyme binding to the surface; C) covalent attachment D) physical adsorption.

For the analytical biosensing, the immobilization of enzymes on solid surfaces has been intensively studied to reduce analysis time and cost as well as increasing detection sensitivity. The main techniques used for immobilization of enzyme on a solid surface are shown in Figure 1.8.

To immobilize enzymes on solid surfaces from the techniques in Figure 1.8, a particular technique can be more appropriate than others depending on the surface used (*e.g.* polymers, glass, metal), the environmental conditions and surface intrinsic properties (e.g. point of zero charge, surface chemistry) (Jonkheijm *et al.*, 2008)(Wong *et al.*, 2009). The characteristic properties of the enzyme (e.g. size, isoelectric point, amino acids residues available on the enzyme surface), desired orientation, concentration, steric conformation after adsorption and the level of order of the adsorbed protein all influence the steps required to achieve a complete immobilisation (Kim and Herr,

2013)(Rusmini, Zhong and Feijen, 2007). A summary of the techniques used to immobilize enzyme on solid surfaces is presented in the Table 1.3. Amongst the immobilization techniques in Table 1.3 the "SAM mediated immobilization and polymeric soft layer mediated immobilization" approach is used in this thesis for attaching the functionalized fabricated bio-inks to the 3D printed object (filaments).

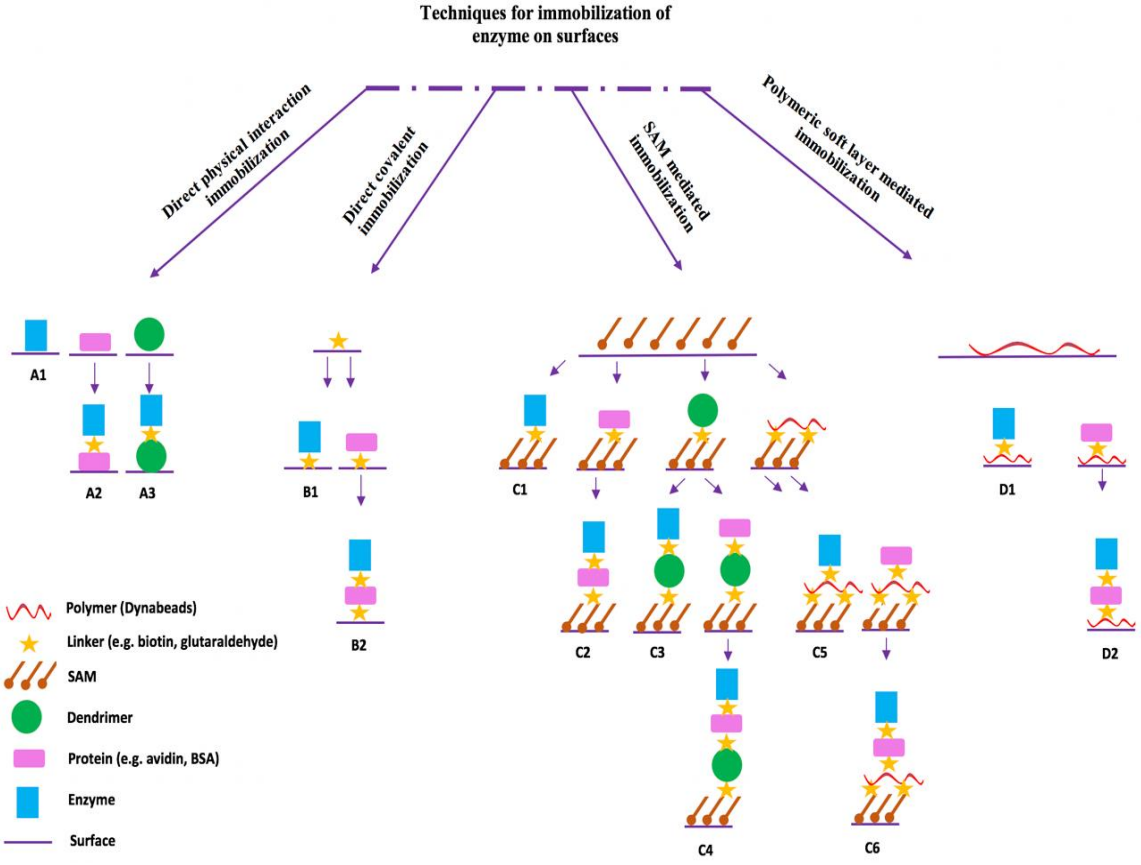

Figure 1.8| **Representations of the techniques for immobilization of enzyme on surface**

Table 1.3 | **Represents the techniques used for immobilisation of enzyme on surfaces**

Techniques for immobilization of enzyme on solid surfaces	Description	Advantages	Disadvantages	References
Direct physical interaction immobilization	Direct nonspecific intermolecular force interaction (i.e. hydrophilic, hydrophobic and ionic) between the enzyme and the surface.	A1) **Quick** (one step)	**1) Random orientation** of enzyme on surface **2) Detaching** due to weak and unstable binding **3) Denaturation** due to strong interaction with surface (i.e. unfolding of the enzyme) **(A2-A3)** 2 and 3 can be overcome to achieve a short time stability by covering the surface with a layer of adsorbed BSA or avidin followed by immobilizing the enzyme to protein layer.	Rusmini, et al., 2007; Puleo and Bizios, 2009; Nakanishi, et al., 2001; Ramsden, 1995; Norde, 1986; Wolny, et al., 2010.
Direct covalent immobilization	**B1)** Is achieved through directly activating the surface (i.e. glass or polymeric fibers) followed by using a linker to immobilize the enzyme. **B2)** If the spacer is immobilized on the surface first, several optimization steps are required.	**Quick** (one step) It is possible to immobilize the linker to enzyme first then attach them to a surface using a support to hold the linker immobilized on the surface	Possibility of denaturation due to direct interaction of the enzyme with the surfaces **B2)** Several optimization steps are required.	Laurell, et al., 1996; Kumar., 2010; El-Zahab, et al., 2004.
Self- assembled monolayer (SAM) mediated immobilization	Immobilization of the enzyme through SAM. Initially the surface is modified by monolayer formed from chemically simple amphiphiles i.e. SiO_2 (ω−substituted siloxane) or thiol on gold. Next the enzyme is adsorbed onto a modified surface.	**Irreversible** (Stable binding) **C1)** Enzyme can be on SAM directly or **C2-4)** on a linking protein i.e. BSA, avidin or dendrimer (in a third step) or **C5-6)** on a polymer (polymer need to be immobilized to SAM first)	**1)** The surface cannot be used further for other successive functionalization since SAM formation is irreversible due to the covalent coupling that is formed between the amphiphiles and the surface. **2)** Requires multi adsorption steps, however it increases the stability of the immobilized enzyme **(C2-C6)**.	Onclin, et al., 2005; Samanta and Sarkar, 2011; Vadgama, 2005.
Polymeric soft layer mediated immobilization	Initially a layer of polymer is formed by using a soft organic layer mediated approach through multiple non-specific ionic and van der wall force interaction between surface and polymer. The surface anchor the polymer and the polymer directly interact with the protein or enzyme for immobilization.	**D1) Quick** (one step) **D2)** Addition of a protein spacer i.e. biotin between the polymer and the enzyme is possible which may **decrease the risk of enzyme denaturation**. Biotin-avidin linker is a milder reaction compare to other techniques and is used very often.	**D2)** Can be a long process	Scholz, 2017 Ruiz-Taylor et al., 2001 Bahulekar, et al., 1991

OBJECTIVES

The goal of this research to develop of FDM 3D printer compatible bio-inks to allow proteins to be decanted onto the surfaces of 3D printed objects. This will facilitate the fabrication and characterisation of bespoke 3D printed objects with a range of biochemical properties.

As a proof of concept the bio-inks developed will be used in 3D printed optical biosensor devices to allow the detection and quantification of glucose and lactose by spectrophotometry. The steps towards accomplishing this task are;

i. To assess the suitability of a range of commercially available FDM 3D printer filaments for use in the application of micro/millifluidic devices.
ii. To assess nonspecific binding of DNA and protein to a range of commercially available thermoplastic filaments for use in microfluidic applications.
iii. Assemble and test a bespoke syringe extruder for the MakerBot Replicator 2X to enable biomolecule to be decanted.
iv. To design, develop and characterize bio-inks for FDM 3D printing and immobilisation in microfluidic/millifluidic devices.
v. Assess bio-ink compatibility with a range of 3D-printer filaments.
vi. Use immobilised bio-inks inside 3D printed devices to perform a coupled set of chemical reactions.
vii. 3D print a biosensor device for UV visible spectroscopy that quantifies glucose and or lactose in a sample.

CHAPTER 2

EXPERIMENTAL SECTION

2.1 Materials and equipment

GOD from *Aspergillus niger* Type VII (E.C.1.1.3.4), HRP Type II (E.C.1.11.1.7), β-Gal from *Escherichia coli* Grade VIII (E.C.3.2.1.23), colloidal gold nanoparticles (AuNPs) monodisperse 20 nm and 50 nm particle diameter stabilised suspension in citrate buffer, D-(+)-glucose, D-lactose monohydrate, *O*-dianisidine dihydrochloride, 11-mercaptoundecanoic acid (MUA), *N*-ethyl-*N*′-(3-dimethylaminopropyl) carbodiimide hydrochloride (EDC), *N*-hydroxysuccinimide (NHS) were purchased from Sigma–Aldrich (UK). Dynabeads^{TM} M280 Tosylactivated were purchased from Fisher Scientific. All aqueous solutions were prepared in water obtained by a Milli-Q Gradient A-10 system (Millipore, 18.2 M cm). All chemicals were of analytical grade and used without further purification.

Samples weighed on an Ohaus Adventurer microbalance AR2140. The optical absorbance of solutions was measured using a Shimadzu UV-2401 PC UV-Visible spectrophotometer. BRAND® disposable polystyrene cuvettes (Sigma-Aldrich UK) were used. Nickel plated neodymium magnets from 2 mm to 6 mm diameter by 1 mm in height were purchased from First4magnets (Tuxford, Nottinghamshire, UK). A Lab oscillator (KJ-201BD) orbital shaker and SLS Lab Basic 12 Place micro-centrifuge, SLS4600 were used for sepration of the AuNPs particles. Fisher brand (FB15060) ultrasonic baths was used to disperse AuNPs samples in solution.

Dynabead samples were separated by μMACS magnetic fields (130-042-602) separation system (Milteny Biotec GmbH, Germany).

2.1.1Buffer Solutions

Buffer A: Trizma®- $MgCl_2$ buffer (50 mM Trizma, 15 mM $MgCl_2$) was prepared by dissolving 0.77 g of Trizma preset crystals (Sigma Aldrich) and 1.43 g of magnesium chloride hexahydrate (Fisher Scientific) in 100 mL of deionised water stirring for 1 hour. The pH was adjusted to 7.2 using NaOH and HCl.

Buffer B: Sodium acetate buffer (50 mM) was prepared by dissolving 3.40 g of sodium acetate, trihydrate, (Sigma Aldrich) in 200 mL of deionised water. The pH was adjusted to 5.1 using NaOH and HCl.

Buffer C: Sodium phosphate buffer (0.1M) was prepared by dissolving 2.62 g of monobasic sodium phosphate monohydrate (MW:137.99, Sigma Aldrich) and 14.42 g of sodium phosphate dibasic dihydrate (MW:177.99, Sigma Aldrich) in 1L of deionised water. The pH was adjusted to 7.4 using NaOH and HCl.

Buffer D: Na-Phosphate Tween 20 buffer (10 mM) with 0.2 mg/mL Tween 20 was prepared by dissolving 0.06 g of monobasic sodium phosphate monohydrate and 8 mL of polyoxyethylenesorbitan monolaurate (Tween 20, Sigma Aldrich) made to 40 mL with deionised water. The pH was adjusted to 6.8 using NaOH and HCl. (This buffer was used in GOD bioconjugation to AuNPs)

Buffer E: Sodium phosphate buffer (10 mM) was prepared by dissolving 0.06 g of monobasic sodium phosphate monohydrate in 40 mL of deionised water. The pH was adjusted to 6.8 using NaOH and HCl. (This buffer was used to prepare 0.8 mg/mL GOD)

Buffer F: Sodium phosphate buffer (0.1M) was prepared by dissolving 0.312 g of monobasic sodium phosphate monohydrate in 20 mL of deionised water. The pH was adjusted to 5.8 using NaOH and HCl. (The GOD/AuNPs bioconjugates were dispersed in this buffer for storage at 4°C).

Buffer G: Ammonium sulfate buffer (3M) was prepared by dissolving 39.64 g of ammonium sulfate (Sigma Aldrich) in Buffer C. The pH was adjusted to 7.4 using NaOH and HCl.

Buffer H: Sodium phosphate buffer (0.01M) was prepared by mixing 10 mL of (Buffer C) with 90 mL of deionised water. The pH was adjusted to 7.4 using NaOH and HCl.

Buffer I: Sodium phosphate buffer with 0.5% (w/v) of Tween 20 was prepared by mixing 0.88 g sodium chloride (MW:58.4 , Sigma Aldrich) and 0.5% w/v of Tween 20 with (Buffer H) to make a 100 mL buffer solution at pH of 7.4.

Buffer J: Sodium phosphate buffer with 0.1% (w/v) of Tween 20 was prepared by mixing 0.88 g sodium chloride (MW: 58.4, Sigma Aldrich) and 0.1% w/v of Tween 20 with 80 mL of (Buffer H) to make a 100 mL buffer solution at pH of 7.4.

2.2 3D PRINTING: materials and methods

3D Printing was performed on a MakerBot Replicator 2X Experimental 3D printer (MakerBot Industries). Autodesk 123D Design Version 1.8.34 (Autodesk Inc. 2015) an open source 3D modelling software program was used to design the 3D printable objects, which were exported as STL files. MakerBot Desktop was used to slice STL files and convert to X3G format for printing. The 3D-printing filaments purchased are summarised in Table 2.1.

Kapton polyimide tape was purchased from MakerBot industries (MakerBot Europe GMbH & Co. KG, Germany). Eurocel blue masking tape (Blue Tape) and Build Tak were purchased from M.E.S (Metacad Engineering Solutions Ltd).

Table 2.1| **List of purchased 3D printer filaments used in this project**

3D printer filaments	Colour	Manufacturer	Purchased From
ABS (Acrylonitrile Butadiene Styrene)	White	MakerBot	MakerBot Industries
PC-ABS Alloy (Polycarbonate ABS Alloy)	White	Proto-Pasta	Metacad Engineering Solutions Ltd
3DXNano ABS	Black	3DXTech	Global FSD (3D Filament Sample Depot)
CF0 Carbon Fiber Reinforced ABS	Black	OO-Kuma	Global FSD (3D filament Sample depot)
PLA (Poly Lactic Acid)	White	MakerBot	MakerBot Industries
Conductive PLA	Black	Proto-Pasta	Metacad Engineering Solutions Ltd
Stainless Steel PLA	Silver	Proto-Pasta	Metacad Engineering Solutions Ltd
Magnetic Iron PLA	Silver	Proto-Pasta	Metacad Engineering Solutions Ltd
Carbon Fiber PLA	Black	Proto-Pasta	Metacad Engineering Solutions Ltd
Biofila Linen	Cream	Two-Bears	Global FSD (3D Filament Sample Depot)
HIPS	White	RepRapper Tech	Global FSD (3D Filament Sample Depot)
XT- Copolyester	White	ColorFabb	Global FSD (3D Filament Sample Depot)
T-Glase	Clear/ Transparent	Taulman 3D	Global FSD (3D Filament Sample Depot)
HD Glass	Clear/ Transparent	Formfutura	Global FSD (3D Filament Sample Depot)
Bridge Nylon	White	Taulman 3D	Global FSD (3D Filament Sample Depot)
SemiFlex	White	NinjaFlex™	Global FSD (3D Filament Sample Depot)
MakerBot Flexible	White	MakerBot	Global FSD (3D Filament Sample Depot)

2.3 ABS print settings

The MakerBot Replicator 2X is optimised for printing ABS filaments the default printing settings are listed in Table 2.2.

Table 2.2 | **Print setting for ABS filament on the MakerBot Replicator 2X**

			Print Quality		
			Low	Standard	High
Device Settings	Extruder Temperature Right (℃)		230	230	230
	Extruder Temperature Left (℃)		230	230	230
	Platform Temperature (℃)		110	110	110
	Travel Speed (mm/s)		150	150	150
	Z- axis Travel speed (mm/s)		23	23	23
	Minimum Layer Duration (s)		5	5	5
Extrusion Speeds	Bridges (mm/s)		40	40	40
	First layer (mm/s)		30	30	30
	First layer Raft (mm/s)		50	50	50
	Floor Surface Fills (mm/s)		90	90	90
	Infill (mm/s)		90	90	90
	Insets (mm/s)		90	90	90
	Outlines (mm/s)		40	40	40
	Raft (mm/s)		90	90	90
	Sparse Roof Surface Fills (mm/s)		90	90	90
Infill	Infill density		10%	10%	15%
	Infill pattern		Hexagonal	Hexagonal	Hexagonal
Model Properties	Layer Height (mm)		0.30	0.20	0.10
	Infill Layer Height (mm)		0.30	0.20	0.10
	Number of Shells (mm)		2	2	2
	Roof Thickness (mm)		0.8	0.8	1
	Floor Thickness (mm)		0.8	0.8	1
	Coarseness (mm^2)		0.0001	0.0001	0.0001
Multi- Material Printing	Support Material Extruder		0	0	0
	Raft Material Extruder		0	0	0
	Purge Wall Settings	*Front Wall length (mm)*	30	30	30
		Side length (mm)	4	4	4
		Wall Pattern Width (mm)	2	2	2
		Base Pattern Length (mm)	10	10	10
		Base Extrusion Width (mm)	2.0	2.0	2.0
		Base Pattern Width (mm)	8	8	8
		Wall Width (mm)	0.5	0.5	0.5
		Wall to Wall Spacing (mm)	1.0	1.0	1.0
		Wall to Model Spacing (mm)	2.0	2.0	2.0
Raft	Raft to Model Spacing (mm)		0.35	0.35	0.35
	Raft Margin (mm)		4.0	4.0	4.0
	Base Layers	*Minimum Base Pattern Gap (mm)*	0	0	0
		Base Pattern Spacing (mm)	0.8	0.8	0.8
		Base Pattern Length (mm)	15.0	15.0	15.0
		Base Layer Angle (degree)	0	0	0
		Base Layer Density	0.70	0.70	0.70
		Base Extrusion Width (mm)	2.5	2.5	2.5
		Base Layer Height (mm)	0.30	0.30	0.30
	Interfaces Layers	*Interfaces Layer Angle (degree)*	45	45	45
		Interfaces Layer Density	0.30	0.30	0.30
		Interface Extrusion Width (mm)	0.40	0.40	0.40
		Interface Layer Height (mm)	0.27	0.27	0.27
	Surface Layers	*Number of Surface Layer Shells*	2	2	2
		Surface Layer Angle (degree)	0	0	0
		Surface Layer Height (mm)	0.20	0.20	0.20
Supports and Bridging	Extra Support	*Support Density*	0.20	0.20	0.20
		Support Margin (mm)	0.5	0.5	0.5
		Support to Model Spacing (mm)	0.4	0.4	0.4
		Support Roof to Model Spacing (mm)	0.4	0.4	0.4
		Support Angle (degree)	68	68	68
		Support Layer Height (mm)	0.3	0.3	0.3
	Bridging	*Maximum Bridge Length (mm)*	80.0	80.0	80.0
Right Extruder	Filament Diameter (mm)		1.77	1.77	1.77
	Retraction Distance (mm)		1.3	1.3	1.3
	Retraction Speed (mm/s)		25	25	25
	Restart Speed (mm/s)		25	25	25
	Extra Restart Distance (mm)		0	0	0
	Extra Restart Speed (mm/s)		25	25	25
Left Extruder	Filament Diameter (mm)		1.77	1.77	1.77
	Retraction Distance (mm)		1.3	1.3	1.3
	Retraction Speed (mm/s)		25	25	25
	Restart Speed (mm/s)		25	25	25
	Extra Restart Distance (mm)		0	0	0
	Extra Restart Speed (mm/s)		25	25	25

2.4 Custom 3D-printer settings

Table 2.3 outlines the modifications that were made to the standard ABS print settings to print the filaments listed in Table 2.1.

Table 2.3| **Final print setting to print with listed 3D filaments on the MakerBot Replicator 2X**

3D Printer Filaments	Device Settings		Extrusion Speeds				
	Extruder Temperature °C (Right & Left)	Platform Temperature °C	Bridges (mm/s)	First Layer (mm/s)	Infill (mm/s)	Insets (mm/s)	Outlines (mm/s)
ABS	**230**	**110**	40	30	90	90	40
PC-ABS Alloy	**255**	**125**	40	30	90	90	40
3DXNano ABS	**240**	**110**	40	30	90	90	40
PLA	**220**	**70**	40	30	90	90	40
Conductive PLA	**230**	**50**	40	30	90	90	40
Stainless steel PLA	**220**	**50**	40	30	90	90	40
Magnetic Iron PLA	**195**	**50**	40	30	90	90	40
Carbon Fiber PLA	**235**	**110**	40	30	90	90	40
Biofila linen	**220**	**70**	40	30	90	90	40
HIPS	**240**	**110**	40	30	90	90	40
XT- Copolyester	**240**	**70**	40	30	90	90	40
T-Glase	**210**	**55**	40	30	90	90	40
HD Glass	**225**	**45**	40	30	30	30	30
Bridge Nylon	**230**	**50**	40	30	30	30	30
SemiFlex	**220**	**50**	40	30	30	30	30
MakerBot Flexible	**100**	**0**	40	30	90	90	40

Optimal adherence of 3D prints to the build platform was achieved by 3D printing on a Kapton polyimide tape for ABS, PLA, Semi-Flex and MakerBot flexible. Blue tape was also used on top of Kapton tape for 3DXNano ABS, conductive PLA, stainless steel PLA, magnetic iron PLA, carbon fibre PLA, Biofila linen, HIPS, and XT-Copolyester. Build Tak was used for PC ABS Alloy, T-Glase, HD Glass and Bridge Nylon.

2.5 Thermoplastic cuboids

Thermoplastic cuboids (9.5 mm W x 9.5 mm L x 2.5 mm H) (Figure 2.1) were printed with a total surface area of 275.5 mm^2. Cuboids were printed at 10% infill, 50%, and 100% infill, as per the specific needs of the study being undertaken.

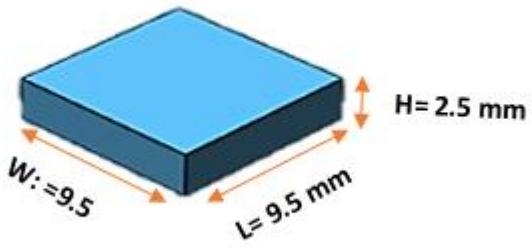

Figure 2.1| **Schematic diagram of thermoplastic cuboid**

2.6 Thermoplastic cuboid integrity: print shrinkage and visual inspection by optical microscopy

Thermoplastic cuboids (Figure 2.1) were analysed to test material shrinkage in X, Y, and Z directions using Vernier calipers (RS Pro150 mm Digital Caliper 0.0005 in, 0.01 mm, UK). Analysis of the surface of the thermoplastic insert was performed using a Moticam Stereo microscope 3.0 MP (Motic Deutschland GmbH; SMZ168 C 0.65x, Germany) at 0.75x and 2x magnifications. The microscope was fitted with photonic PL3000 light, Motic digital image capture and Alicona TEX 1.4.2 reconstruction analysis software (Aicona Imaging GmbH, Austria). The surface of the thermoplastic cuboids was wiped clean with Kimwipe before images of the surface were taken.

2.7 Measuring liquid absorption by immersed thermoplastic cuboids

Thermoplastic cuboids (Figure 2.1) were weighed separately and then placed individually inside a 20 mL container, submerged in 3 mL of purified water or 3 mL (Buffer A). Cuboids were left in solutions at 20 °C for three days, removed, and the surface was wiped with a tissue. The mass after immersion was measured.

2.8 Determination of the contact angle of water drops on 3D printed surfaces

The contact angle of water droplets on the 3D printed thermoplastic cuboids (Figure 2.1) surface was measured using a contact angle goniometer OCA15 plus (a video-based optical contact angle measuring device) running firmware version SCA20 software for OCA. The surface of the thermoplastic cuboids was wiped clean with a Kimwipe before the measurements were taken. Hamilton microliter syringes (DS 500/GT, Gaslight 500 µL) were fixed on the goniometer. The syringe was filled with purified water and rinsed three times before use. A dispensing volume of a water droplet of 5.000 µL at a rate of 0.50 µL/s was used. Images of the droplets were taken after 10 minutes at ambient temperature and three times for each thermoplastic cuboid. Contact angles were determined using both the right and left drop side according to the captive drop method and pendant drop method (Kwok DY & Neumann AW, 1999). Contact angles measurement for the thermoplastic cuboids determined in triplicate. Data were collected, and the average and standard deviation of the droplet contact angle was calculated for each 3D printed thermoplastic cuboid.

2.9 Nonspecific binding of ds-DNA and BSA to 3D printing materials determined by UV visible spectroscopy

2.9.1 Preparation of ds-DNA and BSA solutions

A stock ds-DNA solution of 1 mg/mL was prepared by dissolving 0.02 g of dsDNA (low molecular weight salmon sperm lyophilised powder, Sigma Aldrich) in 20 mL of Buffer A, stirring for 2 hours at 20°C. Subsequently, from these stock ds-DNA solutions of 1.25 µg /mL, 12.5 µg /mL and 50 µg /mL were prepared.

Bovine Serum Albumin (BSA) lyophilised powder ≥ 96% (Sigma Aldrich) solution concentration of 1.5 mg/mL was prepared by dissolving 0.03 g of BSA lyophilised powder in 20 mL of Buffer A. BSA solution was stirred for 1 hour at 20°C. BSA solutions with concentrations of 12.5 µg/mL and 0.5 mg/mL were prepared from this stock solution.

2.9.2 Assessment of ds-DNA and BSA non-specific binding to 3D printed thermoplastics

Thermoplastic cuboids (Section 2.5) were placed inside the cuvette and submerged in 3 mL of ds-DNA or BSA solution in Buffer A. Herasil quartz absorption cuvettes with a path length of 10 mm and 3500 µL chamber volume (Sigma Aldrich) were used throughout. ds-DNA and BSA absorbances were measured at 260 nm and 279 nm respectively. Measurements were taken every 10 seconds for 5 minutes for each solution. Solutions were re-measured every 55 minutes up to 4 hours.

Initial and final optical absorbance spectra were recorded from 200 nm to 800 nm for each solution to assess any possible leeching into solution from the thermoplastic cuboids. Experiments were performed in triplicate. Data were analysed using mean values, standard deviation, and was re-drawn in Excel as UV-Vis spectra.

2.10 Decanting liquids into 3D prints using a bespoke syringe extruder for the MakerBot Replicator 2X

2.10.1 Syringe extruder fabrication and assembly

The syringe extruder for the MakerBot Replicator 2X experimental printer was adapted from the universal paste extruder, an open source design (Thingiverse.com, 2018). Figure 2.2 shows images of the 3D printed parts; a plastic extruder body (Figure 2.2.A), idler block (Figure 2.2.B), gears and drive set (motor gear (Figure 2.2.C), big gear (Figure 2.2.E), double gear (Figure 2.2.F), belt pulley (Figure 2.2.G), syringe pressure block/cap (Figure 2.2.H) and NEM17 motor (Figure 2.2.D).

Other parts required; 5x M3 (10 mm) bolts, 4 x 624 bearings, 1 x 608 bearing, 20 mm M8 smooth rod, M3 set screw, 6 x M3 nuts, 2x springs (30 mm), 2 x M3 (45 mm) bolt, 1x M3 (60 mm) bolt, 7 x M3 washer, 2 x M4 (75 mm) bolt, 1x M4 (55 mm) bolt, 1x M4 (20 mm), 4 x M4 washers, 4x M4 nylock nuts, 2x M4 plain nuts 1x 6 mm wide T5 belt (40 cm) where purchased from the Nut & Bolt Store Ltd, Hove.

A Replicator 2X NEMA17 hybrid stepper motor with 5 mm diameter shaft was purchased from Robot shop (RobotShop inc, USA).

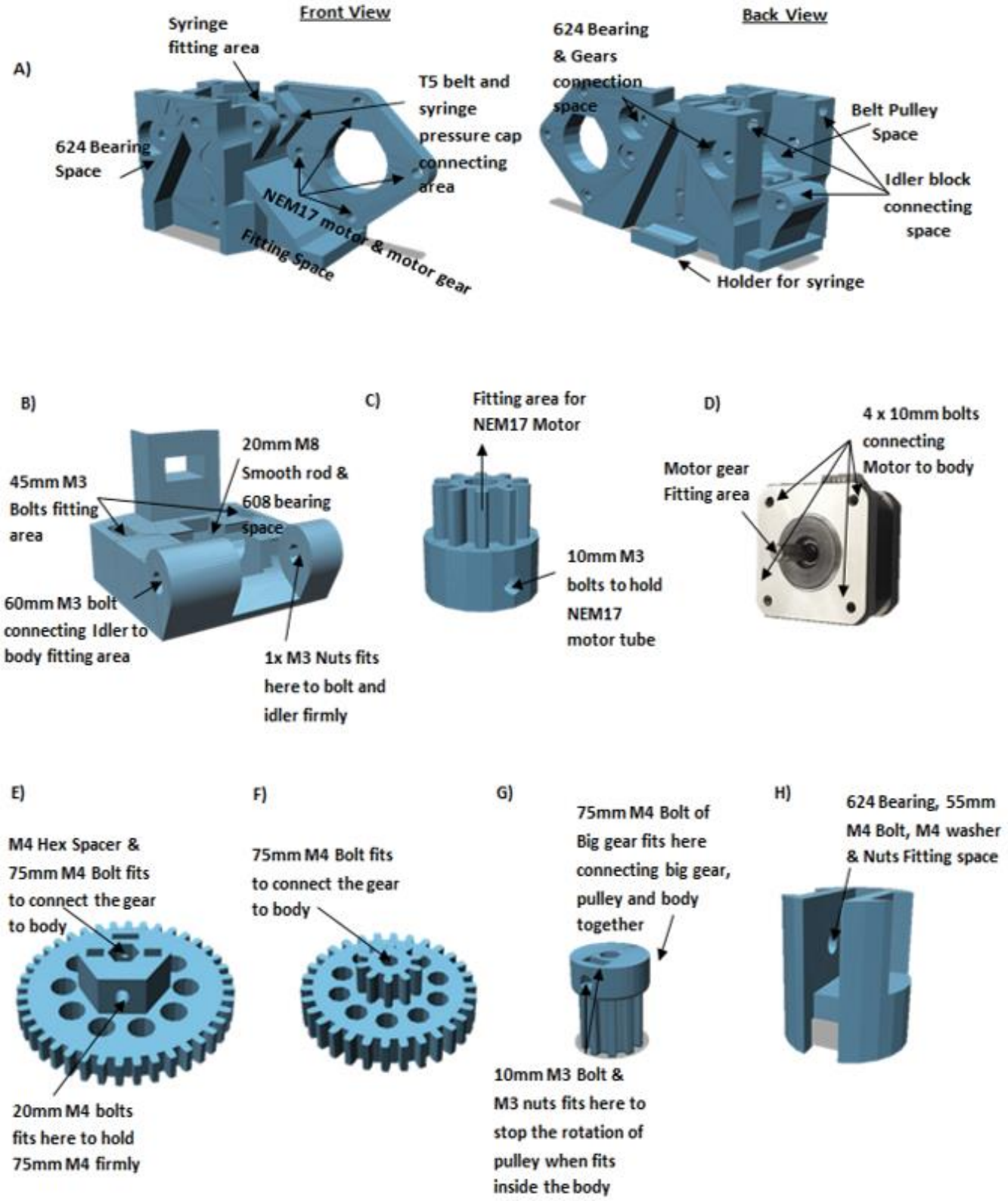

Figure 2.2| **Represent CAD design of parts made-up syringe-based extruder:** A) Body of extruder [47.21(mm) W x 100 (mm) L x 57.5 (mm) H] front view and back view. B) Idler block [38.225(mm) W x 48 (mm) L x 30.225 (mm) H]. C) Motor gear [20.0(mm) W x 20.0 (mm) L x 19 (mm) D) NEMA17 hybrid stepper motor. E) Big gear [58.31(mm) W x 58.31 (mm) L x 12.5(mm) H]. F) Double gear [44.4(mm) W x 44.4 (mm) L x 14

The 3D printing of syringe extruder parts where performed by using the ABS standard setting, slices (Figure 2.2, B, G, H) printed with 10% infill density, and slices (Figure 2.2, A, C, E, F) were printed at 50% infill density. Figure 2.3 shows images of printed parts to make the syringe extruder. Figure 2.3 and 2.4 show steps taken in assembling the syringe extruder.

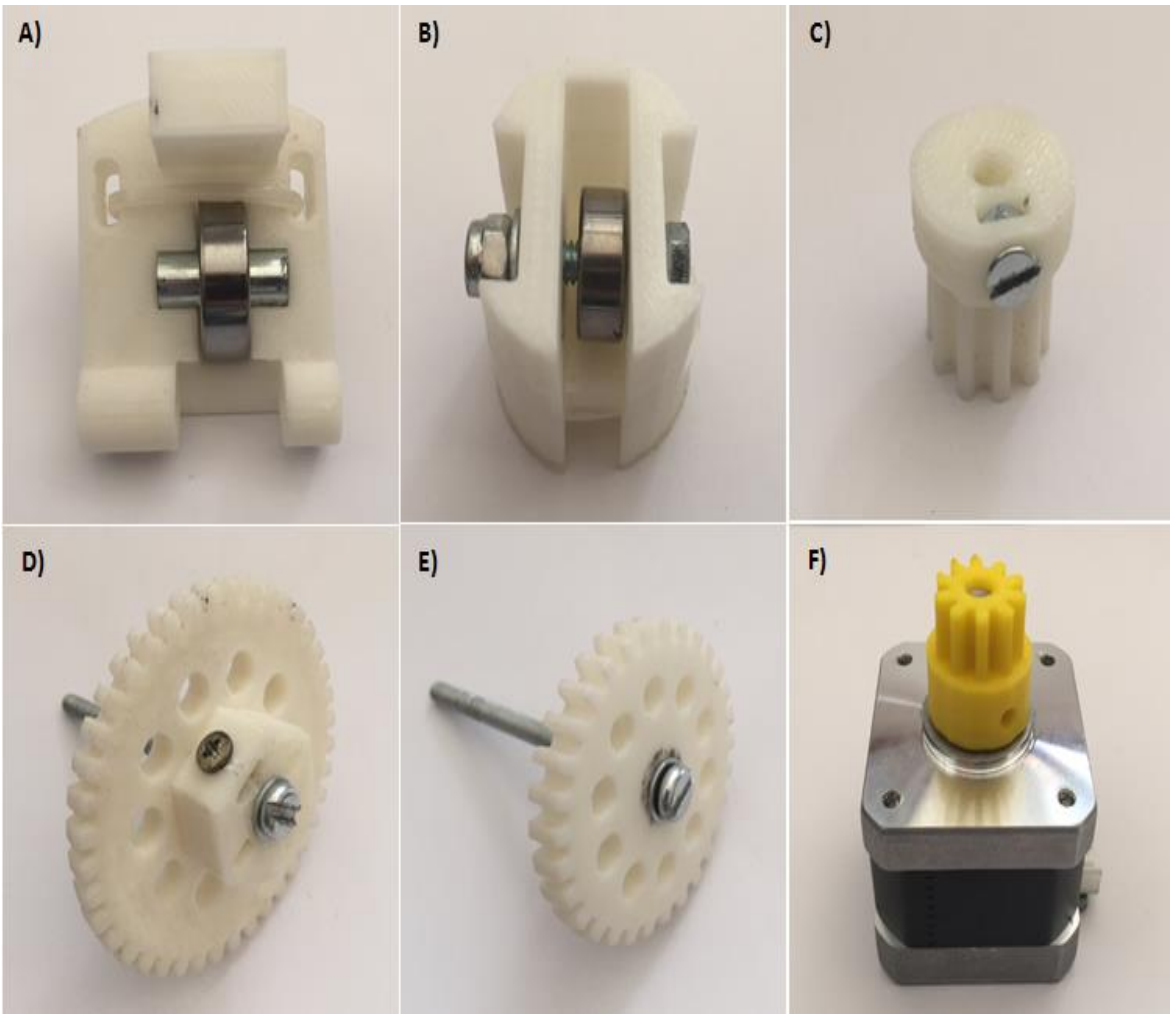

Figure 2.3 | **Images of parts used for making syringe based extruder:** A) Idler block [38.225(mm) W x 48 (mm) L x 30.225 (mm) H]. B) Syringe pressure cap [26(mm) W x 27.31 (mm) L x 26.8 (mm). C) T5 Belt Pulley [18(mm) W x 18 (mm) L x 15 (mm). D) Big gear [58.31(mm) W x 58.31 (mm) L x 12.5(mm) H]. E) Double gear [44.4(mm) W x 44.4 (mm) L x 14 (mm) H]. F) NEMA17 hybrid stepper motor and Motor gear [20.0(mm) W x 20.0 (mm) L x 19 (mm). The size of bolts and nuts used in A-F are explained below.

2.10.1.2 Breakdown of syringe extruder assembling steps showing in Figure 2.3

A) 20 mm M8 horizontal rod was placed inside the 608 bearing for idler (Figure 2.3.A).

B) 55 mm M4 bolt was placed inside the 624 bearing and fit inside the syringe pressure cap. The bolt was secured with an M4 washer and M4 nylock nut (Figure 2.3.B).

C) 10 mm M3 bolt and M3 nut were used for T5 belt pulley (Figure 2.3.C).

D) 75 mm M4 bolt, M4 washer was fitted inside the big gear. M4 nuts and a 20 mm M4 bolt were used to hold the 75 mm M4 bolt firmly in place (Figure 2.3.D).

E) 75 mm M4 bolt, M4 washer was fitted inside the double gear (Figure 2.3.E).

F) Motor gear was placed on a NEMA17 hybrid stepper motor and was fixed firmly by using a 10 mm M3 bolt and M3 nut (Figure 2.3.F).

The syringe extruder was assembled in 4 steps. Figure 2.4 outlines steps taken for assembling the syringe extruder. Arrows are used in Figure 2.4 to outline the changes take place at each point.

2.10.1.3 Breakdown of syringe extruder assembling steps showing in Figure 2.4

1. The motor was fixed on extruder body using 4 x 10 mm M3 bolts (Figure 2.4.1, black arrows). 3 x 624 bearings were fitted on the body (Figure 2.4.1, blue arrows). 60 mm M3 bolt, 2x M3 nuts and an M3 washer where used to connect the idler to the extruder body (Figure 2.4.1, red arrows).

2. A 75 mm M4 bolt and M4 washer were fitted inside the big gear (Figure 2.4.2, red arrows). The big gear was joined to body through the 624 bearing. A 75 mm M4 bolt was also fitted inside the T5 belt pulley and was fixed with an M4

Nylock nut (Figure 2.4.2, black arrows). Once the T5 belt pulley is fitted, the 10 mm M3 bolt inside the pulley is screwed firmly into place.

3. A 75 mm M4 bolt, M4 washer where fitted inside the double gear. The double gear was joined to the body through a 624 bearing and was fixed using two M4 nuts (Figure 2.4.3, red arrows). At the same time, a 5 mm (W) x 40 mm (L) T5 belt was fitted inside the syringe extruder. The 75 mm M4 bolt of the double gear holds the T5 belt in place. T5 is then fitted inside syringe pressure cap (Figure 2.4.3, blue arrows), retained under T5 belt pulley, throw 608 bearing of the idler and subsequently joined to the back of idler (Figure 2.4.3, black arrows).

4. 2x M3 nuts were placed in the extruder body; the inside region is indicated by black arrows in (Figure 2.4.4). Then 2x springs (30 mm) and 2 x M3 (45 mm) bolts were used to hold the idler block to the body. An M3 washer and black 5 mm radius circular rubber were used to hold the spring in place. Finally, a standard 10 mL luer lock syringe was placed inside the syringe extruder as shown in Figure 2.4.4 One Fintip flex 200 pipette tip, was cut to 10 mm in length and fitted to the syringe nozzle.

5. Syringe Fintip flex 200 pipette tips were replaced with a 14 G Hamilton metal hub luer lock and 51 mm needle (Sigma Aldrich) later on in this project for an increase in accuracy when decanting solutions.

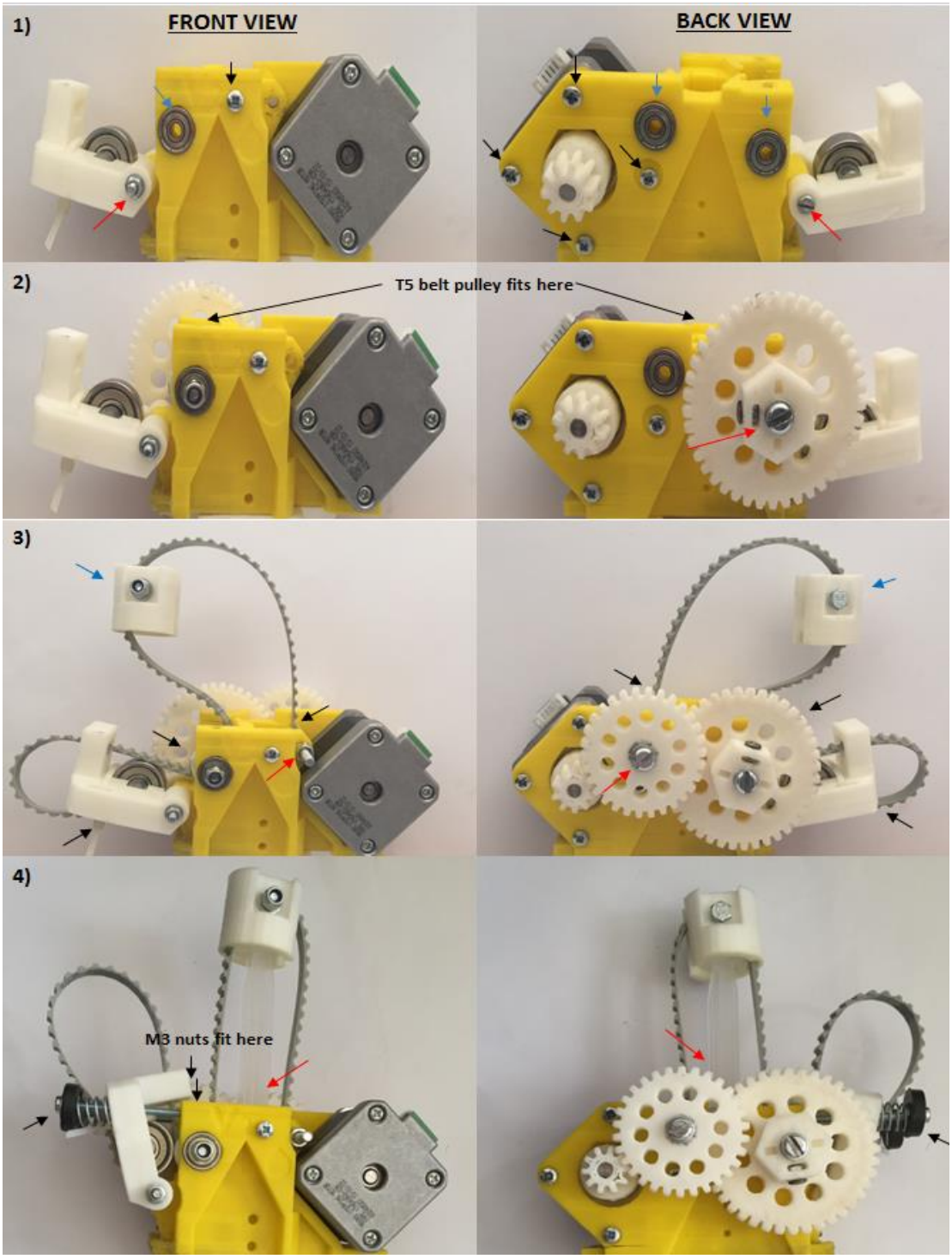

Figure 2.4| **Images of steps taken for assembling syringe extruder parts:** refer to Figures 2 and 3 for more information of parts dimensions and bolt and nuts used for each part.

2.10.2 Modification of the MakerBot Replicator 2X for syringe based extrusion

The MakerBot Replicator 2X experimental 3D printer was modified to enable syringe extrusion by disassembling the left extruder of the 3D printer. The filament guide tube, fan guards, extruder fan, nozzle, lever arms, cartridge heaters, thermal cores, drive blocks, extruder motor and heat sinks were removed in accordance to MakerBot Replicator manual guide (MakerBot User Manual 2015).

To attach the syringe extruder to the MakerBot Replicator 2X printer, a bespoke interface was printed in PLA filament at 10% infill level. The syringe extruder was then bolted to this interface, shown in Figure 2.5. Model A in Figure 2.5 was designed in a similar shape to a NEMA17 stepper motor (Figure 2.3.F) and was connected to extruder fan via 2 x M3 90 mm nuts. The syringe extruder was fixed on the second model B using super glue.

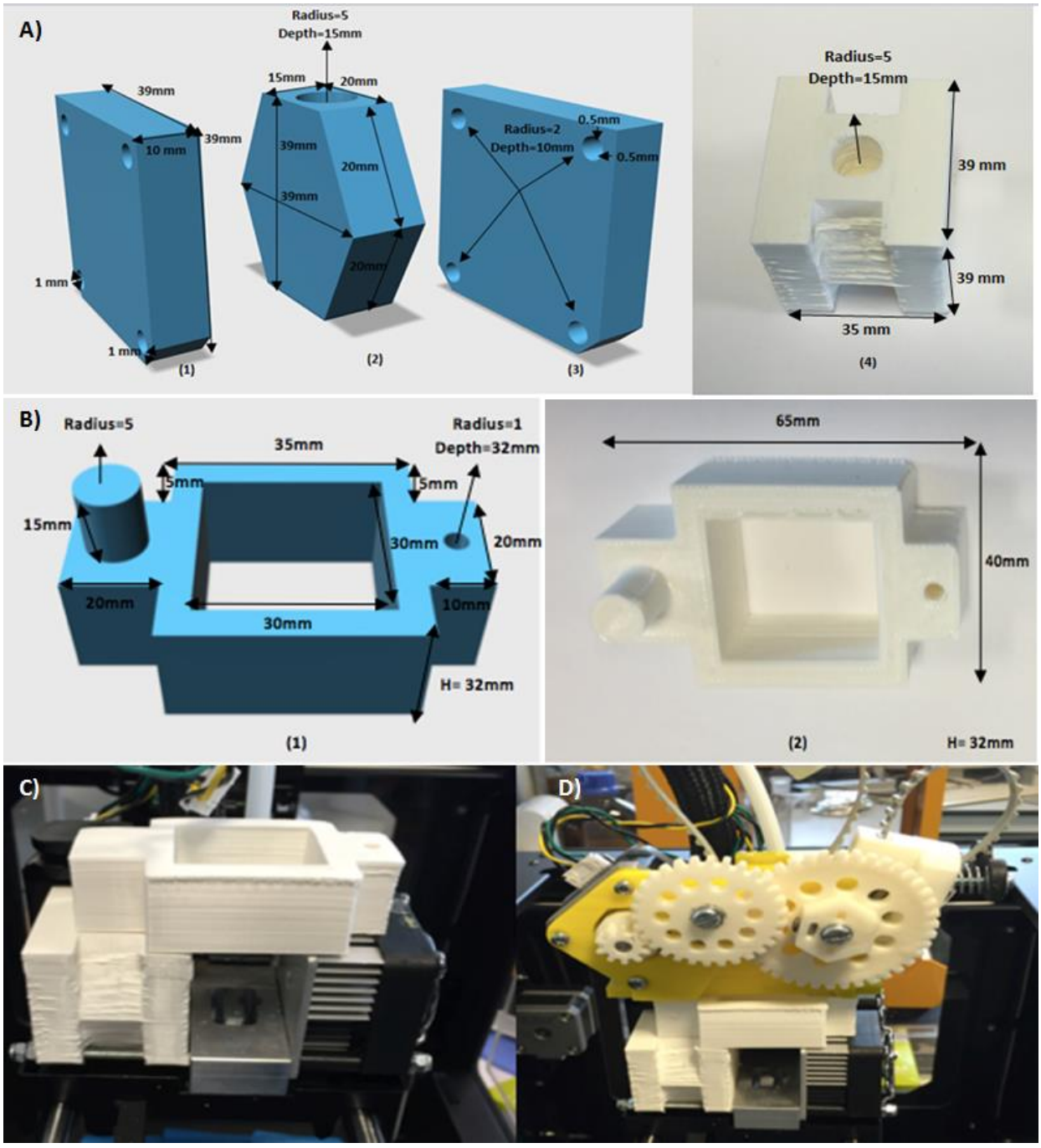

Figure 2.5| **Representation of CAD designs of syringe extruder holder models along with photography of printed model, models and syringe extruder adjustment on the 3D printer:** A) Replacements part made to fill motor space on the extruder. Design made in three pieces 1, 2, 3 joined together to construct the actual model (4). B) Supports design made to keep syringe extruder stable on 3D printing device C) Photography of part A and B fitted on the 3D printing device. D) Photography of syringe extruder assembled on models made on the 3D printing device.

2.10.3 Levelling of syringe-extruder syringe tip height

It is critical that the tip of the syringe extruder in place of the left extruder is the same height as the right extruder nozzle. Hexagonal shaped syringe supports were printed with ABS filament at 25% infill. The object was printed with a height of 2 mm (see Figure 2.6) and was placed on the syringe extruder at the region where the syringe is inserted, to adjust the height of the extruder printing point. Figure 2.6 represents the CAD design of the printed syringe holder support, on the extruder. It also shows the side view of the extruders where the extruder nozzle is at the same height as the syringe extruder tip. The height of designed syringe holder supports was reduced to 1mm when 14 G Hamilton metal hub (luer lock) 51 mm needle was used in syringe extruder to print solutions.

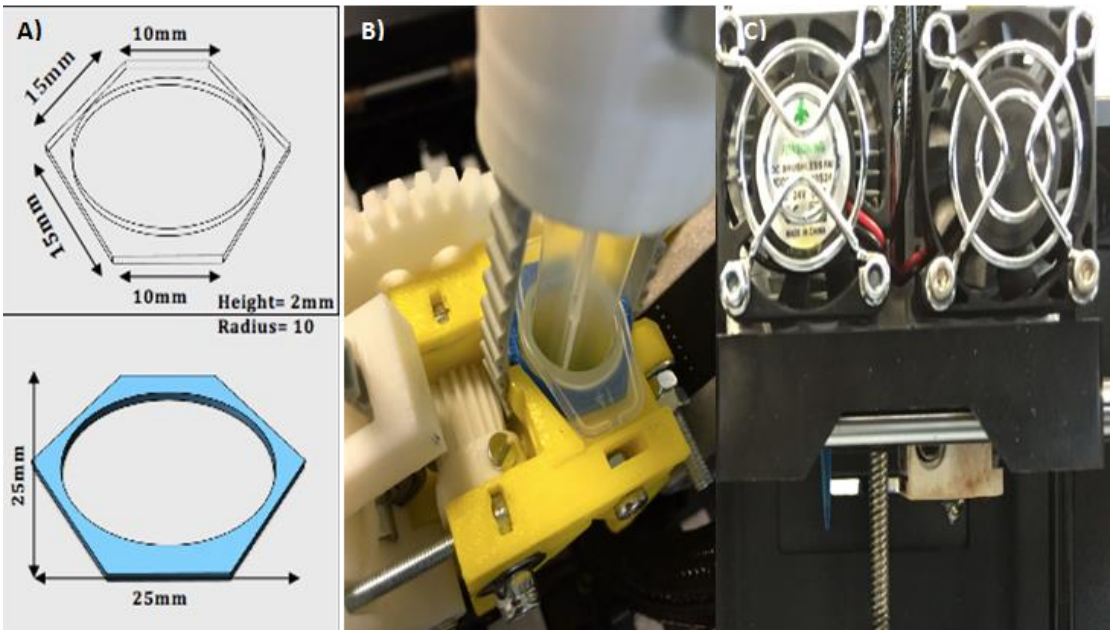

Figure 2.6| **Syringe extruder holder for adjusting syringe height level:** A) CAD designs of syringe holder support made B) syringe holder support on syringe based extruder C) Side view of extruder showing right extruder nozzle and syringe extruder printing tip.

2.10.4 Modification of the NEMA17 motor rotation direction for syringe extrusion

The wiring pattern of the left extruder of the MakerBot Replicator 2X experimental printer was altered for to enable the stepper motor to rotate in the opposite direction to normal. The motor rotation was modified to rotate anticlockwise by altering the arrangement of the four wires connecting to the motor through connecting the wires labelled C in (Figure 2.7) to wire D.

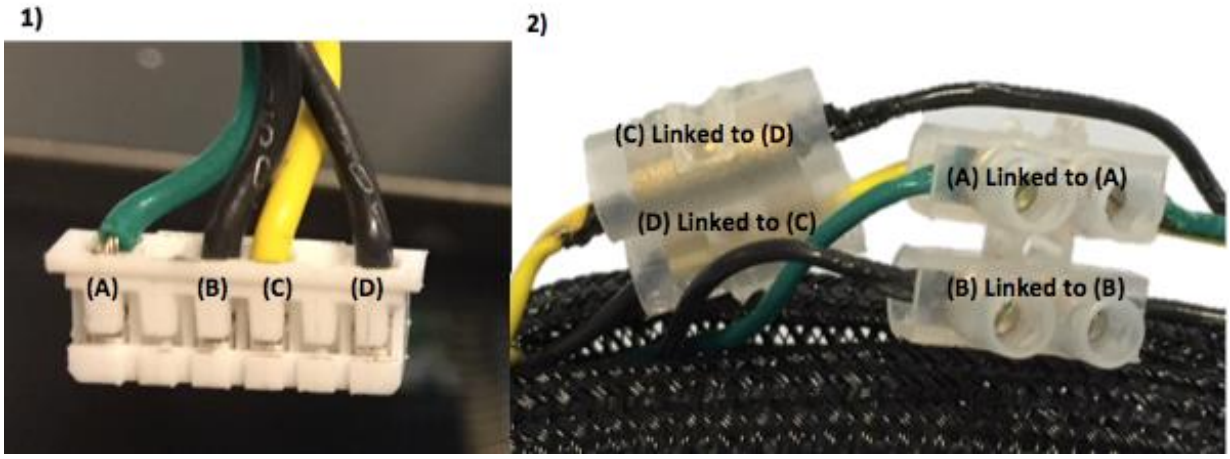

Figure 2.7| **Image of MakerBot Replicator 2X experimental wires connecting to the left extruder and modified wire orientation**: 1) The actual left extruder wires connected to the extruder with labeled wire pattern A to D. 2) modification made to wires for change in motor rotation. The only orientation of wires labeled C and D where changed.

2.10.5 Liquid decanting onto 3D prints

Primary liquid decanting tests onto 3D prints were accomplished using the syringe extruder filled with a mixture of 10 mL of deionised water and five drops of PME Blue concentrated 25G food colouring (Tesco).

No software modifications were necessary to decant solutions with the syringe extruder, and the parameters for ABS printing were used as listed in Table 2.2. Tests were carried out using ABS or PLA as the support material printed with right extruder and liquids were decanted via the left extruder using the dual extrusion capability 3D printing settings for dual extrusion were unchanged except that the purge wall was turned off.

Table 2.4 outlines the modifications that were made to the standard ABS print settings (Table 2.2) for printing liquid using syringe extruder.

Table 2.4| **Print settings to print with syringe extruder on the MakerBot Replicator 2X.** Right extruder temperature and platform temperature is for printing as dual extrusion with ABS filament.

		Print Quality
		Standard
Device Settings	**Extruder Temperature Right** (℃)	**230**
	Extruder Temperature Left (℃)	**0**
	Platform Temperature (℃)	**110**
	Travel Speed (mm/s)	**175**
	Z- axis Travel speed (mm/s)	**23**
	Minimum Layer Duration (s)	**5**
Infill	**Infill density**	**10%**
	Infill pattern	**Linear**
Model Properties	**Layer Height (mm)**	**0.20**
	Infill Layer Height (mm)	**0.20**
Multi-Material Printing	**Purge Wall Settings**	**Turned off**
Left Extruder	**Filament Diameter (mm)**	**1.77**
	Retraction Distance (mm)	**1.3**
	Retraction Speed (mm/s)	**150**
	Restart Speed (mm/s)	**100**
	Extra Restart Distance (mm)	**0**
	Extra Restart Speed (mm/s)	**0**

2.11 Assessing the biocompatibility of 3D printer filaments within enzymatic assays

2.11.1 Circular thermoplastic insert for 96 well flat-bottom plates

Circular thermoplastic inserts were printed as a cylinder of 2 mm (D) x 1 mm (H) (Figure 2.8) using ABS, PLA and HD Glass filaments at 100% infill using the custom printing settings determined previously (Section 2.4).

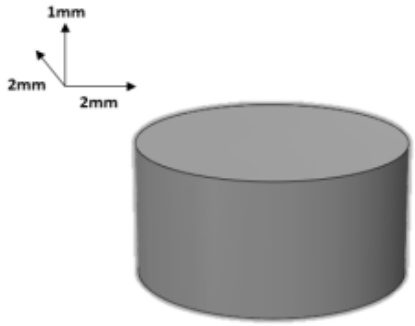

Figure 2.8| **Schematic diagram of a circular thermoplastic insert**

2.11.2 Compatibility of the lactose assay with 3D printed thermoplastics

A MAK017 lactose assay kit containing components of; lactose assay buffer (25 mL), probe in DMSO (0.2 mL), lactase (1 vl), lactose enzyme mix (1 vl), HRP (1 vl), lactose standard, 100 nMole/ µL (0.1 mL) was purchased from Sigma Aldrich. Components were prepared according to the manufacturer's standard protocol, summarized below.

2.11.3 Procedure for the lactose assay in the presence of 3D printed circular thermoplastic insert

Using assay kit components, a 1 nmol/L standard solution was prepared by mixing, a 10 µL of 100 nmol/µL lactose standard with 990 µL of lactose assay buffer. Next, a 96 well flat-bottom plate were filled with 0, 2,4,6,8, and 10 µL of 1 nmol/L lactose standard solution and the volume of each well was made to 50 µL with the lactose assay buffer.

The 3D printed circular thermoplastic inserts were placed in the wells that contain the solution. 2 µL of lactase were added to all of the wells apart from the wells with zero standard solution. To the well with zero standard solution wells, a 2 µL of lactose assay buffer was added to maintain the volume of the wells as equal. Next, 50 µL of a master reaction mix (44 µLof lactose assay buffer, 2 µL of the probe, 2 µL of lactose enzyme mix and 2 µL HRP) was added to each well and was mixed by pipetting. The 96-flat bottom plate was covered with a thin aluminum foil, and the reaction was incubated for 60 minutes at 37℃.

Circular thermoplastic inserts were removed from the wells before measurement. The optical absorbance measurements were made using a BioTek Synergy HT multi-detection microplate reader and Gen5 software. The BioTek plate reader was set to measure at the wavelength of 570 nm for colourimetric lactose assay solutions.

The background of the assay which was the value obtained for the zero-lactose standard (blank) was subtracted from all of the reading using Microsoft Excel. Experiments were performed in quadruple. Data were collected, and the average and standard deviation of the enzymatic assay were calculated for each 3D printed thermoplastic inserts.

2.12 Developing and testing biological inks for 3D printers

2.12.1 GOD assay protocol

Preparation of samples

Reagent A: *o*-Dianisidine solution (0.21 mM) was prepared by dissolving 50 mg of *o*-dianisidine dihydrochloride in 7.6 mL of deionised water. The solution was further diluted in 1.0 mL to 100 mL ratio with Buffer B to make 0.21 mM *o*-dianisidine solution.

Reagent B: A 50 mL of D(+)-glucose substrate solution 10% w/v was prepared by dissolving 5 g of D(+)-glucose in 50 mL of deionised water. The glucose substrate solution was prepared 24 hrs before starting the assay and was left at the room temperature so that the mutarotation of D(+)-glucose shifts from the α to β-anomer.

Reagent C: 0.17 mM *o*-Dianisidine and 1.72% w/v glucose solution (the 'reaction cocktail') was prepared immediately before use. A 29 mL solution was prepared by combining 24 mL of Reagent A with 5 mL of Reagent B. The pH was adjusted to 5.8 if necessary with freshly prepared 1 M HCl or 1 M NaOH.

Reagent D: A solution containing 60 purpurogallin units/mL of HRP was prepared in cold deionised water. The HRPs enzyme was stored in a 1 mL vial and kept at -20°C freezer.

Reagent E: A solution containing 0.8 mg/mL of GOD was prepared in Buffer C and stored in a 1 mL vials at -20 °C.

2.12.2 Protocol for the GOD assay

The GOD assay was carried out according to Bergmeyer (Bergmeyer et al., 1974). In a 3 mL cuvette, 2.90 mL of freshly prepared Reagent C was mixed with 100 µL of a

solution of 60 purpurogallin units/mL of HRP. Next, the cuvette was placed inside a UV-Vis spectrophotometer, and the device was zeroed. Measurements at 500 nm were made immediately after the addition of 100 μL of 0.8 unit/mL solutions of Reagent G.

The glucose oxidase assay was carried out on samples of 3D printing materials. Thermoplastic cuboids (Figure 2.1) were printed of each filament using custom 3D printer setting (Table 2.3). The thermoplastic cuboid was placed inside of the cuvette and subsequently submerged in 3 mL glucose oxidase assay solution to determine if the activity of the enzyme is inhibited in the presence of 3D printed materials.

Measurements were taken every 10 seconds for 5 minutes for each of the individual samples. Spectra wavelength from 200 nm to 800 nm was recorded for the individual assay. Experiments were performed in a triplicate for every solution.

2.12.3 Protocol for conjugating GOD to AuNP

AuNP dispersion of 20 nm and 50 nm with a concentration of 0.80 nM (determined by measuring the absorbance at 520 nm according to Beer's Law) were used for this study.

2.12.3.1 Reaction mixture solutions

1. MUA solution: (0.5 mM) in 1:3 ethanol/ H_2O. (The MUA solution was prepared in a mixture of (25 mL ethanol/75 mL water) using 11-mercaptoundecanoic acid.

2. EDC: NHS mixture: 50 mM (NHS) and 200 mM (EDC). Immediately before use, 4 mL of the reaction mixture was prepared by dissolving 23.01 mg of NHS and 153.36 mg of EDC in deionised water.

3. GOD 0.8 mg/mL solution: was prepared in Buffer E, at pH 6.8.

2.12.3.2 Preparation of alkanethiol MUA-modified AuNPs

In a 1.5 mL vial, 0.5 mL of a citrate-stabilised AuNP dispersion (approx. 0.8 nM) was added to 0.5 mL of Buffer D. The mixture was incubated for 30 minutes to allow for monolayer physisorption of Tween 20 to the AuNPs to be completed. Subsequently, 0.5 mL of 0.5 mM MUA solution was added to the mixture, followed gentle shaking on an orbital shaker at 100 rpm for 5 hours for complete chemisorption of alkanethiol onto the gold surface (Figure 2.9,Step 1). The mixture was centrifuged (2 min at15100 g) and excess alkanethiol removed with pipette without disturbing the supernatant. The supernatant was resuspended in 0.5 mL of Buffer D.

2.12.3.2.2 Fabrication of GOD – AuNPs

Fabrication of GOD – AuNPs was facilitated by reacting the MUA-modified AuNps with 0.5 mL of EDC: NHS mixture (Figure 2.9, Step 2). Orbital shaking at 50 rpm was used to mix the reaction mixture gently for 30 minutes, followed by centrifugation for 3 min at 15100 g). The excess buffer was removed, and the reaction mixture was suspended in a 0.5 mL of Buffer D. An ultrasonicator was used to disperse the as-formed NHS-terminated AuNPs. Next, the reaction mixture was centrifuged for 3 min at 15100 g, the excess NHS-terminated in solution removed with a pipette without disturbing the supernatant and resuspended in Buffer D. After resuspension, NHS-terminated AuNPs were incubated with 0.8 mg/mL GOD for 12 hours or longer (Figure 2.9, Step 3). At this stage, vials containing the reaction mixtures were placed under a nitrogen atmosphere, and the other was without nitrogen treatment. The resultant mixture was centrifuged for 3 min at 15100 g to discard the free GOD and washed with Buffer D. The target GOD/AuNPs bioconjugates were dispersed (5 min) under ultrasonication in Buffer F and stored at 4°C. Experiments were performed in in quadruplet: two vials with nitrogen treatment and two without nitrogen treatment.

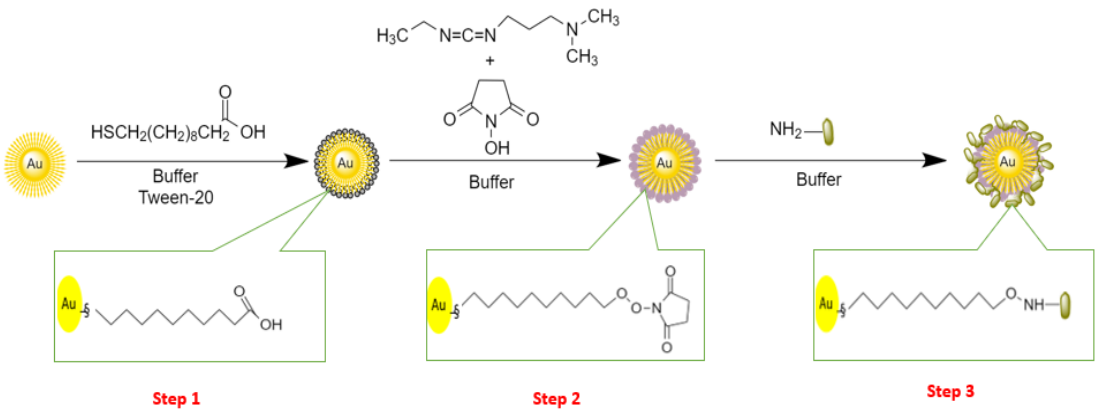

Figure 2.9| **Schematic illustration of the fabrication of the GOD/AuNPs bioconjugates**

2.12.3.3 GOD Enzymatic activity assay of GOD – AuNP

The enzymatic activity of the 20 nm and 50 nm diameter GOD – AuNPs was assessed using the method detailed in section 2.12.2 by replacing the GOD with GOD – AuNP bio-ink in the assay. The volume of the reagent used for this assay was modified to assay the GOD enzyme activity in 1 mL plastic cuvette by dividing the reagent volume by detailed in Section 2.12.1 by the factor of three.

2.12.3.4 Assay the activity of GOD – AuNPs in 3D printed devices

2.12.3.4.1 3D printing device design and printing setting

A 3D printed device that fits inside of a standard plastic cuvette was designed (Figure 2.10). The design was a 9.5 mm (W) x 45 mm (L) x 9.5 mm (H) cuvette with an internal volume space of 1.5 mL. A rectangular opening was placed to allow the cavity to fill directly from the syringe extruder.

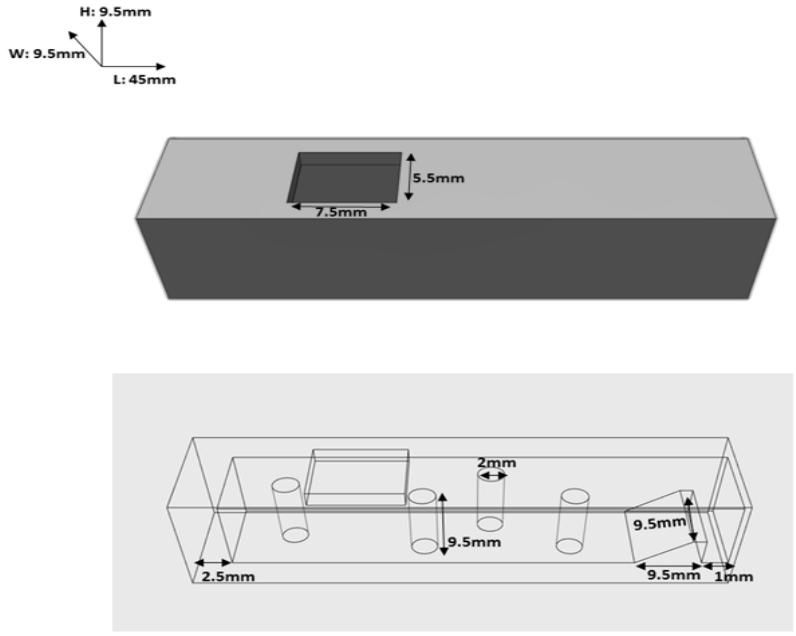

Figure 2.10| **Schematic (CAD design) of the 3D printing device, prepared for assessing GOD – AuNP and HRP – AuNP immobilisation and enzymatic activity in 3D print.** Printed at 50% infill level using ABS filament. 12 min printing time.

2.12.3.4.2 Assessment of the enzymatic activity of GOD – AuNP in 3D printed devices: non-specific bind of AuNPs

The enzymatic activity of the GOD – AuNPs was assessed using an adapted form of the method detailed in Section 2.12.2. The volume of the reagents was reduced for the enzymatic activity of GOD – AuNP in 3D printed devices. Fresh reaction cocktail (Reagent C) was prepared. A 35 µL of GOD – AuNP in solution was added to the 3D printed device (Figure 2.10). The GOD – AuNPs were allowed to settle/dry inside the 3D print for one hour. Next, 1 mL of mixture of the reaction cocktail (Reagent C) plus 35 µL HRPs (Reagent D) was added to the 3D print to start the reaction. After one hour, the solution was decanted from the 3D print into a plastic cuvette for measurement at 500 nm. A control assay was performed alongside in a standard 1mL plastic cuvette (labelled as the sample blank). A control study in a 3D printed device for GOD – AuNPs was performed by omitting the reagents. For a control study, the glucose

solution in the reaction cocktail (Reagent C) was substituted with deionized water. Once the solution was decanted from the 3D print into a plastic cuvette for the control study a 172 μL of Reagent B was added to the mixture. The mixture was left for 1 hour in the plastic cuvette, and the enzymatic activity was assessed as described. A control assay was performed alongside for the control study in standard 1 mL plastic cuvette (labelled as the control blank).

2.12.3.5 Evaluating solvent based bio-inks containing GOD – AuNPs as a method to modify 3D printed devices

Acetone, chloroform, dimethylformamide, dimethyl sulfoxide, hexane and tetrahydrofuran were purchased from Sigma Aldrich.

GOD – AuNPs were suspended in each solvent or solvent-water mixtures in the following ratio of 20:80, 40:60 and 100:0 percent of solvents: water. Solvent-based bio-inks were prepared in 1 mL vials. The enzymatic activity of the solvent based bio-inks containing GOD – AuNP was assessed using the method detailed in section 2.12.3.4. Experiments were performed in triplicate.

2.12.3.6 Assay the activity of HRP – AuNPs in 3D printed devices

Fabrication of HRP – AuNPs was facilitated using the method described in Section 2.12.3.2 by substituting GOD with the HRP enzyme of the protocol. The enzymatic activity of 50 nm GOD – AuNPs was assessed using the method detailed in Section 2.12.3.4 again by substituting the GOD – AuNPs with HRP – AuNPs. For the enzymatic activity assessment, the HRP – AuNP are added first, followed by addition of the reaction cocktail (Reagent C). The glucose oxidase enzyme 0.8 mg/mL was added to initiate the reaction.

2.12.3.7 Protocol for GOD and HRP bioconjugated to Nitmagold and Assessment of their enzymatic activity in 3D printed devices

Nitmagold citrate stabilised 50 nm gold-coated magnetic nanoparticles were obtained from Nitparticles Ltd (Spain). Fabrication of NitmagoldGOD and NitmagoldHRP was facilitated using the method detailed in Section 2.12.3.2.

In this study, the aim was to immobilise the magnetised NitmagoldGOD or HRP by a magnet in the device. A new 3D printing device similar to that shown in Figure 2.10 was printed with a space to allow up to a 6 mm diameter magnet to be inserted. 3D Printing was paused halfway through at seven minutes and the magnet was placed in the 3D device.

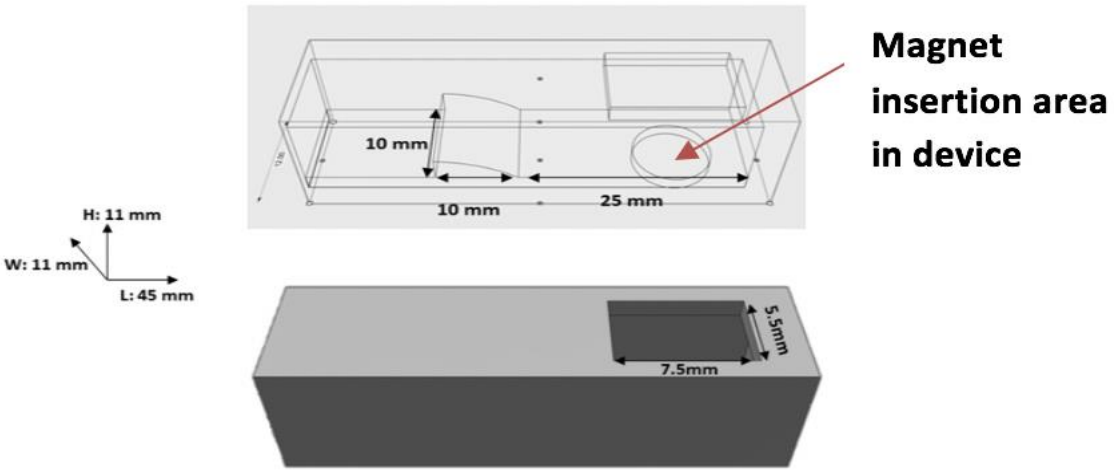

Figure 2.11| **Schematic CAD designs of the magnetic cuvette.** Printed at 50% infill level using ABS filament. 15 min printing time.

The enzymatic activity of the selected NitmagoldGOD and NitmagoldHRP in 3D print was assessed using the method detailed in section 2.12.3.4.2 and 2.12.3.6.

NitmagoldGOD and Nitmagold$_{50nm}$ HRP were added to the region in a 3D printed device where the magnet is present and was left for 1 hr. before initiating the reaction. A calibration curve plot was produced for NitmagoldGOD by measuring the activity of the assay over the time for 80 minutes in a 3D printed device with 2 mm magnet insertion.

The enzymatic assay was carried out in the presence of no magnet and magnets of 2, 3, 4, 5 and 6 mm to determine the influence of magnet size in keeping the NitmagoldGOD stable on the surface of the 3D printed device and the resultant effect on GOD activity.

In a 3D printed device with a 6 mm magnet (Figure 2.11), the enzymatic activity of the NitmagoldGOD was assessed after washing with Buffer C.

Measurements were taken every 10 seconds for 5 minutes for all of the individual samples by UV-Vis. Spectra wavelength from 200 nm to 800 nm was recorded for each assay. Experiments were performed in triplicate for every solution.

2.12.3.8 Binding study of the NitmagoldGOD to the surface of 3D printed devices

To determine if NitmagoldGOD were bound to the surface of the 3D printed device in the presence of magnets (2- 6 mm) a simple experiment was generated. 3D printed devices (Figure 2.11) with 2, 3, 4, 5 and 6 mm magnet size were prepared for this study. The test was started by adding a mixture of 100 µL of NitmagoldGOD and 900 µL of Buffer C was added to the 3D printed devices. The mixture was allowed to settle for one hour in 3D printed devices. Subsequently, the mixture of NitmagoldGOD and buffer solution was transferred into a plastic cuvette for measurement. Spectra were recorded for these samples by UV-Vis at λ_{max} 535 nm for 50 nm gold nanoparticles. For comparison, the procedure was done in a 3D printed device with no magnet inserted. The UV-Vis spectra for the buffer solution and the mixture of NitmagoldGOD and

buffer solution in a plastic cuvette were also determined. The experiment was done in triplicate for the individual magnet sizes.

2.12.4 Protocol for biological proteins bioconjugated to Dynabeads™ M280 Tosylactivated magnetic beads

Proteins that were covalently coupled to Dynabeads™ (M280 Tosylactivated) in this thesis are GOD, HRP and β-Gal. GOD was the first protein coupled to Dynabeads. For GOD assay the bio-inks (GODDynabeads and HRPDynabeads) were prepared to achieve 10 mg beads. For the lactose assay, the Dynabead protein bio-inks were prepared to contain 50 mg beads in the mixture for β-GalDynabeads and GODDynabeads and 10 mg bead for HRPDynabeads. Assuming all proteins are bound to Dynabeads during coupling then the protein ratio after binding to be used for biological assay should be 5:5:1 which is equivalent to the ratio of the enzyme used to detect the lactose concentration in the cited report.

All the proteins were coupled accordingly to Dynabeads for bio-ink preparation. Schematic diagram of Dynabeads® M-280 Tosylactivated to ligands are shown in Figure 2.12. Surface tosyl grups allow direct covalent binding of proteins/peptide via primary amino or sulfhydryl groups.

Dynabeads® M-280 Tosylactivated are 2.8 μm uniform, superparamagnetic, polystyrene beads coated with a polyurethane layer. These Dynabeads bind proteins physically and chemically through primary amino or sulfhydryl groups, with an increasing number of covalent bonds with higher temperature and pH.

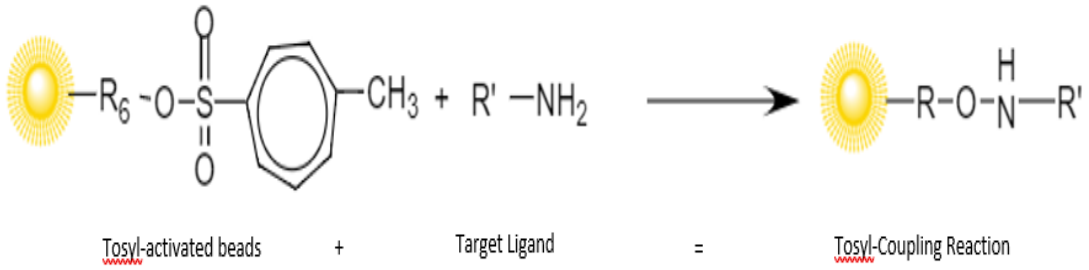

Figure 2.12| **Schematic diagram of direct covalent binding of proteins and peptide to Dynabeads M-280 Tosylactivated**

The following protocol (Section 2.12.4.1) is for 10 mg Dynabead preparations. To achieve 10 mg beads the concentration of protein solution used before coupling need to be 0.8 mg/mL.

2.12.4.1 Dynabeads M-280 Tosylactivated protein coupling protocol

Step 1: Dynabead washing

Before use, Dynabeads in the bottle was resuspended by vortexing for > 30 sec. 335 µL of the beads were transferred to a 1 mL vial, and 335 µL of Buffer C was added vortexing for >30sec to mix. The vial was then placed in a μMACS magnetic field for 1 min and the supernatant was removed with a pipette. Dynabeads were then resuspended in 335 µL of Buffer C.

Step 2: Coupling protein to Dynabeads to make GODDynabeads and HRPDynabeads

Dynabeads (washed in step 1) were transferred and resuspend into a clean 1 mLvial which was placed in the µMACS (1 min), and the supernatant was removed by pipetting. Dynabeads were then suspended in 250 µL of GOD protein, made in Buffer C section 2.1 and HRP in deionised water, plus 150 µL of Buffer C and were mixed

thoroughly by pipetting. A 100 μL aliquot of Buffer G was added to this mixture and was mixed thoroughly by pipetting to give a total volume of 500 μL. This mixture of Dynabeads and protein was incubated at 37 °C for 12–18 hours.

Next Dynabeads were placed on μMACS (2 min), and the supernatant was removed. 1 mL of Buffer I was added to the vial and was incubated at 37°C for 1 hour before the beads were placed on μMACS (2 min) and the supernatant was removed. 1 mL of Buffer J was added to the vial and was mixed for 5–10 sec by pipetting and the beads were washed two times with Buffer J and resuspended in 480 μL of Buffer J to achieve 10 mg beads.

2.12.4.1.2 Preparing GODDynabeads and HRPDynabeads for enzymatic assay

Before using protein coupled to Dynabeads in the enzymatic assay, the required volume of proteins coupled to Dynabeads was transferred individually into a new vial. After centrifugation at 151000 for 3 min, samples were placed on the μMACS for 2 min, and the supernatant was removed with a pipette. Dynabeads proteins were resuspended in the same volume of Buffer C as the initial volume of beads. This process was repeated three times for each Dynabead protein to prepare the GODDynabeads and HRPDynabeads for enzymatic assay in a 3D printed device.

2.12.4.1.3 GOD enzymatic activity assay of GODDynabeads and HRPDynabeads

To determine enzyme activity after binding to Dynabeads, the GOD in the optimised GOD assay was replaced with GODDynabeads or HRPDynabeads and the enzymatic activity was assessed in a plastic cuvette using the method detailed in Section 2.12. The volume of the reagent used for this assay was modified to assay the GOD enzyme activity in a 1 mL plastic cuvette by dividing the reagent volume by detailed in section 2.12.1 by the factor of three. A 50 mL of a 5% w/v D(+)-glucose substrate solution

(Reagent B) was prepared to assess GODDynabeads or HRPDynabeads enzymatic activity.

2.12.4.2 Enzymatic assay of GODDynabeads and HRPDynabeads on 3D-printed devices

The enzymatic activity of GODDynabeads and HRPDynabeads was assessed using the method detailed in sections 2.12.3.4.2 and 2.12.3.6. A large magnet was held underneath the plastic cuvette for 5 min before measurement by UV-Vis to draw the Dynabead protein which to the bottom of the cuvette.

The enzymatic assay was assessed in 3D printed devices containing a 6 mm magnet (Figure 2.10). Protein-modified Dynabeads used for the enzymatic assay were added to the internal compartment of the device, where the 6 mm magnet is present. The DynabeadGOD bio-ink GOD assay was also assessed after washing with a 1mL of buffer solution (Buffer C).

Increase in A_{500nm} for approximately 5 minutes was recorded immediately and after 60 min by UV-Vis Spectrophotometer for all samples. Wavelengths from 200 nm to 800 nm were scanned for the individual assay. Experiments were performed in a triplicate for every solution.

2.12.4.3 Two-step coupled assays of GODDynabeads and HRPDynabeads in transparent 3D-printed devices for applications in UV-Vis spectroscopy

2.12.4.3.1 Optimised GOD assay 3D-printed device designed for UV-Vis spectroscopy

A 3D printed device with dimensions that allow it fit inside of a standard UV-Vis spectrophotometer measuring 20 mm (W) x 47.85 mm (L) x 12.5 mm (H) was designed (Figure 2.13).

The device contains two spaces for a 6 mm magnets insertion with an internal volume space of max 600 µL for each chamber. Magnets were placed inside the device, halfway through the printing process, at 14 minutes. The wall thickness of the device was 2 mm for the reacting mixture. The wall thickness of the absorbance measuring area of the device was 0.4 mm with a path length of 10 mm and 500 µL chamber volume.

The device (Figure 2.13) was printed with PLA filament at 50 % infill level using custom 3D printing setting (Table 2.3) by the MakerBot® Replicator® Mini+ 3D Printer.

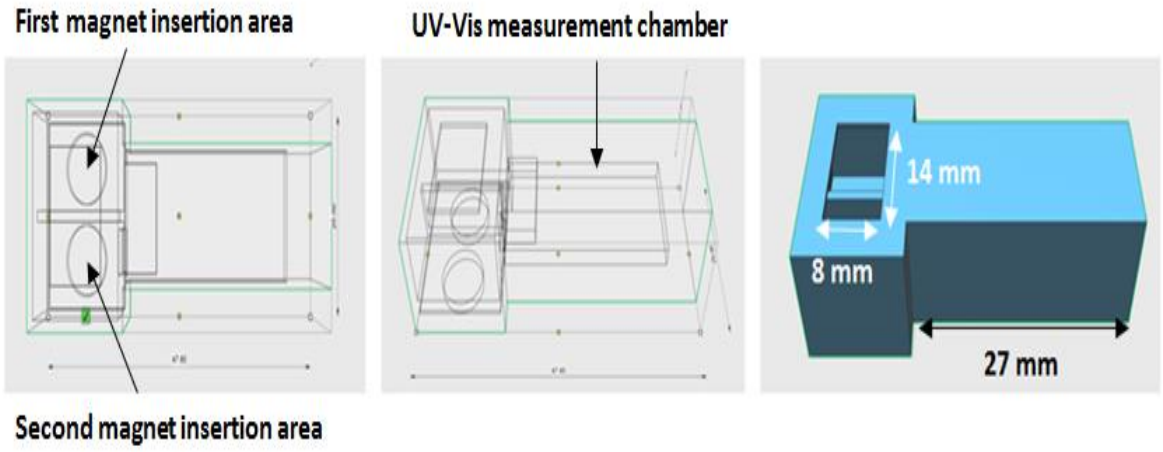

Figure 2.13| **CAD designs of two stage optimised 3D-printed device designed for UV-Vis spectroscopy;** 45 minutes print time.

2.12.4.3.2 Two-step coupled enzymatic assays of GODDynabeads and HRPDynabeads in 3D-printed devices

GODDynabeads and HRPDynabeads were prepared using the method detailed in Section 2.12.4.

The enzymatic activity of the selected Dynabeads was assessed using the method detailed in Section 2.12.2 but the volume of the reagents was reduced for the two-step assay on a 3D printed device. Initially, 35 µL of GODDynabeads were added to the 3D

printed device (Figure 2.13) where the first magnet was placed. This was followed by the addition of 500 µL of freshly prepared reaction cocktail (Reagent C). The mixture was allowed to sit inside of the 3D print for 30 min. Next 35 µL of HRPDynabeads were added to space where the second magnet is present. After 5 min, the solution inside of the 3D print was displaced into the second cavity where the second protein is present by rotating the 3D print device to the left. The reacting mixture was allowed to settle inside of the 3D print for further 30 min. After this time the solution was placed into the cavity where it can be measured by UV-Vis by inverting the device clockwise. The $A_{500\ nm}$ was measured for 5 minutes and the experiment performed in triplicate. Before each measurement, a similar 3D printed device (Figure 2.13) was used as blank to zero the UV-Vis to baseline before determining the absorbance of the solutions.

Two-step GOD enzymatic assay was performed for the glucose solution range of 0-13 mmol/L. As control, assessments were also carried out in the plastic (polystyrene) cuvette using similar approach for comparison. A large magnet was placed underneath the polystyrene cuvette to draw the GOD and HRPDynabeads bind to polystyrene cuvette and to stop them from transferring into the next cuvette at each inversion.

2.12.4.4 Assay the activity of GODDynabead and HRPDynabead bio-inks in 3D printed devices printing technique and setting

An enzymatic assay of the biological ink was carried out on the 3D printing device (Figure 2.11). A simple circle with a radius of a 2 mm, which determines the volume of the biological ink that is decanted by the 3D printer, was added. Figure 2.14 shows the position of the 3D printed designs on the build plate.

To place the biological ink inside of the 3D print a 1 mL syringe was filled with 500 µL of GODDynabeads. The syringe was positioned inside of the syringe extruder. Next,

ABS was used as supporting material to be printed with the right extruder for printing the 3D printing device. Dual extrusion printing process was used. The 3D printing of biosensor device was completed by using the printing setting detailed in Section 2.10.5 (Table 2.4). Platform temperature highlighted in Table 2.4 for ABS filament was changed to 37 °C to ensure GODDynabeads were not denaturing once printed on the device.

A 6 mm magnet was placed inside of the 3D printing device halfway through by pausing the printer.

The enzymatic activity of the selected Dynabeads was assessed using the method detailed in Section 2.12.4.2. Once DynabeadGOD was printed inside of the device, 1 mL of reaction cocktail (Reagent C) and 35 µL of HRP (Reagent D) was added. After one hour, the solution was decanted from the 3D print into a plastic cuvette, and the biological activity of printed ink was measured at 500 nm. Biological inks assessment was performed individually and in triplicate.

The enzymatic activity of HRPDynabeads after printing was also assessed by substituting the GODDynabead with HRPDynabeads.

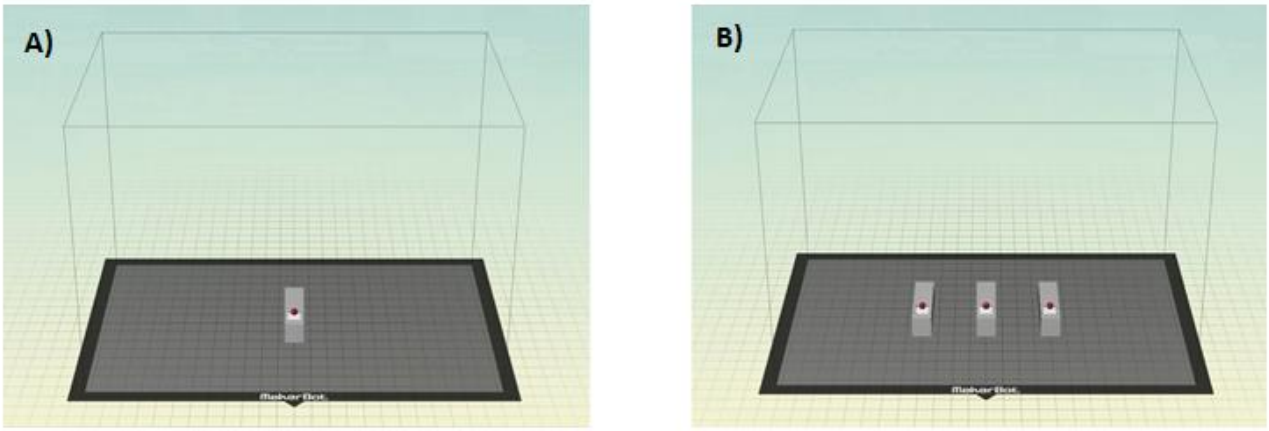

Figure 2.14| **Picture of 3D printed STL design that was used to assess the activity of the biological ink in 3D printed device.** A) Shows a single device, and b) shows how triple device was exported to be printed by the 3D printer.

2.12.5 Protocol for lactose quantification based on coupled enzymatic reactions

2.12.5.1 Optimised protocol for lactose quantification using Amplex Red

Firstly, a stock solution of 10 mmol/L of D-Lactose monohydrate, 3 mmol/L of Amplex Red in dimethyl sulfoxide, β-Gal (1000 U/mL in PBS (50 mmol/L, pH 7.2) containing $MgCl_2$ (2 mmol/L) was prepared. Solutions of GOD (1000 U/mL) and HRP (500 U/mL) were prepared in cold deionised water. All reagents were stored in a freezer (- 20°C). To make proteins-based Dynabeads bio-inks the proteins used for the assay were further diluted to achieve the ratio required for lactose assay. The protein-based bio-inks were prepared as detailed in Section 2.12.4. From the lactose stock solution, lactose solution in ranges of 0.1-6.3 mmol/L were prepared and used through this study (see Chapter 7, Section 7.2-7.3 for more detail) to determine optimum condition for quantification of lactose for this work.

Initially, the enzymatic activity of the selected Dynabeads (β-Gal, GOD and HRP) was assessed in 500 μL cuvette. 50 μL of β -GalDynabeads, GODDynabeads, and HRPDynabeads solutions were added to the polystyrene (plastic) cuvette. Next, a 150 μL of lactose solution and 200 μL of Amplex Red (3 mmol/L) was added to the mixture. The mixture was incubated at 37°C for 1 hour. An experiment was repeated at the room temperature for comparison. Subsequently, the solution mixture was measured by UV-Vis. Measurement at A570 nm for approximately 5 minutes was recorded immediately. The study was done in triplicate. A series of experiments were performed by changing the reagents, concentration, volume, incubation time before determining an optimum condition for quantification of lactose that is detailed.

To ensure the amount of the enzymes used in solution was sufficient for carrying out the reaction within 1hr the same lactose assay solution concentration ranges of 0.1-6.3 mmol/L was re-measured every hour for up to 5 hrs.

2.12.5.2 Lactose quantification by enzymatic reactions using *o*-dianisidine reagent

For an *o*-dianisidine lactose assay reaction, fresh reaction cocktail containing 0.17 mM *o*-dianisidine with 1.72 % w/v lactose substrate of 0.5 mol/L, pH 5.8 was prepared in a 20 mL glass bottle. Next 350 µL of this mixture were mixed with added 50 µL of proteins (β-Gal, GOD, HRP) Dynabeads in 3D printed GD-Glass device to make a 1 mL solution mixture. The mixture was left at room temperature for 1 hour, and the absorbance was measured at 500 nm with a UV-Vis spectrophotometer.

2.12.5.3 Protocol for one-step lactose quantification using β-GalDynabeads, GODDynabeads and HRPDynabeads on 3D-printed devices designed for UV-Vis spectroscopy

2.12.5.3.1 A transparent 3D-printed one step lactose quantification device designed for UV-Vis spectroscopy

A one-step 3D printed device with a size of 20 mm (W) x 47.85 mm (L) x 12.5 mm (H) was designed to contain an internal volume space of max 1.5 mL with positions to allow the insertion of three 6 mm magnets (Figure 2.15). Three magnets were placed inside of the device after 17 minutes, roughly halfway through the printing process. The wall thickness of the device was 2 mm for the reacting mixture. The wall thickness of the absorbance measuring area of the device was 0.4 mm with a path length of 10 mm and 600 µL chamber volume.

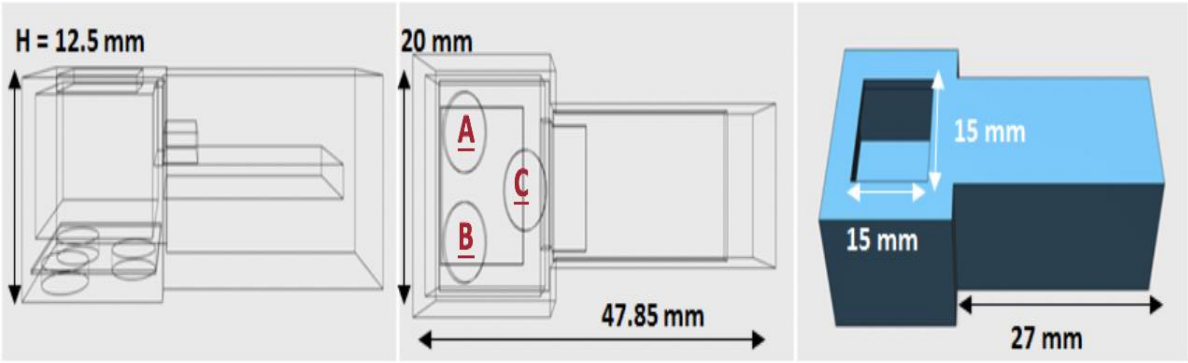

Figure 2.15| **Schematic CAD designs of one step 3D-printed device designed for UV-Vis spectroscopy;** 42 minutes of printing time. (A, B, C shows the magnet insertion area). Three 6 mm magnet were used in device.

2.12.5.3.2 Enzymatic protocol for optimised one-step lactose quantification of β-Gal, GOD and HRP Dynabeads on optimized 3D-printed devices

The enzymatic activity of the selected Dynabeads (β-Gal, GOD and HRP) was assessed in (Figure 2.15) 3D printed device.

50 µL of β-GalDynabead, GODDynabead and HRPDynabead solutions were added to the device separately. Each protein was added to the area where a magnet was present and left to rest for 30 minutes. Next, a 150 µL of lactose solution (0.05 M) and 200 µL of Amplex Red (3 mmol/L) was added to the device. The mixture was incubated at 37°C for 1 hour. An experiment was repeated at the room temperature for comparison. Subsequently, the solution mixture was tipped into the cavity where it can be measured by UV-Vis spectroscopy. Measurement at A_{570nm} for approximately 5 minutes was recorded immediately. The study was done in triplicate. Each time before measurement a similar 3D printed device (Figure 2.15) was used as blank to zero the UV-Vis to baseline before measuring the absorbance of the solutions. As control, assessments were carried out in the polystyrene cuvette for comparison.

2.12.5.4 Protocol for three-step lactose quantification using β-GODDynabeads, GODDynabeads and HRPDynabeads on transparent 3D-printed devices for UV-Vis spectroscopy

A stepwise 3D printing device similar to that shown in Figure 2.15 was designed. The new device (Figure 2.16) contains three chambers with an internal volume space of max 600 µL. Each chamber contains an area for a 6 mm magnet to be inserted. Three magnets were placed inside of the device at T=20 minutes halfway through the printing process.

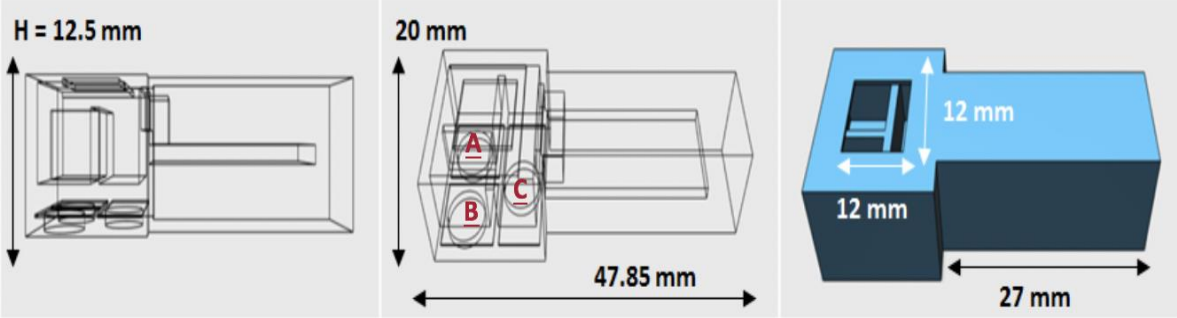

Figure 2.16 |**Schematic CAD designs of a stepwise 3D-printed device designed for UV-Vis spectroscopy;** 47 minutes printing time. Device was printed with clear PLA filaments. (A, B, C shows the magnet insertion area).

After printing (Figure 2.14) the 3D printed device was coated with XTC-3D reagent and allowed to dry. A 50 µL aliquot of β-GalDynabeads was added to the first chamber, followed by the addition of 150 µL of lactose solution (0.05 M) and 200 µL of Amplex Red (3 mmol/L). The reaction mixture was incubated at 37 °C for 30 min. Next, a 50 µL aliquot of GODDynabeads was added to the second chamber. Immediately after 1 min, the solution inside of the first chamber was displaced into the second chambers by rotating the 3D print device to the left and the reaction mixture was incubated at 37°C for 30 min. Finally, the device was rotated clockwise, and the reaction mixture was displaced into the third chamber. A 50 µL aliquot of the HRPDynabeads was added to

the third chamber, and the reaction mixture was incubated at 37°C for a further 30 min. Subsequently, the solution mixture was tipped into the cavity where it can be measured by UV-Vis by inverting the device clockwise. Measurements at A_{570nm} for approximately 5 minutes were recorded immediately. The study was done in triplicate. Each time before measurement a similar 3D printed device (Figure 2.16) was used as blank to zero the UV-Vis to baseline before measuring the absorbance of the solutions. A calibration plot was produced for this study by using variable concentration of lactose solution

2.12.6 Fabrication setting and evaluation for printing optimized 3D-printed transparent millifluidic devices for UV-Vis spectroscopy

The MakerBot® Replicator® Mini+ 3D Printer was used to print out all of the transparent (clear) designs. The printer was controlled by MakerBot® Desktop software.

Clear PLA and HD Glass filaments were purchased from MakerBot, Formfutura, and Taulman3D respectively. These filaments were used to print the designs accordingly to the suitability for the study.

The optimum printing temperatures for the filaments were given by the manufacturers; the filaments were extruded smoothly and at correct consistency. The final settings for all of the clear filaments that were printed by MakerBot® Replicator® Mini+ 3D Printer, producing the finest object with the combination of XTC-3D coating can be found in Table 2.5.

Paint brushes (Silverline 633927 Flat Tipped Brush Set – 12 Pieces) and XTC - 3D® Smooth-On High-Performance 3D Printing Coating were purchased from Amazon (UK), polystyrene cuvettes were supplied from Fisher Scientific.

Table 2.5| **Setting for printing transparent 3D printed filament by MakerBot® Replicator® Mini+ 3D Printer**

3D Printer Filaments	**Device Settings**				
	Extruder Temperature °C (Right & Left)	Platform Temperature °C	Layer Height (mm)	Minimum layer duration)	Filament diameter
ABS	230	110	0.25 mm	10 seconds	1.77
PLA	220	70	0.25 mm	10 seconds	1.77
HD Glass	225	45	0.25 mm	10 seconds	1.75

2.12.6.1 Preparation of XTC - 3D coating

The coating was prepared as per the manufacturer's instruction. In a fume cupboard, 4 mL of part A was carefully poured into a 50mL plastic centrifuge tube and then made to 6 mL mark with part B. The contents were mixed with a plastic stirrer until homogenous in colour liquid was achieved. The coating was then spread onto a folded piece of aluminum foil, which allowed the easier application.

2.12.6.2 Application of XTC - 3D coating on devices

After the preparation stage described in x, the coating was applied to the opposite walls of the device for UV - Vis analysis, covering there outside layer. Devices were then left in upright position on an aluminum foil to dry for 3 hours in a fume cupboard. The application was performed using disposable paint brushes.

2.12.6.3 UV-Vis test analysis

UV-Vis tests were performed in triplicate on empty devices designed for this study, made from ABS, PLA, and HD Glass before and after application of XTC-3D coating. The wavelength range was set at 200 - 800 nm and the scan rate at 5 nm intervals. The instrument before each analysis was blanked with an empty polystyrene cuvette.

CHAPTER 3

CHARACTERISATION OF FDM 3D PRINTING MATERIALS

3.1 Introduction

FDM 3D printing has applications in the fields of constructing equipment materials (Hutmacher *et al.*, 2001), preparation techniques (Kalita *et al.*, 2003) and numerical simulation (Zhang and Chou, 2008). Recent advances in FDM 3D printing technology and increases in the number of polymer materials available as FDM filaments have seen increasing interest in 3D printing applications from industry and academic communities (Chapiro, 2016). However, a fundamental issue endures in that manufacturers do not recommend the use of non-standard filaments, which voids the warranty on some 3D printers. For example, the MakerBot Replicator 2X 3D printer (used in this research) can print in ABS and dissolvable filaments like HIPS but PLA and other filaments are not recommended to be printed. The origin of these recommendations stems from MakerBot 3D printer users experiencing problems like nozzle blockage, incomplete prints, filament cracking/breaking in between the drive gear and poor quality prints.

Conversely, being able to print a range of different filament with one 3D printer can be greatly beneficial for users.

1) there is a reduce in cost and space as there is no need for an additional printer,
2) complex designs with better quality can be made as other material such as HIPS can be used as supports for overhange designs and then dissolve it away in a bath of D-limonene,
3) strong prints based on tensile strength, toughness, thermal strength can be made by using PC filaments or T-Glase,
4) flexible and transparent prints can be made by printing with FDA-approved XT Copolyester, SemiFlex and HD-Glass filaments.

Unfortunately, there is a severe lack of peer-reviewed data and standards relating to 3D printing materials, properties and setting for 3D printer users, which limits the ability of prosumers to develop more sophisticated designs (Go et al., 2019). Recent work has described what effect the orientation of layers may have on the properties of a printed part (Vega et al., 2010). FDM 3D printers have shown a strength dependency on different types of infill patterns and internal structures (Villalpando, Eiliat and Urbanic, 2014) and print orientations (Cantrell et al., 2017). But this have not been explored on a range of material and mostly limited to investigation on PLA and ABS material. Limited study explored printing of range of material by FDM 3D printing but mainly to assess the tensile strength of range of polymer material for FDM 3D printing (Tanikella, Wittbrodt and Pearce, 2017).

To expand on this preliminary knowledge in this chapter, reliable print settings for a range of new to the market 3D-printer filaments on the MakerBot Replicator 2X 3D printer were determined as shown in Table 3.1. Each of the material used in this study were selected for a specific reason for examples ABS, PC ABS Alloy, XT - Copolyester was selected due to high mechanical properties. HIPS can be used as supporting material. PLA is the most popular FDM 3D printing material and is available for the vast majority of 3D printing supplies vendors. Biofila Linen is a biopolymer known as Lignin made of aromatic alcohols extracted from natural source plant. Flexible prints can be made by printing with SemiFlex filament. T-Glase and HD-Glass filaments can be used to print transparent and translucent models. MakerBot Flexible has a relatively low melting point (60° C) showing suitability for biological molecules, which in addition requires less energy to print with than other materials. Majority of these filaments is printed by 3D printing users using optimised FDM 3D printers that allow multi-material printing. All in which printed under guidance of manufacturing setting for the selected filaments and printer, followed by many alteration in standard setting to achieve reliable print quality.

As the fundamental goal of this research is to fabricate bio-inks for use in microfluidic or millifluidic devices, characterisation of these 'novel' filaments was also performed, to provide a set of criteria to determine an optimum filament for the fabrication of a particular device. Physical characterisation of 3D printed filaments was performed in the printed state. 3D Printer filaments were characterised by assessing printing repeatability, layer to layer bonding of printed models (microscopic assessment), resolution and accuracy (shrinkage after printing), layer bonding (water tightness) and hydrophobicity from the water contact angle of the printed material. The techniques used are similar to those used for the evaluation of 3D printed microfluidic chips for cell processing (Lee, Zhang and Yeong, 2016).

Finally, the nonspecific binding of DNA and BSA to the surface of 3D printed filaments in the printed state was also measured.

3.2 Determination of reliable printing settings for novel filaments on the MakerBot Replicator 2X

To identify reliable printing settings for the individual filaments (Section 2.2, Table 2.1), a thermoplastic cuboid of 9.5 mm (W) x 9.5 mm (L) x 2.5 mm (H) (Section 2.5, Figure 2.1) with surface area of 275.5 mm^2 was printed. Once the thermoplastic cuboid was printed as a single solid piece similar to the design layout, 10 repeat prints of the same design were made to ensure reproducible print quality. In this work the reproducibility was determined by counting the fail rate based on the numbers of the successful print. Reproducible print is made when material is extruded smoothly from the nozzle without fail adhering to platform to make 3D object (Kiński et al., 2016).

Initially, standard print settings for ABS (Section 2.3, Table 2.2) were used and printed cuboids were inspected to observe extrusion of filament from the nozzle, binding of the

first printed layer to build plate and quality of printed cuboids after printing, i.e. no warping, no stringing, no gaps between layers and extrusions. Depending on the results of the visual inspection, the 3D printing parameters were changed accordingly. For example, the temperature of extrusion was raised if the filaments were not smoothly extruding from the printer nozzle. Extrusion printing speed was reduced, if the layers of the printed object were not binding well. The build platform temperature and height distance (between extruder tip and build platform) were changed if the print did not stick to the build platform. Build platform covers such as Kapton tape, and the blue tape, was changed if the printed objects started to move halfway through the printing process. Of the purchased filaments (Section 2.2, Table 2.1), CF0 carbon fibre reinforced ABS could not be printed since the filament would break when it loaded into the extruder, blocking the extruder nozzle on each attempt. The remaining filaments were extruded smoothly from the nozzle. For all the filaments, the final reliable print settings are provided in Table 3.1. In addition, Figure 3.1 shows the images of 3D printed cuboids obtained at the reliable print settings. The Chemical structure of the 3D printing material used in this work is also presented in Figure 3.2.

Table 3.1 | **Final print setting to print with listed 3D filaments on the MakerBot Replicator 2X**

3D Printer Filaments	**Device Settings**		**Extrusion Speeds**					**Platform Height Settings**
	Extruder Temperature °C (Right & Left)	Platform Temperature °C	Bridges (mm/s)	First Layer (mm/s)	Infill (mm/s)	Insets (mm/s)	Outlines (mm/s)	The distance between platform and extruder nozzle tip (mm)
ABS	230	110	40	30	90	90	40	0.025
PC-ABS Alloy	255	125	40	30	90	90	40	0.025
3DXNano ABS	240	110	40	30	90	90	40	0.025
PLA	220	70	40	30	90	90	40	0.025
Conductive PLA	230	50	40	30	90	90	40	0.025
Stainless steel PLA	220	50	40	30	90	90	40	0.025
Magnetic Iron PLA	195	50	40	30	90	90	40	0.025
Carbon Fiber PLA	235	110	40	30	90	90	40	0.036
Biofila linen	220	70	40	30	90	90	40	0.036
HIPS	240	110	40	30	90	90	40	0.036
XT- Copolyester	240	70	40	30	90	90	40	0.016
T-Glase	210	55	40	30	90	90	40	0.025
HD Glass	225	45	40	30	30	30	30	0.016
Bridge Nylon	230	50	40	30	30	30	30	0.016
SemiFlex	220	50	40	30	30	30	30	0.036
MakerBot Flexible	100	0	40	30	90	90	40	0.025

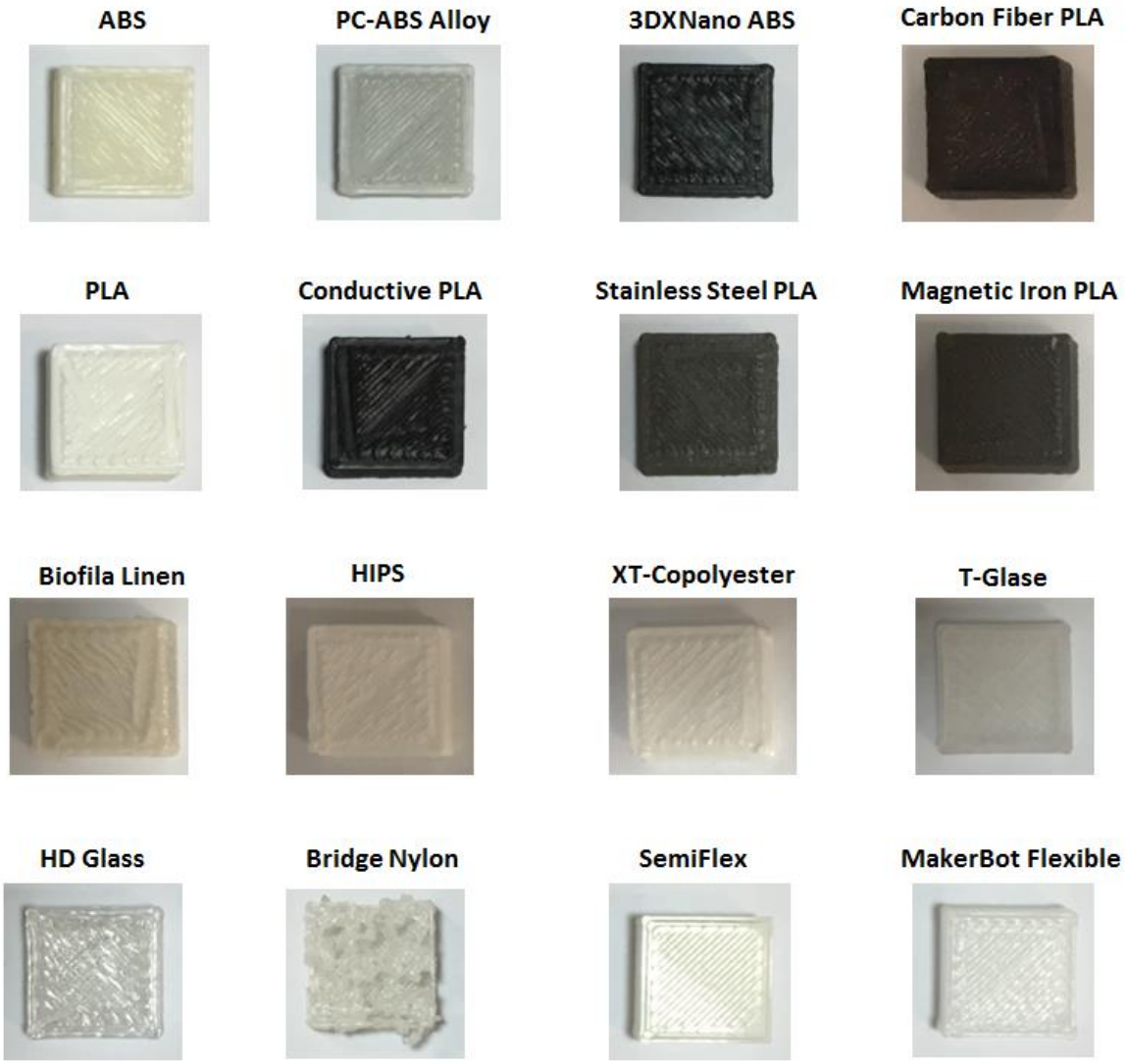

Figure 3.1| **Photographs of thermoplastic cuboids:** Cuboids were printed at 100% infill under reliable printing setting of the 3D printing filaments listed in Table 3.1. Bridge Nylon filament was not printed successfully since the filament was not extruded precisely from the nozzle causing a gap in the layer of print. (The image here shows a poor layer bonding of 3D printed Bridge Nylon model)

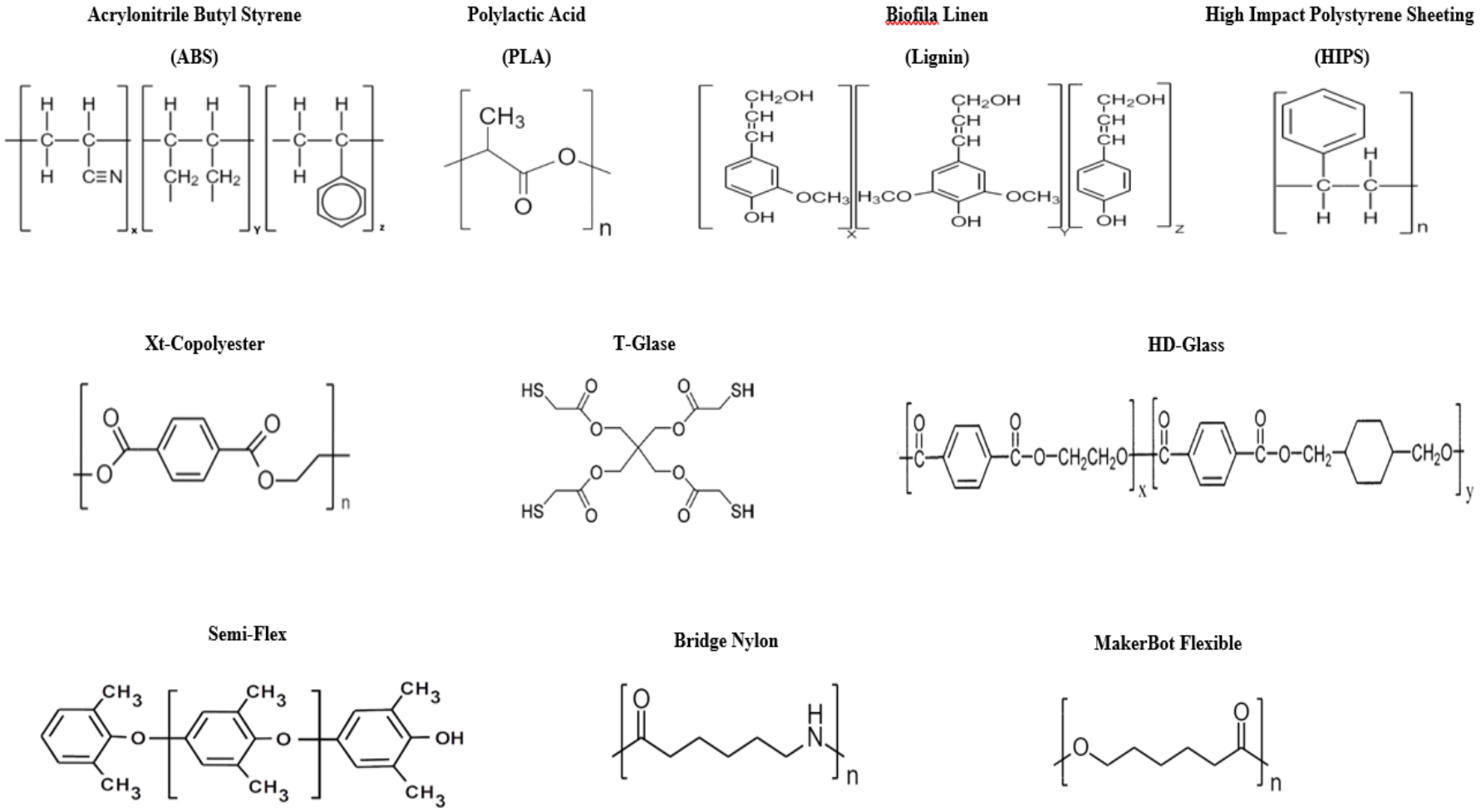

Figure 3.2| **Chemical structure of 3D printer filaments**

Cuboids printed with Bridge Nylon showed low print resolution and gaps in the surfaces of the printed object. However, surface bonding was slightly improved by an increase in infill density as shown in Figure 3.3. This slight improvement did not justify the use of this filament through the study.

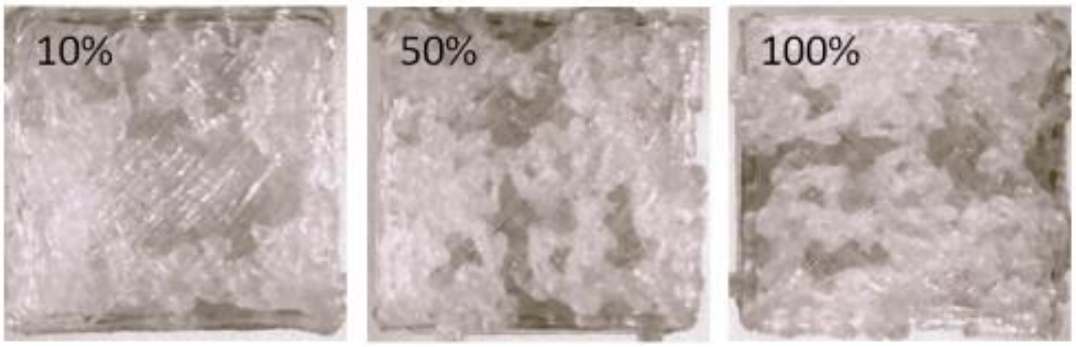

Figure 3.3| **Optical micrographs of thermoplastic cuboids at 2X magnitudes** displaying the low resolution printed thermoplastic cuboids; printed by Bridge Nylon filament at 10, 50 and 100% infill.

Reproducibility in printing thermoplastic cuboids with T-Glase and Bridge Nylon filament was low. For T-Glase 5/10 and Bridge Nylon, 9/10, samples failed to print with decent quality. Cuboids were only printed with 100% infill by the T-Glase filament. All other studied filaments were printed reproducibly when printed by MakerBot Replicator 2X at the final print settings (Table 3.1).

3.3 Microscopic assessment of 3D printed thermoplastic cuboids

Determining the surface properties of the 3D printed models, e.g. layer to layer bonding, is crucial for applications involving fluids (Ho *et al.*, 2015a). Surface layer to layer bonding influences fluid flow in microfluidic/millifluidic channel (Prentner *et al.*, 2010)(Sun et al. 2012). For fabricating devices involving fluid application as the constructing model decrease in size, surface forces become the crucial factors in influencing flow (Lee, Zhang and Yeong, 2016).

Figure 3.3 shows the result of thermoplastic filaments surface topologies. These were examined by observing the thermoplastic cuboids printed at 100% infill under the optical microscope as detailed in Section 2.6.

The inspection was carried out to identify how well bonded each of the filaments were after printing. This inspection is important since it indicates whether or not 3D-printed devices will leak. Furthermore, smooth surfaces are desirable for microfluidic/millifluidic applications.

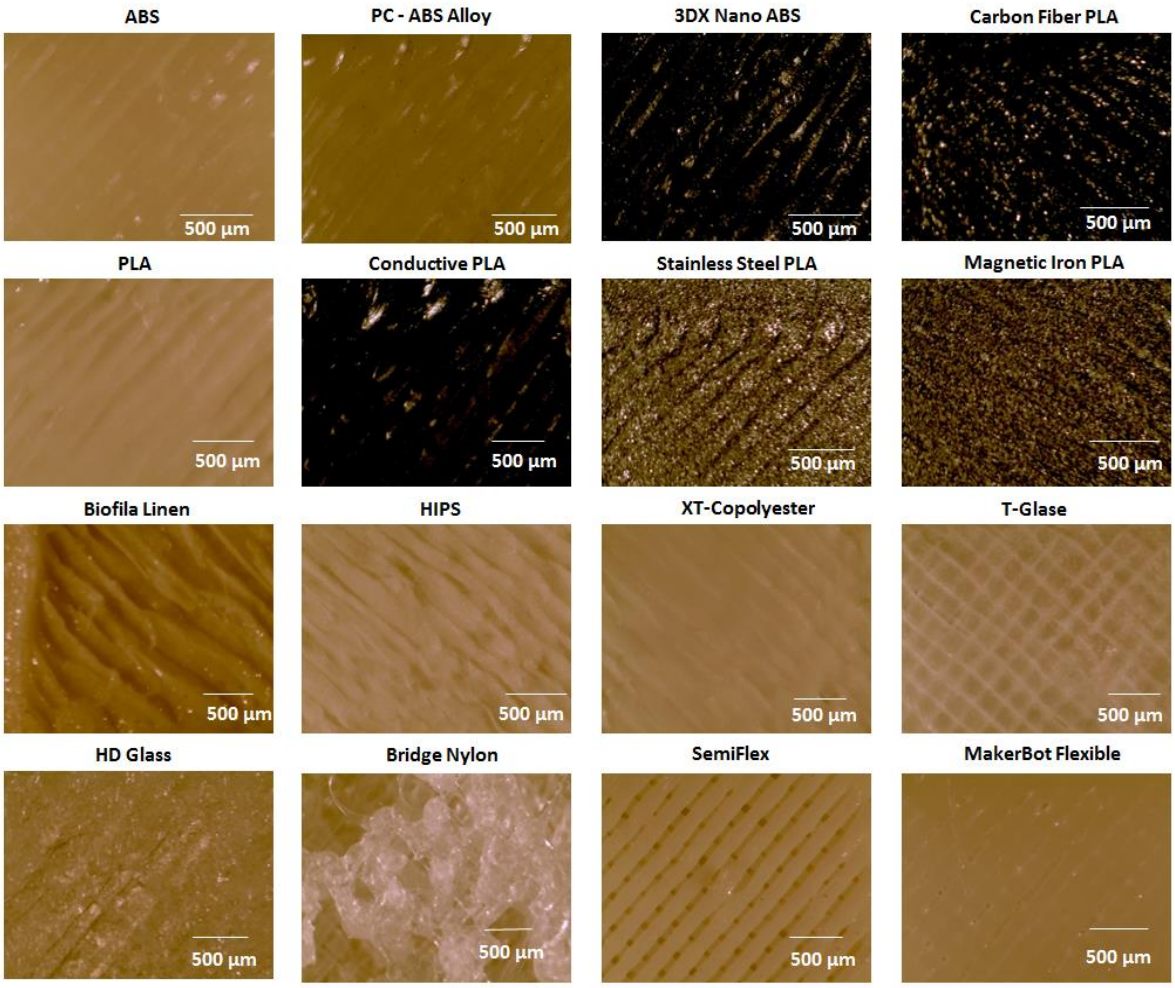

Figure 3.4| **Optical micrographs of thermoplastic cuboids at 4X magnitudes;** inserts were printed at 100% infill.

When observing the thermoplastic cuboids surfaces, printed at 100%, by the naked eye, for the majority of 3D printing filaments, a rough surface finish was observable.

Optical micrographic images also show a ridged topology for the majority of the printed surfaces as shown in Figure 3.4. Although surface roughness varied on different filaments, for instance, ABS, PLA, XT-Copolyester shows a smoother, less ridged surface finish compared to HIPS or Biofila linen filaments.

Voids were detected on the surface of Bridge Nylon, SemiFlex and T-Glase thermoplastic cuboids. MakerBot Flexible prints exhibited a flatter and smoother surface finish when compared with other 3D printed cuboids, however, the surface was covered by bubbles. Bubbles suggest a small volume of air may have been trapped inside thermoplastic cuboids during the printing process. The air gap in a 3D printing model means that the 3D model will possess a low mechanical strength (Hwang *et al.*, 2014)(Sood, Ohdar and Mahapatra, 2010). As a result, there is a high chance that the millifluidic device fabricated by MakerBot Flexible filament would leak. Voids and the air gap in a 3D printing were not significantly improved for filaments such as Bridge Nylon, SemiFlex, T-Glase and MakerBot Flexible when repeats were undertaken by changing the print settings. In general, these four out of 16 studied filaments are likely to be of little use in microfluidic/millifluidic applications.

The FDM 3D printing models surface roughness is typically measured by an instrument known as ‘Profilometer’ where critical dimensions as step, curvature, flatness are computed from the surface topography (Alsoufi and Elsayed, 2018) (Peng and Yan, 2018). Surface roughness can also influence the hydrophobicity of 3D printing material surface properties and liquid flow in microfluidic channels however this technique is recommended for future used to characterise the functionalized surfaces for microfluidic application.

3.4 Assessment of thermoplastic filament shrinkage after printing

One major factor affecting FDM 3D printing, which can decrease the reproducibility of printing and cause leakage in microfluidic/millifluidic applications, is material shrinkage after printing (Lee, Zhang and Yeong, 2016). The study of the shrinkage is fundamental for determining the accuracy for the final size of the printed model especially internal feature such as narrow channels for construction of models (Shallan *et al.*, 2014). Numerous researchers refer to the study of shrinkage as dimension accuracy of 3D printing models in X, Y, Z direction (Ceretti *et al.*, 2017)(Mohamed, Masood and Bhowmik, 2016) (Boschetto and Bottini, 2014).

According to the literature, most print materials experience shrinkage as they change from semiliquid to the solid state after printing (Dao *et al.*, 1999). Therefore, some models that are made can be slightly smaller than their design dimensions. The inaccuracy in size of the 3D printed model can make it difficult to test the design for form, fit and function. As a result, some reports show a mathematical study that makes it possible to construct a 3D model with correct dimensional accuracy by compensating the shrinkage factor values, although it can be time-consuming to do this (B. Fritz and R. Noorani, 1998) (Evans,. *et al.*, 2014).

In a study examining the influence of bed temperature on heat shrinkage shape errors in FDM additive manufacturing of the ABS filament, models were printed at 100% infill density where the material shrunk most (Choi *et al.*, 2016).

In this study, a similar method of determining shrinkage was used, where five identical thermoplastic cuboids were printed at 100% infill density for each filament. To inform any decision about the best filaments to use for the fabrication of simple millifluidic devices the shrinkage was assessed by measuring thermoplastic cuboids in the X, Y and Z directions (Figure 3.5). The average dimensions and the standard deviation of thermoplastic cuboids are displayed in Table 3.2. The percentage difference in

dimensions average of these printed cuboids was also compared to the dimension of the design (Figure 3.5).

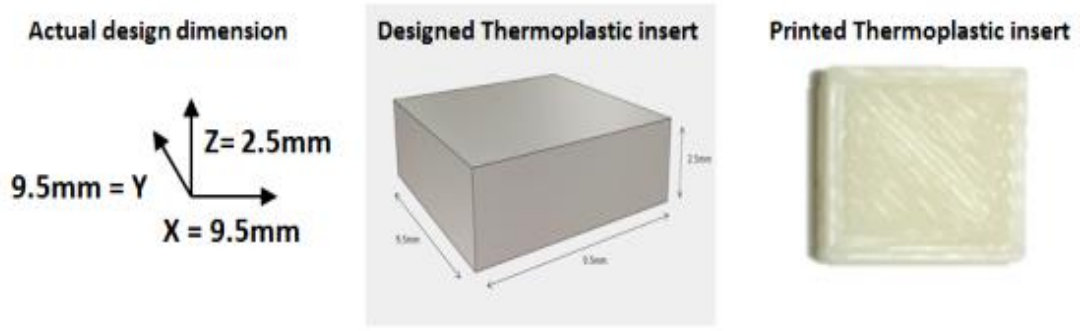

Figure 3.5| **Thermoplastic cuboid;** showing the dimensions of designed cuboid and picture of the cuboid in the printed state (printed by ABS filament)

The results show that ABS and PLA shrinkage is as little as 0.53% in the X and Y directions (Figure 3.5). These filaments showed lower shrinkage compared to all of the other thermoplastic filaments studied since thermoplastic cuboids' print dimensions were closest to those of the print design. The calculated shrinkage percentage for ABS and PLA filaments was much lower than the reported paper with values ranging from 3% for PLA and 34.53% for ABS (Alsoufi and Elsayed, 2018).

PC ABS Alloy, Magnetic Iron and T-Glase thermoplastic cuboids showed a higher percentage of shrinkage (up to 5%) in the X and Y directions. For these filaments, it would be necessary to spend extra time looking at dimensional correction factors to fabricate a 3D model with correct dimension accuracy.

In the Z direction, the majority of the filaments (ABS, 3DXNano ABS, PLA, Conductive PLA, Carbon Fiber, PLA, HD Glass, Semiflex and MakerBot flexible) did not shrink significantly. Interestingly, some filaments (Biofila linen, Hips and XT-Copolyester) tended to expand in the Z direction and increase in height when printed.

Table 3.2| **Thermoplastic cuboids' printed dimensions:** Design dimensions of 9.5 mm (X) x 9.5 mm (Y) x 2.5 mm (Z) for an average of five cuboids printed at 100% infill

Thermoplastics filaments	**Average dimensions of 5 thermoplastic cuboids in the XYZ direction**								
	X axis Dimension (mm)	X axis SD	% Difference in X axis	Y axis Dimension (mm)	Y axis SD	% Difference in Y axis	Z axis Dimension (mm)	Z axis SD	% Difference in Z axis
ABS	9.45	0.12	0.53 %	9.45	0.12	0.53 %	2.50	0.00	0.00 %
PC-ABS Alloy	9.00	0.00	5.26 %	9.00	0.00	5.26 %	2.25	0.00	10.00 %
3DXNano ABS	9.17	0.12	3.47 %	9.17	0.12	3.47 %	2.50	0.00	0.00 %
PLA	9.45	0.00	0.53 %	9.45	0.00	0.53 %	2.50	0.00	0.00 %
Conductive PLA	9.33	0.24	1.79 %	9.33	0.24	1.79 %	2.50	0.00	0.00 %
Stainless Steel PLA	9.33	0.24	1.79 %	9.33	0.24	1.79 %	2.25	0.00	10.00 %
Magnetic Iron PLA	9.00	0.00	5.26 %	9.00	0.00	5.26 %	2.33	0.24	6.80 %
Carbon Fiber PLA	9.42	0.12	0.84 %	9.33	0.12	1.79 %	2.50	0.00	0.00 %
Biofila Linen	9.25	0.00	2.63 %	9.25	0.00	2.63 %	2.93	0.05	17.20 %
HIPS	9.25	0.00	2.63 %	9.25	0.00	2.63 %	2.57	0.09	2.80 %
XT - Copolyester	9.00	0.00	5.26 %	9.17	0.24	3.47 %	2.60	0.14	4.00 %
T-Glase	9.00	0.00	5.26 %	9.00	0.00	5.26 %	2.07	0.05	17.20 %
HD Glass	9.33	0.24	1.79 %	9.33	0.24	1.79 %	2.50	0.00	0.00 %
SemiFlex	9.25	0.00	2.63 %	9.25	0.00	2.63 %	2.50	0.00	0.00 %
MakerBot Flexible	9.42	0.12	0.84 %	9.42	0.12	0.84 %	2.50	0.00	0.00 %

Previous work suggested that material shrinkage is mostly predominant in the X and Y directions of the test models and the thickness is mostly similar to the design dimension or increased in size marginally after printing (Sood, Ohdar and Mahapatra, 2009). The result obtained for thermoplastic cuboids' shrinkage (Table 3.2) for the majority of the filaments assessed is comparable to the findings of Sood *et al*.

Overall ABS and PLA filaments had the lowest shrinkage. The remaining filaments evaluated here may also be appropriate to 3D print microfluidic/millifluidic devices but, depending on the choice of application, it may be necessary to spend time looking at dimensional correction factors. It should also be considered that for a material with high shrinkage, there is a higher chance of delamination between layers of 3D printing models is detectable, leading to more frequent failure of 3D printing (Weng *et al.*, 2016).

3.5 Examination of liquid absorption by 3D printed materials

Reports suggest 3D printing polymers (filaments) may absorb water from the air which will cause the filament to swell (Ligon *et al.*, 2017)(Le Duigou *et al.*, 2016).
Here, the influence of 3D print infill density on liquid absorption by thermoplastic cuboids (Section 2.5, Figure 2.1), using a range of filaments, was assessed. Water uptake was examined in the presence of deionised water and Buffer A (Trizma®-$MgCl_2$ buffer). The aim was to evaluate the tightness of bonding in the 3D prints at different infill densities. The tightness of bonding is a significant factor to consider toward achieving optimal 3D printed microfluidic or millifluidic device. For instance, if a large volume of liquid is absorbed by thermoplastic materials at different infill density, there is a higher chance of detecting leakage from the constructed microfluidic or millifluidic device.

Initially, thermoplastic cuboids were printed at the standard 10%, 50% and 100% infill density and weighed. Next, the potential impact of increasing infill density was evaluated by submerging the thermoplastic cuboids in 3 mL of water and buffer solution over three days (Figure 3.6).

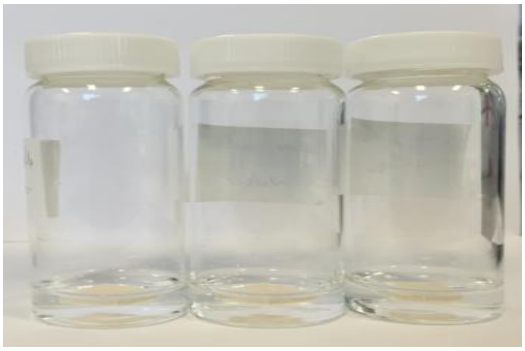

Figure 3.6| **Thermoplastics cuboids submerged in the assay solution;** (Cuboids printed at 10, 50 and 100% infill density).

Data show that thermoplastics cuboids printed at 50% infill density such as ABS (0.80 %, SD = 0.01), 3DXNano ABS (2.48 %, SD = 0.03), Biofila Linen (3.06 %, SD = 0.06), SemiFlex (6.63 %, SD = 0.07), PLA (0.74%, SD = 0.02) absorbed more water when compared to 10% infill density with value of 0.75 % (SD = 0.01), 1.01 % (SD = 0.05), 1.02 % (SD = 0.02), 5.93 % (SD = 0.06) and 0.64 % (SD = 0.01) (Figure 3.6).

In Buffer A thermoplastics cuboids printed at 50% infill density such as 3DXNano ABS (2.58 % (SD = 0.03)), Biofila Linen (1.16 % (SD = 0.02)), Carbon Fiber PLA (0.79 % (SD = 0.03)) and Stainless Steel PLA (0.38 % (SD = 0.01)) absorbed more liquid when compared to 10% infill density with value of (2.05 % (SD =0.05), 1.00 % (SD = 0.02), 0.73 % (SD = 0.04), 0.22 % (SD = 0.05)).

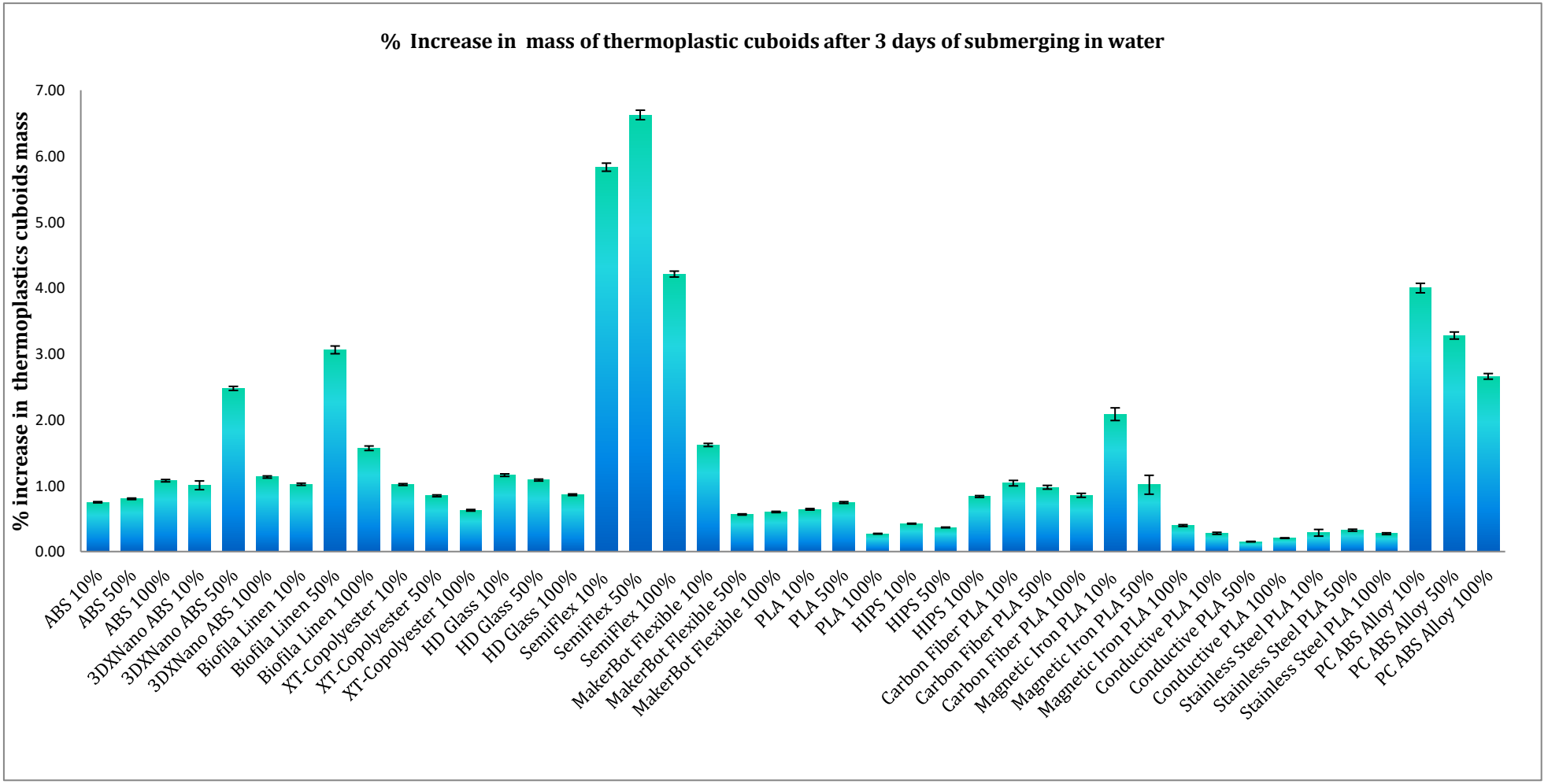

Figure 3.7| **Influence of infill density on water absorption by thermoplastics cuboids;** (printed at 10, 50 and 100% infill density). Error bars on each column represent standard deviations (SD), n=3.

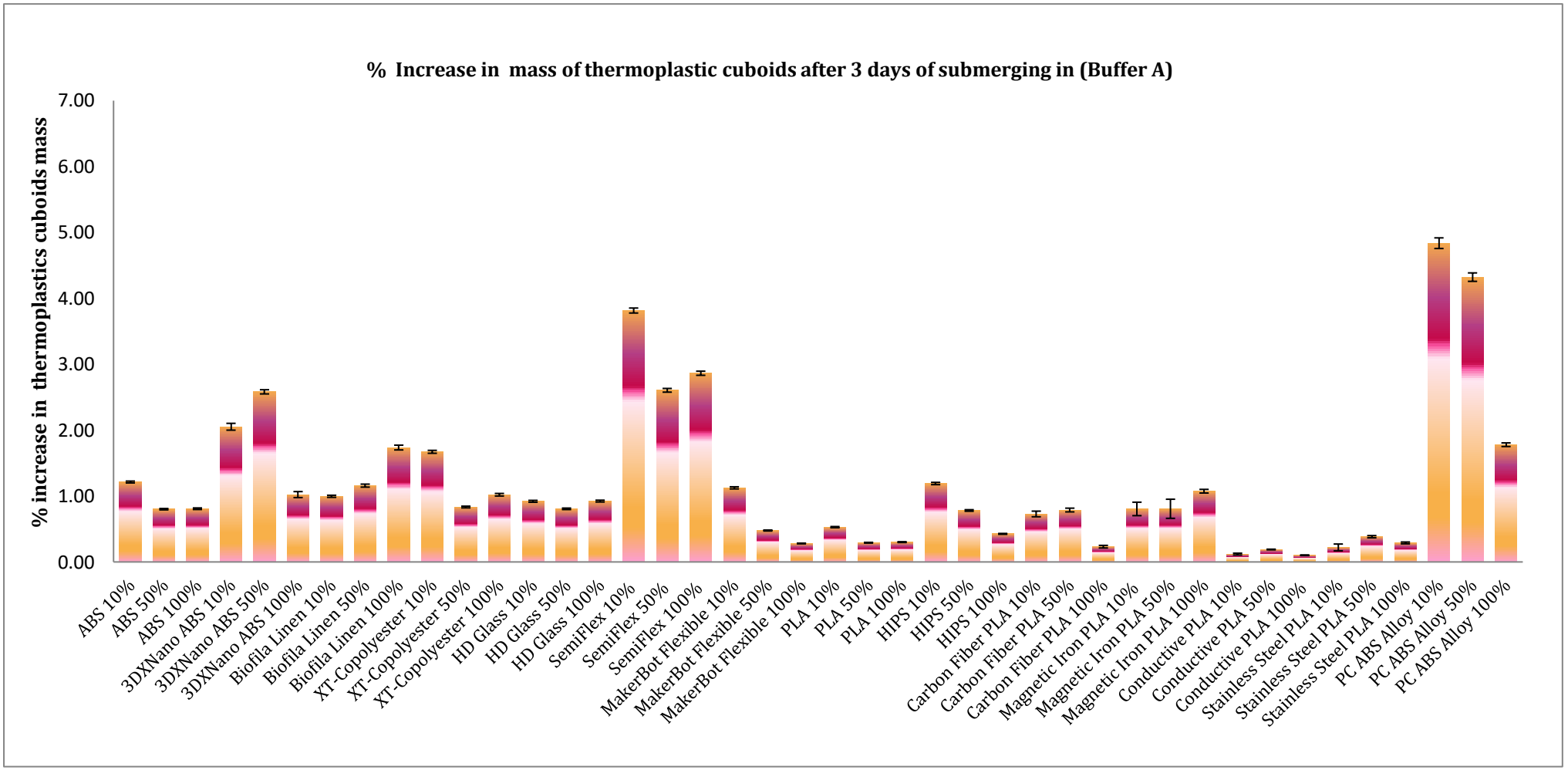

Figure 3.8| **Influence of infill density on (Buffer A) absorption by thermoplastics cuboids;** (printed at 10, 50 and 100% infill density). Error bars on each column represent standard deviations (SD), n=3.

Also, ABS (1.08 %, SD = 0.01) and HIPS (0.84 %, SD = 0.01) cuboids in water solution and Biofila Linen (1.74 %, SD = 0.04) in buffer solution printed at 100 % infill showed a higher liquid absorption compare to 10 and 50% infill density.

Among the filaments studied, SemiFlex and PC ABS Alloy printed at all the examined infill densities had the highest liquid uptake (water and buffer A). In water, SemiFlex cuboids and in Buffer A PC ABS Alloy cuboids printed at 10 % and 50 % infill absorbed more liquid, when compared to other filaments, with an increase in mass of > 4 %.

From the graphs in Figure 3.7 and 3.8, the increase in the mass of thermoplastic cuboids is greater in water than Buffer A. However no difference within error is detectable, when the average percentage increase in mass of all of the cuboids in water (1.41, SD = 1.48) is compared with Buffer A (1.19, SD = 1.11).

Figure 3.9 shows no correlation between water uptake of filaments in water/buffer A solution. It also shows that increasing infill density does not reduce the amount of water/buffer A being absorbed by some filaments. For example, the semi flex filament printed at 50% infill density absorbed more water compared to them ones printed at 100% infill. Also, PC ABS alloy printed at 10% absorbed more buffer A compared to the 50% and 100% models. Subsequently it can also be concluded that increasing the infill density may not improve fabrication of water tightness devices with minimum or no leakage for microfluidic applications.

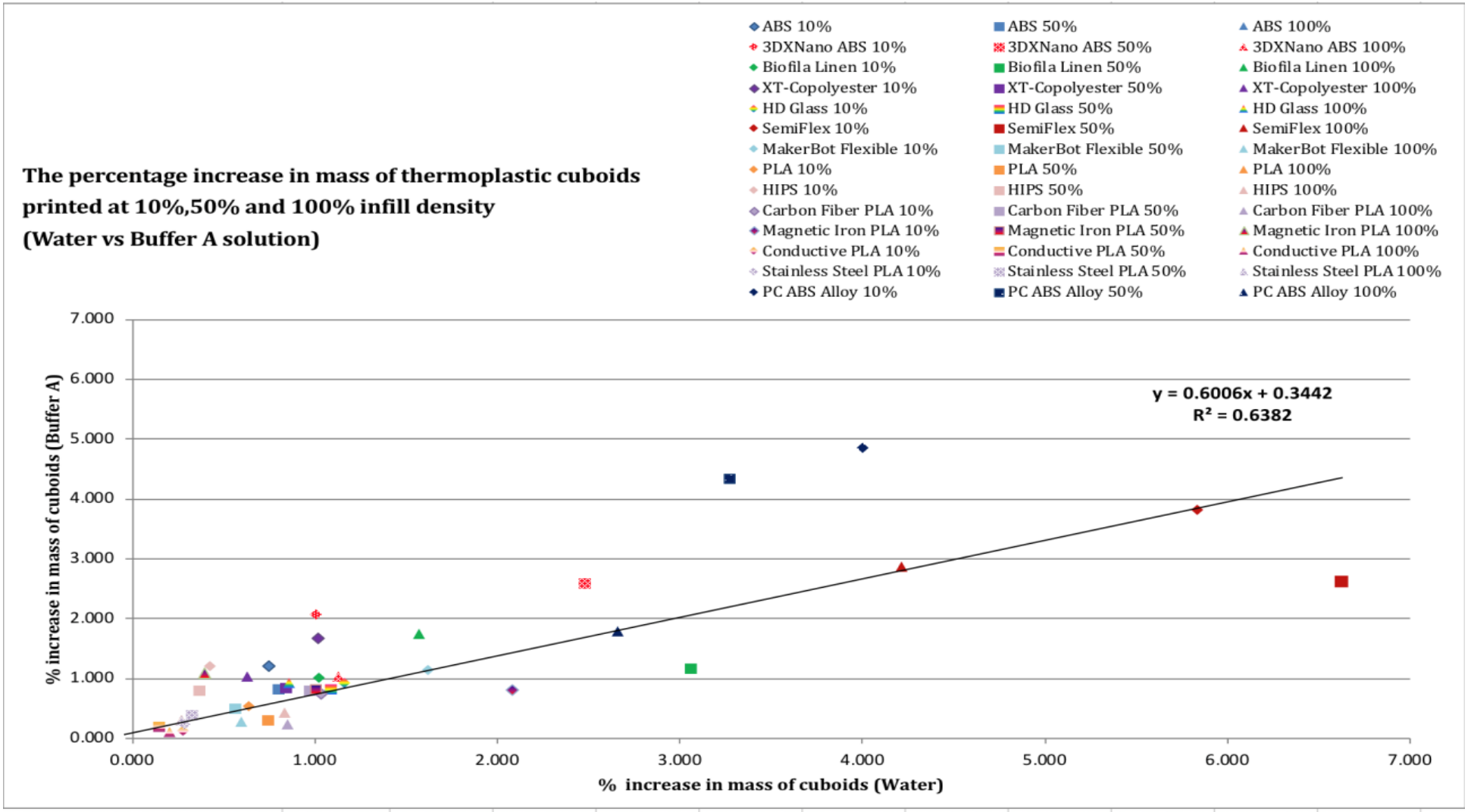

Figure 3.9| **Plots of % increase in mass of thermoplastic cuboid measured;** water vs buffer solution.

According to the data obtained (Figure 3.9), increases the mass of thermoplastic cuboids after removal from liquid solutions are 5% or lower, apart from SemiFlex in water. High liquid uptake by the SemiFlex filament was expected since microscopic inspection detected holes between layers of printed cuboids (Figure 3.4).

According to a report, the printing materials with characteristics that absorb less moisture (liquid uptake) will have better mechanical properties (Le Duigou *et al.*, 2016). Using material with improved mechanical properties means that we can construct microfluidic devices with improved features, e.g. improved surface properties (Ho *et al.*, 2015a). By considering these reports and the data obtained it can be concluded that SemiFlex filament may not be suitable for millifluidic and microfluidic application. There is also a high chance of observing leakage from the 3D-printed devices made from this filament.

3.6 Surface contact angle analysis of 3D printed materials

Contact angles between liquid drops and surfaces can be measured directly from the angle formed at the contact of the liquid and the flat surface (Kwok *et al.*, 1997)(Ingebrigtsen and Toxvaerd, 2007). Drop shape analysis by pendant drop is the most convenient approach for contact angle and surface tension measurement (Ingebrigtsen and Toxvaerd, 2007). Fluids for analysis are loaded via a syringe, an image is taken, and the contact angle determined from this (Becker *et al.*, 2014).

If the water contact angle is larger than 90° (Figure 3.10), the solid surface is considered hydrophobic, and if the water contact angle is less than 90° (Figure 3.10), the solid surface is considered hydrophilic (Förch *et al.*, 2009). The droplet contact angles of water on thermoplastic cuboids made from each filament were measured 3 times, and the average and standard deviation of the droplet (left and right) angles on the thermoplastic cuboids were recorded and presented in (Table 3.2).

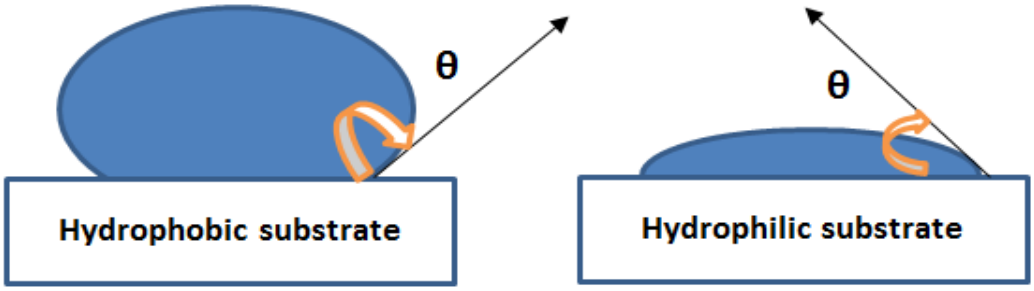

Figure 3.10| **Sketch of a hydrophobic (left) and hydrophilic surface (right)**

Looking at the chemical structure of 3D printing filaments used (Figure 3.2) it can be anticipated that filaments such as Biofila Linen, Bridge Nylon, MakerBot Flexible, T-Glase, Xt-Copolyester and PLA are hydrophilic polymer. This is because there are a lot of polar groups in these polymer (-OH, =NH, =C=O, -C(O)OH, -CN, -C-O-C-,-C-N-C-, and so forth).

Most hydrophilic polymers are grouped by the chemistry of their structure. For example, acrylics include acrylic acid, acrylamide, and maleic anhydride polymers and copolymers. Amine-functional polymers include allylamine, ethyleneimine, oxazoline, and other polymers containing amine groups in their main- or side-chains." Hydrophobic polymers are the opposite of that.

Hydrophilic polymers contain polar or charged functional groups, rendering them soluble in water. However by looking at chemical structure of filaments (Figure 3.2) it is not informal to make decision on suitability of the filaments for microfluidic application based on their hydrophobicity. This is because research has shown that the water contact angle of material is influenced by parameters such as material composition and surface roughness (Moore *et al.*, 2011) (Rosales-Leal *et al.*, 2010).

Contact angle goniometry is typically used to characterise the functionalized surfaces. Researches aim to improve chemical characteristics of the surface for microfluidic application by improving hydrophobicity. ABS and PLA 3D-printed objects have been coated with both hydrophobic and hydrophilic polymers to increase the hydrophobicity of the 3D printed object (Cheng and Gupta, 2017). The microfluidic devices for manipulating fluids with improved surface hydrophobicity are desirable for scientific application to allow ease of fluid flow within a device (Stone, Stroock and Ajdari, 2004).

In this work the water contact angle measurement on the 3D printed thermoplastic cuboids for the range of filaments was measured as detailed in Experimental Section 2.8, to inform decisions about the best filament to use for the fabrication of simple millifluidic devices (Table 3.3).

Table 3.3| **Contact angle measurement of a droplet on thermoplastic cuboids;** Thermoplastic cuboids were printed at 100% infill.

Contact angle measurement of thermoplastic cuboids. n=3

Filaments	Left angle measurement	Left angle SD	Right angle measurement	Right angle SD	Left and Right angle measurement	Left and Right angle SD
ABS	101.00	2.69	97.67	0.54	99.33	2.80
PLA	79.80	0.59	80.93	2.47	80.37	2.06
HIPS	111.20	3.77	114.07	0.82	112.63	3.38
3DXNANO ABS	85.80	4.94	88.63	6.04	87.22	6.24
BIOFILA LINEN	72.97	2.37	76.90	3.04	74.93	3.68
XT-COPOLYESTER	90.70	0.22	93.47	1.75	92.08	2.04
T-GLASE	87.93	1.03	85.97	1.79	86.95	1.93
SEMIFLEX	99.30	2.77	101.47	2.04	100.38	2.92
MAKERBOT FLEXIBLE	96.43	2.21	96.13	1.91	96.28	2.27
HD GLASS	91.57	3.53	92.97	2.52	92.27	3.45
BRIDGE NYLON	67.57	2.54	67.57	0.69	67.57	2.04
PC-ABS ALLOY	82.33	0.37	86.90	2.12	84.62	3.01
CONDUCTIVE PLA	73.97	1.53	76.17	0.38	75.07	1.72
STAINLESS STEEL	85.73	1.37	85.13	3.09	85.43	2.64
MAGNETIC IRON	84.33	2.25	84.50	3.61	84.42	3.30
CARBON FIBRE	62.93	1.03	61.73	3.09	62.33	2.61

Contact angle measurements showed that six out of 16 tested filaments have a hydrophobic surface since the contact angle measurements are greater than > 90°. HIPS filaments exhibited the highest contact angle indicating it has the most hydrophobic surface (Figure 3.11). Bridge Nylon and Carbon Fiber PLA exhibited the lowest contact angle and were thus the most hydrophilic surfaces.

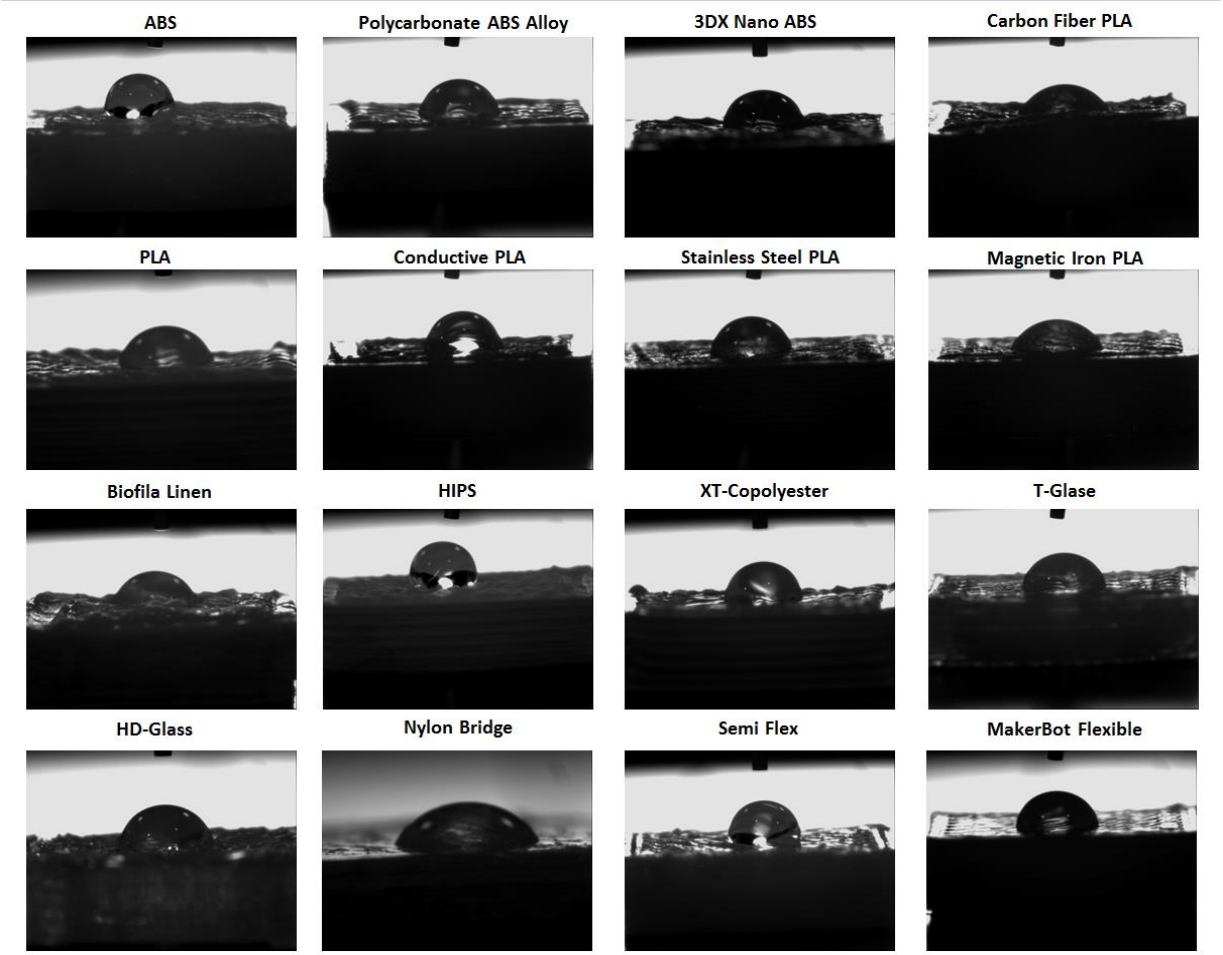

Figure 3.11 | **Contact angle analysis images on thermoplastic cuboids;** images were taken by goniometer OCA15 plus camera. Thermoplastic cuboids were printed at 100% infill. The contact angle measurement was on Nylon Bridge filament was accomplished on the reverse side of the printed cuboids for comparison.

A hydrophobic surface is preferred for millifluidic devices (Lee, Zhang and Yeong, 2016). This suggests that ABS and HIPS filaments are most desirable for fabrication of the microfluidic or millifluidic device and reports show a different value for water contact angle measurement of ABS filaments ranging from (81°- 93°) (Moore et al., 2010) and PLA (73.9°-94.9°)(Salentijn, Hamidon and Verpoorte, 2016), (Lee, Zhang and Yeong, 2016). In this work improved contact angle values for ABS filaments (99.33°, SD= 2.80) and for PLA a mid-range value of (80.37°, SD=2.06) was observed.

The wetting ability of materials is also dependent on many other factors, e.g. the printing process, printing pattern (Serra, Planell and Navarro, 2013), drop size and the 3D printer equipment (Lee, Zhang and Yeong, 2016). Such a detailed analysis of the contact angles is not the main aim of this study, the aim here is to provide a rough estimate of the surface wetting ability between different 3D printing materials for use in fabrication of optimum microfluidic devices. Also, since the surface hydrophobicity can also be improved by post-processing. The result obtained here for contact angle measurement would serve as a guide for preliminary design purpose.

3.7 Assessing Non-Specific binding of DNA and protein to 3D printed materials

The adsorption of biological molecules such as DNA or proteins onto solid surfaces is of major interest in a number of fields such as biology, medicine, biotechnology and food processing (Nakanishi, Sakiyama and Imamura, 2001)(Goebel-Stengel *et al.*, 2011). To use biological molecules such as DNA and proteins within 3D-printed microfluidic/millifluidic biodevices a low non-specific surface binding of DNA and proteins is desirable. Literature reports include the use of diferent plastic materials, however, some may exhibit a high degree of non-specific protein adsorption (Locascio, Perso and Lee, 1999) (Martynova *et al.*, 1997), and binding of DNA or protein molecules within the microfluidic devices can lead to poor device performance (Paul

C.H. Li, 2010). Choosing the appropriate filaments to 3D print biodevices can avoid unpredictable DNA and protein loss on the surface that could result in inaccurate measurements and false conclusions. To determine an optimum thermoplastic filament for the fabrication of biodevices non-specific binding of DNA or protein to thermoplastic cuboids was assessed.

3.7.1 Measuring DNA and protein non-specific binding to 3D printed thermoplastic cuboids using UV visible spectroscopy

Nonspecific binding adsorption of the DNA and proteins to the thermoplastic filaments was evaluated by submerging thermoplastic cuboids (Figure 3.1) printed with a range of different filaments into DNA or BSA solutions. The absorbance of the individual assay solution was monitored by UV/vis spectroscopy.

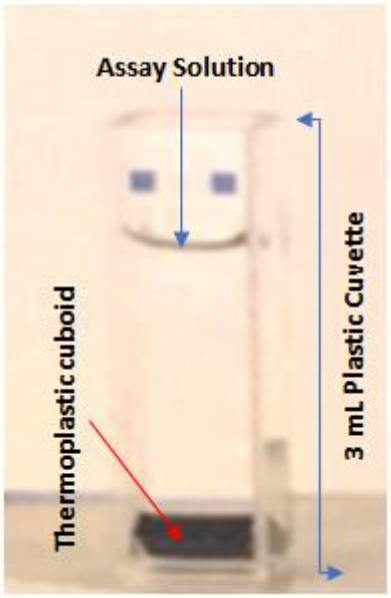

Figure 3. 3| **Conductive PLA submersed in an assay solution:** An example of conductive PLA inserts printed at 10% infill density submersed in 3 mL of 50 µg/mL DNA solution.

Initially, negative controls for adsorption of DNA and protein (BSA) solutions at three different concentrations for each assay sample were evaluated by monitoring the optical absorbance of samples without submerging the thermoplastic cuboids into the solution. The spectrophotometer was set to measure at the wavelength of maximum absorbance (λ_{max}) of each molecule (260 nm for DNA and 279 nm for BSA). Measurements were taken every 10 seconds for 5 minutes for each solution. Solution absorbances were re-measured every 55 minutes for up to 4 hours.

To evaluate the potential impact of increasing infill density on the non-specific binding, a preliminary study of adsorption of DNA and BSA to the PLA thermoplastic were performed at different infill densities. The outcome of the study showed no differences in nonspecific binding absorption of DNA and BSA samples to PLA thermoplastic cuboids at different infill density. As a result, the effect of infill density on DNA and BSA sample nonspecific binding was deemed insignificant.

Nonspecific-binding adsorption of the DNA and proteins to the thermoplastic filaments was evaluated on thermoplastic cuboids printed at 10% infill density. The T-Glase filament was withdrawn from additional assessment since it was not printed at 10% infill density. Bridge Nylon was removed from the study since it was not printed to a suitable quality. Time course absorbance measurements for DNA and BSA solutions of the individual samples were recorded for each filament.

3.7.1.1 DNA adsorption to 3D printed thermoplastic cuboids

The nonspecific binding of DNA to 3D printed thermoplastic filaments was studied at concentrations of 1.25 µg/mL, 12.5 µg/mL and 50 µg/mL. The absorbance value of samples (T = 0 and T = 240 min) for all of the thermoplastic filaments at all DNA concentration were plotted in Figures 3.13 to 3.15.

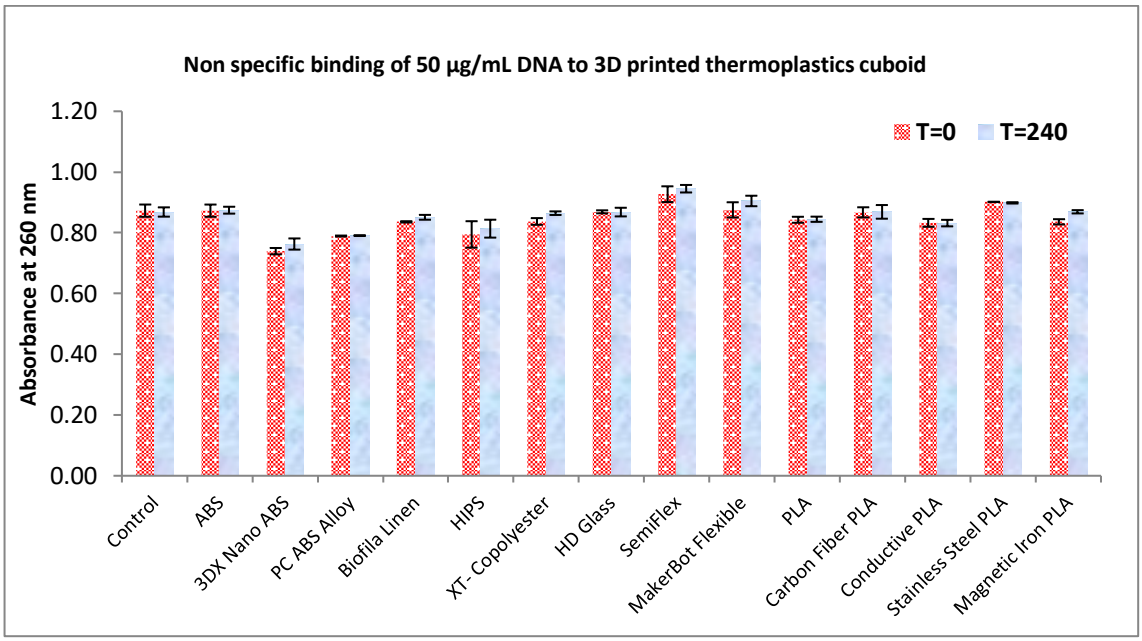

Figure 3.4| **DNA adsorption to 3D printed thermoplastic cuboids nonspecific binding assessment**. Assessment at DNA concentration of 50 µg/mL on thermoplastic cuboids printed at 10% infill density. Error bars on each column represent standard deviations (SD), n = 3. Control represents the absorbance of the mixture with no thermoplastic cuboids.

Figure 3.13 shows no significant increase in absorbance from T = 0 to T = 240 for the majority of the filaments studied. Minor increases in absorbance from T = 0 to T = 240 for 3DXNano ABS, Biofila Linen, XT- Copolyester and Magnetic Iron PLA filaments was observed. However, the error bar overlaps for 3DXNano ABS and Biofila Linen filaments which means that, for these filaments, the increase in absorbance value is not significant.

Five out of 14 filaments tested showed a lower absorbance when compared to the control, which may be due to sample preparation e.g. dilution factor or either non-specific binding absorption. The filaments with lower absorbance compared to control are 3DXNano ABS, PC ABS Alloy, Biofila Linen, HIPS and conductive PLA.

If a similar outcome is observed for the 12.5 µg/mL and 1.25 µg/mL DNA study for these filaments, it can be defined that the decrease in absorbance is due to the non-specific binding adsorption of DNA to thermoplastic cuboids.

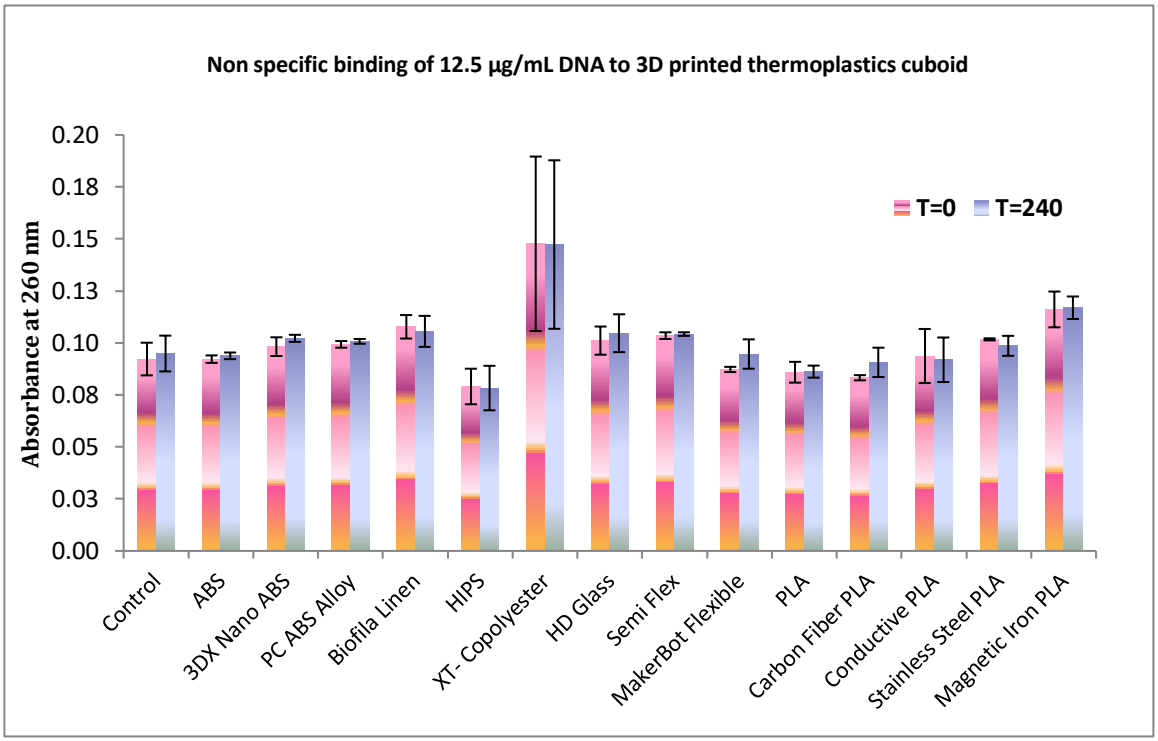

Figure 3.5| **DNA adsorption to 3D printed thermoplastic cuboids nonspecific binding assessment**. Assessment at DNA concentration of 12.5 µg/mL on thermoplastic cuboids printed at 10% infill density. Error bars on each column represent standard deviations (SD), n=3. Control represents the absorbance of the mixture with no thermoplastic cuboids.

At a concentration of 12.5 µg/mL DNA, no significant changes in absorbance from T = 0 to T = 240 for the majority of the filaments studied was detected. For HD Glass, MakerBot Flexible, Carbon Fiber PLA, an increase in absorbance was found but for Conductive PLA a decrease in absorbance from T = 0 to T = 240 was determined. Again, as the error bars overlap, the increase in absorbance value is considered not significant within the error.

Of the assessed filaments, XT-Copolyester showed higher absorbance compared to the control but the large error bar indicates that the value is not significant. HIPS and PLA

filaments showed lower absorbance values when compared to the control but, again, these were not significant.

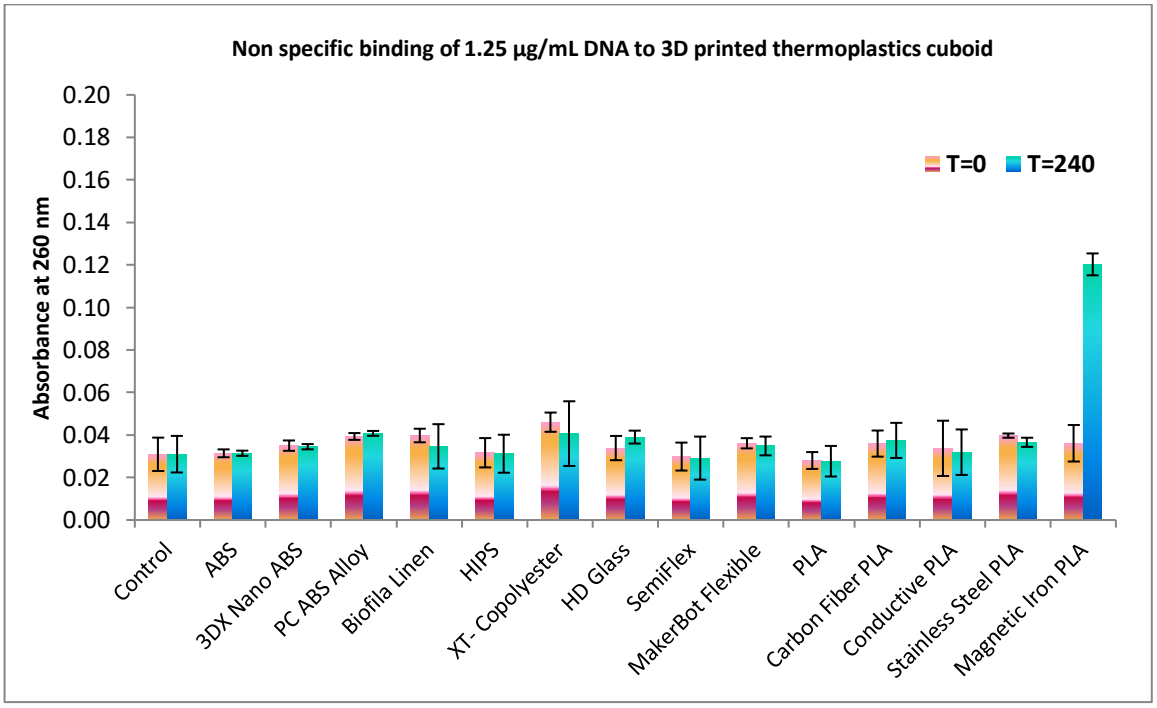

Figure 3.6| **DNA adsorption to 3D printed thermoplastic cuboids nonspecific binding assessment**. Assessment at DNA concentration of 1.25 µg/mL on thermoplastic cuboids printed at 10% infill density. Error bars on each column represent standard deviations (SD), n = 3. Control represents the absorbance of the mixture with no thermoplastic cuboids.

To further understand the non-specific binding adsorption of DNA to thermoplastic filaments, the assessment was also performed at a very low concentrations of DNA. This was necessary since the components present in commercial assay kits are generally in the microgram per milliliter range.

Figure 3.15 shows that at a DNA concentration of 1.25 µg/mL, no significant changes in absorbance from T = 0 to T = 240 for 13 out of 14 assessed filaments. No significant difference was detected for these filaments when absorbance values were compared to the control except for Magnetic Iron PLA at T = 240 min. This positive increase in absorbance was assumed to be due to leaching of thermoplastic materials into the

solution since the colour of the thermoplastic cuboids used for this assay after the completion of assessment was changed from black to brown.

Overall, at DNA concentrations of 1.25 µg/mL no significant changes in absorbance from T = 0 to T = 240 for 15 out of 16 assessed filaments and in comparison, to control was detected. Apart from Magnetic Iron PLA, the remaining filaments assessed used in this study are considered reliable to be used for the fabrication of biodevices using DNA. Magnetic Iron PLA is unlikely to be usable due to leaching of the chemical from thermoplastics materials into a solution, causing erroneous and false conclusions for colorimetric microfluidic/millifluidic applications.

3.7.1.2 BSA adsorption to 3D printed thermoplastic cuboids

The nonspecific binding of proteins (BSA) to 3D printed thermoplastic filaments was studied at concentrations of 12.5 µg/mL, 0.5 mg/mL and 1.5 mg/mL. The absorbance value of monitored samples (T=0 and T=240 min) for all of the thermoplastic filaments at all BSA concentration are shown in Figures 3.16 to 3.18.

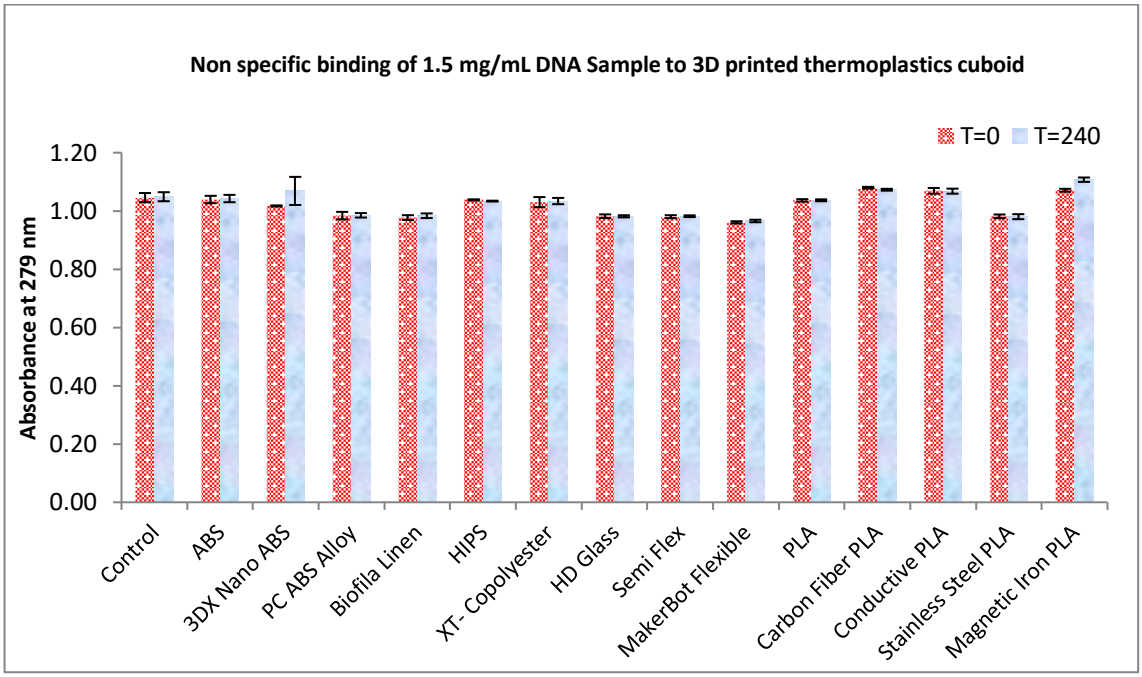

Figure 3.7| **BSA adsorption to 3D printed thermoplastic cuboids nonspecific binding assessment**. Assessment at BSA concentration of 1.5 mg/mL on thermoplastic cuboids printed at 10% infill density. Error bars on each column represent standard deviations (SD), n = 3. Control represents the absorbance of the mixture with no thermoplastic cuboids.

Figure 3.16 shows no significant increase in absorbance from T = 0 to T = 240 for 12 out of 16 studied filaments. Minor increases in average absorbance from T = 0 to T = 240 for 3DX Nano ABS and Magnetic Iron PLA filaments were observed, however these are not significant.

Five out of 14 tested filaments, PC ABS Alloy, Biofila Linen, HD Glass, SemiFlex and MakerBot Flexible, showed a lower absorbance compared to the control. If the similar outcome is observed for the 0.5 mg/mL and 12.5 µg/mL BSA assessment for these filaments, it can be determined that the decrease in absorbance is due to the non-specific binding adsorption of BSA to thermoplastic cuboids.

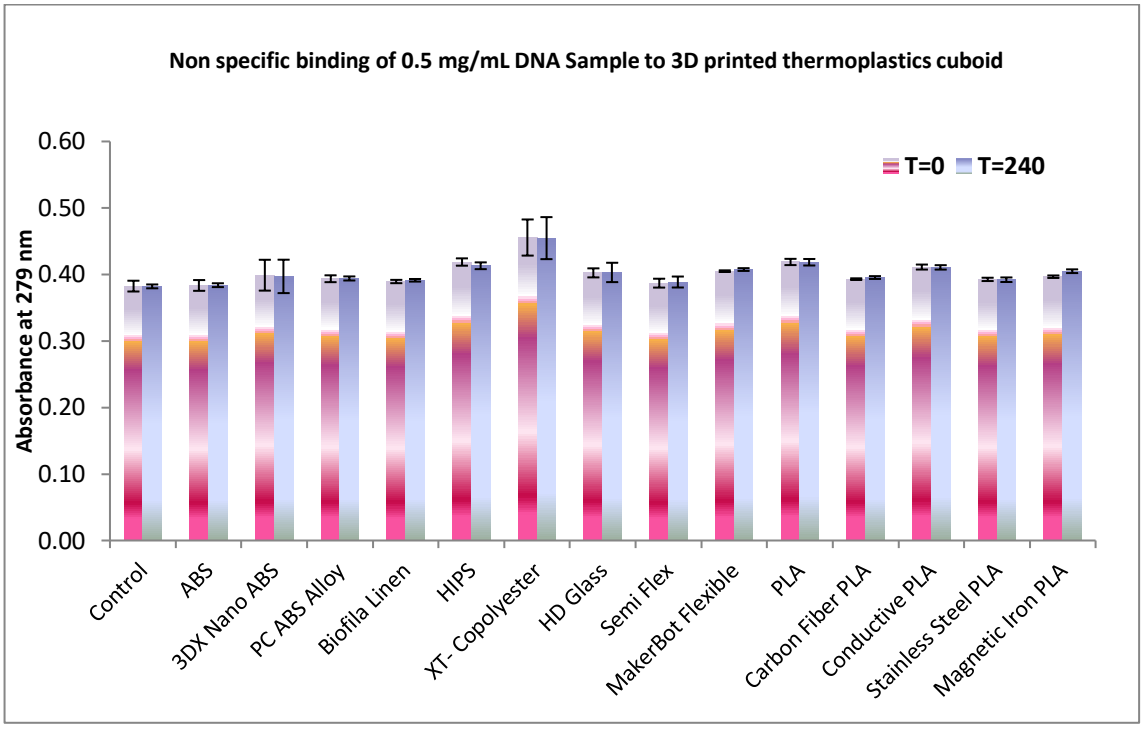

Figure 3.8| **BSA adsorption to 3D printed thermoplastic cuboids nonspecific binding assessment**. Assessment at BSA concentration of 0.5 mg/mL on thermoplastic cuboids printed at 10% infill density. Error bars on each column represent standard deviations (SD), n = 3. Control represents the absorbance of the mixture with no thermoplastic cuboids.

At a concentration of 0.5 mg/mL BSA, no significant changes in absorbance from T = 0 to T = 240 for any of the filaments studied are seen. None of the thermoplastic cuboids showed a lower absorbance compared to the control.

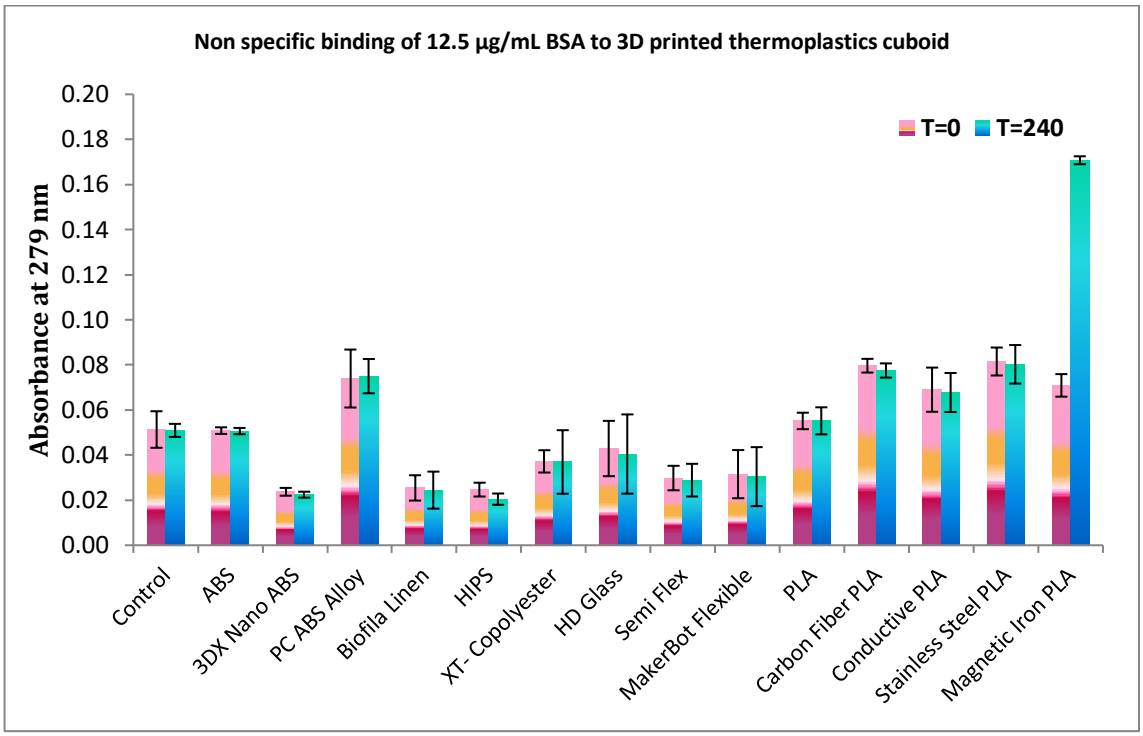

Figure 3.9| **BSA adsorption to 3D printed thermoplastic cuboids nonspecific binding assessment**. Assessment at BSA concentration of 12.5 µg/mL BSA on thermoplastic cuboids printed at 10% infill density. Error bars on each column represent standard deviations (SD), n = 3. Control represents the absorbance of the mixture with no thermoplastic cuboids.

Figure 3.18 illustrates the large difference in absorbance values for thermoplastic cuboids compared to the control at a BSA concentration of 12.5 µg/mL. However, this variation in absorbance value was assumed to be due to sample preparation or dilution factor since experiments were completed at different days.

No significant changes in absorbance value from T = 0 to T = 240 were found for 13 out of 14 assessed filaments (Figure 3.20). A positive increase in absorbance was obtained for Magnetic Iron PLA, which was assumed to be due to the leaching of thermoplastic materials into the solution. This outcome was also observed for this filament for DNA adsorption at 1.25 µg/mL (Figure 3.15).

To determine the suitability of Magnetic Iron PLA filament for further study, the initial (T = 0) and final spectrum (T = 240 min) at 1.25 µg/mL DNA and 12.5 µg/mL BSA were plotted and compared to data for the PLA filament (Figure 3.19 and Figure 3.20).

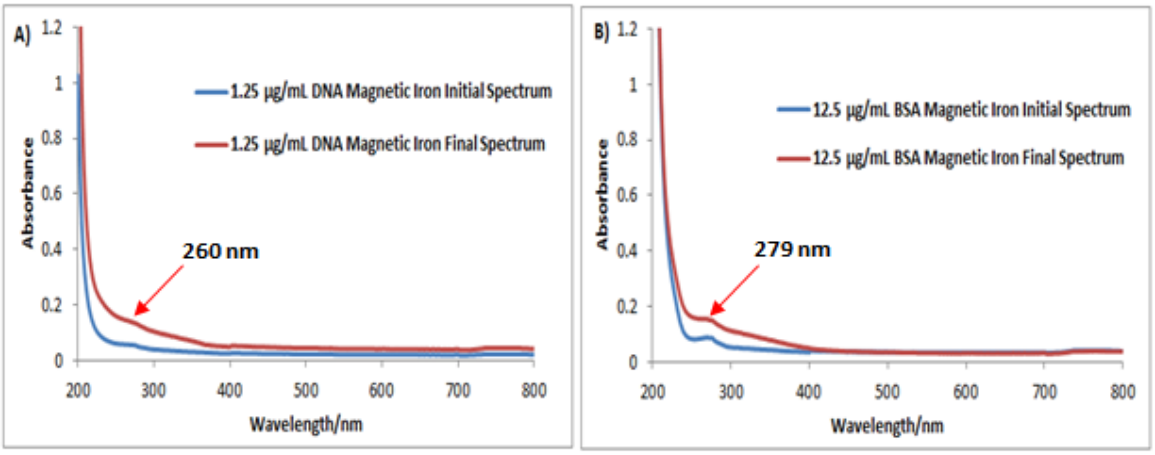

Figure 3.10| **Initial and final spectrum measurement for DNA [A] and BSA [B] solution**; graph of initial and final absorption spectra for DNA [1.25 µg/mL] and BSA [12.5 µg/mL] for Magnetic Iron PLA cuboids printed at 10% infill density.

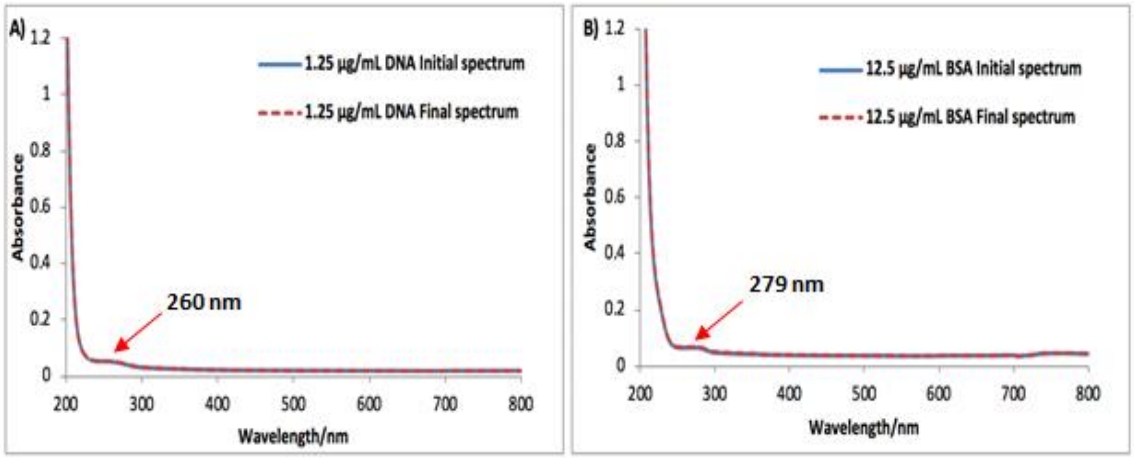

Figure 3.11| **Initial and final spectrum measurement for DNA [A] and BSA [B] solution**; graph of initial and final absorption spectra for DNA [1.25 µg/mL] and BSA [12.5 µg/mL] for PLA cuboids printed at 10% infill density.

Figure 3.20 shows that at 1.25 µg/mL DNA and 12.5 µg/mL BSA the initial and final spectra for PLA thermoplastic cuboids at the assessed concentrations of DNA and BSA is superimposable with no differential peaks. However, the spectra for Magnetic Iron PLA (Figure 3.19) for both the DNA and BSA non-specific binding studies show a higher peak at λ_{max} suggesting that the increase in absorbance is due to the leaching from the thermoplastic. As a more general check, the initial and final UV/vis spectra (200 – 800 nm) for all of the 15 assessed filaments was determined and no new peaks were observed, see Appendix Figure 3.23.

Overall, based on the data obtained for non-specific binding of DNA and BSA to 3D printed thermoplastic cuboids, a majority of the assessed filaments described in Section 3.7, with the exception of Magnetic Iron PLA, were considered appropriate to be used in the fabrication of biodevices.

3.8 Summary and conclusions

In this work reliable printing settings to print 3D models using novel 3D printer filaments were determined. It was found that of 17 assessed filaments only CF0 carbon fibre, Nylon Bridge and T-Glase failed to print reproducibly over a range of infill densities.

The filaments were characterised for use in microfluidic/milifluidic application and the results compared to the current literature. Filaments were characterised by surface roughness (microscopic assessment), shrinkage effect, layer bonding (water tightness) and hydrophobicity from the water contact angle of the printed material. The nonspecific binding of DNA and BSA to the surface of 3D printed filaments in the printed state was also measured.

A microscopic inspection of the surface properties of the 3D printed thermoplastic cuboids showed surface roughness varied on different filaments, for instance, ABS, PLA, XT-Copolyester shows smoother (less ridged) surface finish when compared to HIPS or Biofila linen filaments. However, a ridged topology on printed surfaces of the majority of the evaluated filaments was observed. Voids were detected on the surface of Bridge Nylon, SemiFlex and T-Glase and bubbles were observed on the surface of printed MakerBot Flexible thermoplastic cuboids which makes these filaments of little use in microfluidic applications.

The shrinkage of the thermoplastic filaments in the printed state was assessed by measuring thermoplastic cuboids in XYZ direction. It was determined that for construction of precise 3D print shrinkage correction factor should be considered for all of the assessed filaments. Shrinkage of the 3D printed cuboids was found predominantly in the X and Y directions as reported in the literature (Sood, Ohdar and Mahapatra, 2009). ABS and PLA filaments were found to be the most suitable filaments with the lowest percentage of shrinkage. The calculated shrinkage percentage for ABS and PLA

filaments in the X and Y directions were 0.53% and 0% in the Z direction which is much lower than the reported values ranging from 3% for PLA and 34.53% for ABS (Alsoufi and Elsayed, 2018).

An examination of liquid absorption by 3D printed material showed that the majority of the filaments were suitable for fabrication of microfluidic devices. The calculated liquid uptake by all of the evaluated thermoplastic cuboids in three days was less than 5%. SemiFlex filament was considered unsuitable since holes were detected within the layers of printed cuboids under microscopic inspection (Figure 3.3), which indicate a high chance of leakage from the 3D-printed devices made from this filament. From data obtained no correlation between liquid uptakes for filaments in water/buffer solution was made.

Previous studies have showed limitations in fabrication of microfluidic devices by FDM; leakage was observed in some cases requiring time-intensive alterations to the printing process by changing the percentage infill or the use of post-processing applications (Gross et al.,2014)(Morgan *et al.*, 2016). The outcomes of this study may help researchers to avoid using some filaments for making liquid handling devices and assist them with correct information in which infill density may not be a significant factor to improve fabrication of water tightness devices with minimum or no leakage.

Contact angle measurement on thermoplastic cuboids determined that six out of 16 tested 3D filaments have a hydrophobic surface. Amongst filaments with hydrophobic surfaces, ABS and HIPS had the highest contact angles measurement. Since a hydrophobic surface is preferred for millifluidic devices (Lee, Zhang and Yeong, 2016), ABS and HIPS were found to be the most desirable filaments from the range selected to fabricate microfluidic or millifluidic devices.

The current literature reports values for water contact angle measurement of ABS filaments ranging from (81°- 93°) (Moore et al., 2010) and PLA (73.9°-94.9°) (Salentijn, Hamidon and Verpoorte, 2016), (Lee, Zhang and Yeong, 2016). The contact angle values reported in this work for ABS filaments (99.33°, SD = 2.80) and PLA (80.37°, SD = 2.06) vary slightly to those in the literature because the contact angle is depended on surface roughness which can be influenced by the printing process, printing pattern (Serra, Planell and Navarro, 2013), drop size and the 3D printer equipment (Lee, Zhang and Yeong, 2016).

Finally, in this work, the non-specific adsorption of DNA and BSA to 3D printed thermoplastic filaments was determined over a range of concentrations. From the data obtained it was determined that, apart from Magnetic Iron PLA, a majority of the filaments assessed exhibited low non-specific binding which is appropriate for fabrication of biodevices. Since one of the key problems in microfluidic applications is associated with non-specific adsorption of DNA and BSA to plastics (Martynova *et al.*, 1997), the data obtained here can serve as important guide for eliminating the undesired filament through the study which has not been studied before.

CHAPTER 4

DECANTING LIQUIDS INTO 3D PRINTS USING A BESPOKE SYRINGE EXTRUDER FOR THE MAKERBOT REPLICATOR 2X

4.1 Introduction

The development of technologies to enhance the capabilities of investigators in biological and medical research has always been an essential goal of microfluidics research (Sackmann, Fulton and Beebe, 2014). Recent multi-use bioprinters with a modular system of dual printing nozzles have introduced the ability to print biological material such as bioinks, powder mixtures, hydrogels and synthetic polymers (3D printing filaments). However, these 3D printers are costly. To date, the use of FDM 3D printing technologies for printing with a variety of materials such as liquid, polymer, eutectic metal, powder, ceramics and edible material (He *et al.*, 2016) is growing. Moreover, the fast building time and ease of learning can simplified the fabrication process of microfluidic devices to a single step at low cost (Kitson *et al.*, 2012).

The goal of the research described in this chapter is to develop a 3D printing system for decanting liquids (Bio-inks) onto 3D prints by modifying the FDM MakerBot Replicator 2X 3D printer. This would allow researchers to download and 3D print automated fluid handling devices that can be used to parallelise and automate microfluidic/millifluidic enzymatic reaction making microfluidic research application more accessible to new users.

A key objective of this part of research is to establish methodological approaches that can be used to deposit active biological molecules, e.g. proteins to the surface of the 3D-prints (substrate), using FDM 3D printers. The 3D printing system should operate at a minimum heat to prevent denaturation of the biological molecules on a 3D printing substrate.

The key objectives of this work are to:

4a) Use the FDM 3D printer to deliver specific biological liquid inks in such a way that biological molecules retain their activity.

4b) Evaluate the reproducibility of the modified FDM device to deposit liquid of the desired quantity at a specific point on the 3D printed substrate.

4c) Evaluate prototyping of automated fluidic handling devices by FDM 3D printer through assessment of the reproducibility of the modified FDM device for liquid manipulation in integrated parallel 3D printing (filaments and liquid) and simple channel fabrication.

4.2 Syringe extruder fabrication and assembly on the MakerBot Replicator 2X printer

To enable liquid decanting onto 3D prints, a syringe extruder, customised for the MakerBot Replicator 2X experimental printer, was fabricated and assembled. The mechanical components of this extruder were adopted from an open source design of a universal paste extruder (www.thingiverse.com/thing:591849). Full details of the fabrication, assembly, modification and print settings used by the syringe extruder on MakerBot Replicator 2X are in Sections 2.10.1-5.

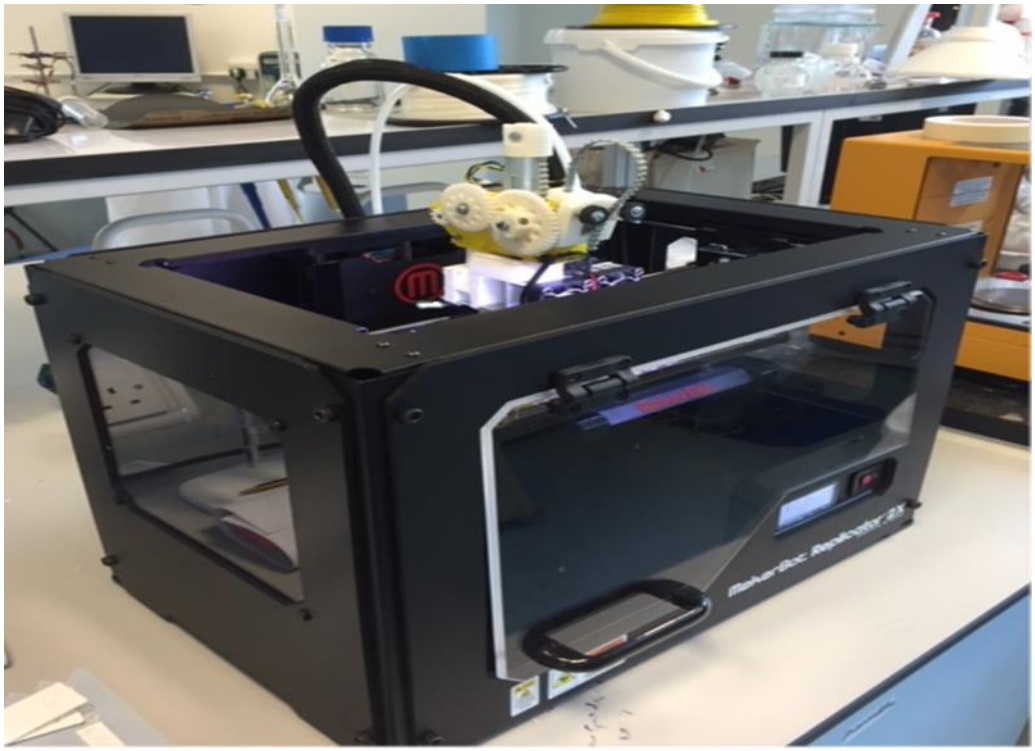

Figure 4.1| **Picture of the MakerBot Replicator 2X 3D printer with assembled syringe extruder**

The body parts of the syringe extruder were reformed and made smaller than the original design to stop it from touching to the side of MakerBot 3D printer during XY movement. The big and double gears griping outer layer were reduced in size slightly, so they can grip together to rotate correctly without a need for the extra drive from the NEMA17 motor. The motor gear fitting area for the NEMA17 motor was made slightly more substantial. T5 belt pulley (Experimental, Figure 2.3.C) was reduced in size and additional inserting area for bolt fitting was made for the big gear (Experimental, Figure 2.4.2 indicated by an arrow) to keep the internal gear more secured. Finally, parts were fabricated and assembled to create the final syringe extruder.

The original left extruder motor was used to power the customised syringe extruder. Performance and usability improvements were made to the customised syringe extruder went through many design iterations. A bespoke interface was designed to assemble the syringe extruder (Experimental, Figure 2.5.A-C) on the 3D printing device without

fasteners, making assembly far simpler. A syringe holder support (Experimental, Figure 2.6) was made to adjust the height of the extruder printing point and was critical for keeping the smaller size syringe stable in place when decanting the liquid. The diameter of syringe holder support was changed accordingly for different syringe sizes application.

The CAD and STL files of customised designs are available in supporting CD, and the exact dimension, sizes, and accessories used for assembling each part are presented in Chapter 2, Section 2.10.1.

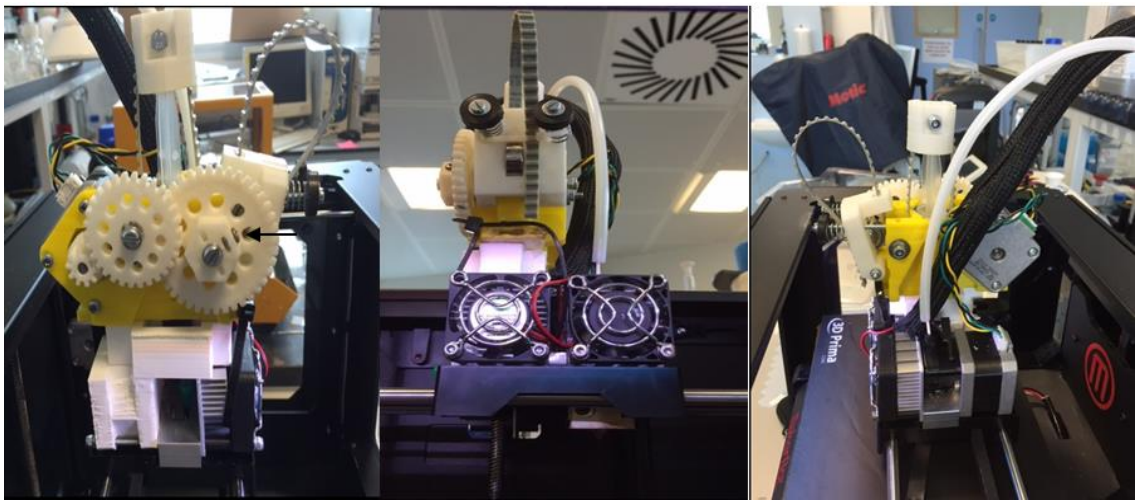

Figure 4.2| **Picture of syringe extruder from a different angle on the device;** extruder body was printed using yellow colour ABS filament.

4.3.1 Decanting liquids by syringe extrusion into 3D prints

Basic liquid manipulations were carried out to test the performance and usability of the customised syringe extruder for liquid decanting onto 3D prints. To achieve this goal, it was important to assess the suitability of the syringe extruder by evaluating a few critical parameters in advance before using the biological molecules. These critical parameters are;

I. Determining print designs and the settings require for decanting the correct volume of liquid using the syringe extruder.

II. Determine the accuracy of the syringe extruder for decanting liquid in a specific position on a 3D print.

III. Determine the smallest possible volume of solution that can be decanted using the syringe extruder.

IV. Identify limitations in liquid manipulation by syringe extrusion in integrated parallel 3D printing (polymer and liquid) and simple channel fabrication.

4.3.2 Preliminary syringe extruder testing: decanting liquid onto 3D-prints

To investigate the suitability of the syringe extruder to decant liquid onto 3D prints simple designs were prepared by Autodesk 123D in different sizes and shapes and each design was tested by printing. ABS thermoplastic filaments were used throughout. The syringe of syringe extruder was filled with an aqueous blue dye solution (Experimental section 2.10.5). A coloured solution was used to allow enhanced visualisation of the position and the volume of decanted liquid dye on a solid substrate.

4.3.2.1 Syringe extruder calibration: Decanting a liquid at a specific location on a 3D-print

To test the accuracy of decanting liquids at a specific point, a cuboid 9.5 mm (W) x 9.5 mm (L) x 1.0 mm (H) was printed as a substrate (Figure 4.3.A (silver square)). The area where the liquid was to be decanted was designed as cylindrical shape (Figure 4.3.A (red cylinder)) with dimensions of 1.00 mm (H) x 2.5 mm (radius) on top of the centre of the cuboid. The design (Figure 4.3 A) was printed by a dual extrusion printing setting (Experimental, Table 2.4) which resulted in the decanting of a droplet of the liquid by syringe extruder on the ABS substrate.

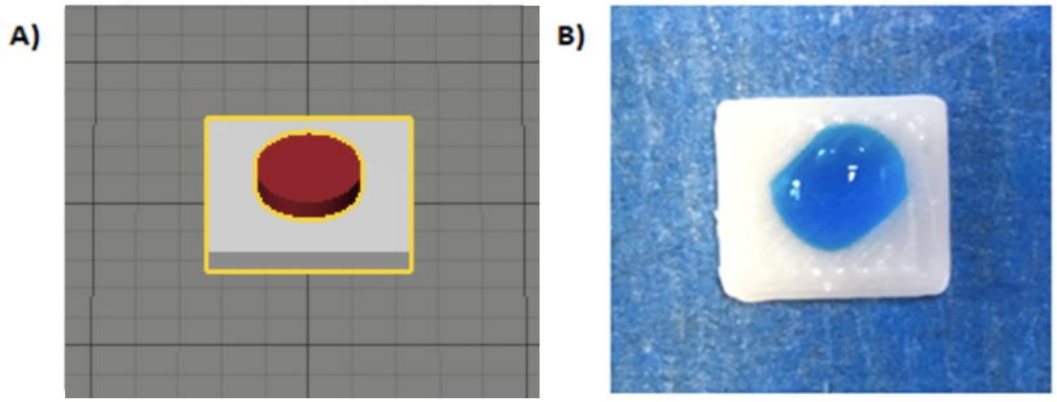

Figure 4.3| **Liquid printing on ABS substrate**. A) Shows designed objects; (Silver colour design (ABS substrate) defines an object to be printed by a right extruder, and red (liquid) define printing by left extruder) B) shows the printed design.

The design was printed 20 times, and it was concluded that the settings of syringe extruder would reproducibly enable a liquid drop to be deposited in the same location on the 3D printed ABS substrate every time.

Next, the smallest volume of liquid that could reliably be decanted using the syringe extruder was determined.

4.3.2.2 Determining the smallest volume of liquid that can be decanted on a 3D-print

To identify the smallest volume of liquid that can be decanted on the thermoplastic material using the syringe extruder, a square-shaped object with dimensions of 9.5 mm (W) x 9.5 mm (L) x 1.0 mm (H) was used as a substrate. Five different cylinder-shaped objects with dimensions of 0.5 mm (H) x 0.5 mm (radius) (A), 1.0 mm (H) x 1.0 mm (radius) (B), 1.5 mm (H) x 1.5 mm (radius) (C), 2.0 mm (H) x 2.0 mm (radius) (D) and 2.5 mm (H) x 2.5 mm (radius) (E) were designed and each was decanted with a syringe extruder in dual extrusion mode on top of the ABS substrate. Changing the volume of

this cylinder allows calibration of the printed shape with respect to the volume of solution that can be extruded.

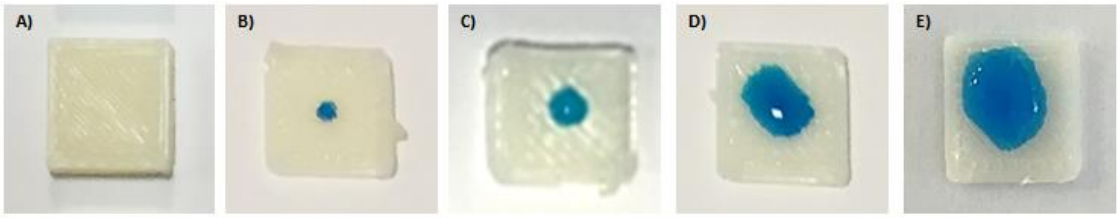

Figure 4.4| **Shows the photograph of the printed designs;** A) represent the substrate design with a dimension of 9.5 mm (W) x 9.5 mm (L) x 1.0 mm (H)and cylinder design with dimension of 0.5 mm (H) x 0.5 mm (radius). B) Substrate + cylinder dimension of 1.0 mm (H) x 1.0 mm (radius). C) Substrate + cylinder dimension of 1.5 mm (H) x 1.5 mm (radius). D) Substrate + cylinder dimension of 2.0 mm (H) x 2.0 mm (radius). E) Substrate + cylinder dimension of 2.5 mm (H) x 2.5 mm (radius). In the photos, the sizes of the printed objects vary slightly since the photograph was taken at a different angle. However, all of the printed substrates were the same size with a different amount of liquid decanted on top of it which was equivalent to the design size of the object decanted on a 3D print by a left extruder.

Apart from the design A, the liquid was decanted successfully on top of the ABS substrate for all designs. The smallest drop that was decanted was for design B. To test the reproducibility of the method each design was printed 20 times. Over the 20 repeats, for design B the liquid was not decanted on top of the substrate at each attempt and 10 out of 20 repeats were successful.

For the remaining designs, shown in Figure 4.4, liquid was decanted successfully on top of ABS substrate 19/20 times for design C, 18/20 for design D and 20/20 times for design E. Accordingly, it was concluded that the smallest droplet of liquid that can reproducibly be decanted using syringe extruder was from object C with dimensions of 1.5 mm (H) x 1.5 mm (radius). To identify the approximate volume/mass of droplet that was decanted for design C, the designs (substrate and cylinder of design C) were reprinted in two steps. Starting with printing the ABS substrate, the printer was paused

to remove the substrate from the platform for weighting. Once the substrate was weighed, it was placed back on the platform at the exact position for printing the liquid droplet by syringe extruder. Subsequently, the printer was restarted, and syringe extruder decanted a droplet on top of the ABS substrate. At this point, the substrate was removed from the platform, and the weight of the substrate with droplet was measured. Five replicate prints were made, and the mass of the substrate before and after decanting the droplet is recorded in Table 4.1.

Table 4.1| **Represent mass of 3D printed substrate with and without decanted droplet.** The density of solution is 1000 kg/m^3 (used for converting mass in milligrams to millilitres).

Attempt	Mass of base with a dimension of (9.5 W x 9.5 L x 1.0 H) mm	Mass of base plus mass of the droplet Droplet design size of (R=1.5, H=1.5) mm	Mass of droplet measured
1	0.1817 g	0.1935 g	0.0118 g
2	0.1818 g	0.1925 g	0.0117 g
3	0.1817 g	0.1935 g	0.0118 g
4	0.1818 g	0.1938 g	0.0120 g
5	0.1802 g	0.1921 g	0.0119 g
		The average mass of the droplet 0.0116 g	**SD** 0.000532

According to Table 4.1, the mass of droplet was 0.0116 g which is equivalent to 0.0116 mL of liquid as the density of water is 1 g/cm^3. The calculated cylinder design C volume is 10.607 mm^3 which, using the formula $V=\pi r^2 h$, gives 10.607 mm^3 as equivalent to 0.0106 mL and comparable to the volume of droplet decanted by syringe extruder.

Table 4.1 also shows reproducible decanting of small liquid drops of approximate weight/volume of less than 0.01 g or 0.01 mL on the substrate by syringe extruder. The standard error for determining the mass of individual droplet was ≤0.05 proving that the measurements using balance were accurate.

4.3.2.3 Determining the smallest possible volume of AuNPs solution that can be decanted on a 3D print

Experiment 4.3.2.2 was repeated using 20 nm AuNPs (Figure 4.5) to ensure an improved overview of the solution printing size and to determine if there would be any difference in the amount of liquid decanted from syringe extruder once a different solution is used. Gold nanoparticles were used here since they were considered as a chemical linker in the development of new bio-ink for FDM printers in this research. The smallest reproducible drop that was decanted using AuNPs was design C.

The average mass of the five repeats of droplets decanted onto ABS substrate using AuNPs was found to be 0.0124 g (SD = 0.00021). The slight increase in size is observable, and it is comprehensible since gold nanoparticles are slightly heavier than water solution (Qian *et al.*, 2013).

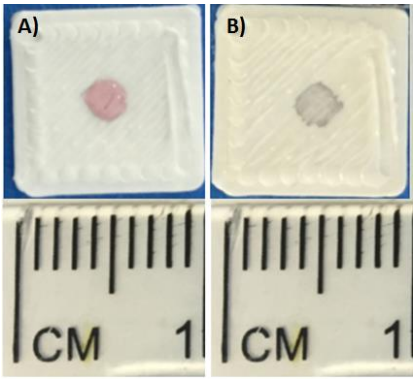

Figure 4.5| **Gold nanoparticles 20 nm diameter decanted on ABS substrate using dual extrusion; A) before and B) after drying**. Picture of ABS substrate + cylinder dimension of (R=1.5, H=1.5) mm decanted using syringe extruder in liquid form.

4.3.2.3 Size comparison between the CAD design object and the decanted liquid volume

The experiment (Section 4.3.2.2) was repeated using 20 nm AuNPs. However, the height of the cylinder design was kept constant. Once again, the ABS substrate of 9.5 mm (W) x 9.5 mm (L) x 1.0 mm (H) and cylinder dimensions of 1.0 mm (H) x 0.5 mm (radius) (A), 1.0 mm (H) x 1.0 mm (radius) (B), 1.0 mm (H) x 1.5 mm (radius) (C), 1.0 mm (H) x 2.0 mm (radius) (D) and 1.0 mm (H) x 2.5 mm (radius) (E) respectively. Each design was printed under the dual extrusion settings. The liquid was decanted on top of the substrate and allowed to dry. Apart from cylinder A, AuNPs were successfully decanted on to a 3D printed substrate in the form of the droplet at each attempt. For each design, the size of dried droplet printed was measured using a ruler in the XY directions (Figure 4.6.A) for calculating the surface area.

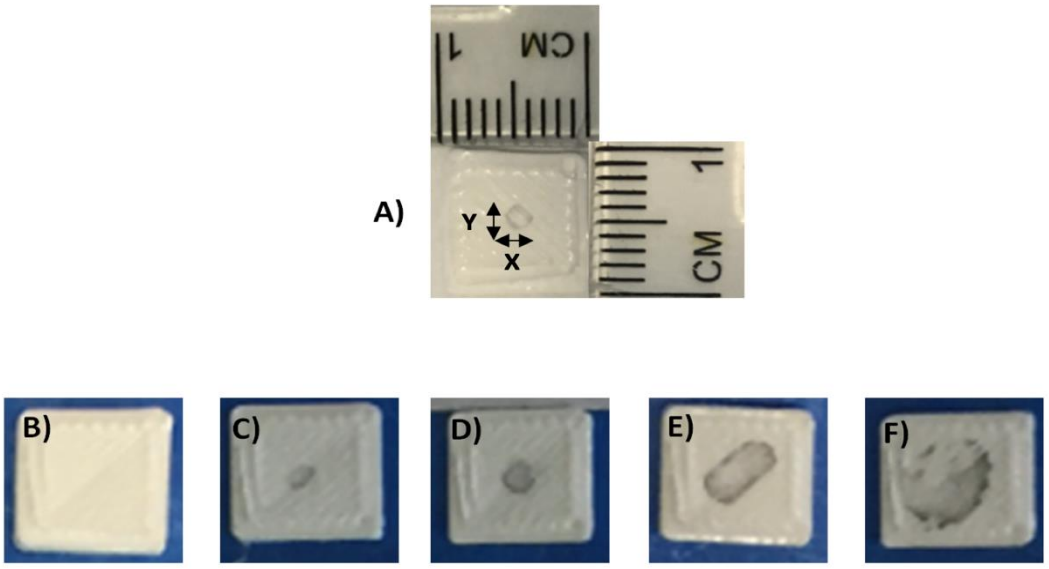

Figure 4.6| **Shows the photograph of the printed designs and dried AuNPs droplet;** A) Illustration of the technique used for measuring the dimension of dried AuNPs on a 3D print. B) represent the substrate design with a dimension of (9.5 W x 9.5 L x 1.0 H) and cylinder design with dimension of (R=0.5, H=1.0) mm. C) Substrate + cylinder dimension of (R=1.0, H=1.0) mm. D) Substrate + cylinder dimension of (R=1.5, H=1.0) mm, E) substrate + cylinder dimension of (R=2.0, H=1.0) mm. F) Substrate + cylinder dimension of (R=2.5, H=1.0) mm.. In the photos, the sizes of the printed objects vary slightly since the photograph was taken at a different angle. However, all of the printed substrates were the same size with a different amount of liquid decanted on top of it which was equivalent to the cylinder design dimension.

Five replicate prints were performed for each design size. The mean and standard deviation of measured droplet correspond to each size was recorded. Accordingly, surface areas of the decanted droplets were determined and compared to the designed surface area of the cylinder base (Figure 4.7).

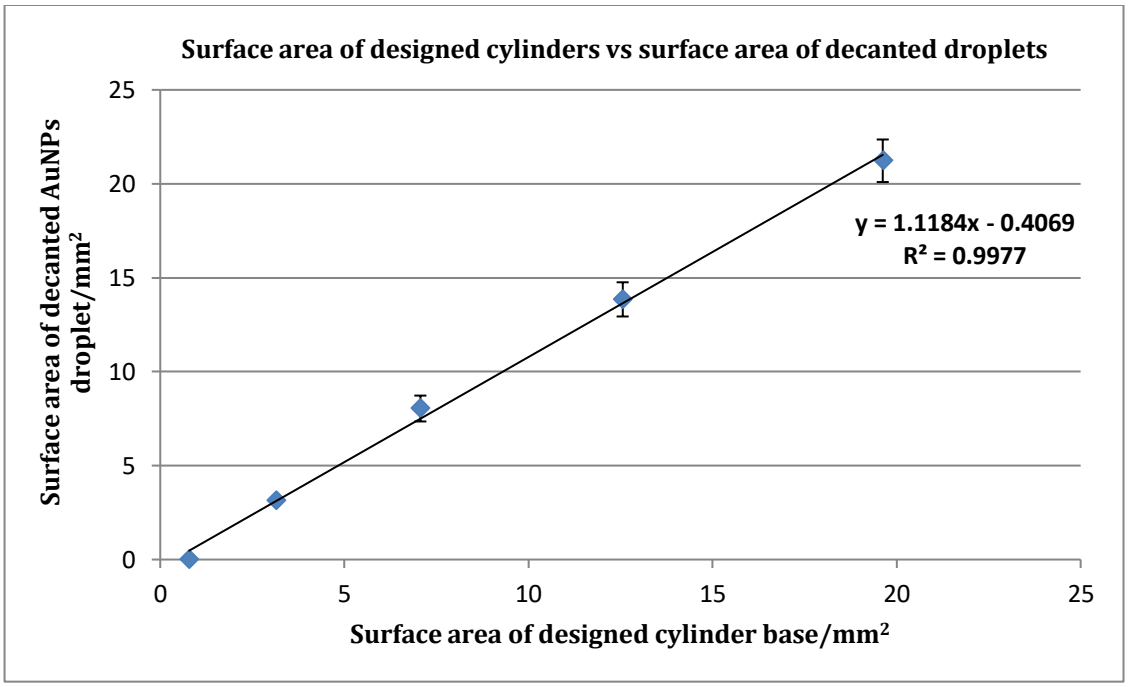

Figure 4.7| **Scatter plot of surface areas of designed cylinders vs. surface area of a decanted droplets;** for designs dimensions specified in section 4.3.2.3. Error bars on each column represent standard deviations (SD), n=3.

The graph shows a positive linear correlation since the R^2 value is close to 1 indicating a close correlation observed between surface areas of designed cylinder and the surface area of the decanted droplet. The closeness of the correlation is probably due to the fact that ABS filament is hydrophobic with contact angle value of 99.33°, which was described in Chapter 3.

4.3.3.1 Liquid manipulation by syringe extrusion

To better understand the performance and usability of the syringe extruder on the MakerBot Replicator 2X 3D printer and to identify limitations in liquid manipulation by syringe extrusion for liquid handling applications a number of 3D printing tests were carried out.

i. The ability of syringe extruder to fill a 3D printed container by decanting liquid at the specific point was tested.
ii. The capability of the syringe extruder to decant multiple droplets in the form of a straight line was determined.
iii. The performance of syringe extruder in decanting liquid into a simple 3D printed channel was assessed.

4.3.3.2 Parallel 3D print and liquid manipulation to fill 3D printed container

To determine the suitability of the syringe extruder to decant liquid into a 3D print several simple 3D printing studies were completed. Two designs were prepared: the first was a square shaped container (Figure 4.8.A) with external dimensions of 15 mm (W) x 15 mm (L) x 10 mm (H) and internal dimensions of 8 mm (W) x 8 mm (L) x 5 mm (H); the second design (Figure 4.8.B) was a cuboid with comparable size to the gap of the container (Figure 4.8.A), designed for liquid manipulation.

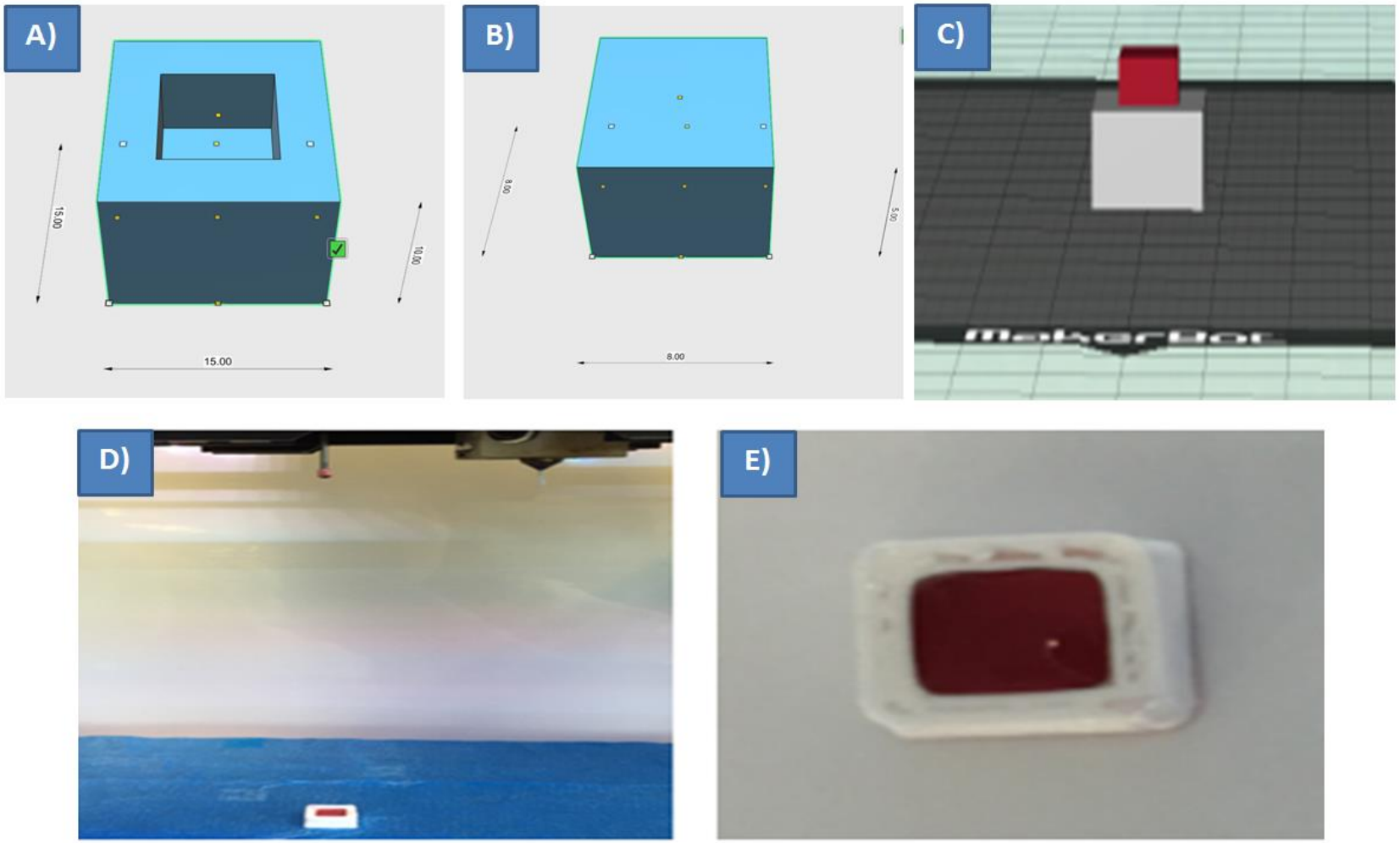

Figure 4.8| **The stepwise layout from 3D designs to 3D printing object.** A) represents the square shape container with external dimensions of 15 mm (W) x 15 mm (L) x 10 mm (H) and internal dimensions of 8 mm (W) x 8 mm (L) x 5 mm (H). B) represents a cuboid, designed for liquid manipulation with dimensions of 8 mm (W) x 8 mm (L) x 5 mm (H). C) shows how designs (A and B) were organised on the platform for printing using the MakerBot desktop program. D) Designs (A and B) once the printing process has completed. E) the printed container and decanted liquid is taken at an improved angle. ABS filament was used to print the design. AuNPs were used for this study.

The liquid was manipulated into the container (Figure 4.8.A) using the syringe extruder under the applied extrusion setting (Experimental, Table 2.4). The design B (Figure 4.8.B) was organised on the top of the design A (Figure 4.8.A) using MakerBot desktop software program (Refer to Figure 4.8.C) so that liquid can be decanted into the substrate when the container is fully printed.

The printing process and liquid manipulation were observed. Five replicate prints were performed. The liquid was decanted successfully inside of the container, but difficulties were encountered such as liquid dropping on the build platform during X, Y and Z movement. Liquid dropping on the platform was observed after 20 layers of the extrusion process. Also in the majority of the tests, a droplet of the liquid was not ejected and remained stuck to the syringe extruder needle (Figure 4.7.D). From this observation, it was determined that liquid manipulation by syringe extrusion for liquid handling applications could be limited to 20 layers of the printing process when filling a small size container.

4.3.3.3 Decanting liquid in the form of droplets in a straight line

Experiments were completed to determine whether the syringe extruder could be used to decanted liquid in the form of droplets in a straight line on the platform or on 3D printed substrate. Decanting multiple similar sized droplets on a 3D print enables multiple biological assays to be performed by one device which could save time and can be cost-effective.

To assess the performance of the syringe extruder to decant liquid in the form of a slight line on the platform. Initially, a 3D design model with dimensions of 1 mm (W) x 30 mm (L) x 1 mm (H) was designed (Figure 4.9.A). The model was set to be decanted by the syringe extruder using the dual extrusion setting (Experimental, Table 2.4) and was inspected visually. Five repeat printings were performed.

At each attempt, the syringe extruder decanted the corresponding 3D design model (Figure 4.9.A) on the platform in the form of unjoined droplets in a straight line (Figure 4.9.B). The size of all printed droplets was approximately equal when observed by the naked eyes.

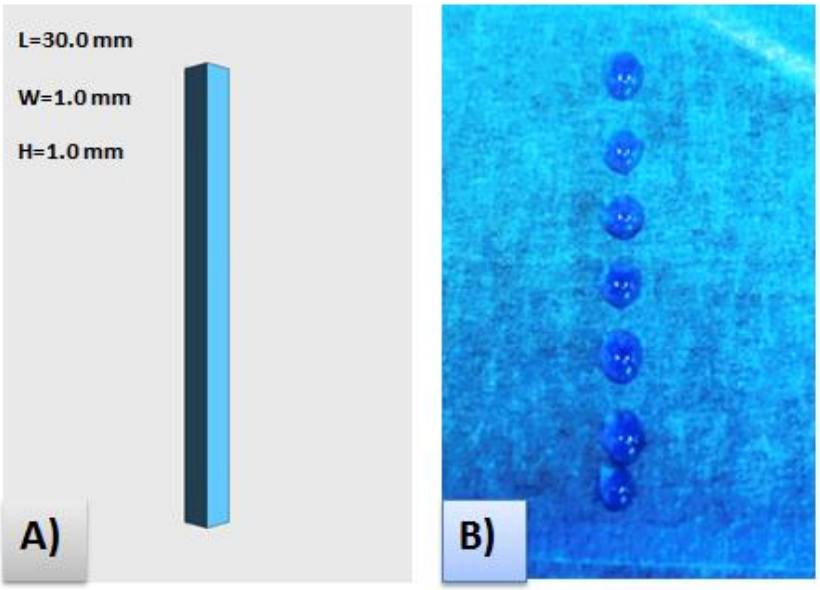

Figure 4.9|**Liquid decanting on the platform dropwise in the form of a straight line.** A) Shows the designed objects, with a dimension of (1 W, 30 L, 1 H) mm being decanted by syringe extruder. B) Picture of decanted liquids droplets in the form of a straight line on the platform by syringe extruder in correspond to the design (A).

From this experiment, it was determined that the syringe extruder could be used to decanted liquid in the form of a straight line on the platform.

Next, a new 3D printing model was designed as a substrate with dimensions of 15 mm (W) x 30 mm (L) x 1 mm (H) and the performance of syringe extruder to decant liquid on a 3D model were assessed (refer to Figure 4.10.A to see the image of prepared 3D design models). The 3D design model (Figure 4.9.A) was decanted on 3D printed ABS substrate under dual extrusion printing setting (Experimental, Table 2.4). The printing process and liquid manipulation were observed. Five replicate printing was performed. Figure 4.10.B shows the picture of the decanted droplet on a 3D print.

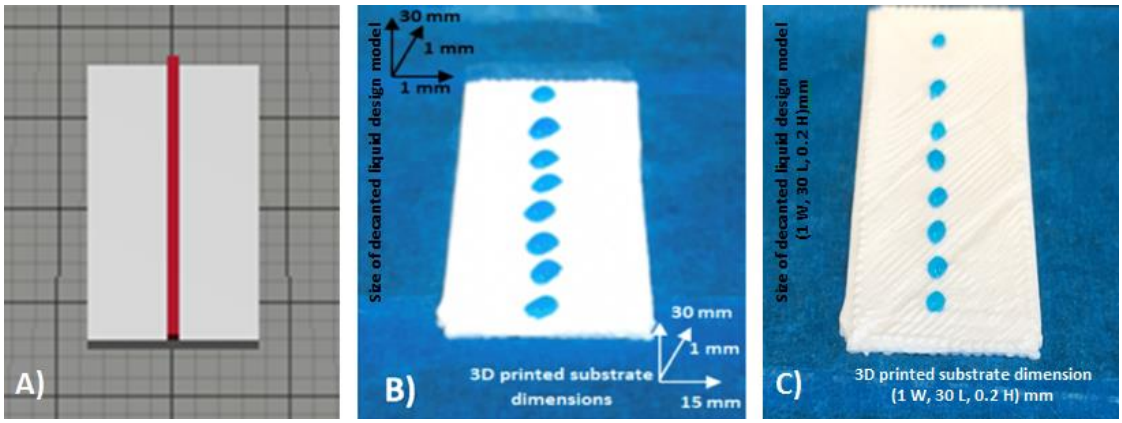

Figure 4.10| **Printing liquid droplets on the 3D printed substrate in the form of a straight line.** A) Represent the design models. The dimension of the designed substrate (Silver rectangle) is 15 x 30 x1 mm. Red is the design prepared for decanting by syringe extruder. B and C) Represent the image of decanted liquid on a 3D printed ABS substrate.

The liquid was decanted successfully on the 3D printed substrate in the form of unjoined droplets in a straight line. To the naked eye, the sizes of the printed droplets were approximately equal. Next, futher assessment was completed to determine if smaller droplets of liquid in the form of a straight line can be decanted on the 3D printed substrate by syringe extruder. To assess this height of the corresponding design with a dimension of 1 mm (W) x 30 mm (L) x 1 mm (H) for liquid decanting (the red design in Figure 4.10.A) was reduced from 1.0 to 0.2 mm. It was determined that smaller liquid droplets in the form of a straight line on 3D print could also be decanted by syringe extruder (Figure 4.10.C).

The overall outcome of these assessments showed that there was no limitation in decanting liquid in the form of small droplets in a straight line on a 3D printed substrate.

4.3.3.4 3D Printing of simple channels to assess the performance of syringe extruder in decanting the liquid in a 3D printed channel

Many microfluidic and milifluidic applications proceed in a narrow channel (Yazdi *et al.*, 2016). To assess the performance of syringe extruder in decanting the liquid into a 3D printed channel two simple designs were prepared. The first design (Figure 4.11.A) was a rectangular shape channel 10 mm (W) x 25 mm (L) x 2 mm (H) with internal dimensions of 0.8 mm (W) x 20 mm (L) x 1 mm (H). The size of the 3D test design (Figure 4.11.B) responsible for filling the channel was the same as the gap of the channel with the dimension of 0.8 mm (W) x 20 mm (L) x 1 mm (H).

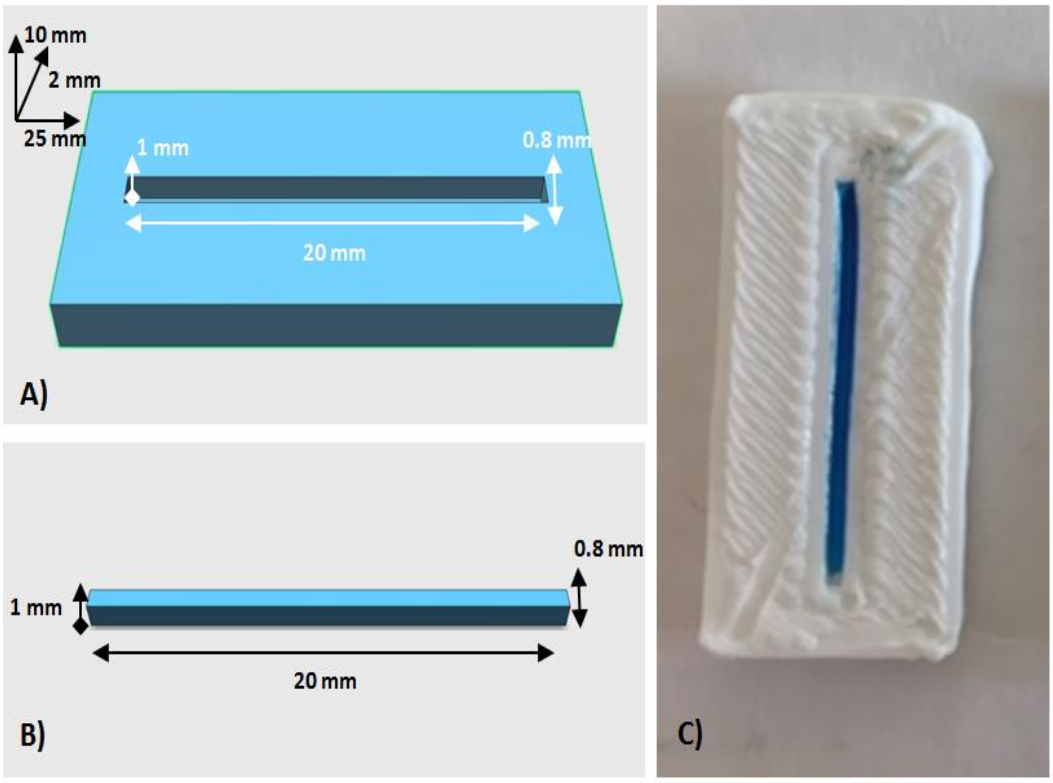

Figure 4.11| **Sketch of the 3D design models and the 3D printed channel after liquid manipulation;** A) represent the designed fluidic channel with dimensions of 10 x 25 x 2 mm with internal dimensions of (0.8 x 20 x 1 mm. B) represents the 3D test design dimensions 0.8 x 20 x 1 mm responsible for filling the channel. C) Picture of the printed fluidic channel after liquid manipulation. The channel was printed with ABS filament.

The designs were printed using the dual extrusion technique (Experimental, Table 2.4) and were inspected visually. Five replicates were manufactured. The liquid was decanted precisely in position and filled the channel (Figure 4.11.C) at each attempt made.

To further test the performance of syringe extruder for decanting liquid in a simple channels the design (Figure 4.12.A) was modified with the internal channel width narrowed to 0.6 mm. The width of the 3D test design (Figure 4.12.B) was also changed to 0.6 mm. Numerous attempts at 3D printing and to decanting the liquid into the 3D printed channel were made. Liquid manipulation into the new, narrow 3D printing channel width was unsuccessful. The syringe extruder did not decant liquid during any of the attempts. The smallest channel width that was reproducibility printed using the 3D printing device with a full volume of liquid deposition to fill the channel was 0.8 mm.

Next, a test of the syringe extruder performance for decanting liquid in more intricate channels was performed. The star fluidic channel (Figure 4.12.A) was made in shape of a square with dimensions of 25 mm (W) x 25 mm (L) x 2 mm (H). A circular space in the middle of the star channel with a radius of 2 mm was made to help with liquid flow (Figure 4.12. B) where channels have a dimension of 1 mm (W) x 20 mm (L) x 1 mm (H) were joined together in the form of a star for liquid decanting. The designs were organised using the MakerBot desktop program (Figure 4.12.C) in a correct geometry and were printed by the dual extrusion technique (Experimental, Table 2.4).

When printing the design (Figure 4.12.D), it was noticed that the volume of the liquid decanted from syringe extruder was slightly more than the desired volume to fill the star channel. This matter was tackled when the dimension proportional to liquid decanting was altered and made smaller in height by 0.2 mm. The issue was assumed to be due to

the properties of the thermoplastic ABS substrate, as this material shrunk when cooling leaving a smaller space for liquid filling.

Further testing for fabricating narrower channel was completed and likewise above it was determined that the smallest channel width that could be filled with liquid was 0.8 mm. Figure 4.12.E shows the successful printed channel. All of the five replicate printing that was performed to test the performance of syringe extruder for decanting liquid in more intricate channels under applied setting was successful.

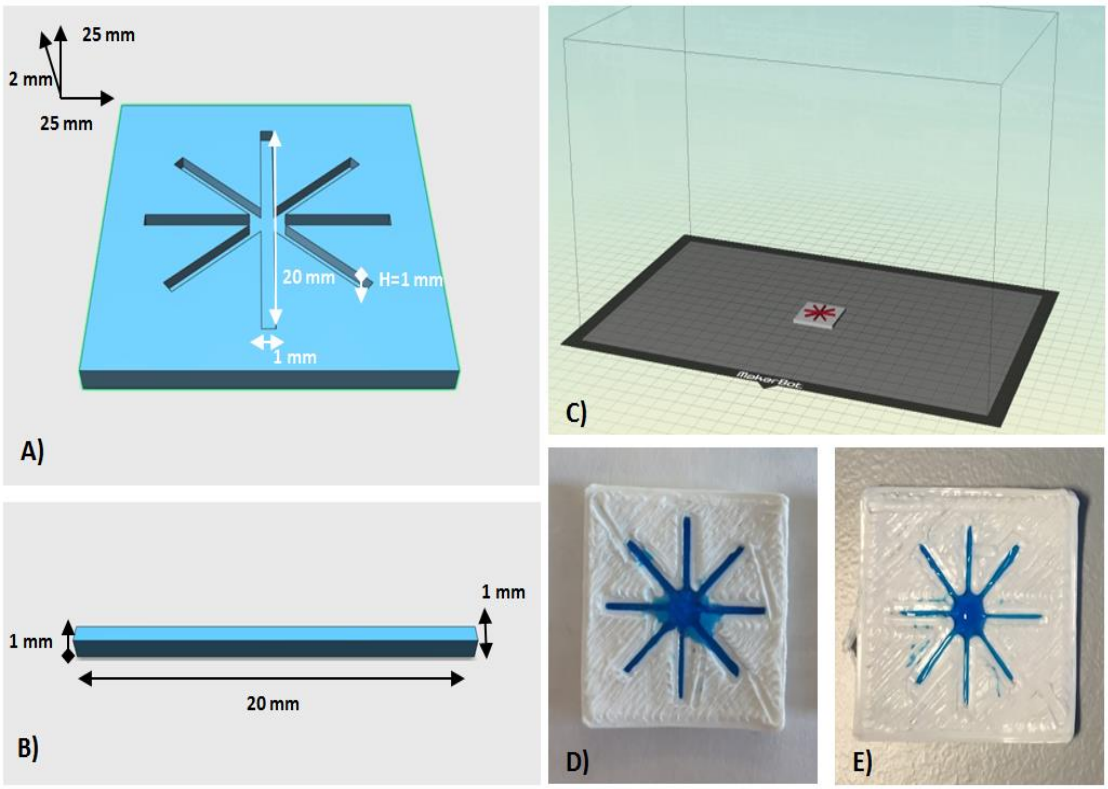

Figure 4.12| **Represents the 3D designs and the 3D printed objects, for the assessment of star channel fabrication.** A) represent the designed star channel with dimensions of 25 x 25 x 2 mm. The design was made with a hollow internal capacity made up of 4 simple straight channel joined together each with dimensions of 0.8 x 20 x 1 mm including a circular hollow space in the middle with a dimension of 2 mm (radius) x 1.0 mm(H). B) represents one out of the four design dimensions 1 x 20 x 1 mm responsible for decanted liquid. C) Demonstrates how designs (A and B) were prearranged on the platform for printing using MakerBot desktop program. D) Picture of the printed star channel with a width of 1.00 mm. E) Picture of the printed star fluidic channel with a width of 0.8 mm.

4.4 Discussion

In this work the MakerBot Replicator2X dual extruder 3D printer was enhanced to enable development of a cheap automated 3D printing system. The full cost of the desktop printer used in this project including full modification cost is approximately £3000 which is far cheaper than the current standard multi-use bio 3D printer by "ROKIT INVIVO" with polymer extruder and bio dispenser which costs around £25000.

Adaptation of 3D printers continues to grow, enabling more researchers to design download, print and use open source labware. The 3D printing approach used in this project has a few advantages over a current few reported modified 3D printing system where a 3D printed syringe pump is used to deposit biological molecules such as DNA in fluidic devices (Patrick *et al.*, 2015). Specifically, our modified syringe extruder does not require a specific customised firmware to be written to control liquid deposition on the surface of a 3D print (Patrick *et al.*, 2015). Moreover, the overall cost of fabrication of the syringe extruder is much less than previously published source syringe pumps (Wijnen *et al.*, 2014).

The modified device allowed printing multi-materials thermoplastic polymers and decanting liquid in parallel for liquid handling application. However, the system may only be useful for simple automated liquid handling applications. Users may need to modify the system slightly and to add a written code for the printing process in order to have better control over using the dual extruders for fabrication of complex microfluidic system.

Other than the necessary 3D printing infrastructure, other barriers remain for the co-development of 3D printed open labware (Patrick *et al.*, 2015). Use of CAD software remains a substantial barrier for many potential designers. Watertight designs are challenging to design for many scientists because they require complex 3D forms. To

overcome the 3D printing barrier to decant liquid microfluidic specific 3D CAD tool could be created to make the fluidic design more accessible.

The fabrication and assembly of a modified syringe extruder on the MakerBot Replicator 2X 3D printer customised for this project were challenging and required additional skills to build. Crafting hardware kits that can be purchased, assembled and modified may promote the dissemination of these form of tools. One successful implementation of this scheme is an OpenPCR platform (Openpcr.org, 2015).

The work described in this chapter focused on optimising the experimental setup to modify the MakerBot Replicator 2X 3D printer and proposes a workflow to automate the bioprinting process for microfluidic application. The approach used here on liquid deposition in 3D printing channel cannot be compared to the literature since there are currently no reports of studies on liquid deposition using FDM printer in fabricating microfluidic and millifluidic reactionware. It is anticipated that further development of this technology will likely lead to widespread applications in areas such as tissue engineering, pharmaceutical testing, and organs-on-chips. Development of biological ink for FDM 3D printing, enhancement of 3D printing technique for multi-material extrusion with, at the same time, precise control of spatial distribution and layer-by-layer assembly of multi-materials such as cells and biomaterials can expand the applications of this printing technique toward microfluidic organ-on-a-chip device development. Currently, Dolomite sells the FDM 3D printer using a cyclic olefin copolymer, named the Fluidic Factory 3D Printer, and have demonstrated the use of FDM technology toward the 3D printing of artificial tissues or chip devices (Jang, Yi and Cho, 2016).

To 3D print a chip device in this study it was determined that the smallest fabricated internal channels width that could be reproducibly 3D printed was 0.8 mm which is

similar to the width of the reported FDM printed fluidic channels fabricated with ABS and PLA material from previous studies (Kitson *et al.*, 2012) (Bishop *et al.*, 2015).

The 3D printing channel made and tested in this work for liquid deposition is relatively comparable to current fabricated fluidic channels made by the FDM 3D printer (Pranzo *et al.*, 2018). The current FDM 3D printed fluidic channels chip complexity is low (Zhou, 2017) and the channels are normally made of a simple shape (Okafor *et al.*, 2017). The channel is made of either a straight line, a diagonal pattern, a ladder or Y shape (Macdonald *et al.*, 2017). The smallest reported fabricated channels range from 100 µm to 400 µm but exhibit low accuracy, a slow build time and lack transparency (Zhou, 2017). The smallest width of the printed hydrophobic barrier is 400 µm which can be expanded to 1000 µm for improved accuracy (Salentijn *et al.*, 2017). For the majority of fabricated fluidic devices, fluids are usually transferred into the device by pipettors which are prone to operator error (Zhou, 2017). The improvement in integrated parallel 3D printing and liquid manipulation technique demonstrated here can replace tedious manual pipetting, which could be cost-effective, save time and resources significantly to allow automation in rapid fabrication of fluidic handeling devices.

4.5 Conclusion

The goal of this chapter was to develop a 3D printing system for decanting liquid onto or into 3D prints. In this work, it was demonstrated that a MakerBot Replicator2X dual extruder 3D printer could be enhanced to enable development of cheap automated 3D printing system which is capable of printing multi-materials thermoplastic polymers and decanting liquid in parallel.

The syringe extruder on the modified 3D printer can decant liquid at room temperature with the absence of physical contact between the print head, and printed support making it likely that biological materials might be detectable.

Herein the performance of the syringe extruder on the 3D device was assessed and showed that the liquid could be printed at a specific point and in a volume as small as 10 µL. The volume of liquid deposited on 3D print using a syringe extruder is comparable to the minimum volume of active biological molecules used in the microfluidic platform (Mark *et al.*, 2010) and assay kits (Thermo Scientific Pierce protein assay technical handbook, 2009).

The syringe extruder was evaluated in the presence of AuNPs. The result of the study showed that AuNP solutions could be printed. In this study is to use AuNPs as to bind biological molecules to the surface of the thermoplastic material which will be explored more in the next chapter.

A simple study was accomplished to identify limitations in liquid manipulation by syringe extrusion to fill a container or simple channels. No significant problem was identified in using syringe extruder for liquid handling application.

CHAPTER 5

DESIGN AND CHARACTERIZATION OF PROTEIN BIO-INKS FOR FDM 3D PRINTING

5.1 Introduction

The current bottleneck in allowing low cost, fast and rapid production of biosensor devices using FDM 3D printing is the availability of versatile bio-inks (Munaz *et al.*, 2016).

Bio-ink developments for FDM 3D printing can be relatively challenging. The developing ink for printing must fulfill the physical, mechanical and biological characteristics, requirements of the printing applications. Considering these factors, the focus of this chapter is to develop and test bio-ink immobilisation on a selected surface of FDM 3D printed objects, keeping in mind applications for millifluidic and microfluidic biosensor production.

Key objectives in this chapter are;

5a) To develop bio-inks that retain biological activity after decanting to a 3D print. These bio-inks should be prepared as a low viscosity solution suitable to be deposited by the syringe extruder of the modified 3D printer to a surface of the 3D printed object.

5b) Bio-inks should be in a form where they are immobilised on the surface of the 3D printed object.

5c) Assay conditions optimised for the formulated bio-inks should be developed so that their biological activity in the printed state can be assessed and calibrated for use in biosensing applications.

To achieve 5a-5c objectives a key challenge in this chapter is to find a method for attaching bio-inks to the surface of a 3D printed object in such a way that they retain their biological activity.

5.2 GOD assay overview

The GOD assay is one of the most popular enzymatic assays in biological research and has been applied widely to the construction of glucose biosensor devices (Bankar *et al.*, 2009). There are several methods published in the literature to assay for glucose oxidase activity (Bergmeyer, 1974). The assay method used in this thesis is widely used to assay for glucose oxidase activity due to its low cost and quick reaction time (Bankar *et al.*, 2009). Moreover, the report shows GOD and HRP maintained activity after decanting as liquid form bioinks by inkjet printing (Settia *et al.*, 2005)(Setti *et al.*, 2007).

The analytical method for detecting GOD activity is based on the principle that GOD oxidises β-D-glucose in the presence of oxygen to β-D-glucono-δ-lactone and H_2O_2 (Bankar *et al.*, 2009). Then H_2O_2 oxidises a chromogenic substrate in the presence of HRP with a resultant colour change that is monitored by a UV-Vis spectrophotometer. The chromogenic substrate used for the GOD reaction here is *o*-dianisidine (Bergmeyer, 1974). The activity of glucose oxidase is determined based on the oxidation of *o*-dianisidine that forms a quinoneimine dye that is measured spectrophotometrically at 500 nm (Petruccioli *et al.*, 1999). Figure 5.1 shows the schematic cascade reaction of glucose quantification based on the practical assessment used in this thesis.

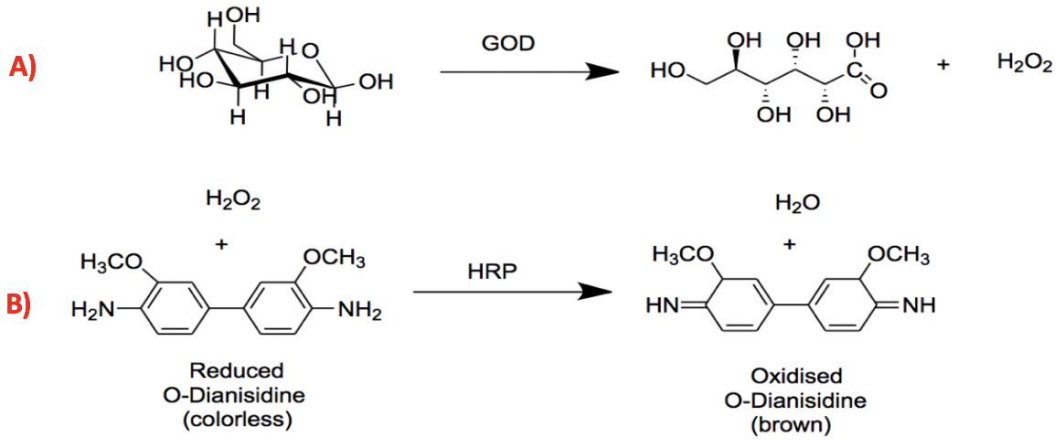

Figure 5.1| **Enzymatic cascade reaction for the quantification of glucose by the GOD assay;** Represents the use of o-dianisidine as a substrate for quantifying the concentration of the coloured product formed. A) The oxidation of β-D-glucose to β-D-glucono-δ-lactone (gluconic acid) and H_2O_2 by GOD enzyme. B) H_2O_2 reacts with o-dianisidine in the presence of HRP to form a coloured product, oxidised o-dianisidine.

The stability of GOD in biosensors depends on many characteristics, although the pH and temperature are the most important (Wilson and Turner, 1992). In this thesis, GOD from *Aspergillus niger* was selected as it possesses good stability when immobilised on both solid and porous glass (Divya, Savitri and Mitra, 1998). It has also been reported that a glucose sensor constructed by GOD and HRP has superior performance (Yang *et al.*, 2017). Immobilization of these proteins on the solid surface allows sensitive and accurate detection of the high concentration of glucose within biological sensors (Yang *et al.*, 2017).

Initially, an optimisation test for the GOD assay was conducted to investigate the use of 3D printed plastic for microfluidic and millifluidic biosensor devices.

5.2.1 GOD assay optimisation

Optimisation tests for the GOD assay were performed in a plastic cuvette in triplicate using the chemical and enzyme concentrations and equipment described in Section 2.12.1-2.

In this chapter, the focus is to assess the enzyme activity at room temperature, to allow easy fabrication of biosensor devices. GOD and HRP enzymes were kept room temperature, and the enzymatic activity was subsequently assessed by repeating the GOD assay every hour for up to 4 hours. From this study, we can determine if the enzyme activity is stable in order to allow an accurate measurement of glucose in solution at room temperature. For each repeated assay, the individual sample absorbance was remeasured after 60 minutes from the initial measurement to ensure the equilibrium reaction point was reached.

The change in absorbance for this study is plotted on a graph shown in Figure 5.2.

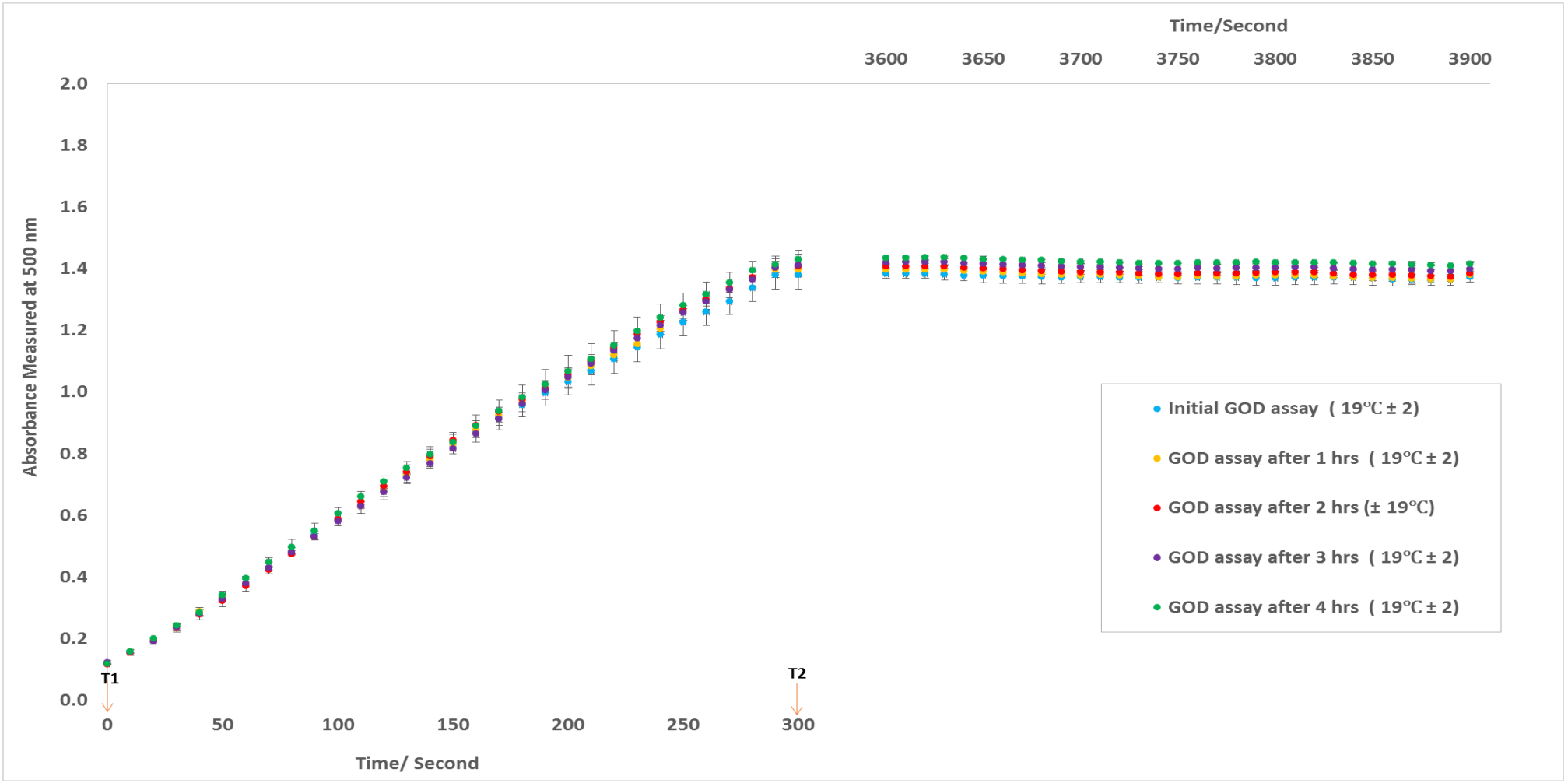

Figure 5.2| The **GOD assay: change in absorbance time course plots.** The enzyme activity was assessed at room temperature for up to 4 hrs. The graph represents the absorbance of GOD assay samples measured at 500 nm immediately at the start of the reaction and the absorbance measured at t = 3600 second. Error bars on all points represent standard deviations for n = 3.

Figure 5.2 shows the concentration of enzymes used in the reaction ensure a fast reaction time (≤ 5 min). The activity of the enzymes stored at room temperature measured over time was reasonably constant when assayed at room temperature (19 ℃ ± 2) during the analysis time (t = 0-300 second) (Figure 5.1). These data suggest no significant change in enzymatic activity occurred over 4 hrs at room temperature (Figure 5.2). This is supported by a report which shows that GOD is not affected by a small changes in temperature (Bankar *et al.*, 2009). The lowest operating temperature for the GOD assay is reported to be 20–30 °C and the highest of 40–60 °C from *Aspergillus niger* (Bankar *et al.*, 2009).

The enzymatic activity of GOD as the concentration of the substrate transformed into the product by the enzyme, c, is calculated by measuring the absorption at the wavelength λ, A_λ, by UV-Vis spectroscopy. The Beer-Lambert law ($A_\lambda = \varepsilon_\lambda \cdot l \cdot c$) is used to determine unit/ml of enzyme.

$$\text{Unit/mL enzyme} = \frac{A\lambda=[A500\ (t2)-A500\ (t1)]}{\varepsilon\lambda \times l}$$

where ε_λ is the molar absorption coefficient of the chromogenic substance at wavelength λ (ε_λ of *o*-dianisidine at 500 nm = 7.5 millimolar), and l is the pathway length.

The GOD activity for the 5 min of assessment at a measured absorbance of 500 nm, for each assay starting from the initial GOD assay, were 0.178, 0.170, 0.172, 0.172 and 0.174 Units/mL (U/mL) enzyme (Figure 5.2), which are comparable to each other.

All samples at A_{500} at t > 3600 seconds showed an absorbance of approximately 1.4 $\pm$ 0.05 AU. The enzymatic activity calculated based on this absorbance is 0.185 $\pm$ 0.005 U/mL. This value is comparable to the values obtained at the initial 5 min of assessment, which suggests that the equilibrium is reached in approximately 5 min. This means that the conditions used are sufficient to allow fast reaction times and accurately quantify glucose in solution.

5.3 Compatibility of 3D printed filaments with the bioassay

Next, the activity of the enzymes (GOD and HRP) in the presence of different 3D printing material was studied. This study allowed us to determine if any of the filaments are unsuitable for biosensor fabrication, since they may inhibit the reaction.

Filaments were evaluated by submerging thermoplastic cuboids (Chapter 3, Figure 3.1) printed with a range of different filaments individually into the assay solution as described in Section 2.12.2. Figure 5.3 shows the absorbance time course plots of the GOD assay in the presence of the 3D printed material.

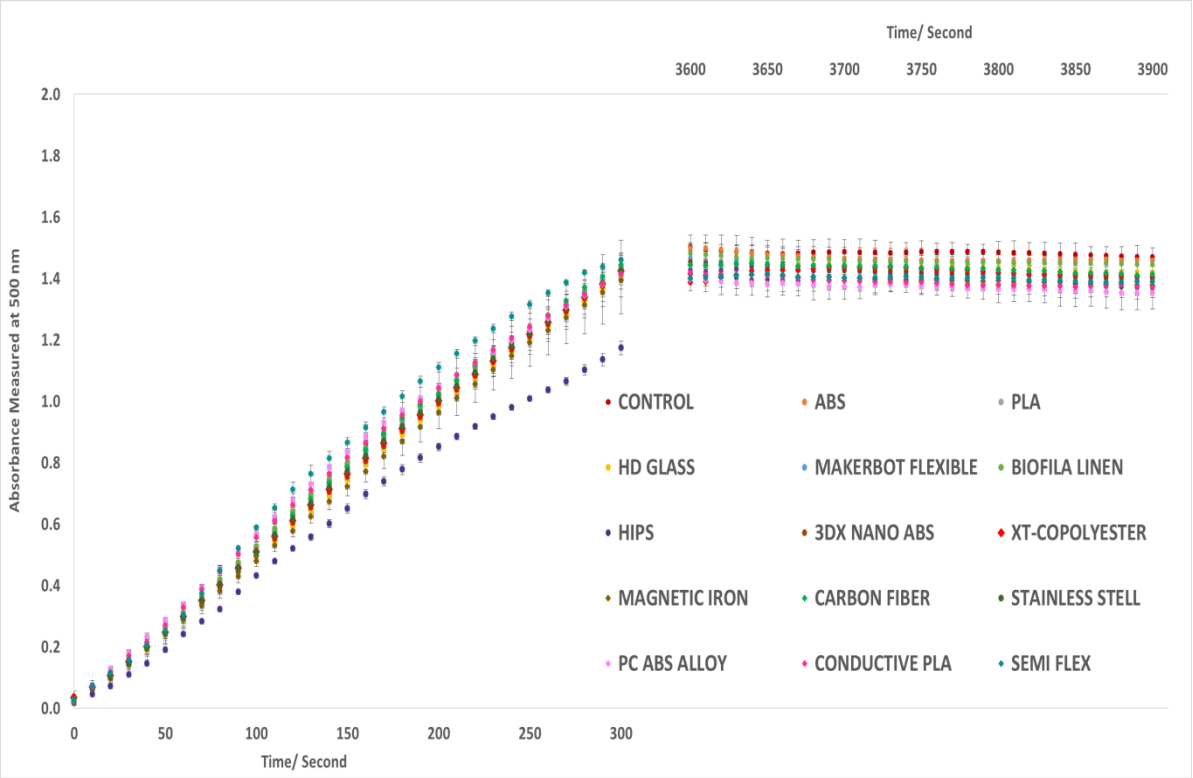

Figure 5.3| **Absorbance time course plots, analysis of the GOD assay in the presence of the 3D printed material.** The graph represents the absorbance of GOD assay samples measured at 500 nm, immediately at the start of the reaction and t = 3600 second. Error bars on all points represent standard deviations for n = 4.

Figure 5.3 shows that the absorbance in the presence of 3D printing filaments for the first 5 minutes of reaction varies slightly when compared to the control (GOD assay without 3D printed material). The GOD activity for the first 5 min of assessment at a measured absorbance of 500 nm, in the presence of 3D printing material, is shown in Figure 5.4.

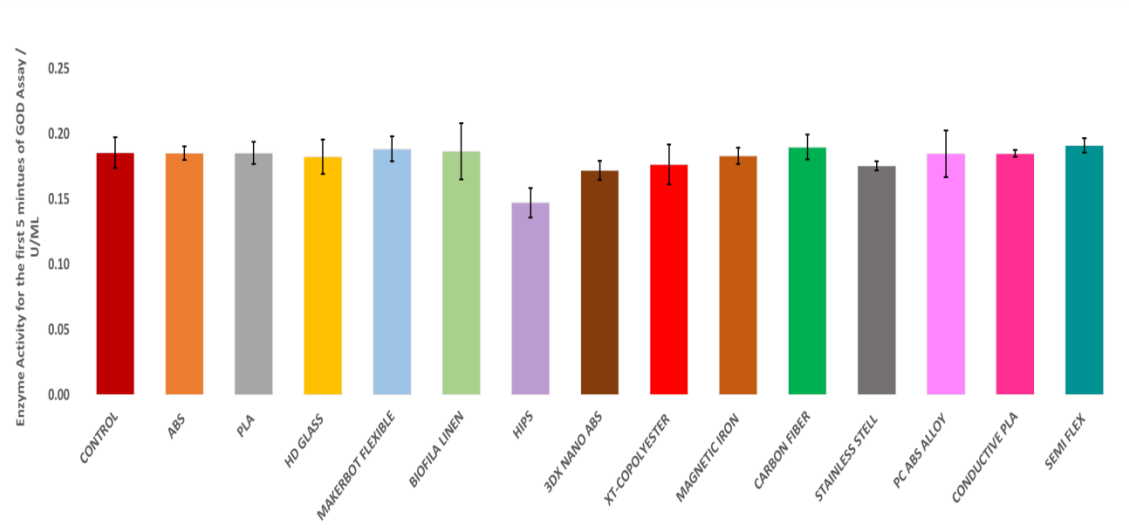

Figure 5.4| **GOD enzymatic activity in the presence of 3D printed materials.** The graph represents the enzymatic activity calculated based on a value obtained at A_{500}, using absorbance of t = 0 and t= 300 second. Error bars on all points represent standard deviations for n = 4.

HIPS and Stainless steel filaments exhibited a slightly lower absorbance value for the 5 min of assessment when compared to control, which suggests the enzyme activity, is slightly inhibited in the presence of these materials. However, at t = 3600 second (Figure 5.3), all filaments show an absorbance of approximately 1.4 AU, suggesting the same reaction equilibrium has been reached. The enzymatic activity was calculated at a standard time t = 3600 second for each filament and presented in Figure 5.4.

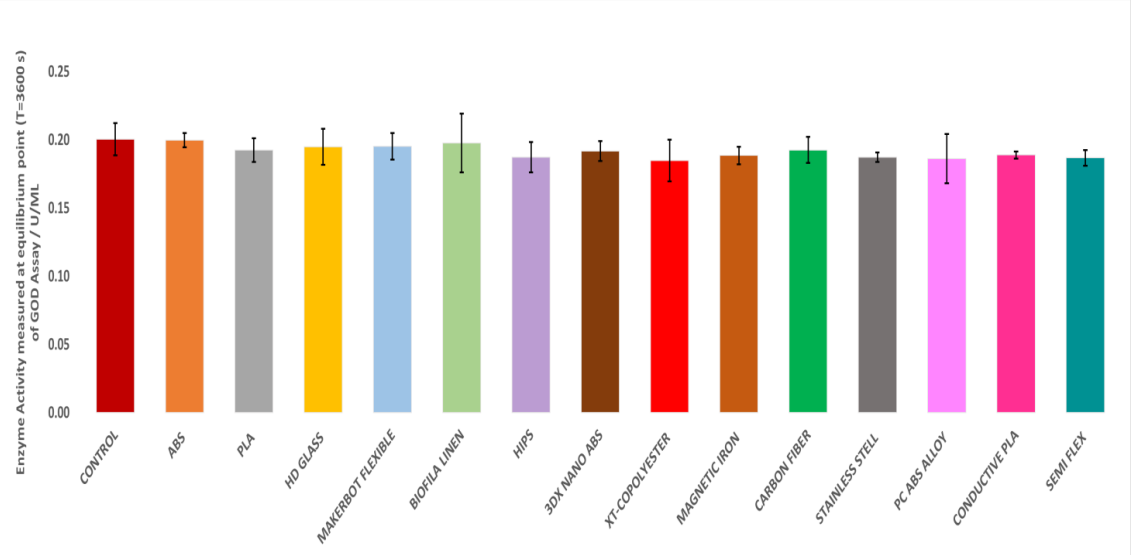

Figure 5.5| **GOD enzymatic activity in the presence of 3D printed materials.** The graph represents the enzymatic activity calculated based on a value obtained at A500 for t = 3600 seconds. Error bars on all points represent standard deviations for n = 4.

From Figure 5.5, it was determined that the enzymatic activity in the presence of the majority of the assessed filaments is comparable to that of the control. The data revealed that the calculated enzyme activity in the presence of HIPS, XT-Copolyester, and stainless steel is slightly lower when compared to the control sample at t = 3600 second (Figure 5.3). However, since the error bars overlap, this difference in enzymatic activity is not significant. The overall conclusion drawn from this study is that the enzyme activity might be lower in the biodevices made from HIPS and stainless steel filaments, although the same reaction equilibrium is reached, within 3600 seconds.

5.4 Assessment of AuNPs as carrier systems for biological molecules in bio-inks

AuNPs have been used widely in microfluidic applications for chemical and biological sensing (Sironi, 2010)(Saha *et al.*, 2012). Immobilisation of the AuNPs in a 3D printing device containing variable functional group provides a practical platform for absorption based colourimetric sensing of any target analyte (Xiaofei, Ruiyi and Zaijun, 2014). A carrier for a biological system is an important aspect for making microfluidic biosensor devices. If enzymes are not covalently attached to the polymer surface, there is a possibility of the enzyme detaching due to the lack of a stable bond. Furthermore random orientations of the enzymes on the surface, and the possible enzyme denaturation due to strong interactions with the surface, e.g. structural unfolding, of the enzyme may occur (Rusmini, Zhong and Feijen, 2007). Consequently, in this section, the focus is on adding AuNPs to the surface of 3D prints to determine the suitability of AuNPs, as carrier systems for biological molecules, to be immobilised on the surface of the 3D printed object. Ideally, AuNPs should have the following properties for optimal usability as a bioink.

I. they should bind to the surface of the 3D print and not be absorbed into the interior. If absorbed, it is highly unlikely the biological activity of any bound molecules will be optimal.
II. assuming they do bind to the surface of the 3D printed objects, the AuNPs should do so firmly and not wash off in the presence of aqueous, buffer and biological solutions.

In this section, initially, the penetration of AuNPs into 3D prints will be investigated. This will be followed by assessment of the tightness of binding of AuNPs to 3-D printed substrates and the AuNPs migration in the presence of a buffer solution.

5.4.1 Characteristics of AuNPs nonspecific binding to 3D print surfaces

The experiment is designed to detect non-specific binding of AuNPs to the surface of the 3D print object. If AuNPs were bound to the 3D printed surface their penetration into the 3D printed surface can be assessed by looking at them under SEM microscope.

The experiment involved adding 50 µL of the 20 nm AuNPs to a surface of a 3D printed PLA object and allowing it to dry for examination (Figure 5.6). PLA 3D printed material was used in this experiment since this filament has been used previously to fabricate PLA/AuNP films for nondestructive evaluation and detection of defects in 3D printed materials using the AuNPs' optical properties (Brubaker et al., 2018).

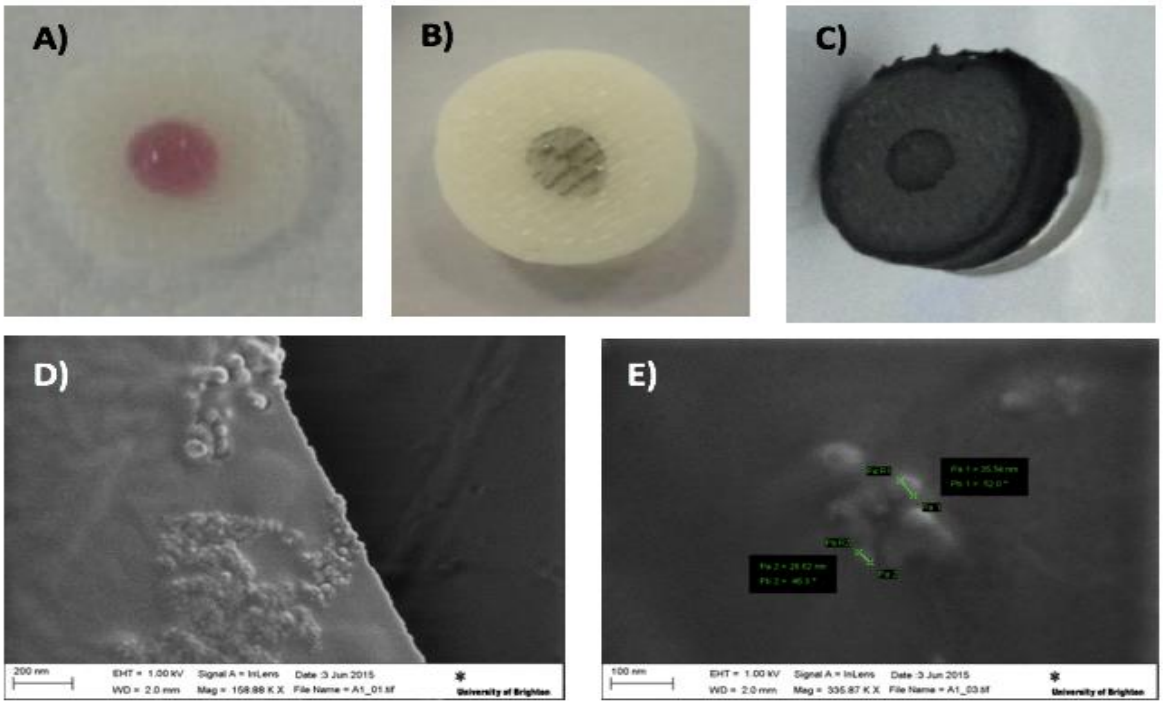

Figure 5.6| **Determining the penetration of AuNPs into 3D printed material experimental images.** A) Image of 50 µL AuNPs (20 nm) on a 3D print. B) 50 µL AuNPs (20 nm) dried on a 3D printed. C) Dried 50 µL AuNPs (20 nm) on a 3D print coated with 2 nm of platinum for SEM analysis. D) Aggregated AuNPs SEM images on a 3D print. E) Glowing circular shape AuNPs particles on the 3D print.

Figure 5.6.B shows that AuNPs bind to the surface of the 3D printed object. The SEM image (Figure 5.6.D-E) also shows the presence of AuNPs on the surface of the 3D printed object suggesting nonspecific binding of AuNPs to the 3D print. However, a

variation of AuNP sizes (Figure 5.6.E) on the 3D print surface from 25 nm to 40 nm (Figure 5.6.E) is observed, which suggests aggregation of AuNPs on the polymer surface has occurred, which may be due to drying.

The second objective of this study was to determine if AuNPs penetrate into the 3D printed object. An attempt was made using SEM, but the 3D printed (ABS) material cracked under high vacuum. Therefore to see if AuNPs penetrated into the 3D printed material, the print was cut across the dried AuNPs (Figure 5.7). For this experiment, AuNPs with two different colloidal sizes were used.

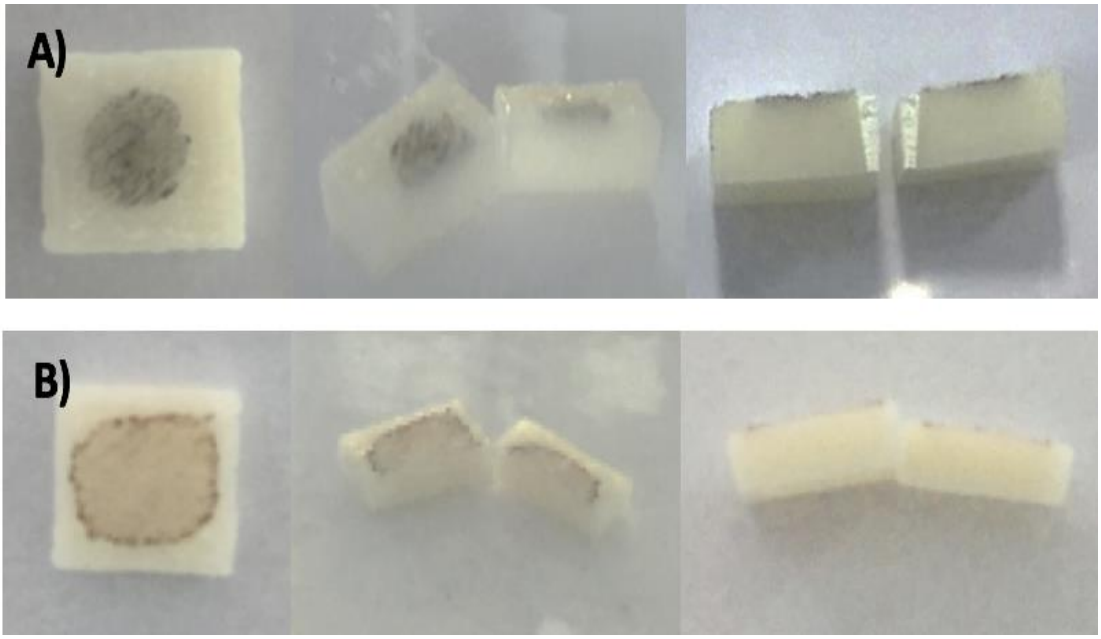

Figure 5.7| **Determining the penetration of AuNPs into ABS 3D printed material.** A) Images of dried 50 µL AuNPs (20 nm) on a 3D print. B) Image of dried 50 µL AuNPs (50 nm) on a 3D print. Only one of the six tested 3D print for a study of the AuNPs penetration into 3D printed ABS of the two tested AuNPs sizes are present here.

Figure 5.7 shows the presence of AuNPs on the surface of the 3D printed polymer. The cut 3D print shows low penetration of AuNPs into a 3D printed slide layers, which means that AuNPs are mainly on the surface of the 3D print. This property makes them suitable for use as a carrier for biomolecules to make bio-inks.

5.4.2 Assessing the reversibility of AuNPs binding to 3D printed substrates

For millifluidic and microfluidic applications, AuNPs should ideally bind tightly to the 3D printed surface, to minimise migration problems and maximise the lifetime of any fluid applications.

This experiment is designed to detect the tightness of binding of AuNPs to a 3D printed substrate. AuNPs were added to a surface of a 3D printed (ABS) object and allowed to dry (Figure 5.8). The dried AuNPs on the 3D print were washed with approximately 50 µL water three times and observed visually for any changes.

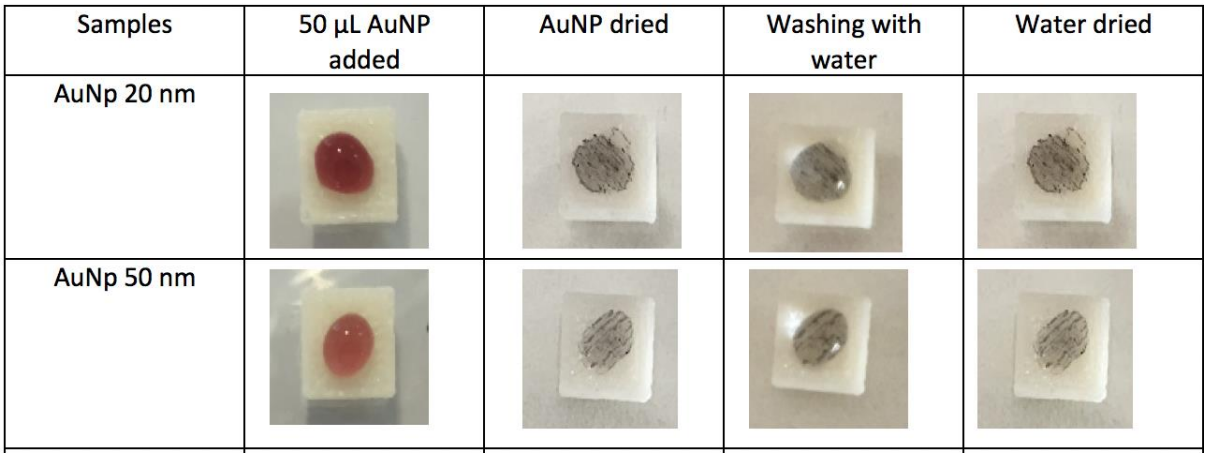

Figure 5.8| **Experimental images assessing the reversibility of AuNPs binding to 3D printed substrates.** The image shows the experimental study steps taken for 20 nm and 50 nm AuNP sizes.

After washing, no visible changes were observed; the AuNPs remained stable tightly bound to the surface of the 3D print, suggesting that AuNPs could be used as a carrier system for biomolecules molecules on 3D printed materials.

5.5 Assessing GOD – AuNP bio-ink: assay optimisation and enzymatic activity testing

GOD–AuNP bio-inks were prepared by conjugating GOD to AuNPs as described in Section 2.12.3. The technique allows the quick production of bio-ink with an extended shelf time (Li *et al.*, 2007). Two sizes of AuNPs (20 nm and 50 nm) were used for bio-ink fabrication, with and without nitrogen treatment for comparison, to determine the best-selected size and technique for bio-inks with the highest enzymatic activity.

The GOD–AuNP bio-ink enzymatic assessment was performed in a plastic cuvette as described in Section 2.12.3. This assessment allows us to determine whether the enzyme remains active when bound to AuNPs.

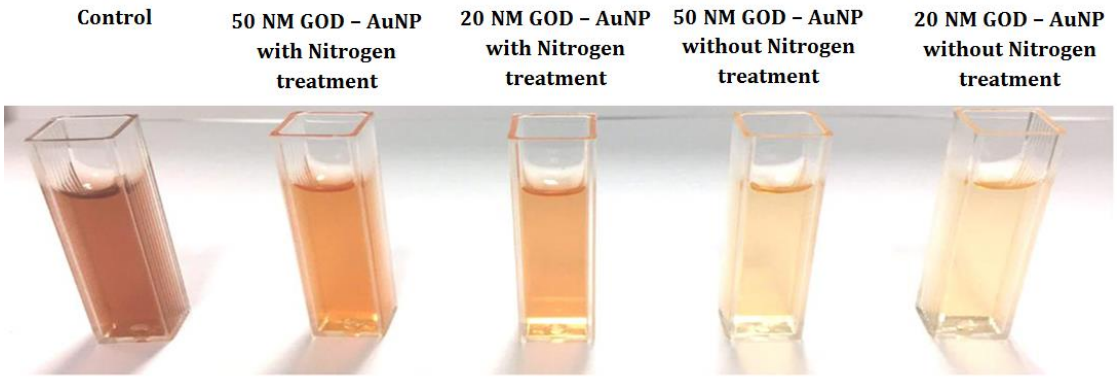

Figure 5.9| **Picture of colour change respond for analysis of AuNPs/GOD Bio-inks enzymatic activity;** Picture was taken for each test assay after 5 minutes from the time GOD assay reaction was initiated.

In this experiment, the enzymatic activity of the bio-ink was compared to a control sample (the GOD assay with no AuNPs) s shown in Figure 5.10.

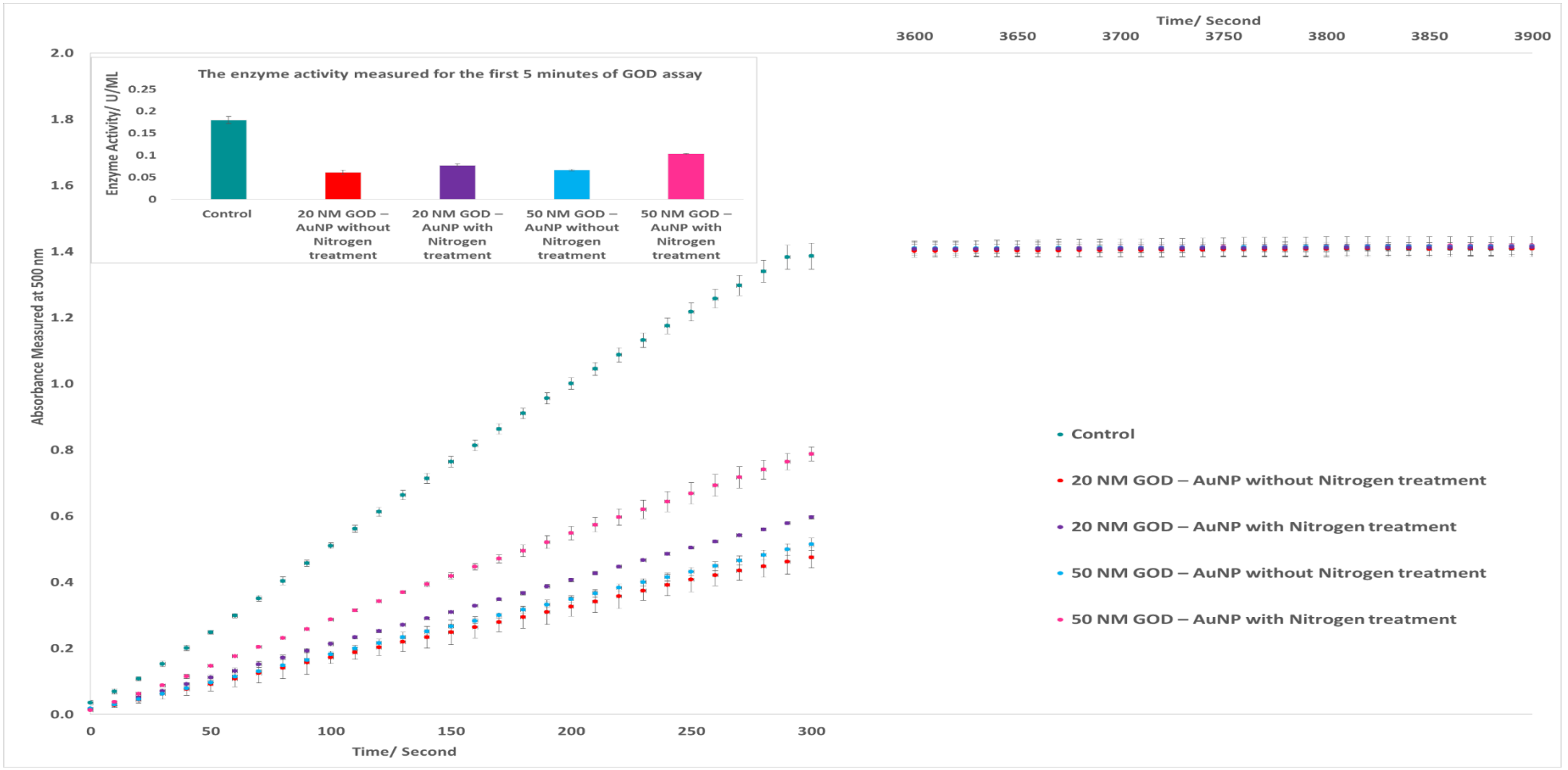

Figure 5.10| **Absorbance time course plots, analysis of GOD–AuNP bio-ink enzymatic activity**; The graph represents the absorbance of GOD assay samples at 500 nm measured immediately at the start of the reaction and the absorbance of assay solution re-measured at t = 3600 second. The bar chart on the left-hand side of the graph represents enzyme activity for each assay; measured from absorbance between t = 0 to t = 300 second. Error bars on all points represent standard deviations for n = 3.

From the data shown in Figure 5.10 an increase in absorbance of GOD–AuNP bio-inks for the GOD assay is observable. This means that the GOD enzyme present in the bio-ink mixture remained active after binding to AuNPs during the conjugation process. Figure 5.10 shows a lower absorbance value for the GOD–AuNP bio-ink enzymatic assay in the frst 5 min of the reaction in comparison to control sample. This is because a smaller amount of enzyme is likely to be available than in the normal enzymatic assay. The low amount of enzyme is present in the bio-ink mixture since in the GOD–AuNP conjugation process some of the GOD may have been lost either in conjugation steps or washing steps. A report suggests in majority of enzymatic studies 100% binding to a surface may not be obtainable due in the binding surface area (Li *et al.*, 2007).

Figure 5.10 also shows the absorbance of GOD–AuNP bio-inks, in an enzymatic assay at $t < 3600$ seconds, is approximately equal to control value for all samples. This means that the amount of the enzyme binded to AuNPs presented in solution is suitable to determine the quantity of 5 mM glucose solution presented in the mixture within one hour.

The 50 nm nitrogen treated GOD–AuNP exhibited a higher absorbance value when compared to other bioconjugated samples. Higher enzyme activity was also detected for the first 5 minutes of the enzymatic reactions (Figure 5.10) using this bio-ink with a value of 0.103 U/mL meaning more GOD is probably bound to 50 nm AuNPs during the conjugation process. Since a faster reaction was achieved using this bio-ink, the 50 nm nitrogen treated GOD–AuNP bio-ink was selected as a suitable choice for the rest of the study.

At the equilibrium point, the calculated enzyme activity for all of the bio-ink samples was comparable to control samples with a value of 0.187 ± 0.004 U/mL.

5.5.1 The GOD–AuNP bio-ink stability test

A GOD enzymatic assay of the 50 nm GOD–AuNP bio-ink (Section 5.5) was performed after six weeks storage to determine the stability and shelf life of the conjugated enzymes. Ideally, we would like to use a bio-ink for which a faster reaction can be achieved with enhanced stability therefore the 50 nm GOD–AuNP bio-ink with nitrogen treatment was the ideal choice since higher enzymatic activity in 5 min of reaction time was detected for this bio-inks with a value of 0.103 U/mL. In this study on the 50 nm GOD–AuNP bio-ink without nitrogen treatment stability was also assessed. The prepared bio-inks' enzymatic activities were compared by plotting them on one graph (Figure 5.11).

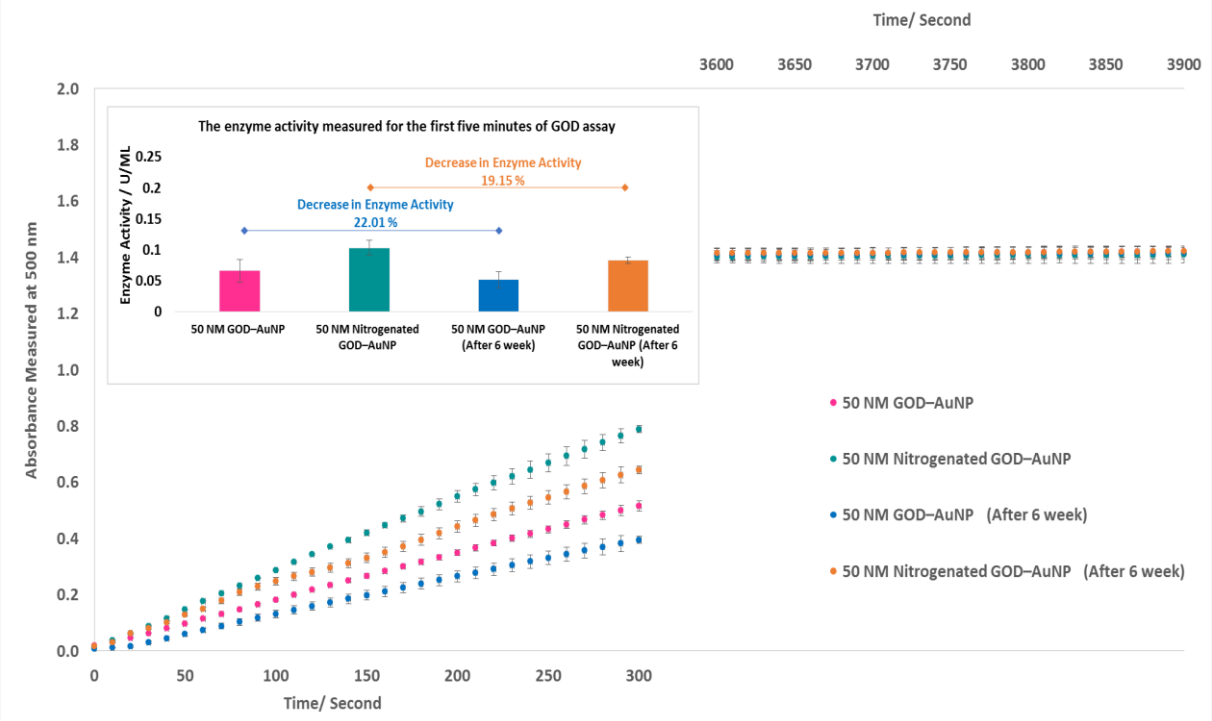

Figure 5.11| **Absorbance time course plots, analysis of 50 nm GOD–AuNP bio-ink enzymatic activity.** Assessing bio-ink stability after 6 weeks: the graph represents the absorbance of GOD assay samples measured at 500 nm immediately at the start of the reaction and the absorbance of assay solution re-measured at t = 3600 second. The bar chart on the left-hand side of the graph represents enzyme activity for each assay; measured from the absorbance of t = 0 to t = 300 second. Error bars on all points represent standard deviations for n = 3.

Figure 5.11 shows a drop in bio-ink absorbance values for the first five minutes of the GOD assay when assessed after six weeks. The calculated drop in enzymatic activity of bio-inks after six weeks, for 50 NM nitrogenated GOD–AuNP was 19.15%, and for 50 NM GOD–AuNP, 22.01% (Figure 10). Figure 5.11 shows the absorbance at equilibrium for all bio-ink assay solutions measured at $t < 3600$ second is approximately 1.4 AU and are equal to each other. The calculated enzymatic activity for all of the bio-ink samples is comparable to control samples with a value of 0.187 ± 0.005 U/mL. This suggests that drop in activity of bio-inks after absorbance of bio-inks assessed after six weeks may be due to errors in the preparation of enzymatic assay, e.g. dilution and pipetting.

Overall from this experiment, it was determined that 50 nm GOD–AuNP bio-inks are active and maintain stability after six weeks and may have a suitable shelf life to be used for glucose biosensing. To determine the actual shelf life of these bio-inks more assessment will be required, and their activities need to be assessed after more extended storage. The reported shelf life of AuNPs is one year and six months for the GOD enzyme when stored at 4˚C (House, Anderson and Ward, 2007). Consequently, the maximum storage shelf life of the bio-ink may be up to six months.

5.5.2 Determining glucose quantities in solution using GOD–AuNP bio-ink

To determine if it is possible to quantify the glucose content accurately in a mixture using the GOD–AuNP bio-ink, the GOD enzymatic assay was performed on the glucose solution between 0 and 10 mmol/L. The as-prepared 50 nm GOD–AuNP bio-ink was used. Figure 5.12 shows the absorbance time course and enzymatic activity for each assay. Likewise, section 5.4.2 the enzymatic activity of the assay solution was calculated for the assessed time course.

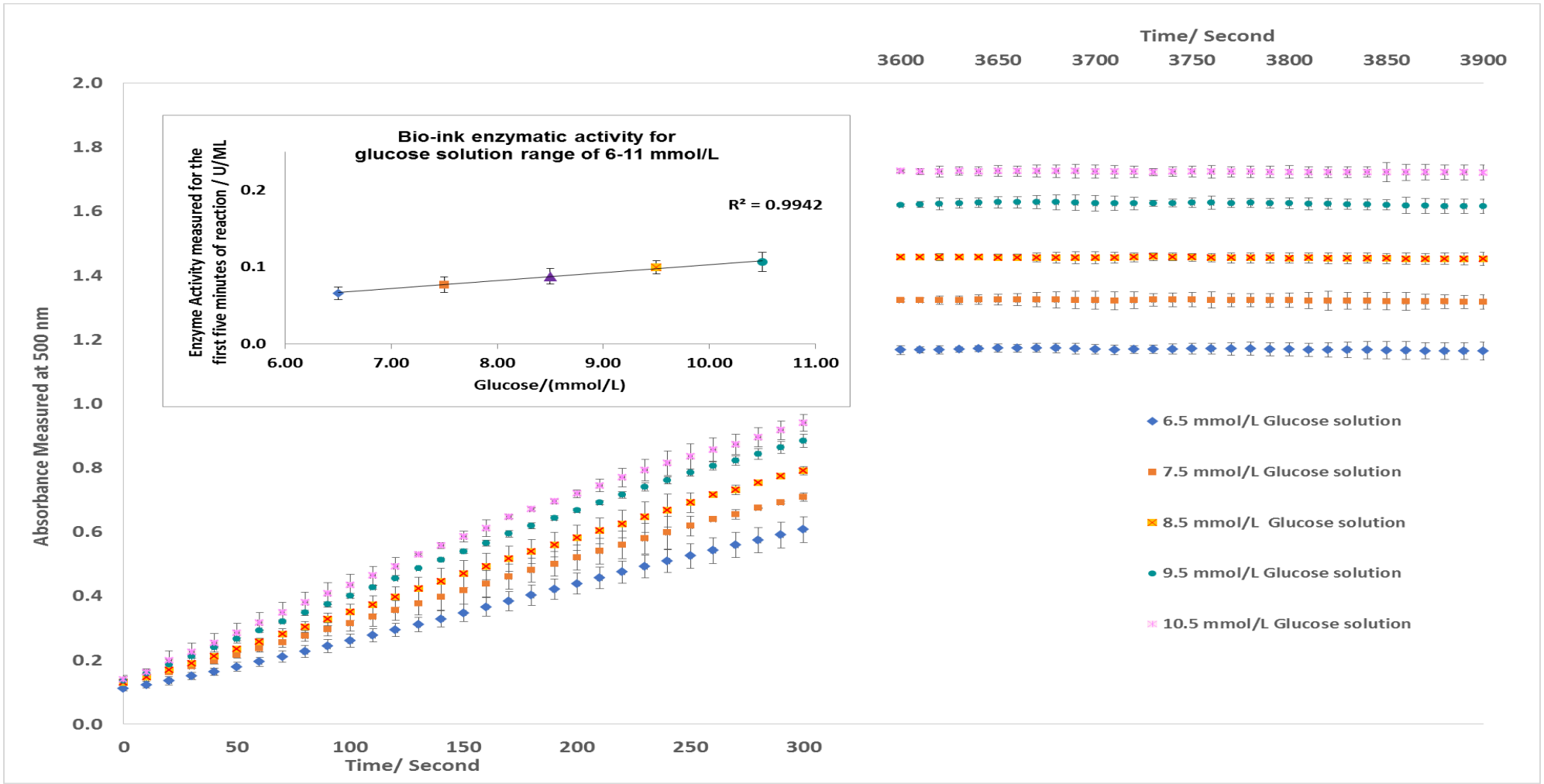

Figure 5.12| **Absorbance time course plots, GOD–AuNP bio-inks GOD assay for glucose solution range of 6-11 mmol/L;** Graph represents the absorbance of GOD assay for GOD–AuNP bio-inks measured at 500 nm immediately and the absorbance of assay solution re-measured at t = 3600 second. The bar chart on the left-hand side of the graph represents the calibration plot produced for the GOD–AuNP bio-ink enzymatic activity for glucose solution range of 6-11 mmol/L; measured from absorbance of t = 0 to t = 300 seconds for all assays. The 8.5 mmol/L glucose solution is the standard glucose concentration used in the previous assay. Error bars on all points represent standard deviations for n = 3.

Figure 5.12 shows that as the glucose concentration increases, the absorbance detected corresponding to the change in the colour of the enzymatic assay solution increases. The calibration curve produced (Figure 5.12) also shows enzymatic activity increases as glucose concentration increases. The R^2 values of 0.9942 obtained for calibration plot, suggest good linearity response at 500 nm to the changes in glucose concentration.

A consistent absorbance value for the GOD assay measured at $t < 3600$ seconds for a glucose solution range of 6-11 mmol/L was obtained, which suggests equilibrium has been reached. These data also suggest that the GOD–AuNP bio-ink is sufficient for quantifying a glucose solution accurately over the biologically relevant range of 6-11 mmol/L within an hour.

5.5.3 Compatibility of 3D printed filaments with GOD–AuNP bio-ink in an enzymatic assay

To investigate if the activity of the bio-ink is inhibited in the presence of different 3D printing materials, the enzymatic activity of the GOD–AuNP bio-ink was carried out in the presence of 3D prints as described in Section 2.12.2.

The four filaments that are intended to be used in this work for fabrication of microfluidic biosensor devices were selected and tested. A time course plot was produced for the enzymatic assay in the presence of the 3D print shown in Figure 5.13.

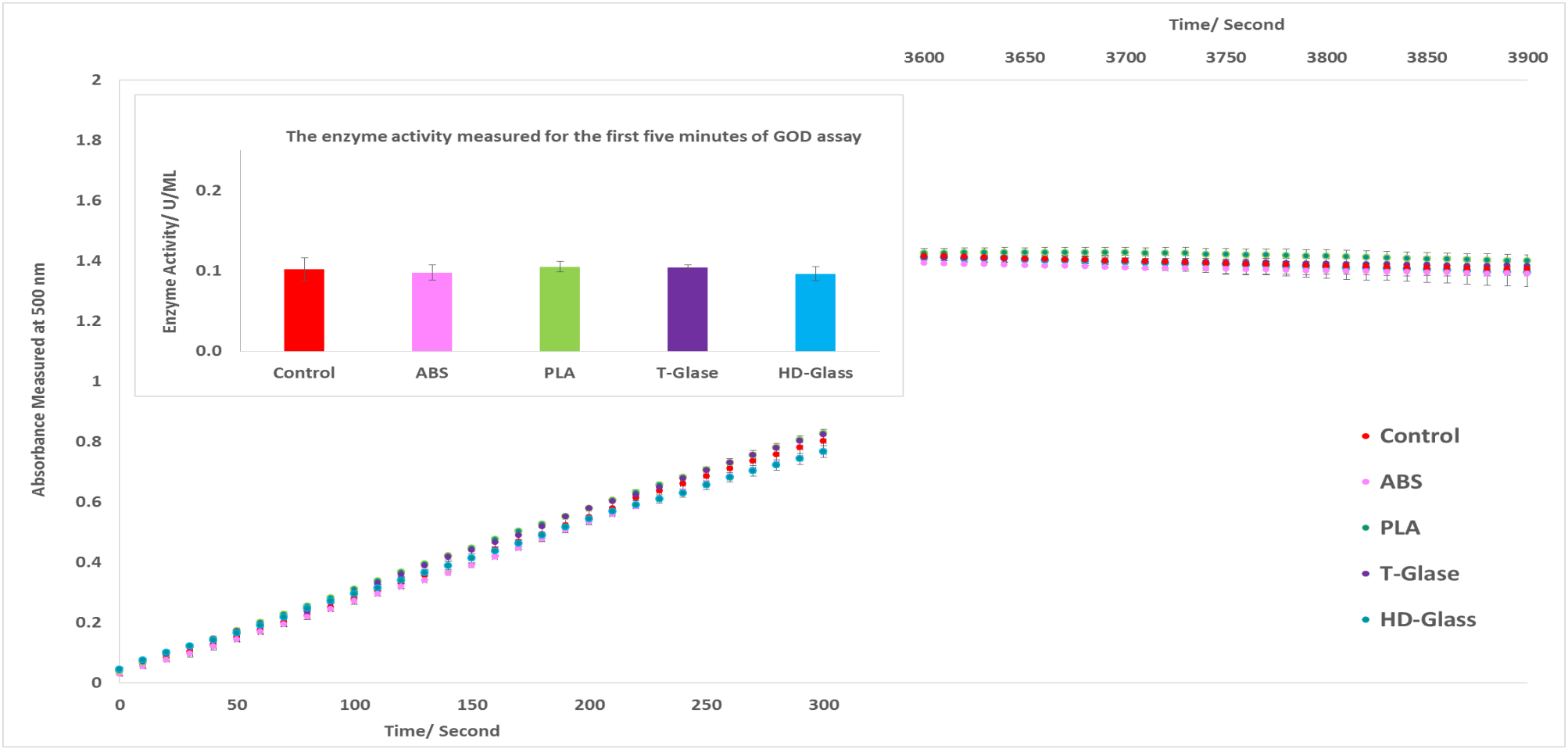

Figure 5.13| **GOD–AuNP enzymatic activity in the presence of 3D printed materials**. The graph represents an absorbance time course plots, GOD–AuNP bio-ink enzymatic activity measured at 500 nm immediately at the start of the reaction and the absorbance of the assay solution re-measured at t = 3600 second. The bar chart on the left-hand side of the graph represents enzyme activity for each assay measured from absorbance between t = 0 to t = 300 second. Error bars on all points represent standard deviations for n = 3.

Figure 5.13 shows absorbance and enzymatic activity of GOD–AuNP bio-ink in the presence assessed 3D printing material is comparable to the control sample. No significant difference for the enzymatic activity of bio-ink in the presence of assessed 3D printing material was detected. The calculated enzymatic activity at equilibrium for all bio-ink samples is also similar to the control value of 0.188± 0.01 U/mL. The outcome of this study suggests that the GOD–AuNP bio-ink is not inhibited in the presence of 3D printed filaments, thus permitting a reliable spectrophotometric determination of GOD activity.

5.5.4 Immobilising GOD–AuNP by non-specific binding to the surface of 3D-printed bio-devices as a route to make bio-inks

The enzymatic activity of the GOD–AuNP bio-ink was assessed in ABS and PLA 3D printed devices. The enzymatic glucose assay of GOD–AuNP bio-ink was performed using an adapted form of the method as described in Section 2.12.3.4. The controls in this experiment were more dilute than the samples. The ABS control and blank control contained an additional 172 µL of water than the ABS and blank samples. As a result, lower absorbance and enzymatic activity is to be expected for these mixtures. Figure 5.14 shows the experimental procedure used.

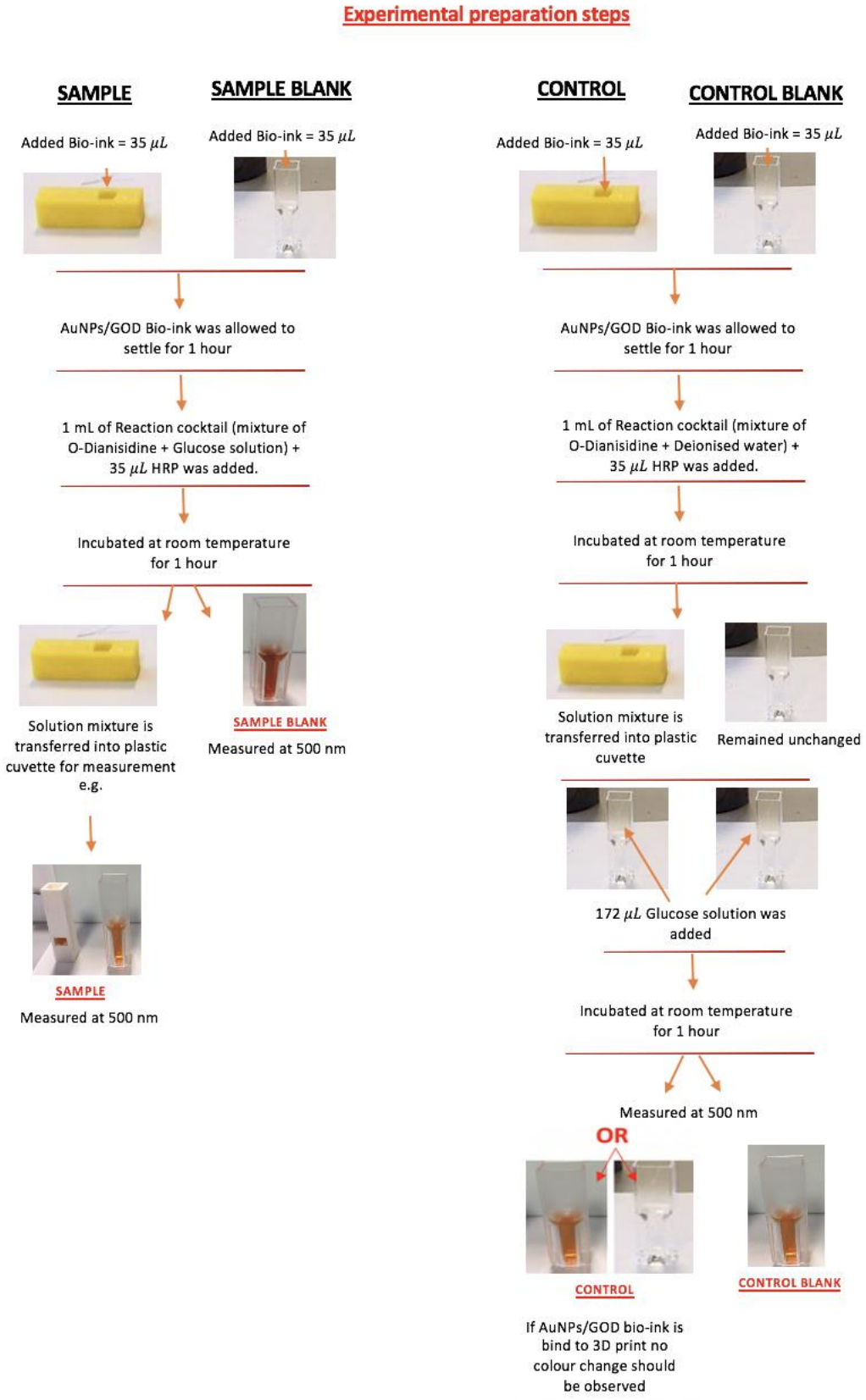

Figure 5.14| **Procedure of the GOD assay completed to assess the enzymatic activity and immobilisation of the GOD–AuNP bio-ink in 3D printed devices:** The control and sample blank assays were performed alongside in a standard 1mL plastic cuvette for comparison.

For this assessment, two forms of the 3D printed device were prepared, sample and control. A sample 3D printed device (Figure 5.14) was prepared to determine the enzymatic activity of GOD–AuNP bio-ink in a 3D printed device. The control 3D printed device was prepared to determine if GOD–AuNP bio-ink remain bound (immobilised) to the surface of the 3D printed devices during the assay.

The enzyme activity of the GOD–AuNP bio-ink was determined after one hour to ensure equilibrium point have reached. Figure 5.15 and 5.16 shows the data obtained for assessing the immobilisation of GOD–AuNP bio-ink in ABS, and PLA 3D printed devices along with blank control samples for comparison.

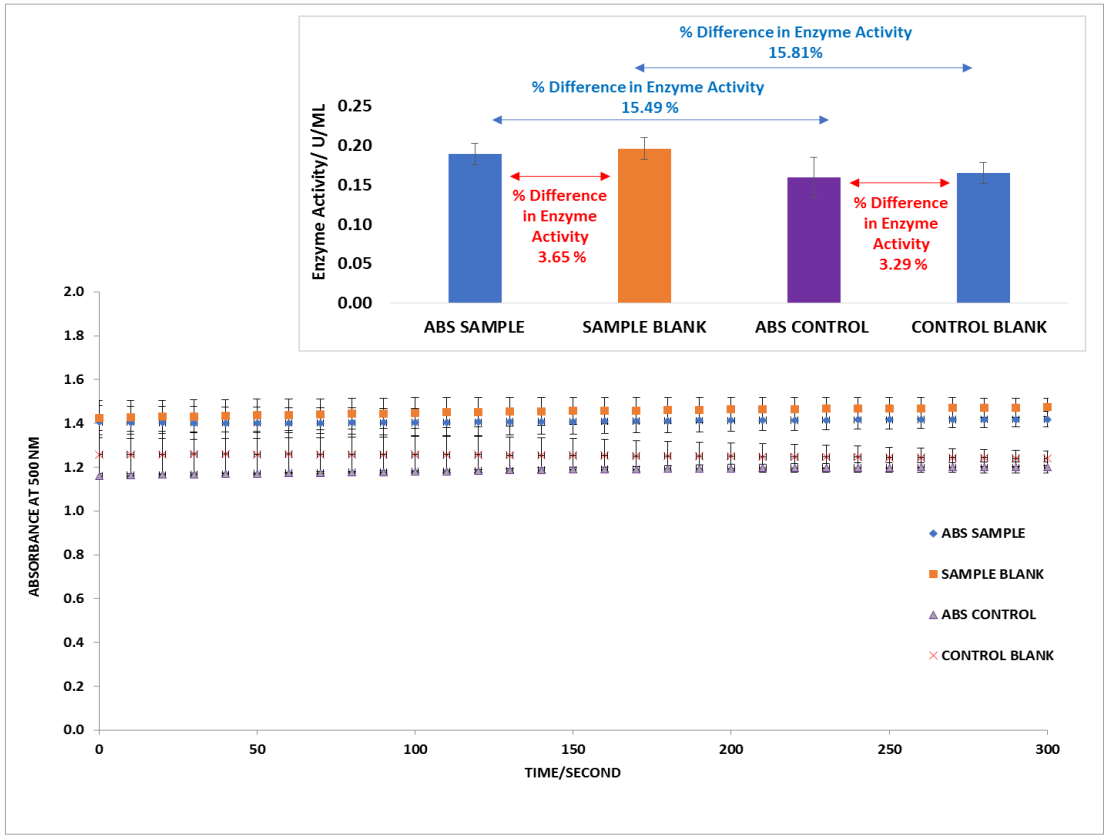

Figure 5.15| **Immobilisation assessment of GOD–AuNP as a bio-ink for development of ABS 3D printed devices.** The graph represents an absorbance time course plots for GOD–AuNP bio-ink enzymatic activity measured at 500 nm. The bar chart on the left-hand side of the graph represents the enzyme activity for each assay. Sample and control blank assays were performed alongside in a standard 1mL plastic cuvette for comparison. Error bars on all points represent standard deviations for n = 3. The percentage differences in enzyme activities between samples were calculated for comparison.

Figure 5.15 shows that the enzymatic activity of the GOD–AuNP bio-ink is not inhibited by ABS. Since no significant difference was found for the absorbance and the enzymatic activity of GOD–AuNP, assessed in 3D printed ABS device, was detected for the control study i.e. the GOD assay prepared in a polystyrene cuvette.

For ABS control samples, an absorbance of 1.18 AU was observed, which suggested the GOD–AuNP bio-ink was not immobilised on the surface of the 3D printed device (Figure 5.13, ABS Control). To determine the amount of GOD–AuNP bio-ink bound to the 3D print, the enzymatic activity for each mixture was calculated and compared. The calculated difference for the enzymatic activity of the ABS sample and ABS control was 15.49%. This value is very similar to the difference between the enzymatic activity of the sample and control blanks with a value of 15.81%. As a result, it can be concluded that a negligible amount of GOD–AuNP bio-ink remained bound to the 3D print.

The same study was repeated using GOD–AuNP bio-ink enzymatic assay with PLA 3D printed devices (Figure 5.16). Similar conclusions to ABS study were found. Figure 5.16 shows no significant difference for the enzymatic activities of GOD–AuNP in the 3D printed device compared to the control.

Overall this study shows that GOD–AuNP bio-ink is not immobilised on a surface of the 3D printed device by nonspecific absorption. This makes this method unsuitable for use in 3D printed biosensor devices.

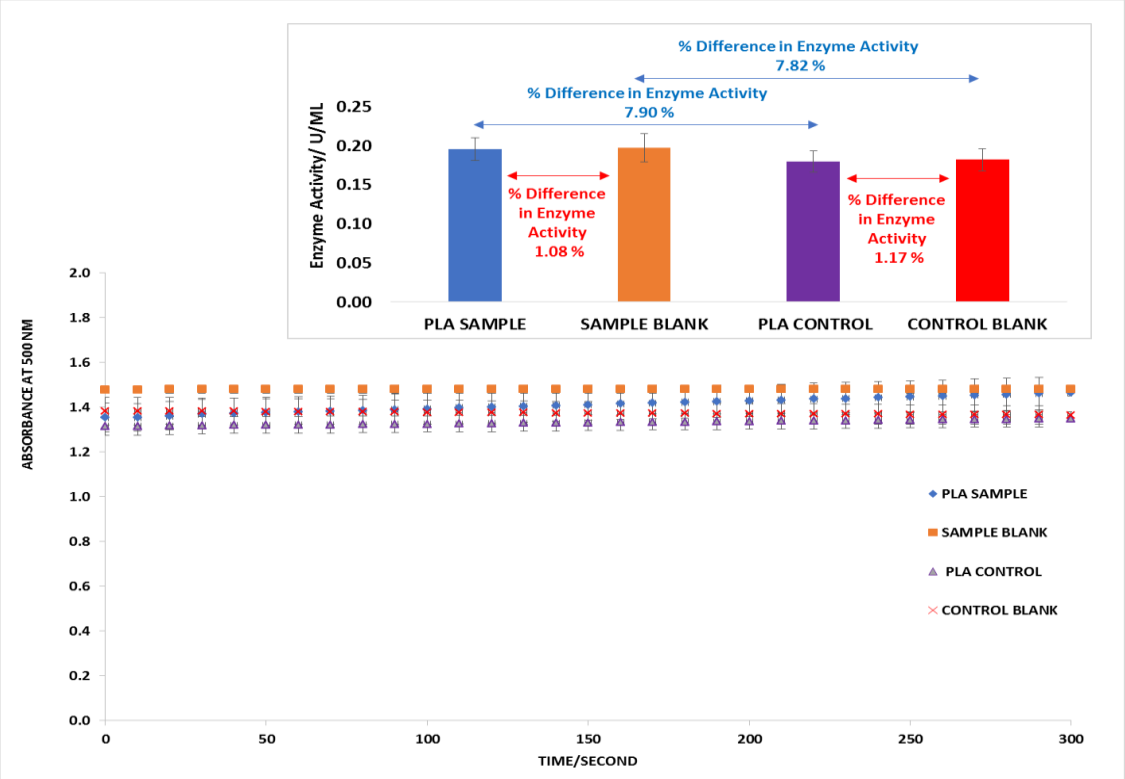

Figure 5.16| **Immobilisation assessment of GOD–AuNP as a bio-ink for development of PLA 3D printed devices.** The graph represents an absorbance time course plots for GOD–AuNP bio-ink enzymatic activity measured at 500 nm. The bar chart on the left-hand side of the graph represents the enzyme activity for each assay. Sample blank and control blank is the blank (control) assay performed alongside in a standard 1mL plastic cuvette for comparison. Error bars on all points represent standard deviations (SD) of three repeats, n=3.

5.5.5 Immobilising HRP–AuNP by non-specific binding to the surface of 3D printed bio-devices as a route to make bio-inks

The HRP–AuNP bio-ink was prepared using the similar technique to GOD–AuNP as described in Section 2.12.3.2 by substituting GOD with HRP. HRP is very stable and is used with GOD for glucose biosensor production (Setti *et al.*, 2007).

As in Section 5.5.4, the enzymatic activity of HRP–AuNP was assessed in a 3D printed ABS device using the method detailed in Section 2.12.3.4. The absorption time course

assessment of the enzymatic activity of HRP–AuNP bio-ink in the 3D printed device is shown in Figure 5.17).

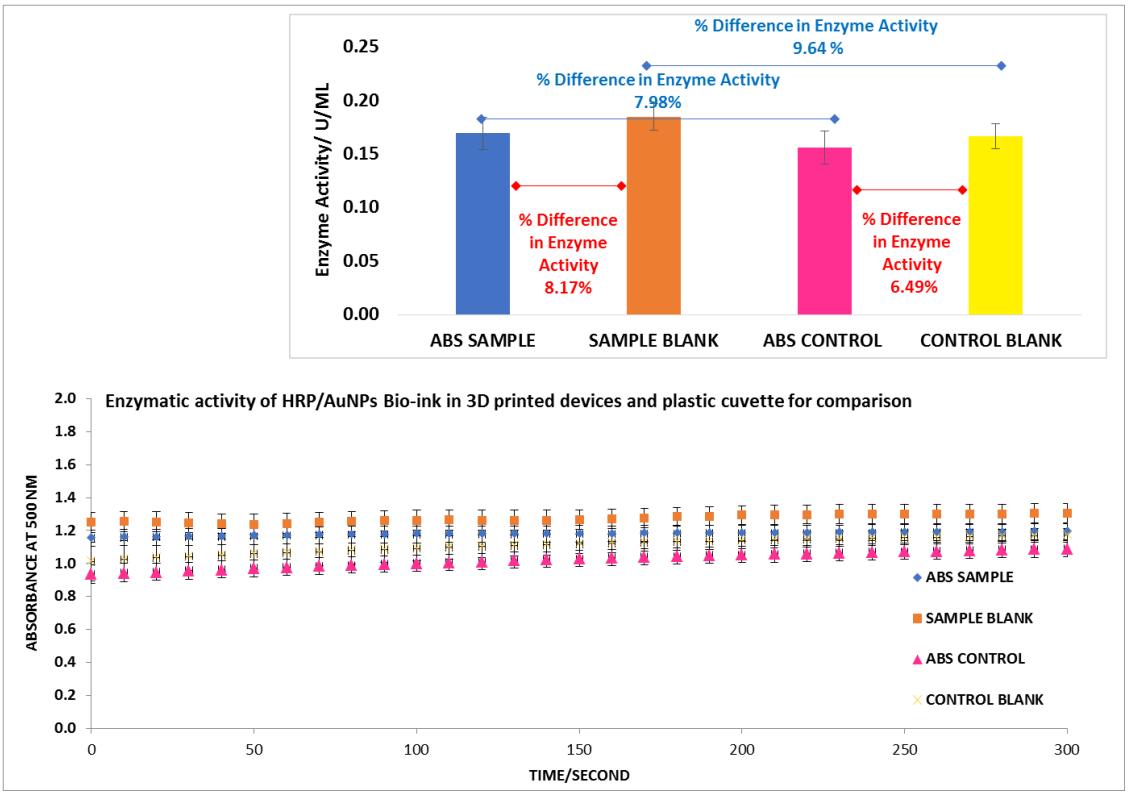

Figure 5.17| **Immobilisation assessment of HRP–AuNP as a bio-ink for development of ABS 3D printed devices.** The graph represents an absorbance time course plots for AuNP/HRP bio-ink enzymatic activity measured at 500 nm. The bar chart on the left-hand side of the represents enzyme activity for each assay measured by using the absorbance value of t = 0 and t = 300 second. Control assays were performed in a standard 1mL plastic cuvette for comparison. Error bars on all points represent standard deviations for n = 3.

The data in Figure 5.17 show that the enzymatic activity of the HRP–AuNP bio-ink is not inhibited in a 3D printed ABS material compared to the control study. This is because no significant difference was detected between the absorbance and enzymatic activity of the bio-ink compared to the control study.

For the ABS control an absorbance of 0.9 AU was observed, which suggests the HRP–AuNP bio-ink was not immobilised on the surface of the 3D printed device (Figure

5.17, ABS Control). The difference in enzymatic activity between the ABS sample and ABS control was 7.98%. This value is very similar to the difference between the enzymatic activity of the sample and control blank with a value of 9.64%. As a result of this outcome, it can be concluded that a negligible amount of HRP–AuNP bio-ink was bound to the 3D print (Figure 5.17, control). For both of this comparison the approximate 8-10% difference between sample and control absorbance was due to the dilution factor.

Overall this study shows that HRP–AuNP bio-ink is not immobilised on the surface of the 3D printed device by nonspecific absorption. This makes this method unsuitable for use in 3D printed biosensor devices.

The ineffective nonspecific binding of the GOD–AuNP and HRP–AuNP bio-inks to 3D print may be due to change in properties of AuNPs. For example, the surface charge of AuNPs might have been changed during/after conjugation to GOD and HRP enzyme. The size of the protein can be the other influencing factor, e.g. the size may be big for the gold nanoparticle size used. Unavailability of the surface on AuNPs can also be the other influencing factors that inhibit them from binding to the polymer surface(Chen and Klok, 2013)(Bao *et al.*, 2014).

5.4.6 Evaluating solvent-based bio-inks containing GOD–AuNP as a method to modify the 3D printed device

Solvent-based GOD–AuNP bio-ink was prepared in different ratios, as detailed in Section 2.12.3.5. This experiment was setup as a strategy to immobilise the bio-ink to the surface of a 3D printed device, using solvents which can dissolve the ABS filament to facilitate the trapping of GOD–AuNPs on the surface of the ABS 3D printed material.

The enzymatic activity of the solvent based GOD–AuNP bio-inks was assessed in 3D printed devices similar to Section 5.5.4 using the method detailed in Section 2.12.3.4. Figure 5.18 shows the outcome of this study.

The data shown in Figure 5.18 demonstrate that the enzyme activity for the GOD–AuNP bio-ink is inhibited as the percentage of the solvent increases from 0% to 100%. An approximate 50% reduction in GOD–AuNP bio-ink enzyme activity is observable when a minimum of 20% solvent is used in the bio-ink mixture. Leakage from the 3D printed material was also detected for the experiments prepared with bio-inks containing ≥ 40% of acetone, chloroform and dimethylformamide solvents.

In the control study, colour changes and absorbance values corresponding to the detection of glucose in solution suggest GOD–AuNP bio-ink was not immobilised to the surface of ABS 3D printed device in the presence of a solvent in the mixture (Figure 5.17, control).

Table 5.1|Represents the % difference between sample and control enzymatic activity for variable ratio of solvent-based bio-inks.

Solvents	Solvent % in Bio-inks mixtures			
	0	20	40	100
Acetone	15.45%	23.34%	12.21%	16.28%
Chloroform	8.06%	1.33%	29.13%	10.68%
Dimethylformamide	13.88%	19.20%	24.87%	4.92%
Dimethyl sulfoxide	12.39%	13.58%	1.21%	19.21%
Hexane	14.62%	16.05%	9.78%	3.73%
Tetrahydrofuran	17.26%	25.09%	4.72%	9.32%

Table 5.1: Represents the % differences between sample and control enzymatic activity for variable ratio of solvent-based bio-inks.

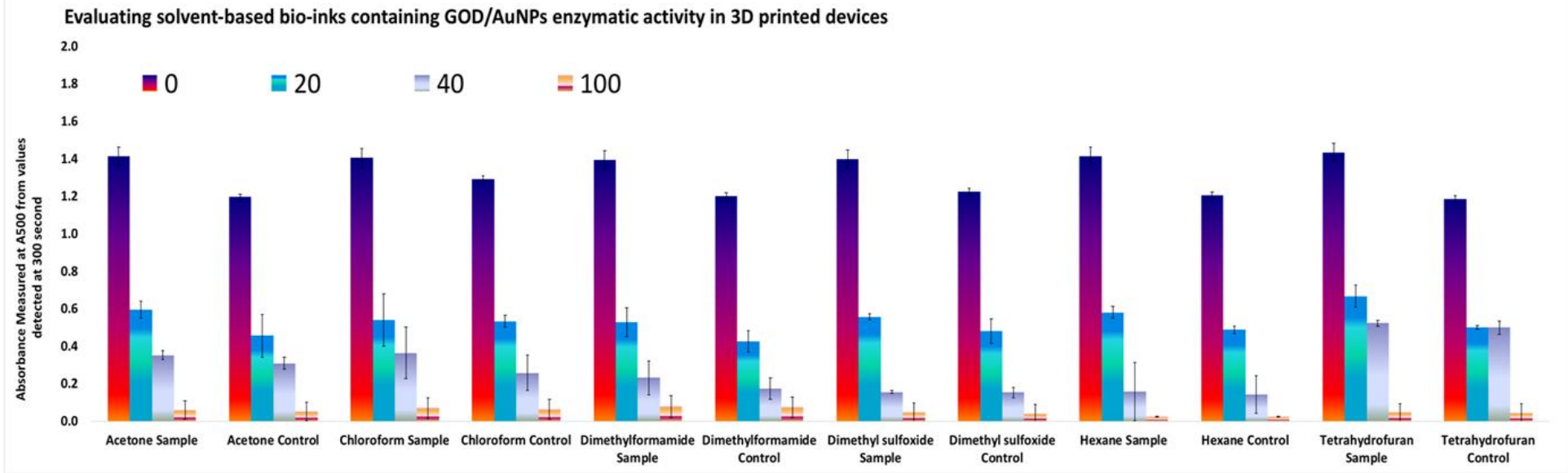

Figure 5.18|**Comparison of GOD enzymatic activity of solvent-based GOD–AuNP bio-ink in a 3D printed ABS device**; the plots compare the absorbance measured at 500 nm values for 200 seconds. The table on the right-hand side of the figure compares the percentage different in enzymatic activity between sample and control study GOD–AuNP bio-ink enzymatic assessment completed in 3D printed ABS for each solvent. In the sample 3D printed device assay mixture containing glucose as a control, water was substituted for glucose. Error bars on all points represent standard deviations for n = 3.

From Figure 5.18 the percentage difference in enzymatic activity between the sample and control was calculated and plotted (Table 5.1 present in Figure 5.18) for comparison. These data show that solvent-based GOD–AuNP bio-ink prepared with 40% of chloroform and 20% of tetrahydrofuran had the highest percentage difference between sample and control enzymatic activity, with the values of 29.13% and 25.09%, respectively. This means that GOD–AuNP bio-ink prepared using these solvents was bound to the 3D print more than the other assessed solvents bio-inks.

The data presented (Table 5.1, Figure 5.18) also show an approximate 8-18% difference between sample and control enzymatic activity for bio-ink without solvents. However, since this range is very similar to what was observed in Section 5.5.4 for the study in 3D printed ABS material, it is assumed that the percentage difference between sample and control studies may be due to the dilution factor as controls contained an additional 172 µL of water.

Overall at least a 50 % reduction in GOD–AuNP bio-ink enzyme activity was observed for all samples when the solvent is used in the bio-ink mixture. It is assumed that using a solvent in the bio-ink mixture may have denatured the enzyme. Therefore, this approach was not considered as an appropriate technique to immobilise bio-inks to the 3D printed surface.

5.6 Discussion

The emphasis of this chapter was to develop and test bio-ink immobilisation on a selected surface of FDM 3D printed. To achieve that goal, this work accomplished the following: 1) An iterative development of a specific protocol to fabricate and assess bio-ink enzymatic activity. 2) the development and assessment of AuNP protein bio-inks for FDM 3D printed biosensing application. 3) an assessment of bio-ink immobilisation to the surface of 3D printed bio-devices

5.6.1 Iterative development of a specific protocol to fabricate and assess bio-ink enzymatic activity

An optimisation assay for the GOD assay to assess the enzymatic activity of biological molecules at room temperature and in a 3D printed material was developed and examined. By using the optimised GOD assay, it was determined that the enzymatic activity of the GOD and HRP enzymes are not inhibited in the presence of the 3D printed material.

Examinations were made to determine the suitability of AuNPs as carrier systems for biological molecules on 3D printed materials. From this study, it was determined that AuNPs bind to the surface of the ABS 3D print by non-specific absorption and are not absorbed into the interior. It was also determined that dried AuNPs on a surface of an ABS 3D print is bound firmly to the 3D printed material and does not wash off in the presence of aqueous, buffer and biological solutions. These experiments show that AuNPs can be suitable carriers that allow bio-inks to achieve enzyme immobilisation on the surface of 3D printed devices.

5.6.2 Development and assessment of AuNPs protein bio-inks for FDM 3D printed biosensing applications

In this work, a set of specific enzymatic bio-inks for FDM 3D printing technology was developed. An AuNP carrier system to immobilise bio-ink on a 3D printed device was selected since plastic 3D printing filaments are relatively inert and lack functional groups that would facilitate protein attachment. Chemical surface preparation is required to induce surface functional groups for protein immobilisation. As a carrier for biological system AuNPs were used in this work since they are accessible, stable at high temperature and pH and are used commonly used for protein immobilisation. In addition, numerous reports on the immobilization of GOD protein employed modified lead nanowires, titania nanotubes, graphene and silica nanoparticles (Wang *et al.*, 2009) (Benvenuto, Kafi and Chen, 2009)(Khalil *et al.*, 2016)(Sun, Zhao and Ren, 2012).

GOD–AuNP and HRP–AuNP bio-inks were produced. To fabricate these bio-inks the method was based on literature methods to immobilisate glucose oxidase onto gold nanoparticles that enhances temperature and pH thermostability. The resulting bio-ink was produced quickly and had extended shelf time (Li *et al.*, 2007).

To fabricate bio-inks that allow faster enzymatic reactions, numerous bio-inks were prepared. AuNPs of 20 nm and 50 nm were used to make these bio-inks. The 20 nm sized AuNPs are equivalent to those commonly reported in the literature. Papers on immobilisation of GOD onto AuNPs mostly highlight the use of an AuNPs of 20 nm or lower (Zhang *et al.*, 2005) (Heddle, 2013). However, in this report, we have also used 50 nm AuNPs to determine whether the size of AuNP affects the rate of enzymatic activity. Using larger AuNPs means there is a greater surface area for GOD binding (Murphy *et al.*, 2010). Ideally, we are interested to determine if greater GOD binding to AuNPs leads to faster enzymatic reactions.

To determine the optimum size and technique for bio-inks with the highest enzymatic activity, the GOD-AuNP bio-inks were prepared with and without nitrogen treatment. According to the literature, nitrogen treatment will increase the yield of GOD to AuNPs during the treatment time (Li *et al.*, 2007). Using the nitrogen treatment in bio-ink preparation resulted in more GOD binding to AuNPsas determined by bio-ink enzymatic activity.

The enzymatic activity and the stability of GOD-AuNP bio-inks were assessed to determine the stability of fabricated bio-ink. From the study, it was determined that 50 nm AuNP-GOD bio-ink maintained stability after six weeks and may have a suitable shelf life for glucose biosensing. To determine the actual shelf life of these bio-inks more assessment is required, and their activities need to be assessed after extended storage. The reported shelf life of AuNPs is one year, and six months for GOD enzyme, when at 4˚C (House, Anderson and Ward, 2007). Consequently, the maximum storage shelf life of this bio-ink should be up to six months.

To determine if GOD–AuNP bio-ink can be used to accurately quantify the glucose content in a mixture, the GOD enzymatic assay was performed for glucose solutions in the range of 0-10 mmol/L. A calibration curve was produced, and the outcome of the study showed that GOD-AuNPs bio-ink can accurately quantify a biological relevant glucose solution in the range of 0-10 mmol/L within an hour.

To investigate if the activity of the enzyme was not inhibited in the presence of different 3D printing materials the enzymatic activity of GOD–AuNP bio-ink was carried out in the presence of the four filaments (PLA, ABS, HD-Glass, and T-Glase) that best suited to fabricate microfluidic biosensor. The outcome showed that the GOD–AuNP bio-ink was still active in the presence of these 3D printed filaments, thus permitting a reliable spectrophotometric determination of GOD activity.

5.6.3 Assessing the efficiency of AuNP protein bio-ink immobilisation to the surface of 3D printed bio-devices

Immobilization methods and chemistries vary significantly depending on the immobilisation surface, protein properties, and specific assay goals. In this work, the immobilisation of bio-inks to the surfaces of the 3D printed device was assessed by assessing the enzyme activity of GOD–AuNP and HRP-AuNP bio-inks in ABS and PLA 3D printed devices. The protocol used to assess bio-ink immobilisation to 3D print was optimised for assessing the enzyme activity in 1 mL bio-device. 35 µL of bio-ink was used in the optimised assay for 3D print which is comparable to the ranges of between 5 and 150 µL reported for active molecules used typically in biosensor devices (Rocha-Gaso *et al.*, 2017) (Eggins, 1997).

In this work, ineffective nonspecific binding of the GOD–AuNP and HRP–AuNP bio-inks to 3D print was achieved which showed the method to be unsuitable for use in 3D printed biosensor devices. Changes in the properties of AuNPs, such as surface charge during/after conjugation to GOD and HRP enzyme, size of protein and unavailability of the surface on AuNPs, were determined to be the factors leading to ineffective bio-ink binding to the 3D printed bio-device (Chen and Klok, 2013).

Solvent-based bio-inks containing GOD-AuNPs were prepared as a method to modify a 3D printed device in order to immobilise the bio-ink on the 3D printed surface. Six different solvents, acetone, chloroform, dimethylformamide, dimethyl sulfoxide, hexane and setrahydrofuran, which can dissolve ABS filaments were used to make solvent-based GOD-AuNP bio-inks.

The solvents used in bio-ink formulation were selected based on those used in the literature. Acetone, dimethyl sulfoxide, tetrahydrofuran and dimethylformamide were used to dissolve ABS in the viscometric determination of compatibility in PVC/ABS

polyblends and to determine the effect of dissolution-based recycling on the degradation and the mechanical properties of the ABS copolymer (Kulshreshtha, Singh and Sharma, 1988)(Arostegui *et al.*, 2006). Hexane and chloroform were used in solvent-assisted microcontact moulding (King *et al.*, 1997). In addition, chloroform, hexane and tetrahydrofuran are the common solvents used in the assembly of binary mixed polymer brush-coated AuNPs (Chen and Klok, 2013).

Solvent-based GOD-AuNP bio-inks were found unsuitable in imobilisation of bio-ink on the 3D printed surface since approximately 50% of the protein in bio-ink mixture lost activity and was denatured. Also, the excess volume of the solvents used in bio-ink mixture induces leakage from the device by disturbing the ABS polymer.

The motivation in this research for bio-ink production was to develop a new technique that is easily integrated to bind the functionalised AuNPs to a 3D printed surface. Therefore, surface preparation technique and other methodological approaches to bind AuNPs to 3D print were not considered. Since the other applications of AuNPs for surface immobilisation are largely focused on the attachment of these molecules to electron probes, glassy carbon electron, silica substrates, graphene oxide sheet and ITO glass, which are mostly used for electrochemical biosensor production (Rim, 2014)(Huang *et al.*, 2008)(Yamanaka, Vestergaard and Tamiya, 2016). These techniques are not appropriate for this work because the preparation of the polymer surface using this technique is costly, time-consuming and it cannot be applied directly.

5.7 Conclusion

In this chapter, a set of specific enzymatic bio-inks for FDM 3D printing technology was developed, and their enzymatic activities were assessed. A MakerBot Replicator 2X 3D printer was used to fabricate working glucose biosensor 3D printing devices. The enzymatic activities of GOD and HRP enzymes (made as bio-inks) were assessed inside the 3D printed device. The assessments confirmed that the enzymatic activity of AuNPs protein bio-inks made for this research is not inhibited in the 3D printed bio-device. The assessment also suggested that the amount of GOD/AuNPs bio-ink utilised is sufficient to accurately quantify a biological relevant of glucose solution in the range of 0-10 mmol/L within an hour.

Numerous techniques were developed to immobilise AuNPs protein bio-inks to the 3D printed devices. However, the nonspecific binding of AuNPs protein bio-inks to the surfaces of 3D printed devices was not achieved. In conclusion, the critical factor for biosensor device fabrication and protein sensing is the immobilisation of the active molecules to the surface of the device (Cordeiro *et al.*, 2016) which was not achieved here.

CHAPTER 6

DESIGN AND CHARACTERIZATION OF MAGNETIC PROTEIN BIO-INKS FOR FDM 3D PRINTING

6.1 Introduction

Following on from objectives 5a and 5b, detailed in Chapter Five, the focus in this chapter is to develop and test bio-inks to enable protein immobilisation on the surface of FDM 3D print. Two approaches were considered using the enzymes GOD and HRP bound to gold-coated magnetic nanoparticle or magnetic beads to enable immobilisation of the bio-inks with a magnet inside the 3D printed object. Once immobilisation of newly formulated bio-inks to the 3D print had been achieved the other objectives in this chapter are:

6a. To assess the activity of the bio-ink after decanting by syringe extruder into a 3D printed object. In particular, from this experiment, we can show the performance and accuracy of syringe extruder (Chapter 3) for decanting reproducible droplet sizes of bio-ink in 3D printed devices in such a way that they would maintain enzymatic activity after printing.

6b. To use immobilised bio-inks inside 3D printed objects that are optimised for UV visible spectroscopy and perform a coupled set of chemical reactions that quantify glucose in a sample.

6.1 Developing NitmagoldGOD and NitmagoldHRP bio-inks as a route to make bio-inks for FDM 3D printed bio-devices

Gold-coated magnetic nanoparticles (Nitmagold50nm), equivalent to the size of AuNPs used in Section 5.5, was used to make bio-inks.

The Nitmagold50nm particles were used since they are magnetised and can be controlled and moved with a magnet in a 3D printed device.

NitmagoldGOD and NitmagoldHRP bio-inks were prepared by conjugating GOD and HRP to Nitmagold50nm as described in Experimental section 2.12.3.

A new 3D printed device similar to the one used in Section 5.5.4 was designed and used for this experiment with a space to allow insertion of magnet diameter of 2 mm up to 6 mm (Figure 6.1).

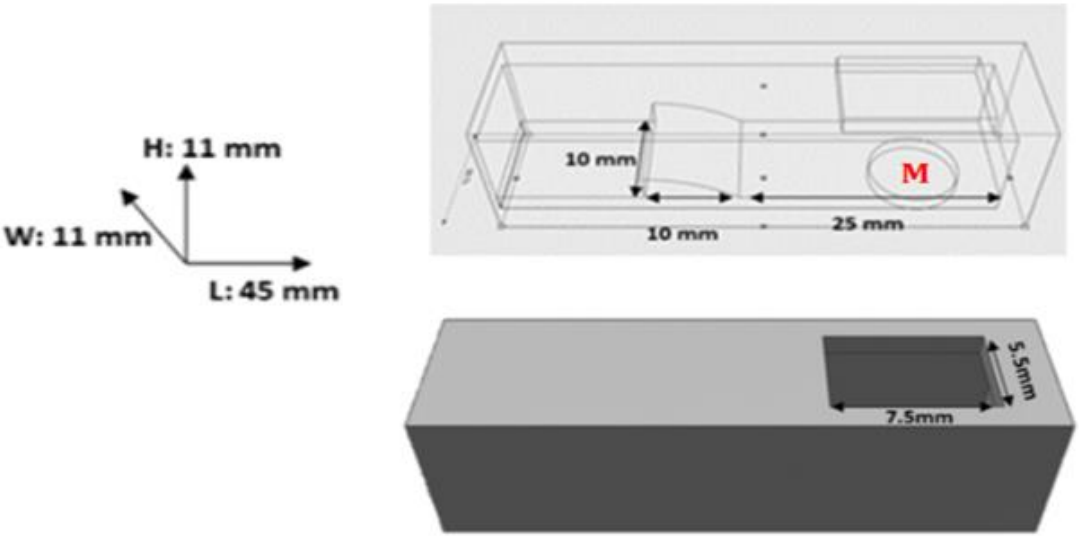

Figure 6.1| **Schematic CAD designs of device used to assess immobilisation of NitmagoldGOD and NitmagoldHRP bio-inks in the 3D printing device.**

To allow a reliable spectrophotometric determination of GOD activity an absorbance versus time plot was produced for NitmagoldGOD and NitmagoldHRP by measuring the activity of the assay until equilibrium is reached. The enzymatic activity of NitmagoldGOD and NitmagoldHRP bio-inks in 3D printed devices (Figure 6.1, no magnet) was assessed as described in Section 2.12.3.7.

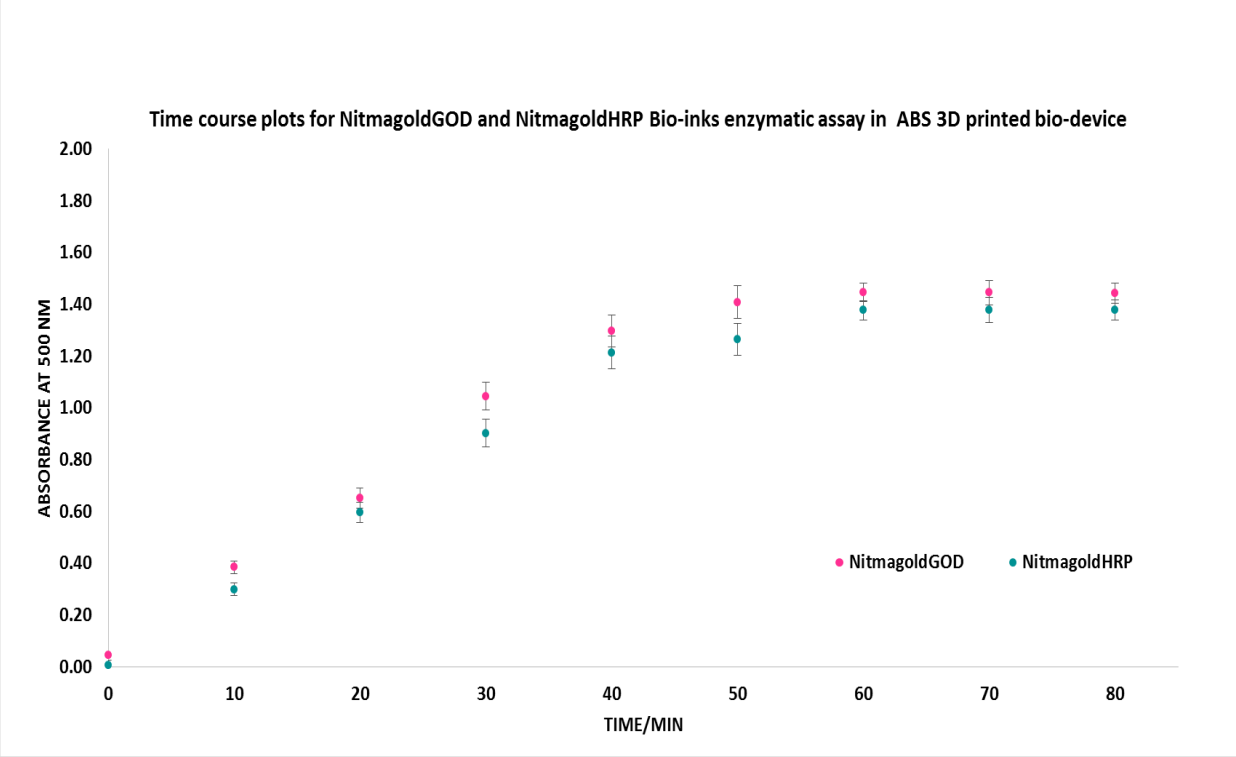

Figure 6.2| **Absorption time course plots, assessment of the enzymatic activity NitmagoldGOD and HRP in 3D printed devices**. Error bars on all points represent standard deviations for n = 3.

Figure 6.2 shows for NitmagoldGOD and HRP in 3D printed devices the GOD reaction reaches an equilibrium point in 60 minutes. This means that the conditions used are sufficient to allow a reliable spectrophotometric determination of GOD activity in one hour.

6.2 Immobilising NitmagoldGOD and NitmagoldHRP bio-inks by a magnet to the surface of 3D printed bio-devices

The enzymatic activity of NitmagoldGOD and NitmagoldHRP bio-inks in 3D printed devices was assessed as described in Section 2.12.3.7. To assess the immobilisation efficiency of the bio-inks, the enzymatic assay was carried out with a 2 mm diameter magnet inside 3D printed bio-devices. The experimental approach used here is comparable to the approach used in Section 5.5.4, Figure 5.14.

The enzyme activity of the NitmagoldGOD and NitmagoldHRP was determined after a minimum of one hour to ensure the equilibrium point had been reached to allow a reliable spectrophotometric determination of GOD activity.

Figures 6.3 and 6.4 show the data obtained from assessing the immobilisation of NitmagoldGOD and NitmagoldHRP bio-inks in 3D printed devices along with control study (sample blank and control blank) for comparison. Blank samples are control assays prepared in polystyrene cuvettes in parallel with assays accomplished in 3D printed devices.

Figures 6.3 and 6.4 show that the enzymatic activity of the NitmagoldGOD and NitmagoldHRP bio-inks in 3D printed ABS material is not inhibited. Since no differences were detected between assays in 3D printed, ABS devices compared to the control study of a blank sample where the GOD assay was determined in a polystyrene cuvette.

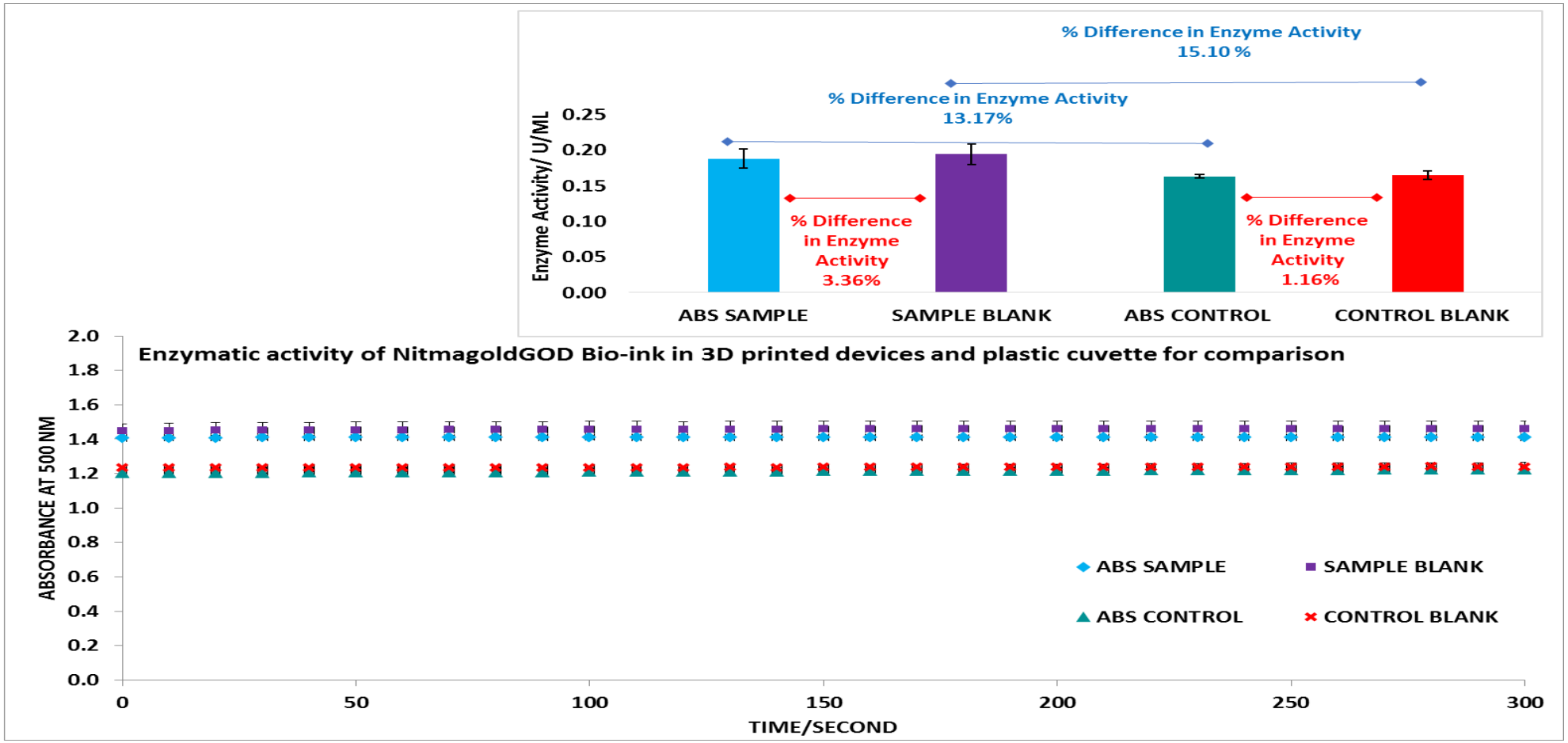

Figure 6.3| **Assessing immobilisation of NitmagoldGOD as a bio-ink by a magnet to the surface of ABS 3D printed bio-devices**. The graph represents an absorbance time course plots for NitmagoldGOD bio-ink enzymatic activity measured at 500 nm, after a minimum of one hour. The bar chart on the left-hand side of the graph represents the enzyme activity of each sample. Sample blank and control blank is the blank (control) assay performed alongside in a standard 1mL plastic cuvette for comparison. Error bars on all points represent standard deviations for n = 3.

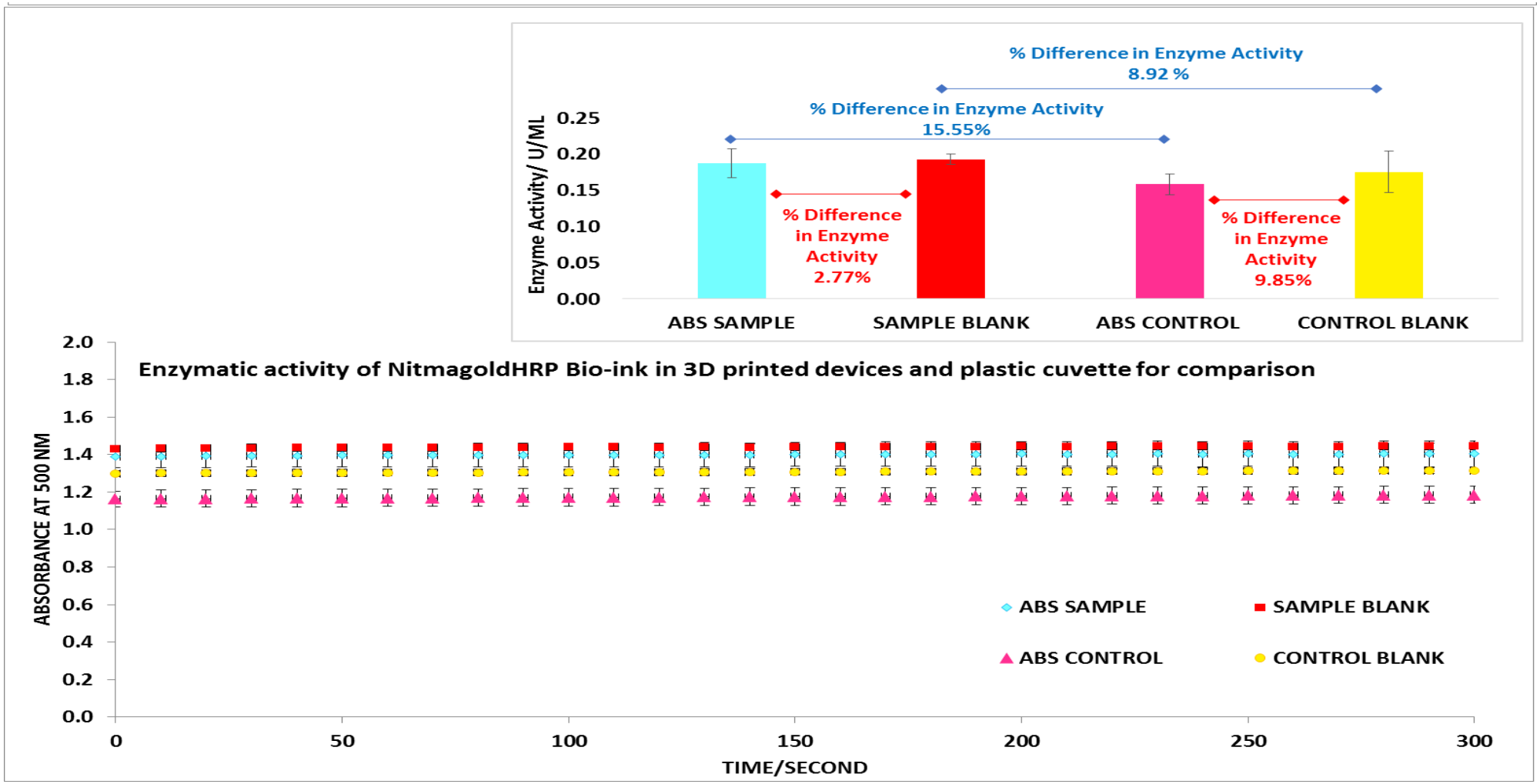

Figure 6.4| **Assessing immobilisation of NitmagoldHRP as a bio-ink by a magnet to the surface of ABS 3D printed bio-devices**. The graph represents an absorbance time course plots for NitmagoldHRP bio-ink enzymatic activity measured at 500 nm, after a minimum of one hour. The bar chart on the left-hand side of the graph represents the enzyme activity for each assay. Sample blank and control blank is the blank (control) assay performed alongside in a standard 1mL plastic cuvette for comparison. Error bars on all points represent standard deviations for n = 3.

Absorbance at 1.2 Au was observed for the ABS control, which suggests that NitmagoldGOD, and NitmagoldHRP bio-inks was not immobilised on the surface of the 3D printed device (Figure 6.3 and 6.4, ABS Control).

To determine the approximate amount of NitmagoldGOD, and NitmagoldHRP bio-inks bound to the 3D print, the enzymatic activities for each mixture were calculated and compared. The calculated difference in enzymatic activity between the ABS sample and the ABS control for NitmagoldGOD was 13.17%. This value is very similar to the difference in enzymatic activity of sample blank and control blank with a value of 15.10%. For NitmagoldHRP study this difference in enzymatic activity between ABS sample and ABS control is 15.55% and for sample blank and control blank is 8.92%.

Overall this study shows that NitmagoldGOD and NitmagoldHRP bio-inks are not immobilised on a surface of the 3D printed device by 2 mm magnet, since no significant difference within error, for enzymatic activities of bio-inks in 3D printed device compared to control was detected.

6.3 Immobilisation of NitmagoldGOD bio-inks in 3D printed bio-devices: magnet size variation study

To determine if increasing the magnet size can influence the bio-ink immobilisation to the surface of the 3D printed device. The NitmagoldGOD bio-ink assay was carried out in the presence of 3, 4, 5 and 6 mm diameter magnets similar to the method detailed in Section 6.2. The assessment was also completed in 3D printed devices with no magnet as a control study for this experiment. Figure 6.5 shows the data obtained for assessing the NitmagoldGOD bio-inks activity in 3D printed devices at all magnet sizes along with control setup for comparison.

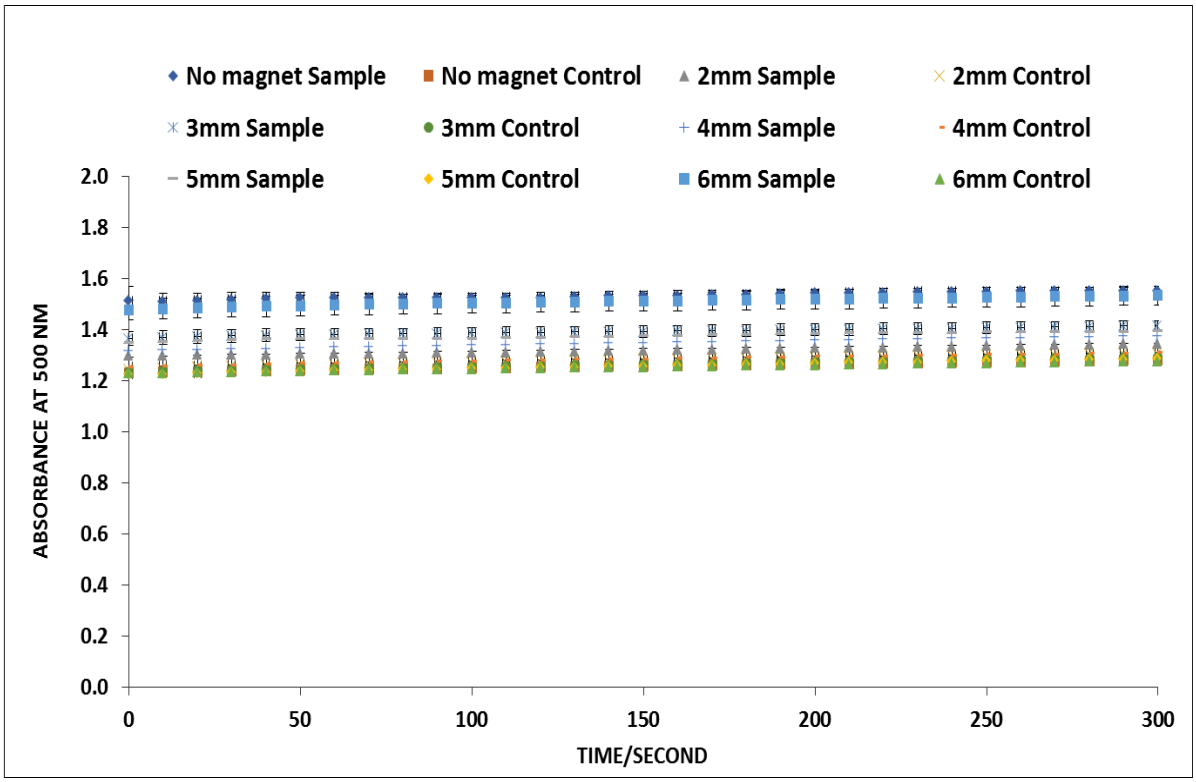

Figure 6.5| **The graph represents an absorbance time course plots for NitmagoldHRP bio-ink GOD assay in the 3D printed device**. The absorbance of the assay mixture in 3D printed device was measured at 500 nm, after a minimum of one hour. Error bars on all points represent standard deviations for n = 3.

By using the absorbance plot in Figure 6.5, the enzyme activity for each sample was calculated from the absorbance detected at the equilibrium point by using the method detailed in Section 5.2. The enzyme activity of NitmagoldGOD bio-inks in 3D printed devices for all magnet sizes is presented in Table 6.1.

Next, by using Table 6.1 values, the percentage difference between the enzyme activity of NitmagoldGOD bio-inks in 3D printed device samples, compared to its control study for all magnet sizes, was calculated and plotted on a bar chart presented in Figure 6.6. This determines the percentage of the bio-inks immobilised to the 3D printed device. From the plot Figure 6.6, no correlation for the influence of an increase in magnet size on bio-ink immobilization to the surface of the 3D printed device was made.

Table 6.1| **Enzyme activity of NitmagoldGOD bio-inks in 3D printed devices for all magnet sizes.** The enzyme activity was calculated for individual samples using the absorbance of assay obtained at equilibrium point.

No magnet Sample	No magnet Control	2 mm Sample	2 mm Control	3 mm Sample	3 mm Control	4 mm Sample	4 mm Control	5 mm Sample	5 mm Control	6 mm Sample	6 mm Control
0.2072±0.024 U/ML	0.1787±0.037 U/ML	0.1795±0.019 U/ML	0.1746±0.022 U/ML	0.1888±0.042 U/ML	0.1723±0.047 U/ML	0.1836±0.003 U/ML	0.1747±0.009 U/ML	0.1859±0.011 U/ML	0.1718±0.007 U/ML	0.2044±0.008 U/ML	0.1704±0.006 U/ML

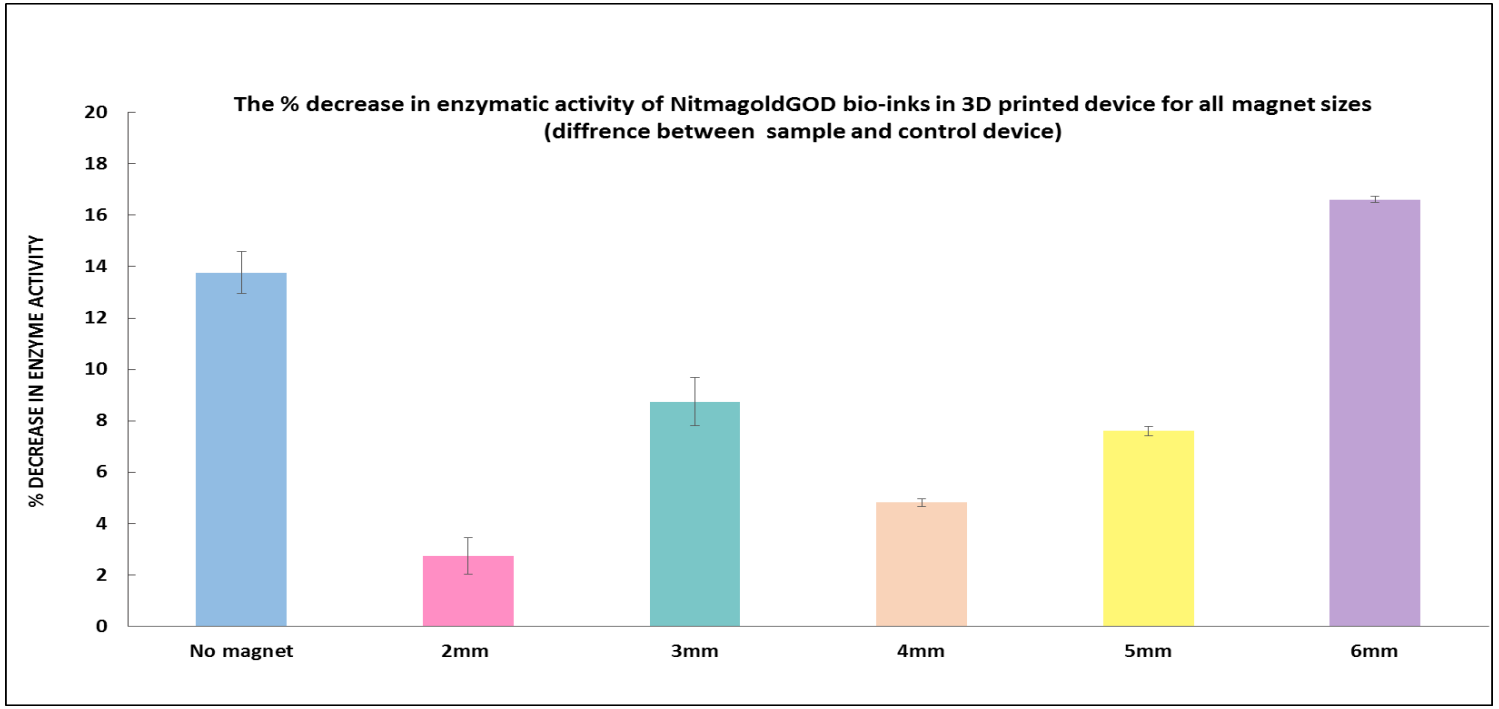

Figure 6.6| **Assessing the influence of magnet on the enzymatic activity of NitmagoldGOD as a bio-ink in ABS 3D printed device**. The bar chart represents the % decrease in enzymatic activity of NitmagoldGOD bio-inks in 3D printed device for all magnet sizes (difference between sample and control device). Error bars on all points represent standard deviations for n = 6.

Figure 6.6 shows the highest percentage decrease in enzyme activity for the 6 mm magnet was 17% which implies that approximately 17% of NitmagoldGOD is bound to the surface of the 3D printed devices. However, the study of devices without magnets had the next highest percentage decrease in enzyme activity of 14%. As a result, it can be concluded that a negligible amount of NitmagoldGOD bio-ink was bound to the 3D print due to the influence of the magnet.

6.4 Binding studies of the NitmagoldGOD binding to the surface of 3D printed devices

A binding study was performed to explore further if NitmagoldGOD was bound to the surface of the 3D printed device in the presence of 2- 6 mm diameter magnets. The assessment was performed by detecting the absorbance of an incubated mixture of NitmagoldGOD and buffer solution in the 3D printed device after 1 hour as detailed in Section 2.12.3.8. If NitmagoldGOD is drawn by a magnet and bound to the 3D print, there should not be any UV-Vis absorbance at 535 nm to suggest the presence of NitmagoldGOD in solution. For comparison, the procedure was done in a 3D printed device with no magnet inserted. The UV-Vis spectra were detected for all of these samples are presented in Figure 6.7 which shows the absorbance of NitmagoldGOD prepared in the plastic cuvette is higher than the absorbance detected for similar mixture prepared in 3D print. This means some of the NitmagoldGOD are bound to the surface of the 3D printed device. The absorbance for the NitmagoldGOD in the plastic cuvette is 0.13 Au where in the 3D printed device ranges from 0.075-0.085 Au. This means that approximately 50% of the NitmagoldGOD is bound to the surface of the 3D printed devices.

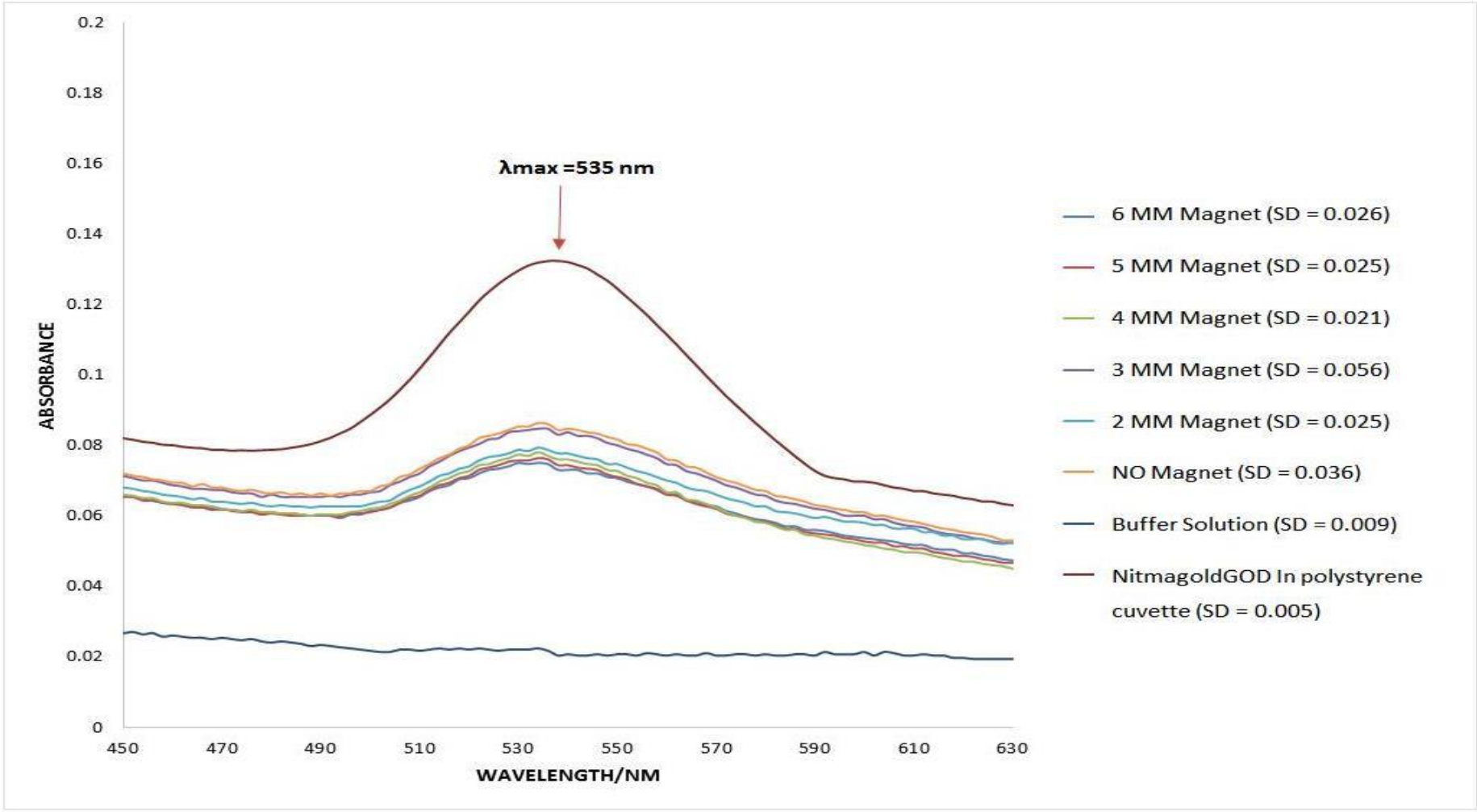

Figure 6.7|**The UV-Vis spectra of the NitmagoldGOD for all magnet sizes binding assessment.** The spectra of buffer solution, NitmagoldGOD are also presented. The standard deviations (SD) of absorbance of three repeats at λ_{max} 535 nm for 50 nm gold nanoparticles are presented next to legends.

Figure 6.7 shows the lowest absorbance value of 0.075 Au for the NitmagoldGOD in a 3D printed device with 6 mm diameter magnet and the highest absorbance of 0.085 Au for a device with no magnet. These data suggest the magnet has a small influence on binding NitmagoldGOD to the 3D print. Absorbance corresponding to the binding of NitmagoldGOD to 3D print was detected in decreasing order for devices with 5 mm, 4 mm, 2 mm and 3 mm diameter magnets.

The conclusion drawn from the NitmagoldGOD studies is that a negligible amount of NitmagoldGOD bio-ink is bound to the 3D print without use of a magnet in the device. The NitmagoldGOD bio-ink binding increases when a 6 mm magnet was used, however, the amount of binding is not enough when a NitmagoldGOD bio-ink enzymatic assay was performed in the 3D printed devices as detailed in Section 6.3. There is also the possibility that during assessing NitmagoldGOD bio-inks' enzymatic activity, GOD dissociated from the Nitmagold into the solution. This makes the immobilisation of the GOD or HRP enzyme by a magnet sing Nitmagold unsuitable for achieving key objective 5b.

6.5 Developing GODDynabead bio-inks as a route to make bio-inks for FDM 3D printed bio-devices

Magnetic Dynabeads were used as a route to make and immobilise bio-inks to the surface of 3D printed bio-devices again using a magnet in the device.
M280 Tosylactivated Dynabeads^{TM} were used as an alternative technique to make bio-ink since they are easy to use, bind to proteins with high affinity, have specifically defined surfaces to allow for efficient capture, separation and downstream handling using a magnet (Zhang, Xu and Chen, 2006). Moreover, Dynabeads are used in a large

number of applications such as direct/indirect isolation of proteins/peptides, and other target molecules (Kurlyandskaya and Levit, 2005) (Nitzsche, Ruhnow and Diez, 2008). Dynabeads have also been used in an immunoassay on biosensor for the detection of biomarkers (Yang *et al.*, 2015). These characteristics make them suitable to be used in this thesis.

The GODDynabeads was prepared by covalently coupling GOD protein to Dynabeads as detailed in Section 2.12.4. To determine if the enzyme retains activity after binding to Dynabeads and to ensure if the equilibrium reaction point is reached in one hour, the enzymatic activity of GODDynabeads was assessed using the method detailed in Section 2.12.4.1.3. The absorbance time course plots of GODDynabead activities are plotted in Figure 6.8.

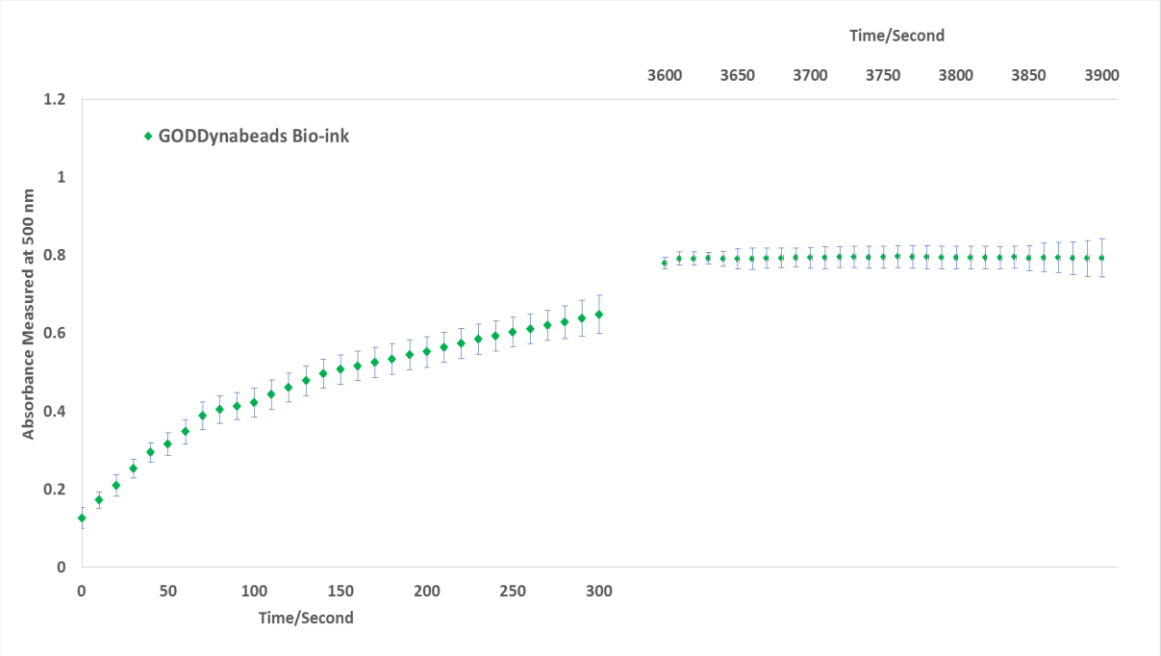

Figure 6.8| **Absorbance time course plots, analysis of GODDynabeads Bio-ink enzymatic activity at room temperature in polystyrene cuvette.** The graph represents the absorbance of GOD assay samples measured at 500 nm, immediately at the start of the reaction and the absorbance measured at t = 3600 second. Error bars on all points represent standard deviations for n = 3.

The data in Figure 6.8 show that the enzymatic activity of the GODDynabeads bio-ink is not inhibited after binding since the change in absorbance in response to the activity of the enzyme was detected. At t = 3600 almost no positive change in absorbance was detected, which suggested that an equilibrium point had been reached. From the plot, the enzyme activity of GODDynabeads in test samples was calculated. The GODDynabead enzyme activities when detecting 5.0 mM glucose in solution at $t \leq 300$ and $t \leq 3600$ were 0.069 ± 0.006 U/mL and 0.106 ± 0.004 U/mL, respectively.

In conclusion, this assessment showed the GOD enzyme retained activity after coupling to Dynabeads and allowed quantification of glucose in solution. This assessment can be used as a comparison guide to identify the accuracy of enzymatic analysis in 3D printing devices for immobilisation assay.

6.5.1 Immobilising GODDynabead bio-inks by a magnet to the surface of 3D printed devices

The enzymatic activity of GODDynabeads bio-inks in 3D printed devices was assessed as described in Section 2.12.4.2. The enzymatic assay was carried out in the presence of 6 mm diameter magnet size in 3D printed bio-device. The enzymatic activity of the GODDynabeads was determined after a minimum of one hour to ensure the equilibrium point was reached to allow a reliable spectrophotometric determination of GOD activity. Figure 6.9 shows the data obtained for assessing the immobilisation of GODDynabead bio-inks in ABS 3D printed devices along with control study for comparison.

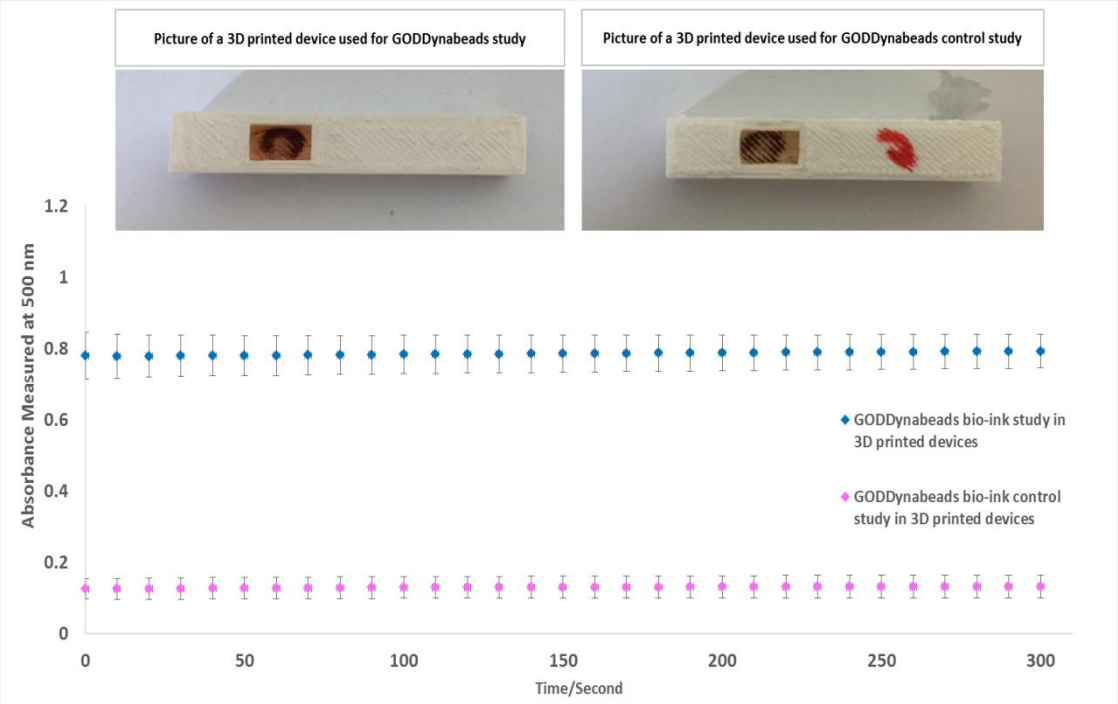

Figure 6.9| **Immobilisation assessment of GODDynabeads bio-inks to ABS 3D printed devices.** The graph represents the absorbance of a GOD assay measured at 500 nm at equilibrium. Error bars on all points represent standard deviations for n = 3.

Figure 6.9 shows an absorbance of 0.8 Au which correlates with the GODDynabeads' enzymatic activity in 3D printed ABS devices. This means that the GODDynabeads' activity is not inhibited in a 3D printed device since this is comparable to the absorbance detected for enzyme activity assessed in a polystyrene cuvette (Figure 6.8).

Figure 6.9 also shows an absorbance of 0.15 Au which correlates with the enzymatic activity for the GODDynabead bio-ink control study (see Figure 5.14 for detail on experimental preparation). The difference in the absorbance values detected between GODDynabeads and control study suggests successful immobilisation of GODDynabeads to the surface of a 3D printed device.

From the data obtained, the enzyme activity of GODDynabead bio-ink for each study was calculated from Figure 6.9. The enzyme activity for GODDynabead bio-ink and control studies were 0.106 ± 0.008 U/mL and 0.018 ± 0.006 U/mL, respectively. The difference between the two is approximately 83%.

Overall, it can be concluded that approximately 83% of the bio-ink added to 3D printed devices was immobilised to the surface of 3D printed bio-devices by a 6 mm diameter magnet but not fully since a negligible enzyme activity of 0.018 ± 0.006 U/mL is detected for the control.

6.5.1.2 Evaluating GODDynabead bio-inks as a method to immobilize enzymes in a 3D printed device after washing with buffer solution

To validate the binding of GODDynabeads bio-ink to the surface of the 3D printed device in the presence of a 6 mm diameter magnet. The experiment detailed in Section 6.5.1 was repeated with slight modification. The enzymatic activity of the DynabeadsGOD was assessed after washing with a buffer solution (Buffer C, Section 2.1) to look for residual GOD activity as detailed in Section 2.12.4.2.

Figure 6.10 shows the absorbance time course plots of the GODDynabeads bio-ink enzymatic activity after washing with a buffer solution along with control study for comparison.

Figure 6.10 shows a lower absorbance for the GODDynabead bio-ink control study when compared to the standard assay in 3D printed devices. This means GODDynabeads are immobilised to a surface of the 3D printed devices tightly and do not wash off or lose activity after washing with a buffer solution.

The calculated enzyme activities for GODDynabead bio-ink and control studies were 0.106 ± 0.011 U/mL and 0.014 ± 0.007 U/mL, respectively, which is comparable to the value obtained in Section 6.5.1. The difference between the enzymatic activity of GODDynabead bio-ink and the control is approximately 87%.

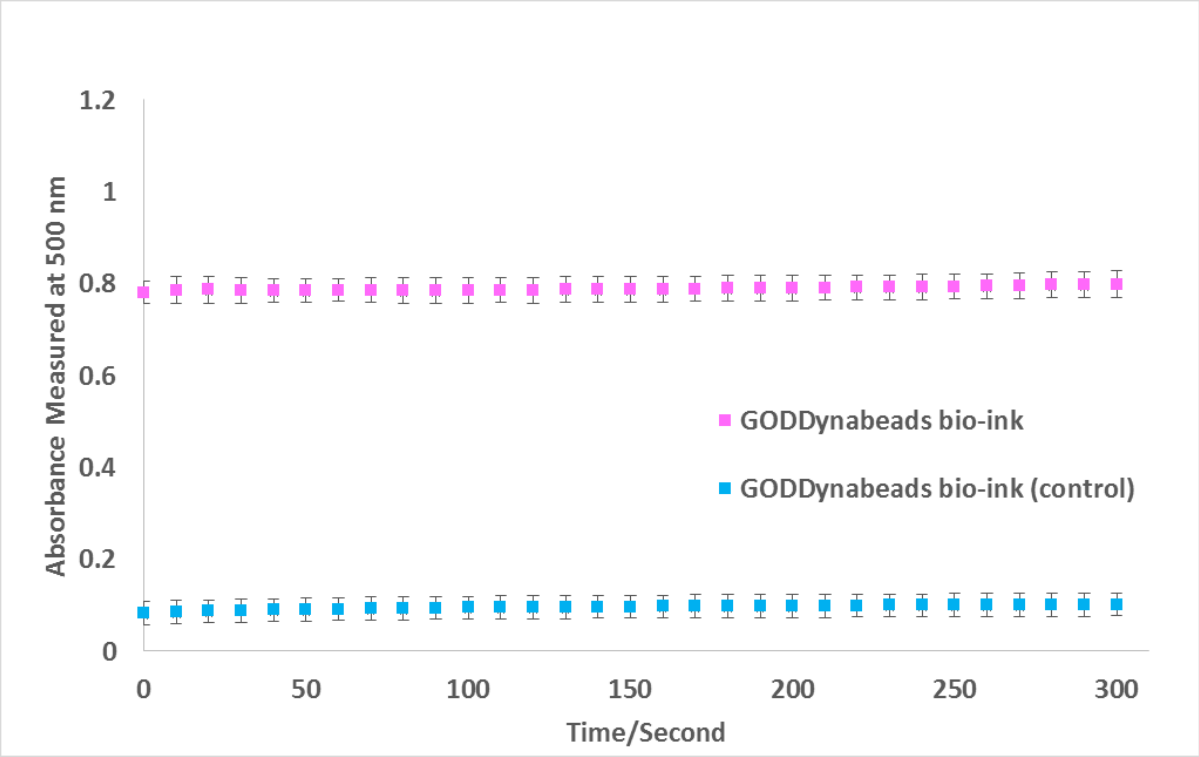

Figure 6.10| **Immobilisation assessment of GODDynabeads bio-inks to ABS 3D printed devices after washing with a buffer solution.** The graph represents the absorbance of a GOD assay measured at 500 nm, after a minimum of one hour (equilibrium). Error bars on all points represent standard deviations (SD) of three repeats, n=3.

To further verify the immobilisation of the GODDynabead bio-ink to the surface of the 3D printed device the GODDynabeads bio-ink control was repeated but with the absorbance of the GOD assay before and after addition of glucose into the mixture detected. Detecting absorbance before and after glucose addition allowed the determination of any GODDynabead release into the mixture. Figure 6.11 shows the absorbance time course plots of the GODDynabead bio-ink control assay before and after glucose addition. No significant change in absorbance for the GODDynabead control assay before and after glucose addition was found.

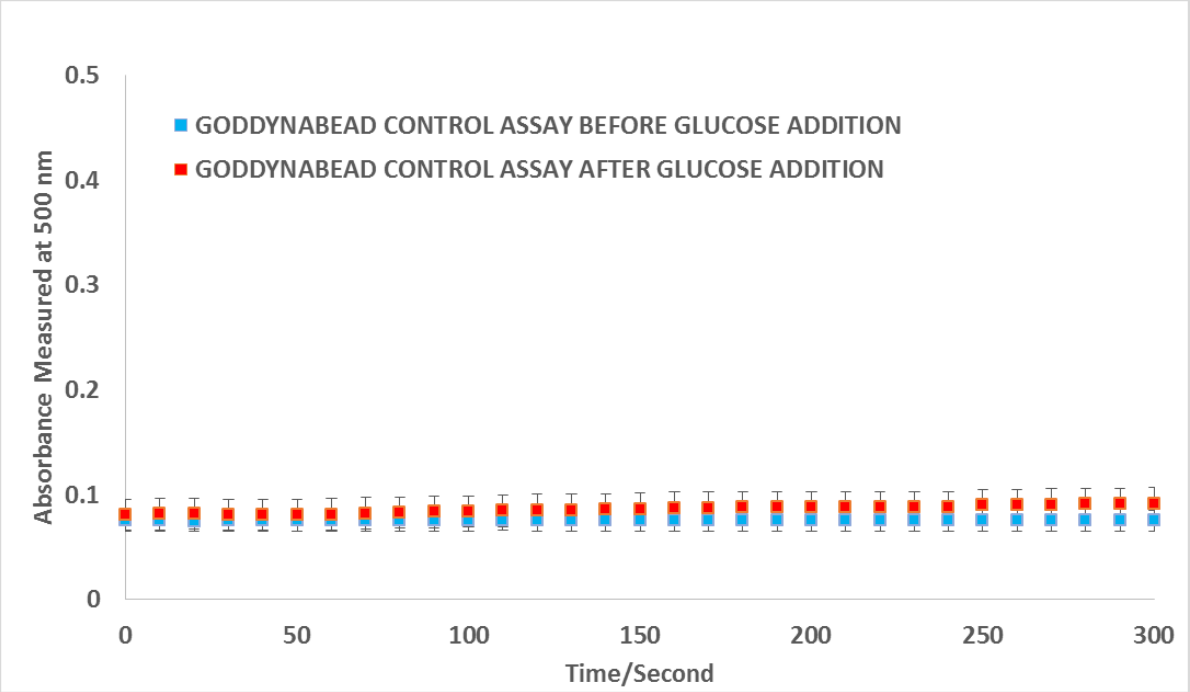

Figure 6.11| **Immobilisation assessment of GODDynabeads bio-inks control assay in ABS 3D printed devices after washing with a buffer solution.** The graph represents the absorbance of GOD assay measured at 500 nm, after a minimum of one hour (equilibrium). Error bars on all points represent standard deviations for n = 6.

The GODDynabead bio-ink control assay enzyme calculated activity before and after the addition of glucose into the mixture was the same with the value of 0.010 ± 0.007 U/mL. As a result, it can be concluded that GODDynabead bio-ink can be immobilised on the surface of ABS 3D printed devices by a 6 mm diameter magnet. The negligible difference in the absorbance values detected for the control assay was assumed to be due to the actual colour of the Dynabeads.

6.5.2 Evaluating HRPDynabead bio-inks as a method to immobilise enzymes in a 3D printed device

The HRPDynabeads bio-inks were prepared using a similar method to GODDynabeads bio-inks as described in Section 2.12.4 but substituting GOD with the HRP enzyme.

The aim was to determine if Dynabeads could be used to make additional bio-ink for FDM 3D printing and glucose biosensor production.

As in Section 6.5, the enzymatic activity of HRPDynabeads was assessed in a polystyrene cuvette using the method detailed in Section 2.12.4.1.3. This was followed by assessing immobilisation of HRPDynabead bio-inks to the surface of 3D printed bio-devices by a 6 mm diameter magnet as detailed in Section 2.12.4.2.

The absorbance time course plots of the enzymatic activities of HRPDynabeads bio-ink in the polystyrene cuvette and 3D printed device are presented in Figures 6.12 and 6.13.

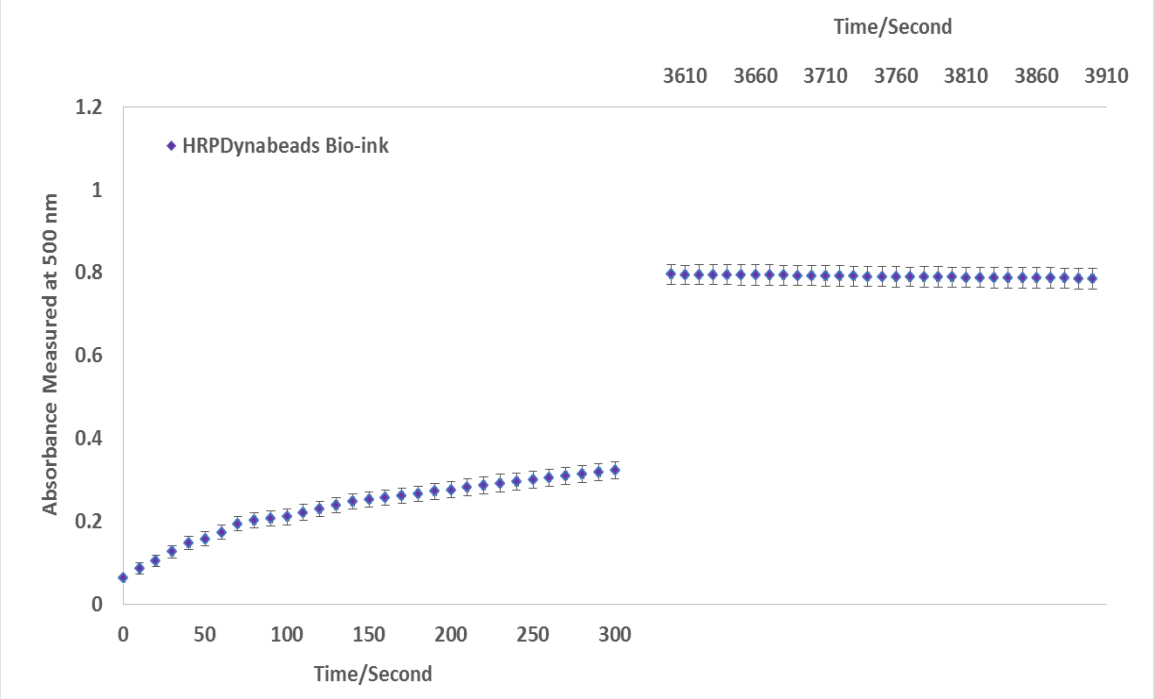

Figure 6.12| **Absorption time course plots, analysis of HRPDynabeads bio-ink enzymatic activity at room temperature in polystyrene cuvette.** The graph represents the absorbance of GOD assay samples measured at 500 nm, immediately at the start of the reaction and at t = 3600 seconds. Error bars on all points represent standard deviations for n = 3.

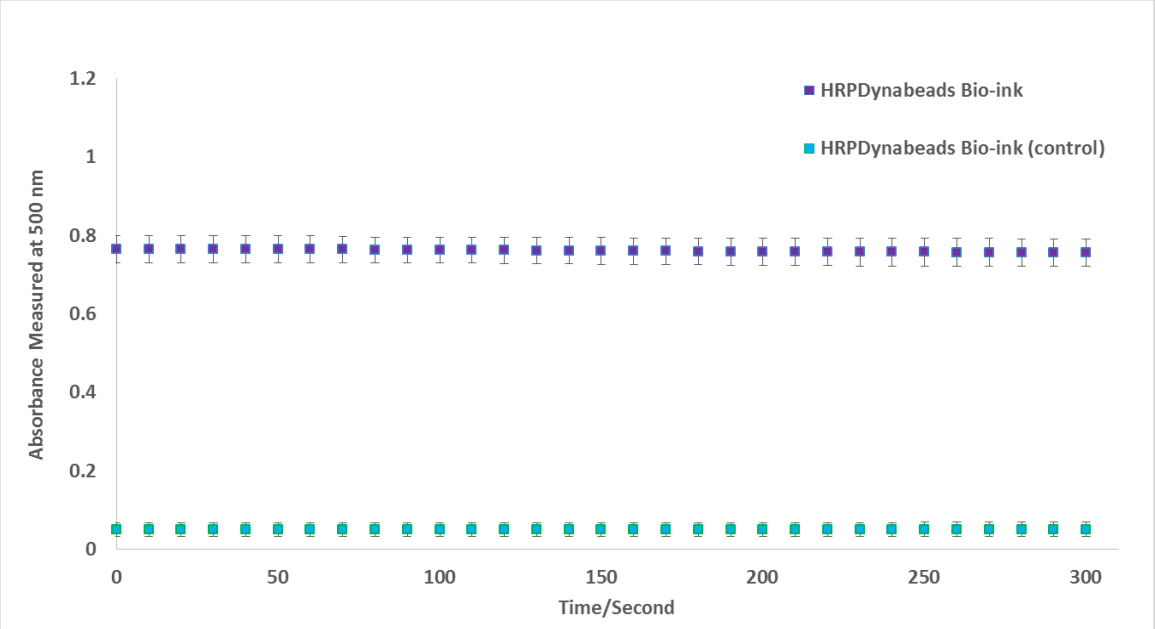

Figure 6.13| **Immobilisation assessment of HRPDynabeads bio-inks in ABS 3D printed devices after washing with a buffer solution.** The graph represents the absorbance of HRP bio-ink assay measured at 500 nm, after reaching equilibrium at 1 hour. Error bars on all points represent standard deviations for n = 3.

The data shown in Figure 6.12 show that the enzymatic activity of the HRPDynabead bio-ink is not inhibited after binding since the change in absorbance in respond to the activity of the enzyme was detected. At t = 3600 almost no positive change in absorbance was detected, which suggested that equilibrium has reached. From Figure 6.12, the enzyme activity of HRPDynabeads in test samples was calculated. The HRPDynabeads' enzyme activity detected in 5.0 mM glucose solution at $t \leq 300$ and $t \leq 3600$ were 0.035 ± 0.009 U/mL and 0.105 ± 0.009 U/mL, respectively.

Figure 6.13 shows lower absorbance for the HRPDynabead bio-ink control study when compared to the standard assay in 3D printed devices. This means the HRPDynabead bio-ink is immobilised onto the surface of 3D printed devices strongly and is not washed off or loses activity after washing with a buffer solution.

The enzyme activity for HRPDynabead bio-ink and control studies were 0.102 ± 0.013 U/ML and 0.007 ± 0.006 U/ML, respectively. The difference between the enzymatic activity of HRPDynabead bio-ink and control is approximately 93%.

As in Section 6.5.1.2, to further verify the immobilisation of the HRPDynabead bio-ink the control assay absorbance before and after addition of glucose into the mixture was determined. Figure 6.14 shows the absorbance time course plots of the HRPDynabead bio-ink control assay before and after glucose addition.

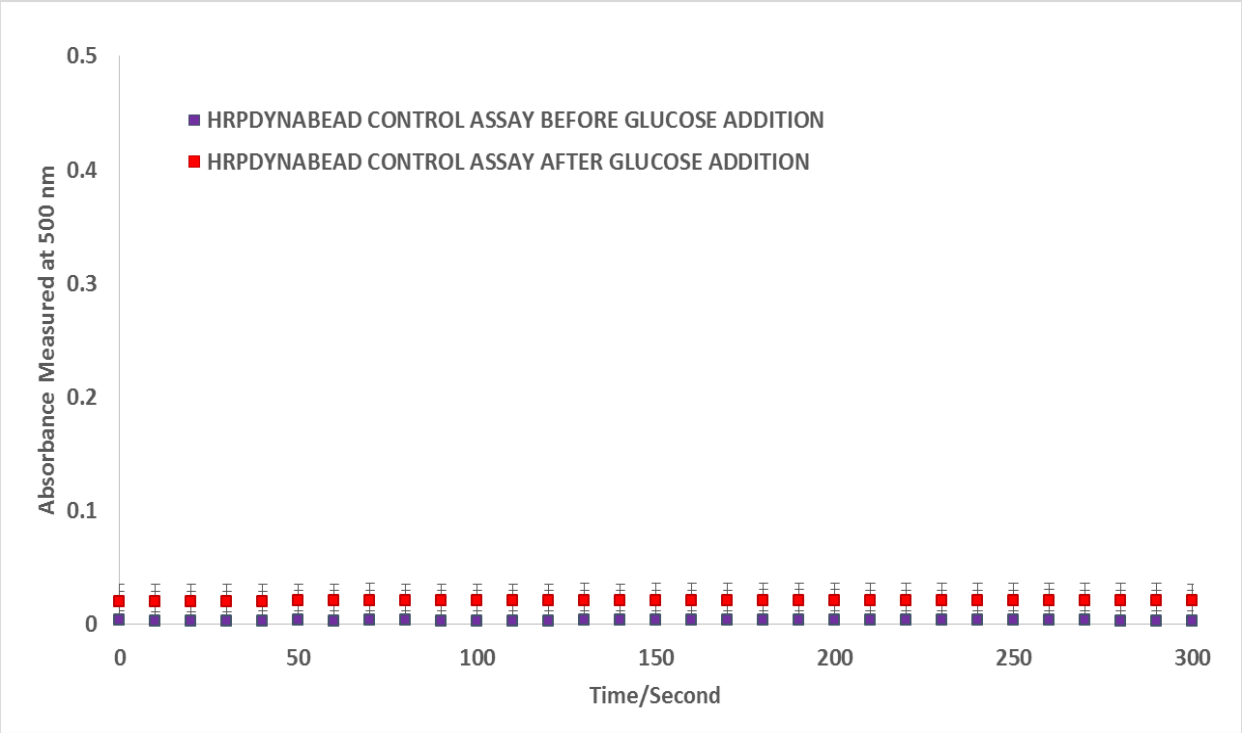

Figure 6.14| **Immobilisation assessment of HRPDynabeads bio-inks control assay in ABS 3D printed devices after washing with a buffer solution.** The graph represents the absorbance measured at 500 nm at one hour equilibrium. Error bars on all points represent standard deviations for n = 6.

Figure 6.14 shows no significant change in absorbance for HRPDynabead bio-ink control assays before and after glucose addition. The calculated HRPDynabead bio-ink control assays enzyme activity before and after the addition of glucose into the mixture was exactly the same with the value of 0.003 ± 0.001 U/mL.

Overall, similar conclusions to the GODDynabead study in Section 6.5.1 were found, which verifies that Dynabeads are suitable as a medium to immobilise bio-inks by using a 6 mm diameter magnet to the surface of 3D printed bio-devices.

6.6 Assaying the activity of GODDynabead and HRPDynabead bio-ink in 3D printed devices after decanting by syringe extruder

One of the key objectives (iii) in this thesis was to develop the protocols to be able to decant biomolecule to the surface of the 3D-prints in such a way that they retain their biological activity. Previously, in Chapter 4, a MakerBot replicator 2X 3D printer was modified to allow liquid deposition through syringe extrusion on 3D print. A promising protocol for decanting liquid droplets to a surface of 3D printed design and into a microfluidic device by using MakerBot replicator 2X 3D printer was demonstrated and tested. A significant aspect that was proven in the study was that the modified syringe extruder could decant liquid at room temperature with the absence of physical contact between the printhead, and printed support makes it possible to deposit materials on contact sensitive substrates. However, the performance of the device with an active bio-ink to achieve objective 4a was not assessed. The goal is to determine if the modified MakerBot Replicator 2X 3D printer can decant bio-ink into 3D printing devices where no, or minimum, heat damage is made to the active bio-inks during or after the 3D printing process. To assess this the parallel 3D printing and liquid manipulation technique demonstrated in Chapter 4, Sections 4.3.2.1-4.3.3.4, was applied. The GODDynabead and HRP Dynabead bio-inks were decanted into 3D printing devices under controlled command as described in Section 2.12.4.4 and their enzymatic activity was assessed. Figure 6.15 shows the absorbance time course plots of the bio-inks after decanting into the 3D printed devices.

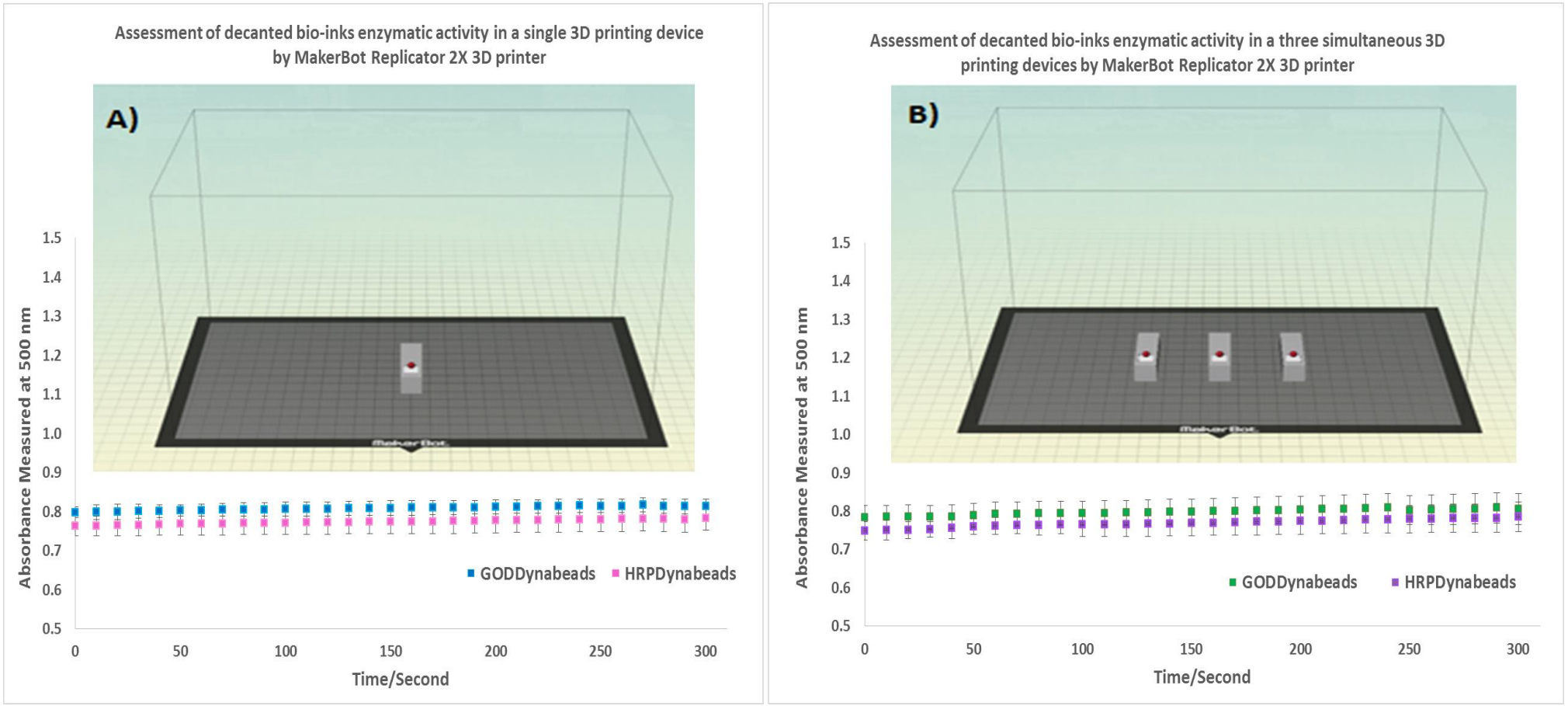

Figure 6.15| **Absorbance time course plots of decanted GODDynabeads and HRP Dynabeads bio-inks by syringe extruder into 3D printed bio-devices.** The graph represents the absorbance of a GOD assay measured at 500 nm at equilibrium. A) Represent the data for single printing bio-device and liquid bio-ink manipulation. B) Represents the data for triple printing bio-device and liquid bio-ink manipulation. Error bars on all points represent standard deviations for n = 6 for individual bio-inks. The print times for parallel printing of a single bio-device was15 minutes and a triple bio-device was 45 minutes.

Figure 6.15 shows an absorbance of 0.78-0.80 Au, corresponding to the GODDynabeads' and HRPDynabeads' enzymatic activities, assessed in 3D printed ABS devices. This is comparable to the absorbance detected in Section 5.5 when assessing the GODDynabeads' and HRPDynabeads' enzymatic activity. Accordingly, it can be established bio-inks activity is not inhibited after printing. It is also clear that the bio-inks are not affected by the heated bed of the 3D printer set at 37°C after they have been decanted into fabricating devices.

From the absorbance data in Figure 6.15, the enzyme activities of GODDynabead and HRPDynabead bio-inks for were calculated for each assay. The enzyme activity of decanted GODDynabead and HRPDynabead bio-ink in the single printing bio-device study were 0.107 ± 0.009 U/mL and 0.105 ± 0.011 U/mL, respectively. The enzyme activity of decanted GODDynabead and HRPDynabead bio-inks in the triply printed bio-device assessment were 0.106 ± 0.021 U/mL and 0.104 ± 0.019 U/mL, respectively. The similarity in values obtained for enzymatic activities of the decanted bio-inks suggests that decanting of the bio-ink droplet in 3D printed devices by syringe extruder was reproducible.

To assess the reproducibility of syringe extruder to decant bio-inks in a specific position and into 3D printed devices the printing process and liquid manipulation was observed. Two out of the 12 single devices failed since the liquid bio-ink was stuck to the syringe tip and was not decanted into the 3D print.

In the triply printed assessment, four out of 12 repeats failed. Two of these were because of wrapping and lifting of the 3D printing device halfway through from the platform. Consequently, the bio-ink droplet was decanted on the platform and not into the 3D print. The other remaining two multi-printing assessment failed since a droplet of the liquid was not ejected and remained stuck to the syringe extruder needle.

In conclusion, this study shows that a syringe extruder on the 3D printing device allows specific biological liquid inks to be delivered in such a way that biological molecules retain their activity.

The formulated GODDynabead and HRPDynabead bio-inks are suitable for FDM 3D printing since their activities are not inhibited by platform temperature after printing. As a result, it can be concluded that automated fabricating bio-devices can be made by a FDM modified 3D printer. The advantage of this technology is that it can replace manual fluids handling of pipettors for biosensing application (Zhou, 2017).

6.7 Manipulation of immobilised GODDynabead and HRPDynabead bio-inks inside micro-channels to perform two-step coupled assays

The methods presented in Section 6.5 for enzyme immobilisation inside bio-devices may enable multistep chemical reactions within one lab-on-a-chip bio-devices. Substrates could, in theory, be introduced over the first immobilised enzyme, and the products may then continue downstream to additional sets of immobilised enzymes for further reactions. This approach could enable complex multistep syntheses to be performed. To demonstrate this principle with the chemistry developed in Section 6.5, a simple two-step process, often exploited for the detection of glucose, was designed. A new bio-device compatible for this experiment was designed and fabricated for this assessment as detailed in Section 2.12.4.3.1. A schematic diagram of the bio-device made to perform the two-step chemical reaction is shown in Figure 6.16. The 3D printed bi-device was further optimised for UV-Vis spectroscopy through coating with XTC-3D coating as detailed in Section 2.12.6.

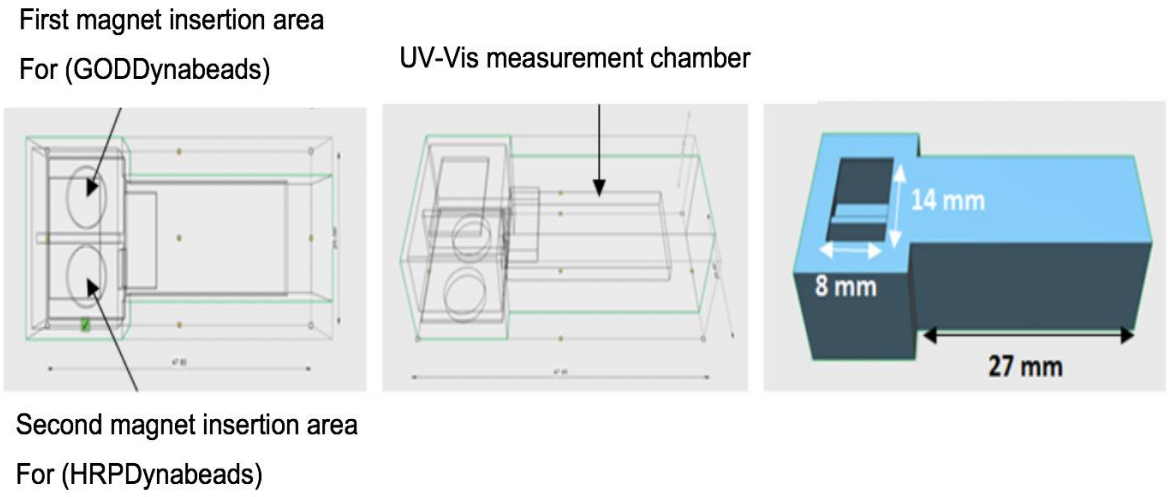

Figure 6.16| **Schematic CAD diagram of the 3D printed device used for the coupled set chemical reactions, optimised designed for UV-Vis spectroscopy;** 45 minutes print time. Contains two spaces for 6 mm magnets insertion, each chamber has an internal volume space of max 600 µL. The wall thickness of the absorbance measuring area of the device was 0.4 mm with a path length of 10 mm and 500 µL chamber volumes.

Enzymatic activity of immobilised bio-inks inside the micro-channels performed in two-step were as detailed in Section 2.12.4.3. Figure 6.17 shows the absorbance time course plots of the GODDynabead and HRPDynabead bio-inks GOD-coupled assay. The enzymatic activity of the coupled chemical reaction was also determined after two hours to ensure the reaction equilibrium point was reached. Figure 6.17 shows consistent absorbance values for the GOD assay measured after 1 hour for a 5 mmol/L glucose solution were obtained, which suggests equilibrium has been reached. No significant difference between the re-measured GOD assay absorbance after 2 hours was detected when compared to this sample, which suggests equilibrium is reached after 1 hour for two-step chemical reaction. In conclusion, this data suggest that the assessment time is sufficient for quantifying accurately a biological relevant of 5 mmol/L glucose solution within an hour.

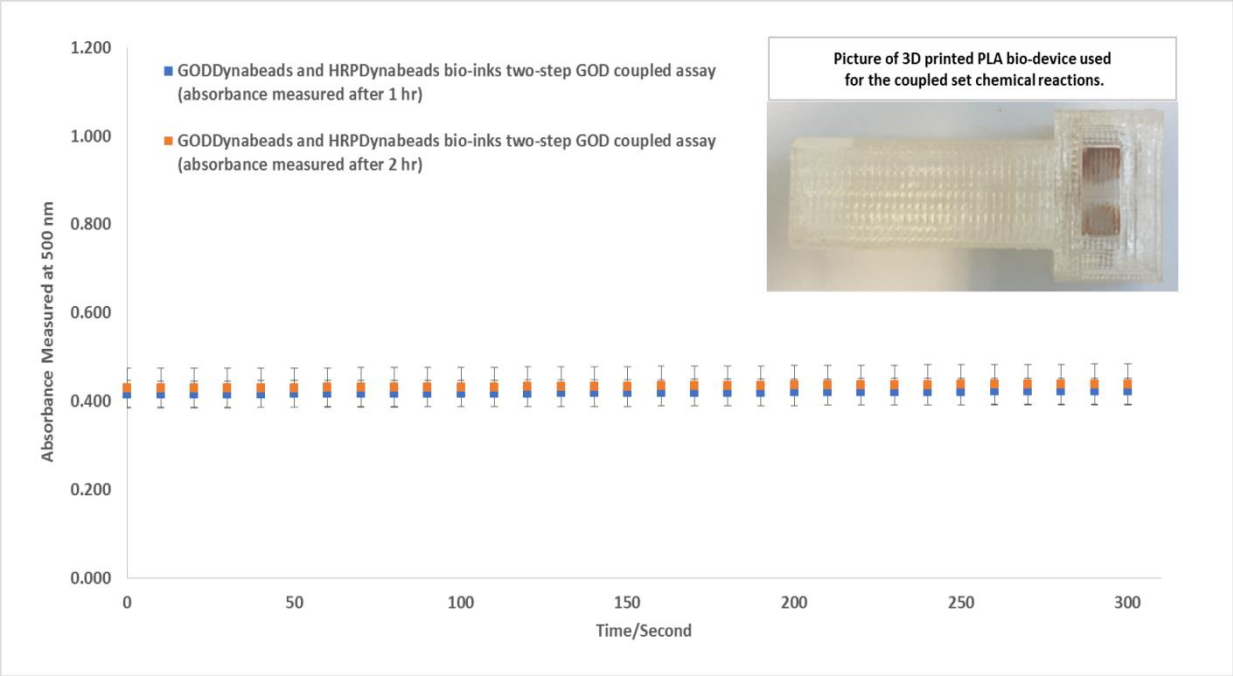

Figure 6.17| **Absorbance time course plot for the enzymatic assessment of bio-inks by performing two-step GOD coupled assay inside of the 3D printed PLA bio-devices.** Assay for detecting 5.0 mM glucose in solution. Error bars represent standard deviations for n = 3.

The equilibrium enzyme activity for the bio-ink of the two-step chemical reaction was 0.056 ± 0.016 U/mL. This value is slightly lower than that obtained in Section 6.5 for enzyme activity of one immobilised bio-ink in 3D print. This difference in absorbance was assumed to be due to the transparency of 3D printed PLA bio-device that was used in this assay. Next, to determine if it is possible to quantify the glucose content accurately in a mixture by performing two-step GOD coupled assays, the GOD enzymatic assay was performed for glucose solutions over the 0-13 mmol/L range. As a control, the experiment was also performed in polystyrene cuvette as detailed in Section 2.12.4.3.2.

Figure 6.18 shows the absorbance plot of two-step GOD-coupled assays for glucose solutions in the 0-13 mmol/L range assessed in PLA 3D printed device and polystyrene cuvette.

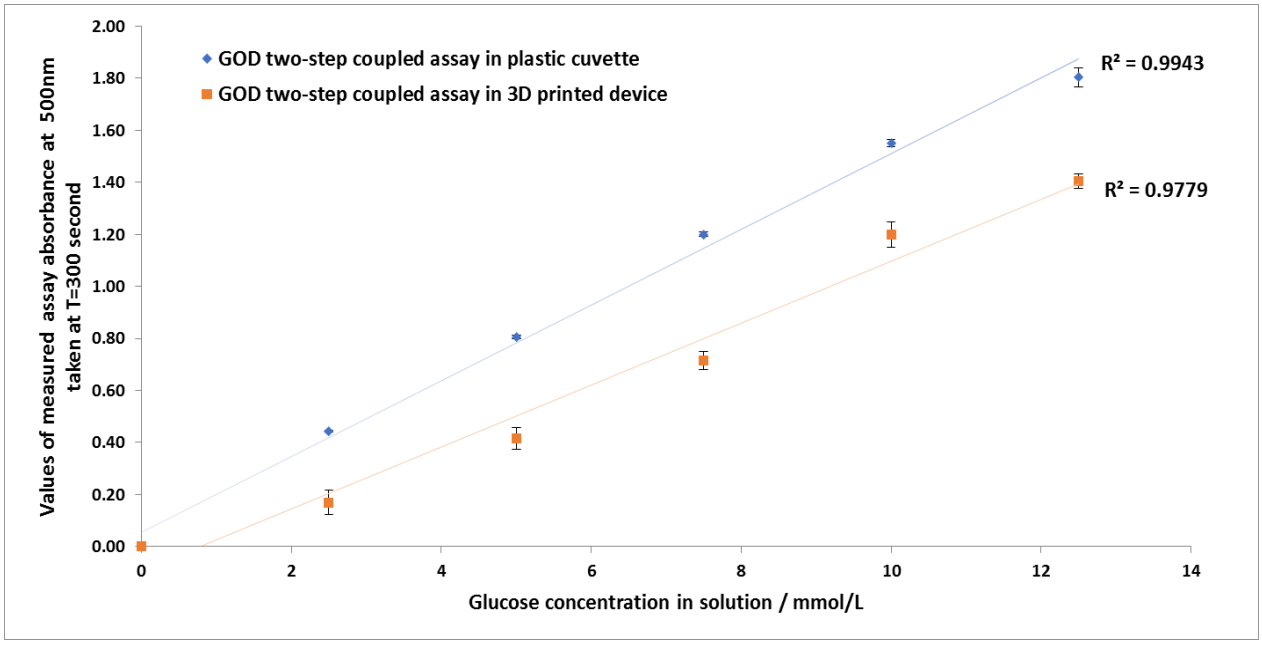

Figure 6.18| **Absorbance of two-step GOD coupled assay of glucose solution standards range from (0-13 mmol/L) detected at λ_{max} 500.** Data represent the assessment absorbance at different glucose concentration for the assay completed in the plastic cuvette and 3D printed devices. The absorbance was taken at t = 300 seconds from the absorbance measuring time plot obtained for each assay that is not presented here. The data represent the mean values for n = 3.

Figure 6.18 shows that as the glucose concentration increases, the absorbance corresponding to the change in colour of the enzymatic assay solution increases.

The glucose assay regression line has the R^2 value of 0.9943 for the plastic cuvette experiment and 0.978 for the 3D printed device experiment which suggests a good linearity response at 500 nm in both cases.

This data also suggest that the immobilised GODDynabead and HRPDynabead bio-inks in 3D printed PLA bio-device is sufficient to accurately quantifying a glucose solution in the biologically relevant range of 0-12 mmol/L within an hour.

Figure 6.18 also shows a higher absorbance value for the glucose standard in a plastic cuvette compared to the 3D printed device. However, this is assumed to be due to the transparency of the 3D printed device as will be explored more in Chapter 7. Overall it can be concluded that reliable spectrophotometric determination multi-step colorimetric glucose assay can be conducted in the 3D printed PLA bio-device.

6.8 Discussion and Conclusions

The increase in the cost of health care services such as the NHS, due to increases in the aging population, diabetes epidemic and obesity epidemic, encourages innovations in the cost of point-of-care testing (Christenson, 2007). New developments in economical analytical screening tools such as lab-on-a-chip (Mirasoli *et al.*, 2014) and microfluidic analysis (Livak-Dahl, Sinn and Burns, 2011) systems to detect patient glucose levels, focus on miniaturisation and disposability to improve performance, speed, and portability is require in high demand for health care services (Tothill *et al.*, 2017). 3D Bioprinting of biological molecules offers great potential to automate the fabrication of fluid containing devices with precise control of structure, sample volume, mechanics and biological matter, e.g. enzymatic components, proteins, and cells (Ji and Guvendiren, 2017). As discussed in the literature, FDM 3D printing offers the users the advantage of designing, testing and constructing bespoke 3D microfluidic devices and plastic prototypes targeted to their own individual application. A good example is integrated low cost transparent microfluidic devices printed by FDM PLA 3D filament that allow detection of colorimetric enzymatic glucose level through a cascade assay (Tothill *et al.*, 2017). However, to allow automation and to further reduce cost and time for screening, improved systems for biosensor fabrication are required. The lack of suitable bio-inks has emerged as one of the most significant obstacles to the advancement of using FDM 3D bioprinting for microfluidic research. There are many reports on the use of 3D printers for application in biotechnology where the researchers aimed at developing new bioinks (Jose *et al.*, 2016)(Gopinathan and Noh, 2018). Currently, there are no reports on the development of low viscosity bio-inks for FDM 3D printers (Khatiwala *et al.*, 2012)(Jose *et al.*, 2016). This technology could help to reduce the cost of biosensor production.

Therefore, the main target of this research was on the development of specific bio-inks for FDM 3D printers where a good application is to make glucose biosensors. Since

glucose sensors are used in clinical biochemistry, environmental, and food analysis they make up 85 % of all sensors in the healthcare market (Wang, 2008).

To prepare inexpensive, rapid and reliable devices able to determine glucose in solution, this chapter accomplished three goals:

1) the development and assessment of magnetic bio-inks immobilisation on a selected surface of FDM 3D printed device.

2) an assessment of the activity of bio-ink after decanting by syringe extruder on the modified 3D printer into 3D printing bio-device

3) immobilisation of bio-inks inside 3D printed biosensor device that is optimised for UV visible spectroscopy to perform a coupled set of chemical reactions.

6.8.1 Development and assessment of magnetic bio-inks immobilisation on a selected surface of FDM 3D printed device.

In this work, a set of enzymatic bio-inks for FDM 3D printing technology has been developed. Initially, bio-inks were made using Nitmagold magnetic nanoparticles. Nitmagold particles were used since they are highly versatile (Liu *et al.*, 2013)(Kouassi, 2011)(Tintoré *et al.*, 2015), used widely in analytical and biomedical applications, specifically for glucose sensing (Rossi, Quach and Rosenzweig, 2004). The optical and magnetic properties of the Nitmagold particles can be tuned to tailored to applications by changing their charge, size, shape, gold shell thickness and surface modification (Moraes Silva *et al.*, 2016).

A magnet was used to immobilise the NitmagoldGOD and HRP bio-inks onto the surface of 3D printed bio-devices. This integrated application is frequently used in biomedical applications to gain control over the magnetic nanoparticles (Stanciu *et al.*, 2009). Magnetic nanoparticles to surface-modify 3D printed nylon substrates to

promote successful cell growth by keeping the cell intact (Jackson *et al.*, 2018). Another study used the magnetic nanoparticles to prepare a 3D printing ink formulation which gave better control over the shape of the 3D construct (Kokkinis, Schaffner and Studart, 2015). In this work, it was determined that a magnet could control the Nitmagold and partially bind NitmagoldGOD and HRP in a 3D printed device. However, the target was to see considerable binding of the bio-inks to the surface of the 3D print with support of small magnet was not achieved.

Next bio-inks for FDM 3D printing were developed using GODDynabeads and HRPDynabeads. Magnetic beads were used due to their large surface area, chemical and mechanical stability and suitable size for use in micro-channels (Zhang, Xu and Chen, 2006). Many recent reports also incorporated magnetic beads into microfluidic devices as enzyme supports since they can be appropriately positioned within microchannels using a mechanical barrier or magnetic devices (Gumpenberger *et al.*, 2006)(Kim *et al.*, 2006).

The GODDynabeads and HRPDynabeads bio-inks were immobilised to selected surfaces of an ABS 3D printed device by a 6 mm magnet. The immobilisation of bio-inks was confirmed by assessing the enzyme activity of GODDynabeads, and HRPDynabeads bio-inks in 3D printed ABS bio-devices. From this study, it was determined that the GODDynabeads or HRPDynabeads immobilised on the surface of the 3D printed devices did not lose their ability to bind the substrate and at the same time to form a product. The volume of GOD or HRPDynabead bio-inks that was immobilised in the device to detect glucose in solution was 35 µL which matches the volume of an immobilized enzyme that is used in the microfluidic system (Srinivasan, Pamula and Fair, 2004).

Choice of enzyme immobilisation technique depends mostly on the application such as long-term stability, stability at room temperature, work in flow conditions, ease of

preparation, etc. There is no universal standard method for enzyme immobilisation. There are also no reports on the immobilisation of bio-inks, such as enzymatic-magnetic beads, to the surface of a FDM 3D printed device. The only approach that is partially comparable to this technique is immobilisation of GOD glass microbeads and HRP in an entrapping hydrogel microarray for detecting glucose in a reaction (Kim, Lee and Koh, 2009). This analysis technique report is based on fluorescent intensity detection to investigate enzyme-substrate reactions and is different to the work reported here (Kim, Lee and Koh, 2009).

6.8.2 Assessing the activity of bio-ink after decanting by syringe extruder on the modified 3D printer into 3D printing bio-device

The enzymatic activity of GODDynabead bio-ink after decanting by syringe extruder into a single and multi 3D printed devices was determined. This assessment was accomplished to evaluate the reproducibility of the modified FDM device for deposition of bio-ink of desired quantity at a specific point in such a way that biological molecules retain their activity. It was also shown that bio-inks are not affected by the heated build platform of the 3D printer, once decanted into 3D printed devices using this methodological approach. It was shown that the modified 3D printer allows fabrication of reproducible single or multiple automated fluidic handling bio-device containing active biological molecules.

In conclusion, in this chapter, a new approach to deposit GOD and HRP enzymes by 3D printing technology to make glucose biosensor devices which is distinct from glucose sensors fabricated by piezoelectric inkjet printing (Setti *et al.*, 2007)(Settia *et al.*, 2005)(YUN *et al.*, 2011). The bio-inks were developed as a liquid to be decanted by syringe extruder on the modified FDM 3D printer. Functionalised GODDynabeads and HRPDynabeads bio-inks were developed in order to perform GOD enzymatic cascade reaction, suitable for glucose biosensing. This approach is a step towards creating an

open source, inexpensive and rapidly protocol for 3D-printed microfluidic and millifluidic biosensor devices, which can be used to perform glucose quantitation in solution.

6.8.3 Immobilisation of bio-inks inside 3D printed biosensor device that is optimised for UV visible spectroscopy to perform a coupled set of chemical reactions.

In this thesis, a simple two-step process often exploited for the detection of glucose in solution was designed. Immobilization of GODDynabeads and HRPDynabeads inside 3D printed transparent PLA bio-device afforded the opportunity to run multistep chemical reactions. This was confirmed through assessing the glucose solution range of 0-13 mmol/L in the PLA transparent devices.

The 3D printed biosensor device designed in this work was used to perform a multi-step colorimetric glucose assay, optimised for UV-Vis spectroscopy. This enables cheap fabrication of glucose biosensor devices for UV-Vis assays. Similar integrated FDM 3D printed fluidic systems optimised for UV-Vis have also been reported but not from PLA filament (Pisaruka and Dymond, 2016). There are reports of the fabrication and optimisation of a fused filament 3D-printed microfluidic platform (Tothill *et al.*, 2017), a low-cost microfluidic biosensor device with PLA filaments was made for UV-Vis that allows quantification of glucose in solution. However, in this thesis, a protocol has been developed such that bio-inks and a cheap FDM 3D printed glucose biosensor device can be used in a simple two-step process to detect glucose rather than costly PDMS printed microfluidic systems (Mao, Yang and Cremer, 2002).

This chapter also demonstrated how FDM 3D printing enables reproducible fabrication of rapid glucose biosensor device. Limitations currently exist with printing millifluidic and microfluidic systems using FDM 3D printers (Zhou, 2017) and on-demand printing

services, particularly print resolution, part to part variability and device with optical transparency. However, 3D printing machinery is rapidly improving due to considerable academic and industrial interest. These limitations could be overcome by an increase in 3D printing research interest as the technology develops.

In conclusion recent efforts to construct a glucose biosensor resulted in the establishment of miniaturized and highly sensitive devices reliable for routine assays (Vigneshvar *et al.*, 2016). However, high sensitivity is not a crucial parameter because glucose is presented in high levels in biological samples, e.g. blood, so the selectivity is a more important parameter for glucose detection (Huggett and Nixon, 1957) . Despite promising findings, further characterization of advanced technologies is necessary before determining whether the analytical figures of merit of the new sensors are significantly better than parameters of the current devices. One main require characteristic for glucose biosensor production is the immobilisation of the enzymes (as bio-recognition elements) on the surface of the device which was covered in this chapter. The immobilisation of enzymes on device enables repeated use of an enzyme, control over stability and release of hydrogen peroxide (Rocchitta *et al.*, 2016)(Guzik *et al.*, 2014)(Mohamad *et al.*, 2015).

CHAPTER 7

DEVELOPMENT OF 3D PRINTED BIOSENSORS FOR UV-VIS SPECTROSCOPY TO QUANTIFY LACTOSE

7.1 Introduction

Recent demands that high quality food products meet customer needs have opened up new interest in development of improved techniques for making lactose biosensor that are coupled with production processes for quality control and consumer assurance (Ammam and Fransaer, 2010).

Lactose is hydrolyzed by lactase to glucose and galactose, which are further metabolized. Lactase (β-Galactosidase) is produced in the cells of the epithelium of the small intestine. Lactose is one of the main constituents of humand and animal milk and is used today in a large number of foodstuff as well as in the pharmaceutical industry. However, the lactose-intolerant people are discouraged from consuming lactose-containing milk (Wilson, 2005). An excessive amount of lactose in blood indicates gastrointestinal malignancy. Effective control of the lactose in food stuffs is also important to those who are unable to digest lactose. The inability of humans to digest lactose has enormous health consequences, particularly among the poor population of the world where milk is the only economical and fairly available source of nutrition (Scrimshaw and Murray, 1988). Therefore, it becomes essential to detect lactose in milk, food products and biological fluids in cost effective way.

Screening of enzyme activity using high-throughput techniques such as 3D printed microarrays will encourage assessing a wider range of biomolecular functionality. Also, the ability to manufacture detailed and complex 3D printing prototypes in a fast, efficient and cost-effective way is the focus of many areas of research and development. To date, the use of 3D printing in the optical and biosensors field is limited due to the

limitations of the FDM material 3D printing resolution and setting (Elsholtz and Harper, 2015) and the availability of bio-inks.

Key objectives for this chapter are;

1. To design, print and assess optical transparent 3D printed devices for UV-Vis spectroscopy
2. To develop and test new bio-ink (β-GalDynabeads) to allow assessing a wider range of biomolecular functionality such as lactose in a sample.
3. To 3D print a biosensor device for UV visible spectroscopy to quantify lactose in a sample.
4. To use immobilised bio-inks inside 3D printed biosensor devices to perform a coupled set of chemical reactions.

Each of these objectives was thoroughly and critically evaluated as reported below.

7.2 Fabrication and optimization of transparent 3D-Printing devices for UV-Vis Spectroscopy.

To fabricate 3D printed devices optimised for UV-Vis spectroscopy, three transparent filaments were selected: transparent ABS, transparent PLA and HD-Glass. Initially, a 3D printing device with dimensions of 20 mm (W) x 47.85 mm (L) x 12.5 mm (H), optimised to fit into a standard UV visible spectrometer, was designed. A CAD design of the 3D printed device is shown in Figure 7.1.

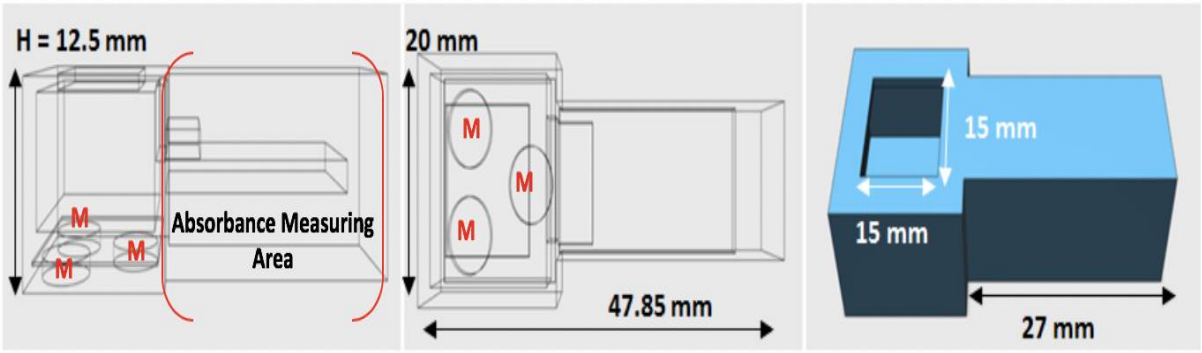

Figure 7.1| **Schematic CAD designs of one step 3D-printed device designed for UV-Vis spectroscopy;** 42 minutes of printing time. M shows the position of the magnets that are placed in the device.

To identify reliable printing settings for the transparent filaments on a 3D printing device, five repeat prints of the same design Figure 7.1 were made to ensure reproducible print quality.

To print transparent filaments the minimum layer duration of standard print setting for ABS Section 2.3 Table 2.2 was increased from 5 to 10 seconds, since it would help to prevent depression of the extruded layer below by allowing the lower layer to have more time to solidify.

Also the devices were printed at 0.25 mm layer height to ensure improved optical transparency for the absorbance measuring area (Figure 7.1) as the literature suggests that FDM 3D printed PLA microfluidic devices with 0.25 mm are reproducible and possess good optical transparency (Tothill *et al.*, 2017). Also, in this thesis (Chapter 3) it was also determined that 0.25 mm layer height was the best setting to achieve reliable 3D print on the MakerBot Replicator 2X using the listed 3D filaments (Table 3.1).

Final reliable 3D printing settings for the transparent filaments are provided in Chapter 2, Table 2.5. All of the transparent filaments used were printed reproducibly under these applied setting.

Next, the 3D printed devices were assessed for leakage. An inspection was carried out to ensure the biosensor device was appropriate for the microfluidic or millifluidic application. The leakage was evaluated by observing the device filled with water containing blue dye for up to 24 hours. A photo of the devices 3D-printed by transparent filaments (PLA, ABS, and HD-Glass) containing dye are shown in Figure 7.2.

No leakage was observed from the 3D printed devices made by all of the transparent filaments during the assessment period. As a result, the reliable 3D printing setting used for transparent filaments (Table 2.5) was deemed appropriate for making microfluidic or millifluidic biosensor devices.

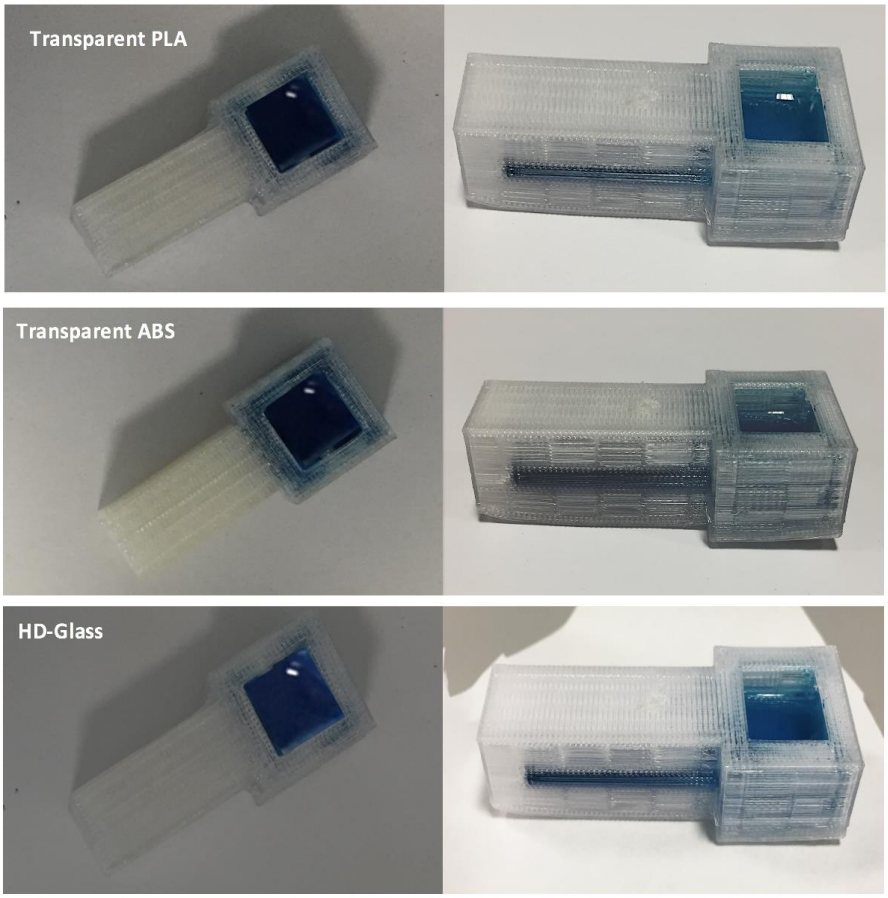

Figure 7.2| **Photograph of a 3D-printed device designed for UV-Vis spectroscopy;** Devices made from PLA, ABS and HD-Glass filaments with a 42 minute printing time. The minimum and maximum volumes for liquid manipulation in the 3D printed device are 3 and 5 ml respectively. The absorbance measuring area of the device can be filled with max 600 µL liquid. Wall thickness of absorbance measuring area was 0.4 mm.

7.2.1 Assessment of XTC-3D coating on the 3D-printed device

The smooth surface on a 3D print can be achieved by exposing the model to acetone vapour (for ABS filament), chemical treatment, e.g. chloroform (for PLA filament) and XTC-3D coating (all transparent filaments).

The XTC-3D coating can provide an optically transparent smooth surface by filling up the striation which could reduce light scattering, rough feels and the detecting absorbance for the devices.

In this thesis to assess the application of XTC-coating on optical transparency of transparent filaments the 3D printed devices optimised for UV-Vis in section 7.1 were reprinted with transparent ABS, transparent PLA and HD-Glass filaments using reliable print settings detailed in Table 2.5.

Initially, the optical performance of these printed devices to reflect or transmit light was determined using UV-Vis, as described in Section 2.12.6.3, before coating with XTC-3D and was compared to the performance of a polystyrene cuvette.

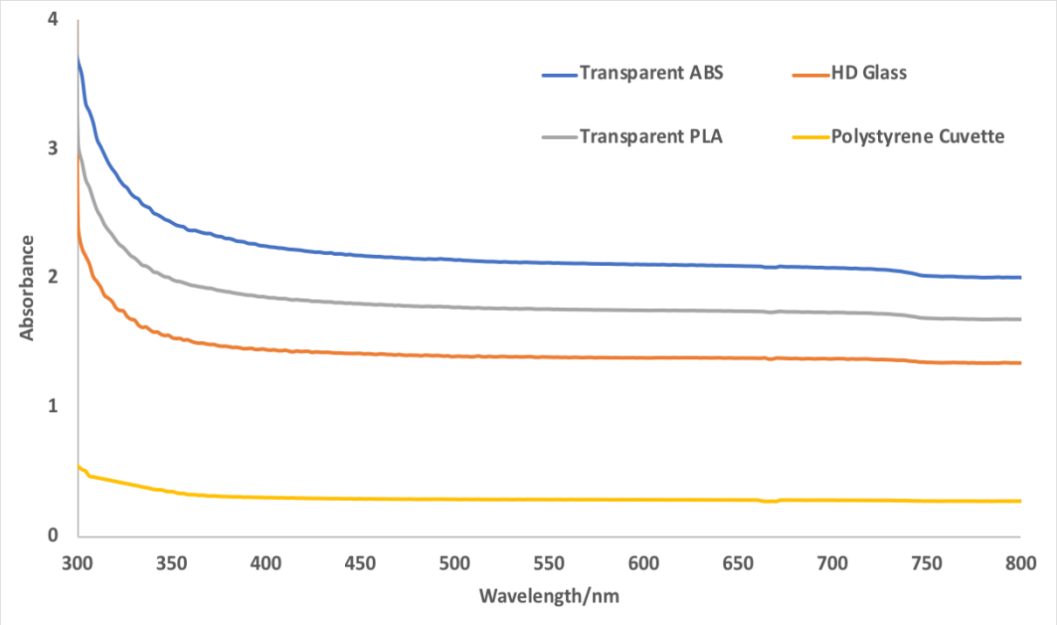

Figure 7.3| **UV-Vis spectrum of polystyrene and 3D-printed fluidic (PLA, ABS, and HD-Glass) devices designed.** Data represent the mean values for n = 3.

The UV-Vis spectra of individual filaments (Figure 7.3) show significant differences in absorbance values between the 3D-printed devices. At 550 nm the highest absorbance value of 2.126 ± 0.056 was observed for the transparent ABS device. The lowest value of 1.385 ± 0.039 was observed for HD-Glass device. The absorbance value of the transparent PLA device and the polystyrene cuvette were 1.755 ± 0.023 and 0.2803 ± 0.023, respectively.

Compared to polystyrene cuvette, the apparent absorbance detected for all of the filaments, which was most likely caused by the scattering, was relatively high, ranging from 1.385 to 2.126, especially when considering the photometric range of the UV-Vis spectrophotometer is limited to maximum absorbance of 3.3 AU (Thomas and Ando, 1997) (Dimitrijević et al., 2013). Possible reasons for this high absorbance of the filaments could be: 1) layer height, 2) haze of the material absorbing the light, 3) striations on the surface which increase light scattering by internal reflections and general unevenness of the printed layers.

Next, the 3D-printed ABS, HD-Glass and PLA devices were coated with XTC-3D to determine the influence of coating on the optical absorbance of the devices for individual filaments. A photo of a coated HD glass device can be found in Figure 7.4 and Figure 7.5 shows UV-Vis data after XTC-3D coating.

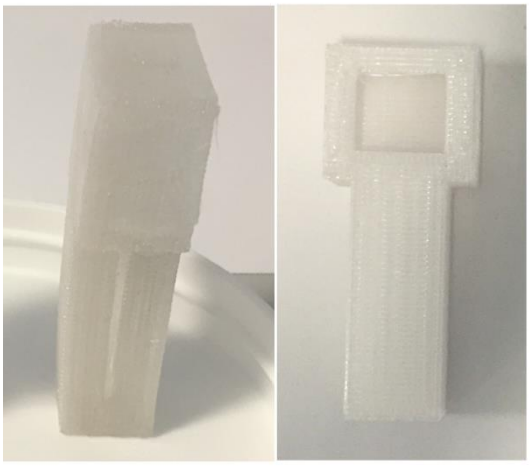

Figure 7.4| **Photograph of XTC- Coated HD-Glass 3D-printed millifluidic device**

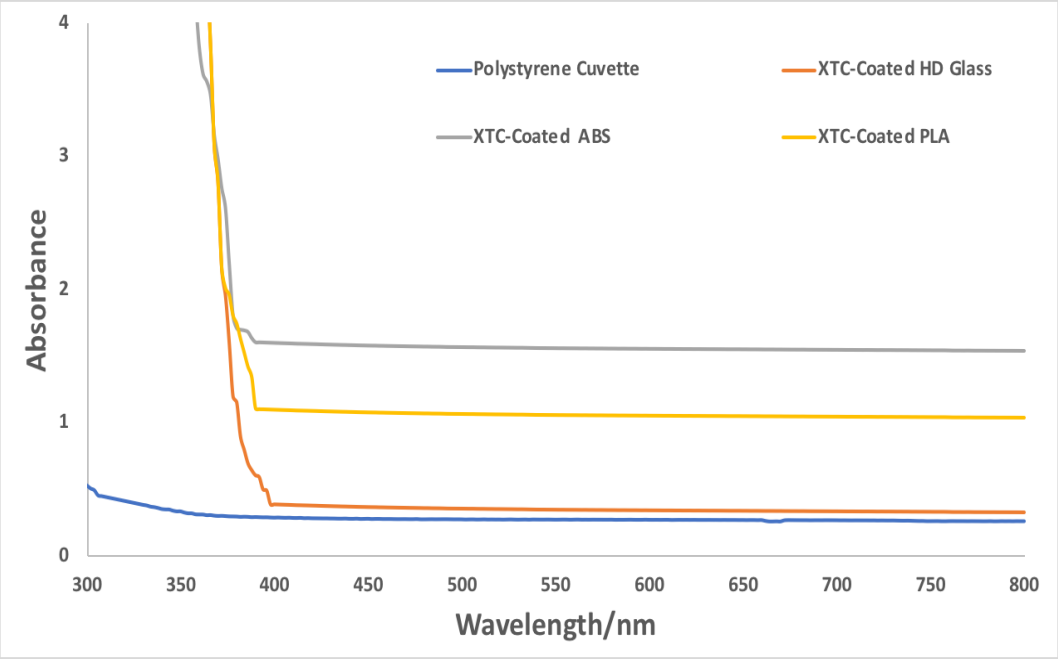

Figure 7.5| **UV-Vis spectrum of polystyrene and coated 3D-printed fluidic (ABS, HD-Glass and PLA)) devices designed.** Data represent the mean values of three repeats.

Figure 7.5 shows a sharp increase in absorbance for all coated devices below approximately 400 nm, a response that was not seen in uncoated filaments (Figure 7.3). This observation implies that components of XTC-3D coating have prohibitive UV light absorption below the stated wavelength.

The data also shows a decrease in absorbance of UV-Vis spectrum for 3D-printed ABS, HD-Glass and PLA devices after application of the coating. At 550 nm, yet again the highest absorbance value of 1.556 ± 0.041 was observed for the transparent ABS device. The lowest value of 0.348 ± 0.023 was observed for the HD-Glass device. The absorbance value of transparent PLA device was 1.056 ± 0.019. When these values are compared with those obtained earlier before coating (Figure 7.3), a significant drop in absorbance was noticeable. Improved transparency of 27% in ABS, 40% in PLA and 75% in HD-Glass was determined.

The difference in absorbance value for the UV-Vis spectra of devices after coating, when compared to polystyrene cuvette with absorbance value of 0.280± 0.010 at 550 nm, were 82% (ABS), 73% (PLA), and 19% (HD-Glass), respectivel. This value could be improved if the inner layer of the device was coated with XTC-3D.

Overall this work shows XTC-3D coating improved optical transparency of the assessed filaments. This was determined by observing a decrease in overall absorbance of the evaluated filaments in the 380-800 nm range. HD-Glass exhibited the greatest reduction in absorbance after XTC-3D coating against other assessed filaments which shows this filament is more suitable to fabricate devices to conduct UV-Vis spectroscopy colorimetric assays.

In conclusion, the 3D printed transparent devices on their own show some optical transparency but possibly not enough to conduct colorimetric assays accurately, whereas coated devices are more suitable to be used to obtain certain colorimetric assays. These coated transparent devices optimised for UV-Vis are only suitable to detect absorbance between the ranges of 400-800 nm.

It should be noted that the optical transparency after the application of a coating can vary from design to design and the 3D printing technique used. Moreover, the application of the XTC-3D coating can vary from person to person. The type of application technique used can also have influence, for example using different paint brushes. Keeping that in mind, the coating layer of the 3D model should still be as even as possible without any dirt or air trapped underneath to achieve a good effect.

In this work, the interaction of XTC-3D with different chemical or biochemical species was not assessed, though it may interact with various chemical solvents as it contains epoxy resins (Kalenda and Kalendová, 1995)(Kawahara *et al.*, 2001). However, in this

work, XTC-3D was only added to the outer layer of the device is coated to improve the transparency.

7.3 Compatibility of transparent 3D printed filaments with Lactose assay

To investigate if the activity of the enzyme in the lactose assay was inhibited in the presence of different 3D printing materials, the lactose assay was carried out in 3D prints as described Section 2.11-2.11.3. The three transparent filaments that are intended to be used in this work for fabrication of microfluidic (biosensor) devices were selected and tested. Figure 7.6 shows the effect of 3D printing material on lactose assay.

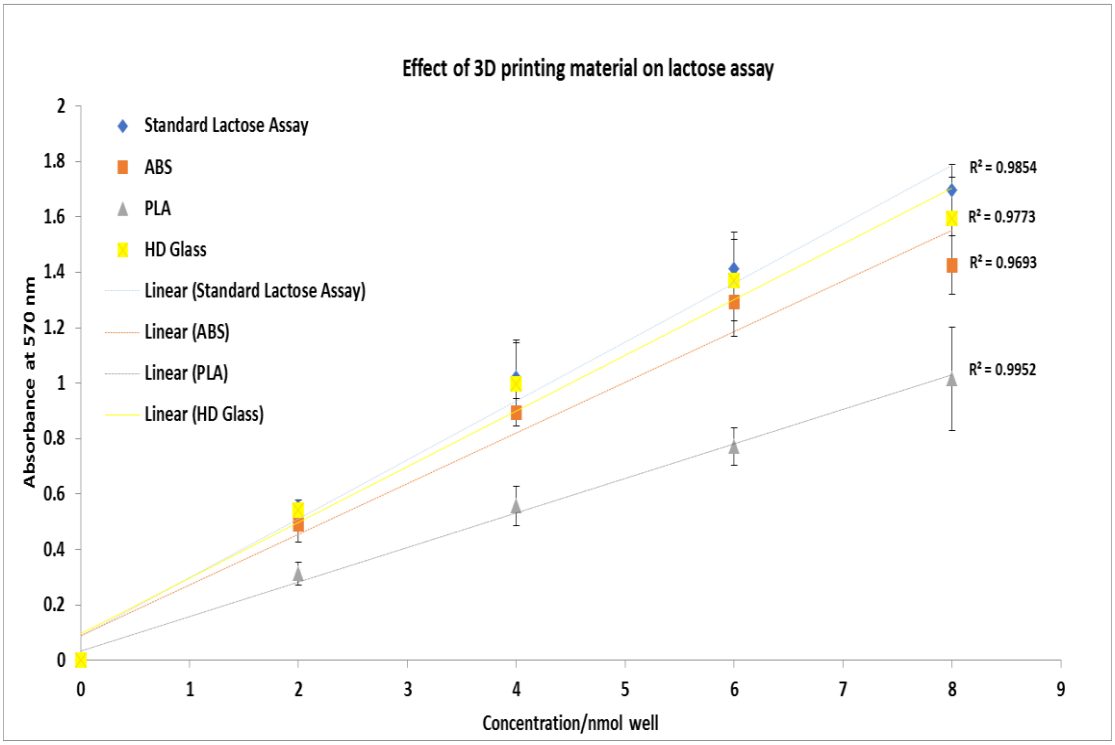

Figure 7.6| **Effect of 3D printing material on lactose assay.** The lactose assay mixture was detected in the presence of thermoplastic material at 570 nm using a BioTek plate reader. The spectrum represents the mean values for n = 4.

Figure 7.6 shows that, apart from PLA, no significant differences between the absorbance detected for the lactose assay in the presence of each 3D printing

material when compared to the standard lactose assay control.

The linearity of the lactose assay regression line displays the R^2 ranges from 0.97 to 0.99 which are comparable to each other. This value obtain suggests a good linear response at 570 nm to the changes in lactose concentration is achieved using 3D printed devices. The best response was achieved for the lactose assay in the presence of PLA (Figure 7.6).

The outcome of this study suggests that the enzyme in the lactose assay is not inhibited by ABS and HD-Glass 3D printed filaments, thus permitting a reliable spectrophotometric determination of enzyme activity. These filaments can be used to fabricate 3D printing devices for detection of lactose in solution.

7.4 Lactose quantification based on coupled enzymatic reactions assay

The combination of the β-Gal, GOD, HRP proteins and a colorimetric probe will allow quantification of a wider range of biomolecular functionality such as lactose in solution, milk and dairy products (Conzuelo *et al.*, 2010). Therefore to detect lactose in solution a new protein β-GalDynabead bio-ink was fabricated by covalently coupling β-Gal to Dynabeads as described in Section 2.12.4. Figure 7.7 shows the schematic cascade reaction of lactose quantification based on the practical assessment used in this thesis.

In this work, the lactose quantification assay was designed and completed by optimising the method taken from a report on optimisation of lactose quantification based on coupled enzymatic reactions for UV-Vis spectrophotometry (Condezo *et al.*, 2014).

The proteins-based bio-inks for this assay was prepared to contain 50 mg Dynabeads in the mixture for β-GalDynabeads and GODDynabeads and 10 mg bead for HRPDynabeads). Briefly, if we assume all proteins are bound to Dynabeads during coupling. The protein ratio after binding to be used for biological assay should be

(5:5:1) which is equivalent to the ratio of the enzyme used to detect the lactose concentration in the cited report (Condezo *et al.*, 2014).

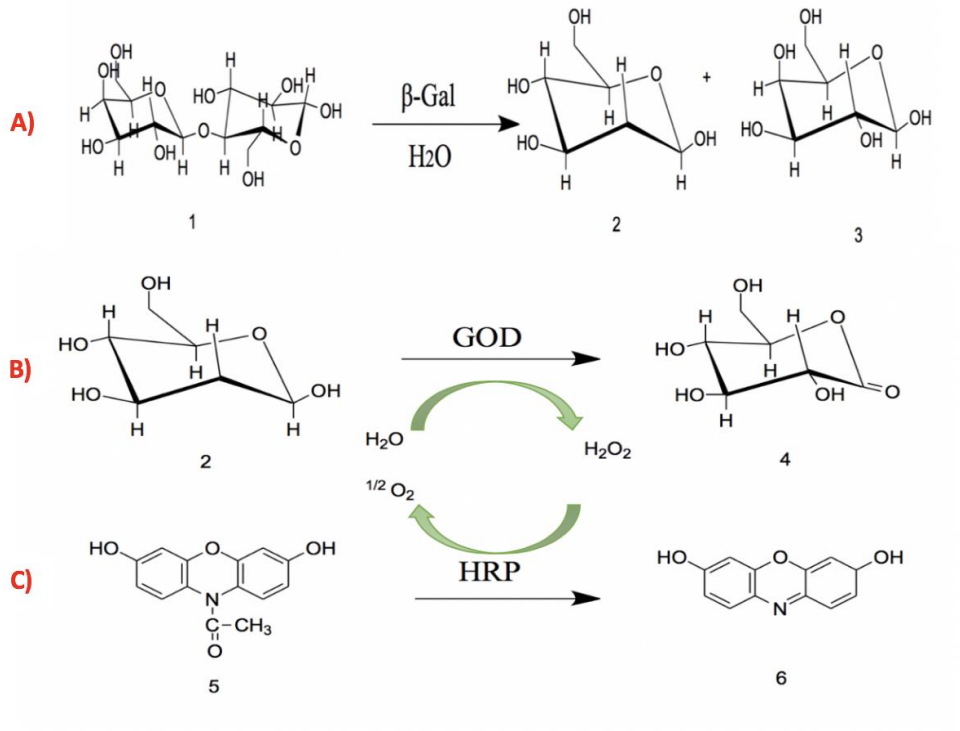

Figure 7.7|**Enzymatic cascade reaction for the quantification of lactose**. Three steps enzymatic reaction. A) hydrolysis of lactose (1) by β-Gal to D-glucose (2) and D-galactose (3). B) In the presence of oxygen at room temperature, the β-D-glucose is oxidised by GOD to glucono-δ-lactone (4) and H_2O_2. C) The H_2O_2 reacts with Amplex Red in the presence of HRP in a 1:1 ratio to form a coloured product that can be detected spectrophotometrically.

Amplex Red (AR) was used as a probe for measurement of extracellular H_2O_2 in a biological system. This probe was used since faster lactose detection is achieved by Amplex red when compared with other chemical probes, for example, *o*-phenylenediamine (Fornera, Yazawa and Walde, 2011). The lactose quantification assay was performed using protein coupled Dynabead bio-inks as detailed in Section 2.12.5.1.

The sensitivity of the lactose assay was estimated by the limit of detection (LOD) and limit of quantification (LOQ) as follows: (LOD = 3.3 σ/S) and (LOQ = 10 σ/S where σ is the SD of absorbance and S is the slope of the standard curve (Shewiyo et al.,

2012). The coefficient of variation was evaluated through relative standard deviation (RSD) percentage as follows: RSD%= SD/mean of each sample) x100.

The absorbance of the mixture was measured at λ_{max} 570 nm for AR, which is associated with resourufin formation by oxidation of AR (Rhee *et al.*, 2010)(Rodrigues and Gomes, 2010). The wavelength of the maximum absorption AR was also confirmed experimentally from the spectrum, by montitoring the absorbance for lactose standard 0.5 at (20℃ and 37℃) between 300 to 800 nm (Figure 7.8).

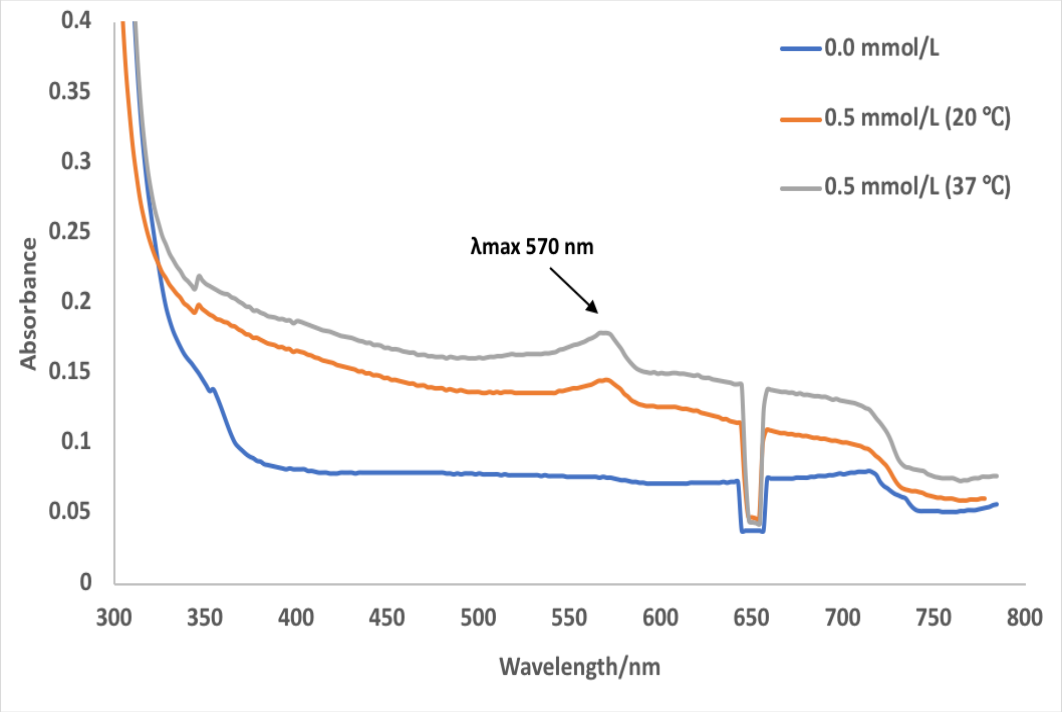

Figure 7.8| **UV-Vis spectrum of absorption in the presence of lactose (0.5 mmol/L),** 50 mg beads β-GalDynabeads and GODDynabeads and 10 mg bead for HRPDynabeads bio-inks. A maximum absorbance at 570 nm is observed for oxidation of AR, obtained for assessment at 20℃ and 37℃. The absorbance detected at λ_{max} 570 nm were 0.075 (SD=0.0069) for 0.0 mmo/L lactose, 0.145 (SD=0.0015) and 0.178 (SD=0.0017) for 0.5 mmol/L at 20℃ and 37℃. The spectrum represents the mean values of three repeats.

Next, to determine if the colorimetric probe AR could be used to carry out the reaction at room temperature, the lactose quantification assay was carried out using the bio-inks for lactose in a standard concentration range of 0.1-0.5 mmol/L after incubation at 20℃.

As a control the reaction was also carried out over the lactose standard concentration range of 0.1-0.5 mmol/L after incubation at 37℃. From the data obtained a standard curve of lactose were constructed to evaluate the linearity of the enzymatic assay shown in Figure 7.9.

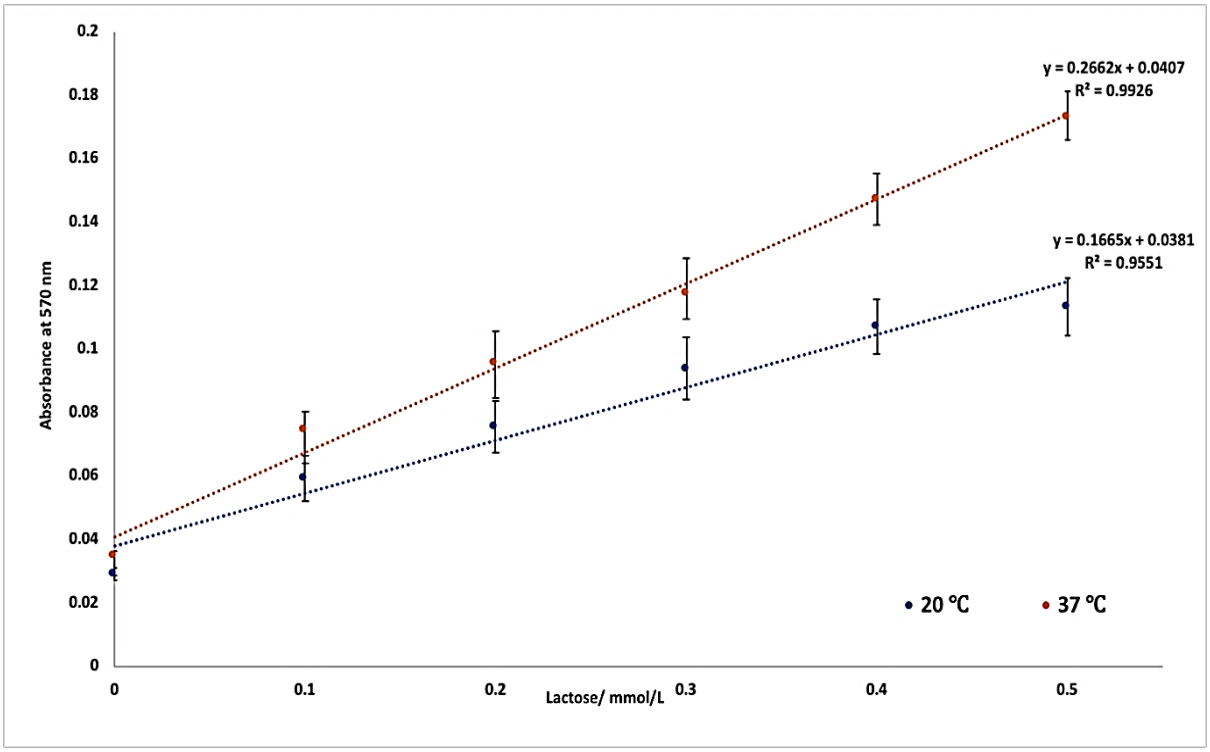

Figure 7.9| **Absorbance of reaction for lactose standard range from (0.1-0.5 mmol/L) detected at *λ*max 570.** Data represent the effect of temperature on the lactose standard curve assessed after 1 hr. incubation at 20℃ and 37℃. The absorbance was taken at t = 300 seconds from the absorbance measuring time plot obtained that is not presented here. The enzyme activity in reaction reached equilibrium in 1 h. This was supprted by remeasuring the absorbance for all assays concentration for up to 5 hrs. The re-measured absorbance for all samples was the same as the value presnted here (not shown) which confirmed that the amount of the enzymes used in the solution is sufficient for carrying out the reaction within (1h). The table on the plot shows the change in absorbance after deducting the blank absorbance (0.0 mmol/L lactose) for all lactose concentrations. The data represents the mean values for n = 3.

Figure 7.9 shows a higher absorbance value for the lactose standard is obtained when the sample is incubated at 37℃ compared to 20℃. The calculated increased in the average slope of the lactose standard curves for incubation of the lactose standard of

0.1-0.5 mmol/L at 37℃ compared to incubation at 20℃ is by 1.39 ± 0.25-fold. This output is comparable or even slightly lower than the assay optimised by (Condezo *et al.*, 2014) for the 0.1-0.5 mmol/L lactose standard which increased by 2.5 ± 0.2-fold.

The coefficient of variation for each slope was below 10%. The linearity of the lactose assay regression line displays the R^2 value of 0.9926 for incubation at 37℃ and 0.9551 at 20℃. These values confirm the linearity of the assay at both temperatures.

The sensitivities of the lactose assay LOD incubated at 20℃ were 0.147 and 0.093 for 37℃. The LOQ were 0.447 (20℃) and 0.282 (37℃). The sensitivity of lactose standard (0.1-0.5 mmol/L) assay obtained in this work is approximately 3 times greater than previously reported values obtained using microplate reader by Condezo et al., 2014. It is assumed that the greater sensitivity was achieved since it is best to quantify the absorbances in the range of 0.1-1.0 AU by UV-Vis spectrometer to maintain optimum spectrophotometric performance (Chamran and Keiser, 1978). At around 0.3-0.5 absorbance (50% absorption), the accuracy is greatest, however, other researchers have found that detection of biological molecules was optimal at a maximum UV-Vis absorption range of 0.1-1.5 AU (Kirschenbaum, 1978). The slope of the standard (0.266) at 37℃ after 1 hr reaction is comparable with the slope obtained by Condezo et al., 2014 (0.261) and Fornera et al., 2011 (~0.27) after 7 hrs reaction.

Consequently, based on the outcome of this experiment, it was determined the lactose assessment using AR can be determined at 20℃ but it is best at 37℃. As a result, the assessment at 37°C was selected as the optimal assay condition to perform a faster reaction time.

Since this thesis intends to perform lactose assay in a 3D printed device optimised for UV-Vis spectroscopy to have a better indication of the colour change in respond to lactose concentration the concentration of the lactose used in assay solutions is to be increased for the further assays.

7.5 Assessment of lactose quantification based on a coupled enzymatic reaction assay in transparent HD-Glass 3D printed devices

To quantify lactose in 3D printed devices optimised for UV-vis spectroscopy, the device detailed earlier in Section 7.2 was used (Figure 7.1). It was designed with the intention of allowing immobilisation of three different enzymatic bio-inks in 3D printed devices with a 6 mm magnet using the technique evaluated in Chapter 6, Sections 6.5 and 6.7.

The three bio-inks employing β-GalDynabeads, GODDynabeads, and HRPDynabeads were immobilised in 3D printed devices as detailed in Section 2.12.5.3.1. The lactose quantification assay was performed for a diluted lactose standard range of 0.5-6.3 mmol/L at 37℃ as described in Section 2.12.5.3.2 The experiment was completed in parallel with disposable polystyrene cuvettes for comparison. Photographs of a one-step optimised transparent HD-Glass 3D-printed device coated with XTC-3D used for this experiment is presented in Figure 7.10.

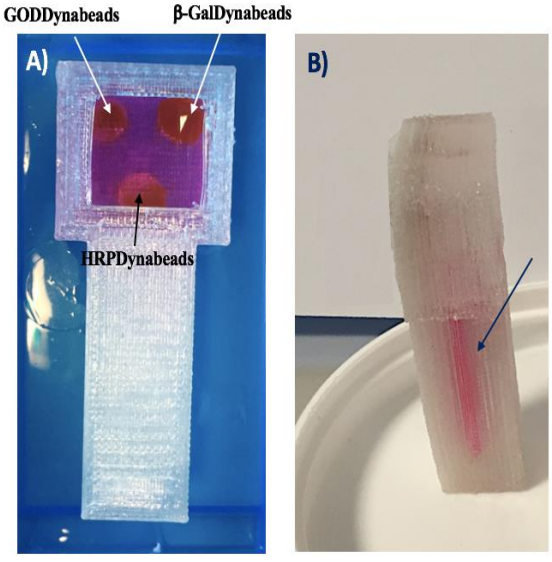

Figure 7.10| **Photograph of a one-step optimised transparent HD-Glass 3D-printed devices coated with XTC-3D.** A) the device with containing assay solution mixture. The place where the magnets were placed in the device and the location of each immobilized bio-ink in the device is marked by an arrow. B) the same device after rotating clockwise. The reaction mixture was transferred into the capacity marked by an arrow for measurement by UV-Vis spectrophotometer.

Figure 7.11 shows UV-Vis data for one-step lactose quantification using β-GalDynabeads, GODDynabeads, and HRPDynabeads for standard lactose range of 0.5-6.3 mmol/L determined after 1 hr of incubation at 37℃.

Figure 7.11 show higher absorbance values for the lactose standard obtained in a plastic cuvette compared to 3D printed devices. The increased in the average slope of the standard lactose curves (0.5-6.3 mmol/L) prepared in a polystyrene cuvette compared to the absorbance obtained with 3D printed devices was by 1.25 $\pm$0.2-folds. The linearity of the lactose assay regression line displays the R^2 value of 0.998 for the lactose assay obtained in polystyrene cuvette and 0.996 for 3D printed devices. These values suggest good linearity response at 570 nm to the changes in lactose concentration is achieved in 3D printed devices. The coefficient of variation for both slopes was below 7%.

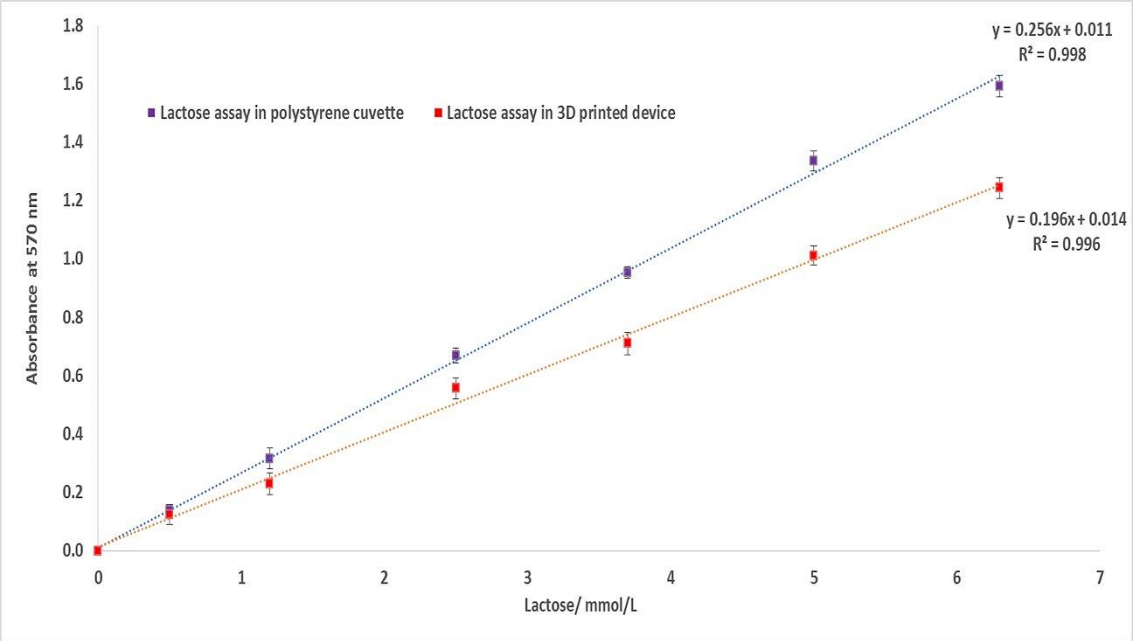

Figure 7.11| **Absorbance of reaction for lactose standard range from (0.5-6.3 mmol/L) detected at λ_{max} 570.** Data represent the assessment absorbance at different lactose concentration for the assay completed in the polystyrene cuvette and 3D printed devices. The absorbance was taken at t = 300 second from the absorbance measuring time plot obtained that is not presented here. The data represents the mean values of three repeats.

The sensitivity of the lactose assay LOD in polystyrene cuvettes and 3D printed devices were 0.032 and 0.051 respectively. The LOQs were 0.097 for polystyrene cuvettes and 0.155 for 3D printed devices. The sensitivity of the lactose standard for the 0.5-6.3 mmol/L assay is lower than that for the range of 0.1-0.5 mmol/L reported in Section 7.2. This suggests a concentration range of 0.5-6.3 mmol/L for lactose is more suitable for this assay.

The sensitivity of the lactose assay obtained here is comparable to previously reported values for a LOD of 0.043 and a LOQ of 0.131 mmol/L by Condezo et al., 2014. A lower LOD value can only be obtained if a more sophisticated instrument is used (Conzuelo *et al.*, 2010) such as ion-pair reversed phase HPLC which can achieve a LOD of 5.8 μmol/L (Erich, Anzmann and Fischer, 2012). Nevertheless, these techniques are expensive and difficult to implement for routine analysis of lactose.

Overall from this experiment, it can be concluded that the colorimetric lactose assay can be conducted in the HD-Glass devices coated with XTC-3D. These data also suggest that immobilised bio-ink in the HD-Glass 3D printed device accurately quantify a lactose solution over the biological relevant range of 0.5-6.3 mmol/L within an hour with a good linear response.

Slightly lower absorbances were obtained for the lactose assay range of 0.5-6.3 mmol/L in a HD-Glass 3D printed device when compared to a polystyrene cuvette however, by simplifying the device to obtain a better printing quality, the lactose concentration can be assessed more precisely by UV-Vis spectroscopy. This work also shows that the leak-free HD-Glass 3D printed device is ideal to assess biological activity at 37℃.

7.6 Lactose quantification by enzymatic reactions using the *o*-dianisidine reagent

To investigate if the lactose in solution could be quantified using *o*-dianisidine as a chromogenic substrate at room temperature, the enzymatic activity of the bio-ink was determined in the HD-Glass 3D printed device as described in Section 2.12.5.2.

This experiment was designed to see if the same chromogenic substrate that was used to detect glucose in solution can be used to detect lactose. If successful, this technique would allow multiple coupled sets of reactions to be performed to detect both glucose and lactose in one device.

The lactose detection for the concentration range of (0.5-6.3 mmol/L) using the *o*-dianisidine reagent is compared with the technique as described in Section 7.5, using AR as a probe, and is presented in Figure 7.12.

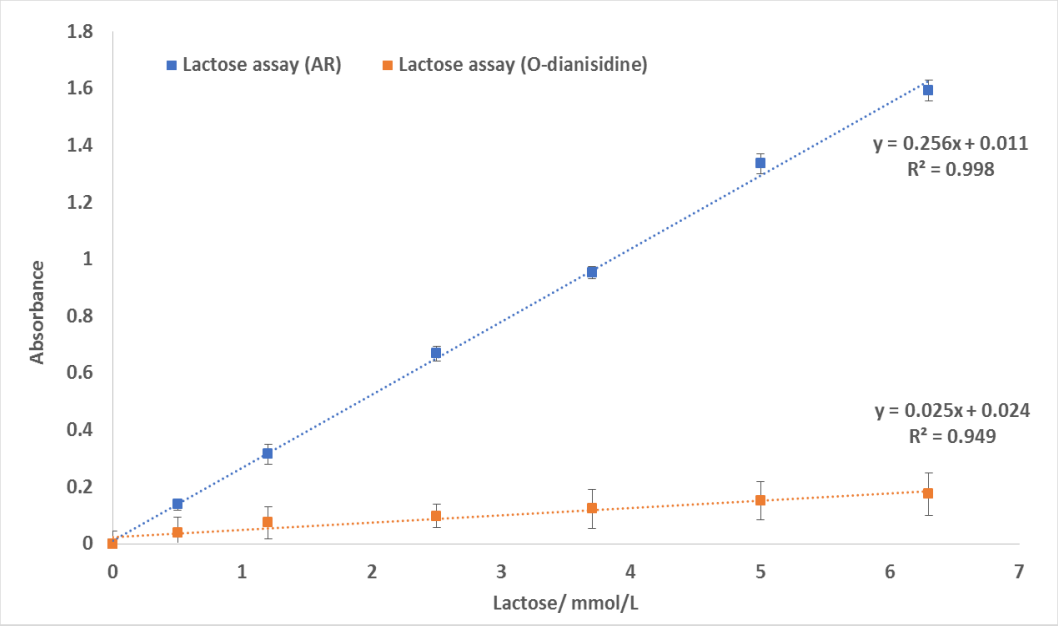

Figure 7.12| **Absorbance of reaction for lactose standard range from (0.5-6.3 mmol/L) detected at λ_{max} 570.** Data represent the absorbance at different lactose concentrations for the assay completed in 1hr using different chemical probes (o-dianisidine and AR). The absorbance was taken at t = 300 second and measured at a λmax of 570 nm for AR and 500 nm for o-dianisidine. The absorbance is the mean value for n = 3.

Figure 7.12 show a higher absorbance value for the lactose standard obtained using AR chemical probe compared to *o*-dianisidine. The calculated increase in the average slope of the lactose standard curves was 0.5-6.3 mmol/L for AR compared to the absorbance obtained for *o*-dianisidine is 6.7 $\pm$ 3-fold. The coefficient of variation for AR was below 4% and for *o*-dianisidine was above 61%.

The R^2 value linearity of the lactose assay regression line was 0.998 for AR and 0.949 for *o*-dianisidine. This suggests a good linearity response to the changes in lactose concentration is achieved for both assays prepared using a different chemical probe. The sensitivities of the lactose assay LOD for AR and *o*-dianisidine were 0.032 and 0.971, respectively and the LOQs were 0.097 for AR and 2.94 for *o*-dianisidine.

As previously the absorbances of each lactose mixture were re-measured for up to 5 hrs to determine if the equilibrium was reached within an hour. This experiment revealed that for lactose assay by AR the absorbance of the re-measured sample remained unchanged which suggest that the equilibrium point has reached. However, for *o*-dianisidine lactose assay, the absorbance increased every hour (data not shown). It is assumed that since the absorbance increased the *o*-dianisidine chemical probe could also be used to determine the level of lactose in solution but that a longer reaction time may be required. According to the majority of reports on spectrophotometric quantification of lactose in solution, the enzymatic cascade reaction using chemical probes such as *o*-phenylenediamine (OPD) and *o*-dianisidine can take up to 7 hrs (Fornera, Yazawa and Walde, 2011).

In conclusion, based on the outcome of this experiment, AR was selected as a more suitable option to allow fast reaction times and accurately quantify lactose in solution by UV-Vis spectroscopy.

7.7 Three step lactose quantification using β-GODDynabeads, GODDynabeads and HRPDynabeads on transparent 3D-printed devices for UV-Vis spectroscopy

To enable a multistep chemical reactions within one device, a simple three-step process often exploited for the detection of lactose in solution was designed. The lactose in solution was quantified in three steps on XTC-3D coated HD-Glass 3D printed biodevices after immobilisation of bio-inks in micro-channels as detailed in Section 2.12.5.4. Figure 7.13 shows photographs of three-step lactose quantification in a 3D printed biosensor device using immobilised protein-Dynabeads bio-inks.

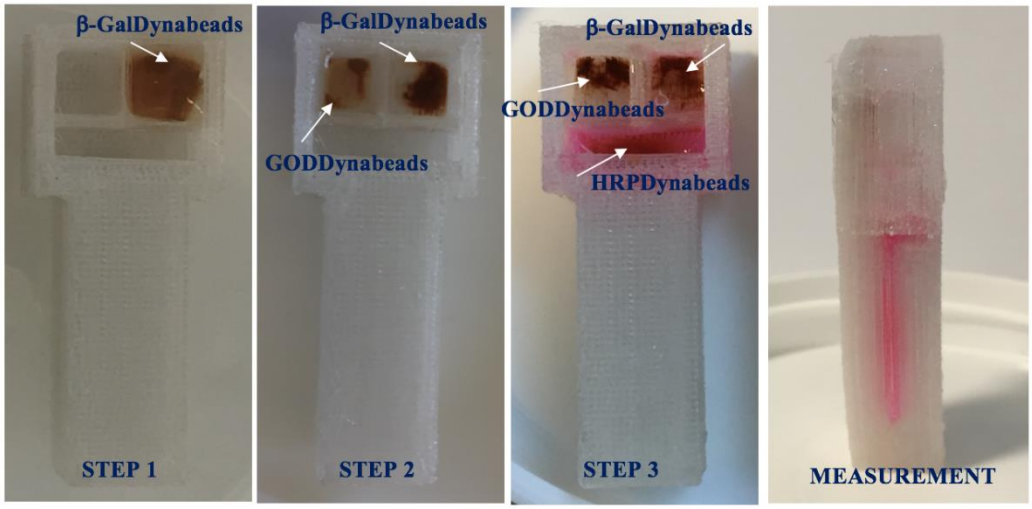

Figure 7.13| **Illustration of three-step lactose quantification in a 3D printed biosensor device, by using immobilised protein-Dynabeads bio-inks.** These images show how each step was taken for lactose quantification. Figure 7.12. A shows the final device that was used. In the device used, the top section, where the biological assay occurred (the reaction chamber area) was sealed to allow the biological assay from to be moved from one chamber to another easily.

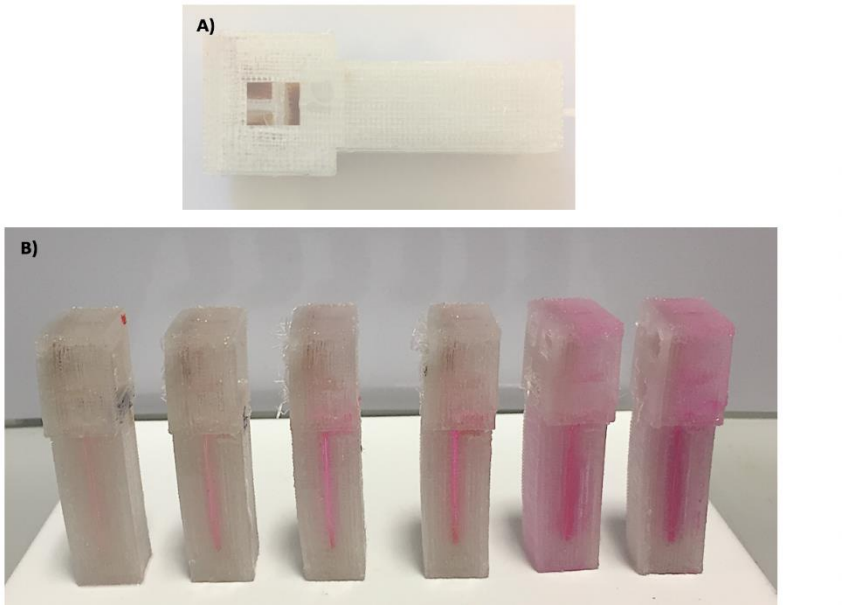

Figure 7.14| **Photograph of the three-step optimised transparent HD-Glass 3D-printed device coated with XTC 3D.** A) shows the device side-on. B) shows a device used to quantify lactose concentrations in the range of 0.5-6.3 mmol/L, with each device showing the colour difference.

The data for three-step lactose quantification in 3D printed device and polystyrene cuvette for lactose concentration range of 0.5-6.3 mmol/L is presented in Figure 7.15.

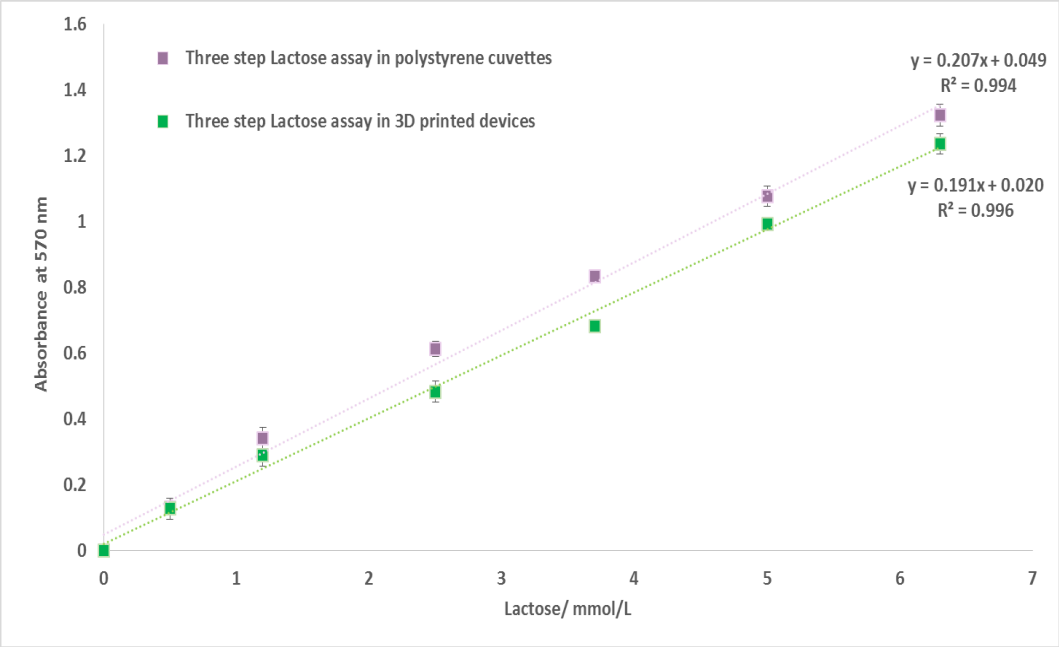

Figure 7.15| **Absorbance for three-step lactose standards from 0.5-6.3 mmol/L at λ_{max} 570.** Data represent the assessment absorbance at different lactose concentrations for the assay completed in polystyrene cuvettes and 3D printed devices. The absorbance was taken at t = 300 seconds. The data represent the mean values of three repeats.

Figure 7.15 shows a higher absorbance value for the lactose standard obtained in polystyrene cuvettes compared to 3D printed devices. The increased in the average slope of the lactose standard curves 0.5-6.3 mmol/L prepared in polystyrene cuvettes compared to the absorbance obtained with 3D printed devices is by 1.14 $\pm$0.1-folds.

The lactose assay regression line has a R^2 value of 0.994 in polystyrene cuvettes and 0.996 for 3D printed devices. These values are comparable which suggests a good linear response at 570 nm to the changes in lactose concentration is achieved using 3D printed devices. The coefficient of variation for both slopes was 4%.

The sensitivity of the lactose assay LOD for assay in polystyrene cuvettes and 3D printed devices were 0.036 and 0.042, respectively with LOQ values of 0.109 in polystyrene cuvettes and 0.127 in 3D printed devices. The sensitivity of the lactose assay obtained here using the bio-inks is comparable to previously reported values LOD = 0.043 and LOQ = 0.131 mmol/L (Condezo et al., 2014). Moreover, the absorbance obtained here shows identical trends to those reported in Section 7.3 for lactose concentrations of 0.5-6.3 mmol/L. This similarity demonstrates the feasibility of employing immobilized enzymes in different channels to carry out multistep chemical reactions. In conclusion, multi-step colorimetric lactose assays can be conducted in the HD-Glass devices coated with XTC-3D.

7.8 Conclusion

In this chapter, transparent ABS, transparent PLA and HD-Glass filaments were used to design, print and assess optically transparent 3D printed devices for UV-Vis spectroscopy. The transparency of each filament was assessed before and after XTC-3D coating. HD-Glass was selected as the most suitable filament to be used to fabricate 3D printed devices to conduct colorimetric assays by UV-Vis spectroscopy because it exhibited the most improved optical transparency after XTC-3D coating.

A β-GalDynabead bio-ink was developed for FDM 3D printing and, in combination with GODDynabeads and HRPDynabeads, allowed lactose to be quantified in solution. Optimal assay conditions for the formulated bio-inks were developed to assess the biological activity of bio-inks in the printed state and to calibrate them for use in biosensing applications.

The β-GalDynabead, GODDynabead and HRPDynabead bio-inks were immobilised in a 3D printed device for UV-Vis spectroscopy. A lactose quantification assay was performed in one and three steps in 3D printed biosensors and polystyrene cuvettes for comparison.

A good linear response to the changes in lactose concentration at 570 nm was achieved using 3D printed biosensor devices. Reliable spectrophotometric determinations and multi-step colorimetric lactose assays could be conducted in the 3D printed HD-Glass bio-devices with comparable sensitivity to the literature (Condezo et al., 2014).

Slightly lower absorbances were obtained for the lactose assays in HD-Glass 3D printed devices when compared to plastic cuvettes, however, by simplifying the device for obtaining better printing quality the lactose concentration could be assessed more precisely by UV-Vis spectroscopy.

In conclusion, this work shows the possibility of 3D printing leak free and reproducible millifluidic devices with good optical transparency using FDM 3D printing technology to quantify lactose in solution by UV-Vis spectroscopy. The use of FDM printing offers great accessibility to microfluidic and millifluidic fabrication as the falling costs and rising resolution of these printers makes them affordable to most laboratories. These 3D print designs can be easily shared between researchers which has the potential to widen accessibility further by eliminating the design barrier in addition to the fabrication barrier largely limiting access to microfluidic technology at present.

CHAPTER 8

8.1 A SUMMARY OF CHAPTERS

The work described in this thesis aimed to develop a set of protein-based bio-inks for FDM 3D printers to allow the delivery of biological components, on 3D printed devices. To achieve this goal, FDM 3D printing filaments were characterised to determine suitable filaments to fabricate millifluidic or microfluidic devices. Next, a protocol to allow print/decant functional biomolecules to the surface of the 3D-prints in such a way that they retain their activity was developed. As a proof of concept, the use of FDM 3D printing for making millifluidic or microfluidic devices that utilize 3D-printed objects functionalized with protein molecules was shown. Generally, by combining the aspects of 3D printing, microfluidics and biochemical disciplines, such as an enzymatic application, the potential use of FDM 3D printing to allow open source, inexpensive and rapidly produced 3D-printed milifluidic biosensor devices were further explored.

Following chapters covering the survey and experimental methods, the remaining chapters can be summarised as follows:

Chapter 3

Initially, reliable print settings were determined for a range of new-to-the-market 3D-printer filaments on the MakerBot Replicator 2X 3D printer. A thermoplastic cuboid of 9.5 mm (W) x 9.5 mm (L) x 2.5 mm (H) was designed and used as a model to assess the reproducibility of print quality. The 3D printing filaments assessed were: ABS, CF0 carbon fibre-reinforced ABS, PC-ABS Alloy, 3DXNano ABS, PLA, Conductive PLA, Stainless steel PLA, Magnetic Iron PLA, Biofila linen, HIPS, XT-Copolyester, T-Glase, HD-Glass, Bridge Nylon, SemiFlex, and MakerBot Flexible.

Of these filaments, CF0 carbon fibre-reinforced ABS filament could not be printed since it would break when loaded into the extruder, blocking the extruder nozzle on each attempt. The remaining filaments were extruded smoothly.

Reproducibility in printing thermoplastic cuboids with T-Glase and Bridge Nylon filament was low. For T-Glase 5/10 and Bridge Nylon, 9/10, samples failed to print with good quality. Cuboids printed with Bridge Nylon showed low print resolution and gaps in the surfaces of the printed object and were only printed with 100% infill by the T-Glase filament. All other studied filaments were printed reproducibly at a range of infill densities when printed by MakerBot Replicator 2X at the final print settings (Chapter 3, Table 3.1).

As the fundamental goal of this research was to fabricate bio-inks for use in microfluidic or millifluidic devices, characterisation of these 'novel' filaments was also performed, to provide a set of criteria to determine an optimum filament for the fabrication of a particular device. 3D Printing filaments were characterised by surface roughness of printed models (microscopic assessment), resolution and accuracy (shrinkage after printing), layer bonding (water tightness) and hydrophobicity (water contact angle of the printed material) and non-specific DNA/protein binding. All of these aspects were critically evaluated and discussed and compared with current related literature within the chapter.

The conclusion based on the overall studies in this chapter was that, apart from CF0 carbon fibre, Nylon Bridge, T-Glase, SemiFlex, and Magnetic iron PLA, all other assessed thermoplastic filaments are suitable for fabrication of 3D printed microfluidic or millifluidic (biosensor) devices. The outcomes of these characterising studies may help 3D printing users and researchers to avoid using specific 3D printing filaments for making liquid handling devices which could save time and cost for their research.

Chapter 4

To develop a 3D printing system for decanting liquid biological components such as proteins onto 3D prints by FDM 3D printers, the MakerBot Replicator 2X desktop 3D printer was modified. A custom build syringe extruder was constructed and assembled on the device. Optimal printing settings for printing liquid using syringe extruder on 3D printing device was determined.

A number of tests were completed to establish methodological approaches that could be used to deposit active biological molecules, e.g. proteins, to the surface of the 3D-prints using FDM 3D printers. From these studies, it was determined that the syringe extruder on the modified 3D printer could decant liquid at room temperature with the absence of physical contact between the print head and printed support making it likely to decant biological molecules in order to fabricate functional 3D printed devices.

Also by assessing the performance of the syringe extruder on the 3D device, it was demonstrated that liquid and AuNP solutions comparable to the minimum volume of active biological molecules used in the microfluidic platform of approximately 10 µL (Mark *et al.*, 2010) could be decanted at a specific point onto the 3D print.

A simple study was accomplished to identify limitations in liquid manipulation by syringe extrusion to fill a container or simple channels. No significant problem was identified in using syringe extruder for liquid handling application.

The applications demonstrated in Chapter 4 would allow a researcher to download and 3D print automated fluid handling devices that can be used to parallelise and automate microfluidic/millifluidic research application more accessible to new users.

Chapter 5

A set of specific liquid bio-inks for FDM 3D printing were developed that retain biological activity after decanting to a 3D print. GOD and HRP enzymes were used to develop bio-inks due to high selectivity, stability and widely application use for biosensor production (Settia *et al.*, 2005)(Setti *et al.*, 2007). Optimised assay conditions were developed for the formulated bio-inks to assess their biological activity in the printed state and to calibrate them for use in biosensing applications. Initially, by using the optimised GOD assay, it was determined that the enzymatic activity of the GOD and HRP enzymes were not inhibited in the presence of the 3D printed material.

Next, the use of AuNPs as carrier systems to deliver functional biological molecules, such as proteins (GOD and HRP) bound to the surface of the ABS 3D printed objects by nonspecific binding absorption, was assessed. The preliminary assessment showed AuNPs bind to the surface of the ABS 3D print by non-specific absorption and are not absorbed into the interior. It was also determined that AuNPs on a surface of ABS 3D print are bound firmly to the 3D printed material and is not washed off by aqueous, buffer and biological solutions which makes them suitable carriers to formulate bio-inks with the intention of achieving enzyme immobilisation on the surface of 3D printed devices.

A set of GOD–AuNP and HRP–AuNP bio-inks was produced and assessed. Bio-inks prepared under nitrogen treatment from 50 nm GOD–and HRP–AuNPs were found to achieve a fast enzymatic reaction. It was also determined that GOD-AuNPs bio-ink is sufficient to accurately quantify a glucose solution in the biological relevant range of 0-10 mmol/L, within an hour.

To investigate if the activity of the enzyme is not inhibited in the presence of different 3D printing materials the enzymatic activity of the GOD–AuNP bio-ink was carried out in the presence of four filaments (PLA, ABS, HD-Glass, and T-Glase) that were best

suited for use in fabrication of microfluidics. The GOD–AuNP bio-ink was still active in the presence of these 3D printed filaments, thus permitting a reliable spectrophotometric determination of GOD activity.

The immobilisation of these bio-inks on a selected surface of FDM 3D printed objects was also assessed for applications in millifluidic and microfluidic biosensor production. A number of tests were completed to assess immobilisation of these bio-inks to the surface of 3D printed devices. Ineffective nonspecific binding was observed for the GOD–AuNP and HRP–AuNP bio-inks which marked the method unsuitable for use in 3D printed biosensor devices. Changes in properties of AuNPs, such as surface charge during/after conjugation to GOD and HRP enzyme, size of protein and unavailability of the surface on AuNPs, were determined to be influencing factors leading to ineffective bio-ink binding to the 3D printed bio-device (Chen and Klok, 2013).

Solvent-based bio-inks containing GOD-AuNP were prepared to modify 3D printed devices to immobilise the bio-ink on 3D printed surface. Six different solvents, acetone, chloroform, dimethylformamide, dimethyl sulfoxide, hexane and tetrahydrofuran, which can dissolve ABS filaments were used to make solvent-based GOD-AuNP bio-inks. Solvent-based GOD-AuNP bio-inks were found unsuitable to immobilise the bio-ink on the 3D printed surface since approximately 50% of the protein in bio-ink mixture lost activity and were denatured.

The motivation in this research for bio-inks production was to develop a new technique that is easily integrated to bind the functionalised AuNPs to a 3D printed surface. Therefore, surface preparation technique and other methodological approaches to binding AuNPs to 3D print was not considered. Also the preparation of the polymer surface can be costly, time-consuming and it cannot be applied directly (Huang et al., 2008).

Chapter 6

To enable protein-based bio-inks immobilisation on the surface of FDM 3D print, new sets of enzymatic bio-inks for FDM 3D printing were developed using two methodological approaches. GOD and HRP were bound to magnetic AuNPs (NitmagoldGOD and NitmagoldHRP) and magnetic beads (GODDynabeads and HRPDynabeads) to immobilise the bio-inks with a magnet incorporated in the 3D printed object. Immobilisation of these bio-inks on a selected surface of FDM 3D printed objects were also assessed by assessing the enzymatic activity of bio-ink in 3D printed devices. The immobilisation of NitmagoldGOD and NitmagoldHRP bio-inks by using magnet size range from 2-6 mm in diameter to 3D printed devices was not completely achieved. However, evaluating immobilisation of GODDynabeads and HRPDynabeads to 3D printed devices containing 6 mm magnets was accomplished.

Next, the enzymatic activity of GODDynabead bio-ink was determined after decanting into a single and multi 3D printed devices by syringe extruder. This was to evaluate the reproducibility of the modified FDM device to deposit bio-ink of the desired quantity at a specific point so that that biological molecules retain their activity. It was also shown that bio-inks were not affected by the heated build platform of the 3D printer, once decanted into 3D printed devices using this methodological approach. The modified 3D printer allowed fabrication of reproducible single or multiple automated fluidic handling bio-device containing active biological molecules.

As final approach in this chapter, a simple two-step process was designed to detect glucose in solution in an optimised FDM 3D printed transparent PLA insert for spectroscopy. Immobilization of GODDynabeads and HRPDynabeads inside a 3D printed transparent PLA bio-device afforded the opportunity to run multistep chemical reactions. This was confirmed by assessing a glucose solution in the range of 0-13 mmol/L in PLA transparent devices by UV-Vis spectrophotometer.

Chapter 7

To further demonstrates the advantages of promising utility of bio-inks in FDM 3D-printed devices to fabricate customised, integrating compact, lost-cost, effective optical and multifunctional microfluidic and millifluidic devices, three transparent filaments were used.

Transparent ABS, transparent PLA and HD-Glass filaments were used to design, print and assess optical transparent 3D printed devices for UV-Vis spectroscopy. Devices optimized for UV-Vis spectroscopy were printed using these three transparent filaments, and the transparency of each filament was assessed before and after XTC-3D coating. Amongst assessed filaments, HD-Glass was determined as the most suitable filament to 3D print devices/inserts for UV-Vis spectroscopy.

Next a supplementary protein bio-ink β-GalDynabeads to be used to perform enzymatic cascade reactions in FDM 3D printed biosensor devices was developed. The optimised assay was generated to allow quantification of lactose in solution through using all of the β-GalDynabead and GODDynabead and HRPDynabead bio-inks.

The β-GalDynabead and GODDynabead and HRPDynabead bio-inks were immobilised in optimised 3D printed device for UV-Vis spectroscopy. A lactose quantification assay was performed in one step and in three steps in 3D printed biosensors as well as polystyrene cuvettes for comparison. A good linear response at 570 nm to the changes in lactose concentration is achieved using 3D printed biosensor devices. It was determined that reliable spectrophotometric determination and multi-step colorimetric lactose assays could be conducted in 3D printed HD-Glass bio-devices.

Also, the sensitivity of the lactose assay obtained using the bio-inks in the 3D printed device was compared to sensevity of previously reported values obtained for “lactose

quantification based on coupled enzymatic reaction" (Condezo et al., 2014) which was found comparable.

The overall outcome of the study showed that it is possible to produce cheap microfluidic devices with good optical transparency using FDM 3D printing technology to quantify the different concentration of lactose in solution by using developed bio-inks.

8.2 FUTURE WORKS

In the past decade, there has been a significant interest for an killer application that would outperform existing traditional methods for microfluidics (Ho *et al.*, 2015). In recent years, the integration of 3D printing with microfluidic has gained in popularity (Kitson *et al.*, 2012). 3D Printing offers a promising prospect to fabricate microfluidic devices, but current limitations, such as cost and long processing times, accessibility for combinational research needs improving to increase uptake by biochemists and biologists (Streets and Huang, 2013) (Hong *et al.*, 2017). In this research, it has been shown that FDM 3D printing can be a promising technique to overcome these limitations due to the availability of wider range of material, reduced cost, accessibility, and increase of operation time. This thesis developed a set of biomolecular inks (bio-inks) and a methodological approach for printing biological component such as a protein by FDM 3D printers onto the surfaces of 3D printed objects. However, the potential impacts of this basic technology other than the one used here are very diverse and can provide a new area for research with a large range of biological and chemical properties to be designed and printed for many potential applications (Skardal, 2018). Potential applications are transcription/translation modules used to deliver functional RNA (siRNA, aptamers and protein transcripts) and functional proteins, such as bioactive peptides (e.g. insulin) for utilization in 3D-printed medical devices, implant and novel wound healing dressings (Zhang *et al.*, 2011). Another potential use of the demonstrated FDM 3D printing methodological approach in this thesis is to increase research outputs in biological studies for point of care diagnostics (Nge, Rogers and Woolley, 2013) and organ on chips (Huh, Hamilton and Ingber, 2011) development.

The use of FDM 3D printing techniques to deliver biological molecules can also be further explored if permission is given by 3D printer manufacturer to allow further changes to the coding system to have better control over fabrication of 3D models and functionalized bio-inks for research productivity. A range of functionalised polymer

methodologies to link proteins to surfaces in biomedical assays is yet to be developed to allow immobilisation of more functionalise biological molecules without the need of accessories for example magnet. A standard test is also required in order to set a foundation to obtain a printed product with good quality, more reproducible, reliable, safe and suitable for use (Lee, Ann and Chua, 2017). Customised FDM 3D printing filaments can be developed for the 3D printing of integrated multifunctional devices that are not limited to UV curable resins (Waheed et al., 2016), and new filaments are to be characterised for use in the microfluidic application.

The use of FDM 3D-printing to produce cost-effective tools for microfluidic and biomedical applications with much significant potential application is to be further explored (Ballyns *et al.*, 2010)(Patrick *et al.*, 2015). Especially multifunctional microfluidic biosensors devices for determining glucose and lactose in solution, food and blood, which is the focus of many bioanalytical research laboratories (Sharafeldin, Jones and Rusling, 2018) (Ali et al., 2017) (Thakur and Ragavan, 2012).

REFERENCES

Achilli, E., Minguzzi, A., Visibile, A., Locatelli, C., Vertova, A., Naldoni, A., Rondinini, S., Auricchio, F., Marconi, S., Fracchia, M. and Ghigna, P. (2016) '3D-printed photo-spectroelectrochemical devices forin situandin operandoX-ray absorption spectroscopy investigation'. Journal of Synchrotron Radiation, 23(2), pp.622-628.doi: 10.1107/S1600577515024480.

Ahn, S., Montero, M., Odell, D., Roundy, S. and Wright, P. (2002) 'Anisotropic material properties of fused deposition modeling ABS'. Rapid Prototyping Journal, 8(4), pp.248-257.doi: 10.1108/13552540210441166.

Ali, J., Najeeb, J., Asim Ali, M., Farhan Aslam, M. and Raza, A. (2017). Biosensors: Their Fundamentals, Designs, Types and Most Recent Impactful Applications: A Review. Journal of Biosensors & Bioelectronics, 08(01), pp 343-347.doi: 10.4172/2155-6210.1000235

Allen, P., Khaing, Z., Schmidt, C. and Ellington, A. (2014) '3D Printing with Nucleic Acid Adhesives', ACS Biomaterials Science & Engineering, 1(1), pp.19-26. doi:10.1021/ab500026f.

Alsoufi, M. and Elsayed, A. (2018) 'Surface Roughness Quality and Dimensional Accuracy—A Comprehensive Analysis of 100% Infill Printed Parts Fabricated by a Personal/Desktop Cost-Effective FDM 3D Printer'. Materials Sciences and Applications, 09(01), pp.11-40.doi: 10.4236/msa.2018.91002.

Ammam, M. and Fransaer, J. (2010). Two-enzyme lactose biosensor based on β-galactosidase and glucose oxidase deposited by AC-electrophoresis: Characteristics and performance for lactose determination in milk. Sensors and Actuators B: Chemical, 148(2), pp.583-589. doi:10.1016/j.snb.2010.05.027

Anitha, R., Arunachalam, S. and Radhakrishnan, P. (2001) 'Critical parameters influencing the quality of prototypes in fused deposition modelling', Journal of Materials Processing Technology, 118(1–3), pp. 385–388. doi: 10.1016/S0924-0136(01)00980-3.

Armstrong, J., Burke, M., Carter, B., Davis, S. and Perriman, A. (2016). 3D Bioprinting Using a Templated Porous Bioink. Advanced Healthcare Materials, 5(14), pp.1724-1730. doi: https://doi.org/10.1002/adhm.201600022|

Arostegui, A., Sarrionandia, M., Aurrekoetxea, J. and Urrutibeascoa, I. (2006) 'Effect of dissolution-based recycling on the degradation and the mechanical properties of acrylonitrile–butadiene–styrene copolymer'. Polymer Degradation and Stability, 91(11), pp.2768-2774. doi: 10.1016/j.polymdegradstab.2006.03.019.

Au, A., Huynh, W., Horowitz, L. and Folch, A. (2016) '3D-Printed Microfluidics', Angewandte Chemie International Edition, 55(12), pp. 3862–3881. doi: 10.1002/anie.201504382.

Ballyns, J., Cohen, D., Malone, E., Maher, S., Potter, H., Wright, T., Lipson, H. and Bonassar, L. (2010) 'An Optical Method for Evaluation of Geometric Fidelity for Anatomically Shaped Tissue-Engineered Constructs', Tissue Engineering Part C: Methods, 16(4), pp. 693–703. doi: 10.1089/ten.tec.2009.0441.

Bankar, S., Bule, M., Singhal, R. and Ananthanarayan, L. (2009) 'Glucose oxidase - An overview', Biotechnology Advances. Elsevier Inc., 27(4), pp. 489–501. doi: 10.1016/j.biotechadv.2009.04.003.

Bao, C., Conde, J., Polo, E., del Pino, P., Moros, M., Baptista, P., Grazu, V., Cui, D. and de la Fuente, J. (2014) 'A promising road with challenges: Where are gold nanoparticles in translational research?', Nanomedicine, 9(15), pp. 2353–2370. doi: 10.2217/nnm.14.155.

Becker, S., Urbassek, H., Horsch, M. and Hasse, H. (2014) 'Contact angle of sessile drops in Lennard-Jones systems', Langmuir, 30(45), pp. 13606–13614. doi: 10.1021/la503974z.

Benvenuto, P., Kafi, A. K. M. and Chen, A. (2009) 'High performance glucose biosensor based on the immobilization of glucose oxidase onto modified titania nanotube arrays', Journal of Electroanalytical Chemistry. Elsevier B.V., 627(1–2), pp. 76–81. doi: 10.1016/j.jelechem.2008.12.022.

Bergmeyer, H.U.,Gawehn, K. and Grassl, M. (1974) 'Methods of Enzymatic Analysis' (Bergmeyer, H.U. ed) Volume I, 2nd ed. Academic Press, Inc., New York, NY. pp.457-458. doi:10.1016/B978-0-12-091302-2.X5001-4.

Bhattacharjee, N., Urrios, A., Kang, S. and Folch, A. (2016) 'The upcoming 3D-printing revolution in microfluidics'. Lab on a Chip, 16(10), pp.1720-1742. doi: 10.1039/c6lc00163g.

Bhushan, B. and Caspers, M. (2017) 'An overview of additive manufacturing (3D printing) for microfabrication', Microsystem Technologies. Springer Berlin Heidelberg, 23(4), pp. 1117–1124. doi: 10.1007/s00542-017-3342-8.

Bishop, G., Satterwhite, J., Bhakta, S., Kadimisetty, K., Gillette, K., Chen, E. and Rusling, J. (2015) '3D-Printed fluidic devices for nanoparticle preparation and flow-injection amperometry using integrated prussian blue nanoparticle-modified electrodes', Analytical Chemistry, 87(10), pp. 5437–5443. doi: 10.1021/acs.analchem.5b00903.

Boschetto, A. and Bottini, L. (2014) 'Accuracy prediction in fused deposition modeling', International Journal of Advanced Manufacturing Technology, 73(5–8), pp. 913–928. doi: 10.1007/s00170-014-5886-4.

Brisendine, J., Mutter, A., Cerda, J. and Koder, R. (2013) 'A three-dimensional printed

cell for rapid, low-volume spectroelectrochemistry', Analytical Biochemistry. Elsevier Inc., 439(1), pp. 1–3. doi: 10.1016/j.ab.2013.03.036.

Cantrell, J., Rohde, S., Damiani, D., Gurnani, R., DiSandro, L., Anton, J., Young, A., Jerez, A., Steinbach, D., Kroese, C. and Ifju, P. (2017). Experimental characterization of the mechanical properties of 3D-printed ABS and polycarbonate parts. Rapid Prototyping Journal, 23(4), pp.811-824.doi:10.1108/rpj-03-2016-0042

Capel, A., Edmondson, S., Christie, S., Goodridge, R., Bibb, R. and Thurstans, M. (2013)'Design and additive manufacture for flow chemistry', Lab on a Chip, 13(23), pp. 4583–4590. doi: 10.1039/c3lc50844g.

Ceretti, E., Ginestra, P., Neto, P., Fiorentino, A. and Da Silva, J. (2017) 'Multi-layered Scaffolds Production via Fused Deposition Modeling (FDM) Using an Open Source 3D Printer: Process Parameters Optimization for Dimensional Accuracy and Design Reproducibility', Procedia CIRP, 65, pp. 13–18. doi: 10.1016/j.procir.2017.04.042.

Chae, M., Rozen, W., McMenamin, P., Findlay, M., Spychal, R. and Hunter-Smith, D. (2015) 'Emerging Applications of Bedside 3D Printing in Plastic Surgery', Frontiers in Surgery, 2, pp. 1–14. doi: 10.3389/fsurg.2015.00025.

Chamran, M. and Keiser, R. (1978). Maintaining optimum spectrophotometer performance. Part 1, Laboratory Medicine, Volume 9, 4th ed, Überlingen: Bodenseewerk Perkin-Elmer & Co. pp.33-39. doi: 10.1093/labmed/9.4.33

Chapiro, M. (2016) 'Current achievements and future outlook for composites in 3D printing', Reinforced Plastics. Elsevier Ltd, 60(6), pp. 372–375. doi: 10.1016/j.repl.2016.10.002.

Chen, L. and Klok, H. A. (2013) 'Multifaceted" Polymer Coated, Gold Nanoparticles', Soft Matter, 9(45), pp. 10678–10688. doi: 10.1039/c3sm51789f.

Cheng, C. and Gupta, M. (2017) 'Surface functionalization of 3D-printed plastics via initiated chemical vapor deposition', Beilstein Journal of Nanotechnology, 8(1), pp. 1629–1636. doi: 10.3762/bjnano.8.162.

Chimene, D., Lennox, K., Kaunas, R. and Gaharwar, A. (2016) 'Advanced Bioinks for 3D Printing: A Materials Science Perspective', Annals of Biomedical Engineering, 44(6), pp. 2090–2102. doi: 10.1007/s10439-016-1638-y.

Chisholm, G., Kitson, P., Kirkaldy, N., Bloor, L. and Cronin, L. (2014) '3D printed flow plates for the electrolysis of water: An economic and adaptable approach to device manufacture', Energy and Environmental Science. Royal Society of Chemistry, 7(9), pp. 3026–3032. doi: 10.1039/c4ee01426j.

Chiulan, I., Frone, A., Brandabur, C. and Panaitescu, D. (2017) 'Recent Advances in 3D Printing of Aliphatic Polyesters', Bioengineering, 5(1), pp. 2-4. doi: 10.3390/bioengineering5010002.

Choi, Y., Kim, C., Jeong, H. and Youn, J. (2016) 'Influence of Bed Temperature on Heat Shrinkage Shape Error in FDM Additive Manufacturing of the ABS-Engineering Plastic', World Journal of Engineering and Technology, 04(03), pp. 186–192. doi: 10.4236/wjet.2016.43D022.

Christenson, R. H. (2007) 'National Academy of Clinical Biochemistry Laboratory Medicine Practice Guidelines for Utilization of Biomarkers in Acute Coronary Syndromes and Heart Failure', Clinical Biochemistry, 53(4), pp. 545–546. doi: 10.1016/j.clinbiochem.2007.07.003.

Chudobova, D., Cihalova, K., Skalickova, S., Zitka, J., Rodrigo, M.A., Milosavljevic, V., Hynek, D., Kopel, P., Vesely, R., Adam, V., and Kizek, R. (2015) '3D-printed chip for detection of methicillin-resistant Staphylococcus aureus labeled with gold nanoparticles', Electrophoresis, 36(3), pp. 457–466. doi: 10.1002/elps.201400321.

Condezo-Hoyos, L., Mohanty, I. P. and Noratto, G. D. (2014) 'Technical note: Optimization of lactose quantification based on coupled enzymatic reactions', Journal of Dairy Science. Elsevier, 97(4), pp. 2066–2070. doi: 10.3168/jds.2013-7436.

Conzuelo, F., Gamella, M., Campuzano, S., Ruiz, M., Reviejo, A. and Pingarrón, J. (2010) 'An integrated amperometric biosensor for the determination of lactose in milk and dairy products', Journal of Agricultural and Food Chemistry, 58(12), pp. 7141–7148. doi: 10.1021/jf101173e.

Cook, C. C., Wang, T. and Derby, B. (2010) 'Inkjet delivery of glucose oxidase', Chemical Communications, 46(30), pp. 5452–5454. doi: 10.1039/c0cc00567c.

Cordeiro, M., Ferreira Carlos, F., Pedrosa, P., Lopez, A. and Baptista, P. (2016) 'Gold nanoparticles for diagnostics: Advances towards points of care', Diagnostics, 6(4),pp 43-45. doi: 10.3390/diagnostics6040043.

Cui, X., Dean, D., Ruggeri, Z. and Boland, T. (2010) 'Cell damage evaluation of thermal inkjet printed chinese hamster ovary cells', Biotechnology and Bioengineering, 106(6), pp. 963–969. doi: 10.1002/bit.22762.

Cui, X., Gao, G., Yonezawa, T. and Dai, G. (2014) 'Human Cartilage Tissue Fabrication Using Three-dimensional Inkjet Printing Technology', Journal of Visualized Experiments, (88), pp. 1–5. doi: 10.3791/51294.

Dao, Q., Frimodig, J., Le, H., Li, X., Putnam, S., Golda, K., Foyos, J., Noorani, R. and Fritz, B. (1999) 'Calculation of Shrinkage Compensation Factors for Rapid Prototyping (FDM 1650)', Computer Applications in Engineering Education, 7(3), pp. 186–195. doi: 10.1002/(SICI)1099-0542(1999)7:3<186::AID-CAE7>3.0.CO;2-Q.

Deckard, C., Beaman, J. and Darrah, J. (1992) 'Method for selective laser sintering with layerwise cross-scanning'. Available at: http://www.google.co.uk/patents/US5155324.

Delamarche, E. (1997) ‘Patterned delivery of immunoglobulins to surfaces using microfluidic networks’, Science, 276(5313), pp. 779–781. doi: 10.1126/science.276.5313.779.

Dimitrijević, S., Rajčić-Vujasinović, M., Alagić, S., Grekulović, V. and Trujić, V. (2013). Formulation and characterization of electrolyte for decorative gold plating based on mercaptotriazole. Electrochimica Acta, 104, pp.330-336.

Desai, R. (2017). 3D PRINTING. [Blog] An Educational Blog. Available at: http://drrajivdesaimd.com/2017/06/26/3d-printing/comment-page-1/#comment-3727851 [Accessed 5 Nov. 2018].

Divya, P., Savitri, D. and Mitra, C. (1998) ‘Covalent enzyme immobilization onto glassy carbon matrix-implications in biosensor design’, Bioscience, 23(2), pp. 131–136.

Drummer, D., Cifuentes-Cuéllar, S. and Rietzel, D. (2012) ‘Suitability of PLA/TCP for fused deposition modeling’, Rapid Prototyping Journal, 18(6), pp. 500–507. doi: 10.1108/13552541211272045.

Eggins, B. R. (1997) ‘Biosensors - An Introduction’, Biosensors & bioelectronics, 12(1), pp. 1–2. doi: 10.1007/s10462-010-9185-7.

Elsholtz, C. and Harper, A. J. (2015) ‘Additive decompositions of sets with restricted prime factors’, Transactions of the American Mathematical Society. Elsevier B.V., 367(10), pp. 7403–7427. doi: 10.1016/j.addma.2015.10.001.

Erich, S., Anzmann, T. and Fischer, L. (2012) ‘Quantification of lactose using ion-pair RP-HPLC during enzymatic lactose hydrolysis of skim milk’, Food Chemistry. Elsevier Ltd, 135(4), pp. 2393–2396. doi: 10.1016/j.foodchem.2012.07.059.

Evans, T.C., Gavrilovich, E., Mihai, R.C. and Isbasescu, I., E. L. et al. (2014) ‘3D printing shrinkage compensation using radial and angular layer perimeter point

information', 202(15), pp. 354-359. doi: 10.1037/t24245-000.

Förch, R, Schönherr, H & Jenkins, A (2009) Surface Design: Applications in Bioscience and Nanotechnology. Volume 7, 2nd ed Weinheim, Wiley-VCH. pp.55-80. doi:10.1002/9783527628599.ch3

Fornera, S., Yazawa, K. and Walde, P. (2011) 'Spectrophotometric quantification of lactose in solution with a peroxidase-based enzymatic cascade reaction system', Analytical and Bioanalytical Chemistry, 401(7), pp. 2307–2310. doi: 10.1007/s00216-011-5312-9.

Fritz, B and Noorani, R. (1998). 'Calibrating X and Y shrinkage compensation factors for the Sanders prototype and stereolithography systems'. Northrop Grumman Corporation, Pico Rivera, CA, p. 1.

Gerstle, L., Ibrahim, A., Kim, P., Lee, B., Lin, S. (2014) 'A plastic surgery application in evolution: Three-dimensional printing', Plastic and Reconstructive Surgery, 133(2), pp. 446–451. doi: 10.1097/01.prs.0000436844.92623.d3.

Go, J., Schiffres, S., Stevens, A. and Hart, A. (2019). Rate limits of additive manufacturing by fused filament fabrication and guidelines for high-throughput system design. doi: 10.1016/j.addma.2017.03.007

Godoi, F. C., Prakash, S. and Bhandari, B. R. (2016) '3d printing technologies applied for food design: Status and prospects', Journal of Food Engineering. Elsevier Ltd, 179, pp. 44–54. doi: 10.1016/j.jfoodeng.2016.01.025.

Goebel-Stengel, M., Stengel, A., Taché, Y. and Reeve, J (2011) 'The importance of using the optimal plasticware and glassware in studies involving peptides', Analytical Biochemistry. Elsevier Inc., 414(1), pp. 38–46. doi: 10.1016/j.ab.2011.02.009.

Gopinathan, J. and Noh, I. (2018) 'Recent trends in bioinks for 3D printing',

Biomaterials Research. Biomaterials Research, 22(1), pp. 1–15. doi: 10.1186/s40824-018-0122-1.

Gordeev, E. G., Galushko, A. S. and Ananikov, V. P. (2018) 'Improvement of quality of 3D printed objects by elimination of microscopic structural defects in fused deposition modeling', PLoS ONE, 13(6). doi: 10.1371/journal.pone.0198370.

Gross, B., Erkal, J., Lockwood, S., Chen, C. and Spence, D. (2014) 'Evaluation of 3D printing and its potential impact on biotechnology and the chemical sciences', Analytical Chemistry, 86(7), pp. 3240–3253. doi: 10.1021/ac403397r.

Gumpenberger, T., Sato, T., Kurosaki, R., Narazaki, A., Kawaguchi, Y. and Niino, H. (2006) 'Fabrication of a novel microfluidic device incorporating 2-D array of microbeads', Chemistry Letters, 35(2), pp. 218–219. doi: 10.1246/cl.2006.218.

Guzik, U., Hupert-Kocurek, K. and Wojcieszynska, D. (2014) 'Immobilization as a strategy for improving enzyme properties- Application to oxidoreductases', Molecules, 19(7), pp. 8995–9018. doi: 10.3390/molecules19078995.

Hartmann, M. and Jung, D. (2010) 'Biocatalysis with enzymes immobilized on mesoporous hosts: The status quo and future trends', Journal of Materials Chemistry, 20(5), pp. 844–857. doi: 10.1039/b907869j.

He, Y., Wu, Y., Fu, J., Gao, Q. and Qiu, J. (2016) 'Developments of 3D Printing Microfluidics and Applications in Chemistry and Biology: a Review', Electroanalysis, 28(8), pp. 1658–1678. doi: 10.1002/elan.201600043.

Heddle, J. (2013) 'Gold Nanoparticle-Biological Molecule Interactions and Catalysis', Catalysts, 3(3), pp. 683–708. doi: 10.3390/catal3030683.

Helena N Chia and Wu, B. M. (2015) 'Recent advances in 3D printing of tissue engineering scaffolds', Methods in Molecular Biology, 868, pp. 257–267. doi:

10.1007/978-1-61779-764-4_15.

Hinton, T., Jallerat, Q., Palchesko, R., Park, J., Grodzicki, M., Shue, H., Ramadan, M., Hudson, A. and Feinberg, A. (2015) 'Three-dimensional printing of complex biological structures by freeform reversible embedding of suspended hydrogels', Science Advances, 1(9), pp. 1–10. doi: 10.1126/sciadv.1500758.

Ho, C., Ng, S., Li, K. and Yoon, Y. (2015) '3D printed microfluidics for biological applications', Lab on a Chip, 15(18), pp. 3627–3637. doi: 10.1039/c5lc00685f.

Holland, S., Foster, T., MacNaughtan, W. and Tuck, C. (2018) 'Design and characterisation of food grade powders and inks for microstructure control using 3D printing', Journal of Food Engineering. Elsevier Ltd, 220, pp. 12–19. doi: 10.1016/j.jfoodeng.2017.06.008.

Hong, N., Yang, G., Lee, J. and Kim, G. (2017) '3D bioprinting and its in vivo applications', Journal of Biomedical Materials Research - Part B Applied Biomaterials, 106(1), pp. 444–459. doi: 10.1002/jbm.b.33826.

Horowitz, V. R., Awschalom, D. D. and Pennathur, S. (2008) 'Optofluidics: Field or technique?', Lab on a Chip, 8(11), pp. 1856–1863. doi: 10.1039/b816416a.

House, J. L., Anderson, E. M. and Ward, W. K. (2007) 'Immobilization techniques to avoid enzyme loss from oxidase-based biosensors: A one-year study', Journal of Diabetes Science and Technology, 1(1), pp. 18–27. doi: 10.1177/193229680700100104.

Huang, X., Li, Y., Chen, Y. and Wang, L. (2008) 'Electrochemical determination of nitrite and iodate by use of gold nanoparticles/poly(3-methylthiophene) composites coated glassy carbon electrode', Sensors and Actuators, B: Chemical, 134(2), pp. 780–786. doi: 10.1016/j.snb.2008.06.028.

Huggett, A. and Nixon, D. (1957). 'Use of glucose oxidase, peroxidase, and O-

dianisidine in determination of blood and urinary glucose'.The Lancet, 270(6991), pp. 368-370. doi: 10.1016/S0140-6736(57)92595-3

Huh, D., Hamilton, G. A. and Ingber, D. E. (2011) 'From 3D cell culture to organs-on-chips', Trends in Cell Biology. Elsevier Ltd, 21(12), pp. 745–754. doi: 10.1016/j.tcb.2011.09.005.

Hull, C. W. and Arcadia, C. (1986) 'Apparatus for Production of Three-Dimensional Objects By Stereolthography', 2(19). pp. 185-188. doi: US005485919A.

Hutmacher, D., Schantz, T., Zein, I., Ng, K., Teoh, S. and Tan, K. (2001) 'Mechanical properties and cell cultural response of polycaprolactone scaffolds designed and fabricated via fused deposition modeling', Journal of Biomedical Materials Research, 55(2), pp. 203–216. doi: 10.1002/1097-4636(200105)55:2<203::AID-JBM1007>3.0.CO;2-7.

Hwang, S., Reyes, E., Moon, K., Rumpf, R. and Kim, N. (2014) 'Thermo-mechanical Characterization of Metal/Polymer Composite Filaments and Printing Parameter Study for Fused Deposition Modeling in the 3D Printing Process', Journal of Electronic Materials, 44(3), pp. 771–777. doi: 10.1007/s11664-014-3425-6.

Illg, T., Löb, P. and Hessel, V. (2010) 'Flow chemistry using milli- and microstructured reactors-From conventional to novel process windows', Bioorganic and Medicinal Chemistry. Elsevier Ltd, 18(11), pp. 3707–3719. doi: 10.1016/j.bmc.2010.03.073.

Ingebrigtsen, T. and Toxvaerd, S. (2007) 'Contact angles of Lennard-Jones liquids and droplets on planar surfaces', Journal of Physical Chemistry C, 111(24), pp. 8518–8523. doi: 10.1021/jp0676235.

Jackson, R., Patrick, P., Page, K., Powell, M., Lythgoe, M., Miodownik, M., Parkin, I., Carmalt, C., Kalber, T. and Bear, J. (2018) 'Chemically Treated 3D Printed Polymer

Scaffolds for Biomineral Formation', ACS Omega, 3(4), pp. 4342–4351. doi: 10.1021/acsomega.8b00219.

Jang, J., Yi, H. G. and Cho, D. W. (2016) '3D Printed Tissue Models: Present and Future', ACS Biomaterials Science and Engineering, 2(10), pp. 1722–1731. doi: 10.1021/acsbiomaterials.6b00129.

Ji, S. and Guvendiren, M. (2017) 'Recent Advances in Bioink Design for 3D Bioprinting of Tissues and Organs', Frontiers in Bioengineering and Biotechnology, 5(1), pp. 1–8. doi: 10.3389/fbioe.2017.00023.

Jonkheijm, P., Weinrich, D., Schröder, H., Niemeyer, C. and Waldmann, H. (2008) 'Chemical strategies for generating protein biochips', Angewandte Chemie - International Edition, 47(50), pp. 9618–9647. doi: 10.1002/anie.200801711.

Jose, R., Rodriguez, M., Dixon, T., Omenetto, F. and Kaplan, D. (2016) 'Evolution of Bioinks and Additive Manufacturing Technologies for 3D Bioprinting', ACS Biomaterials Science and Engineering, 2(10), pp. 1662–1678. doi: 10.1021/acsbiomaterials.6b00088.

Kadimisetty, K., Mosa, I., Malla, S., Satterwhite-Warden, J., Kuhns, T., Faria, R., Lee, N. and Rusling, J. (2016) '3D-printed supercapacitor-powered electrochemiluminescent protein immunoarray', Biosensors and Bioelectronics. Elsevier, 77, pp. 188–193. doi: 10.1016/j.bios.2015.09.017.

Kalenda, P. and Kalendová, A. (1995) 'Improved chemical resistance of epoxy resin-based coating compositions', Dyes and Pigments, 27(4), pp. 305–312. doi: 10.1016/0143-7208(94)00070-I.

Kalita, S., Bose, S., Hosick, H. and Bandyopadhyay, A. (2003) 'Development of controlled porosity polymer-ceramic composite scaffolds via fused deposition

modeling', Materials Science and Engineering C, 23(5), pp. 611–620. doi: 10.1016/S0928-4931(03)00052-3.

Kawahara, H., Matsufuji, S., Goto, T., Okamoto, Y., Ogura, H., Kage, H. and Matsuno, Y. (2001) 'Epoxy resin/acrylic composite latexes: Reactivity and stability of epoxy groups with carboxyl groups', Advanced Powder Technology. Society of Powder Technology Japan, 12(4), pp. 521–532. doi: 10.1163/15685520152756651.

Khademhosseini, A. and Bong, G. C. (2006) 'Microscale technologies for tissue engineering', 2009 IEEE/NIH Life Science Systems and Applications Workshop, LiSSA 2009, 103(8), pp. 56–57. doi: 10.1109/LISSA.2009.4906708.

Khalil, I., Julkapli, N., Yehye, W., Basirun, W. and Bhargava, S. (2016). 'Graphene–gold nanoparticles hybrid—synthesis, functionalization, and application in a electrochemical and surface-enhanced raman scattering biosensor'. Materials, 9(6), pp.406-409.doi: 10.3390/ma9060406.

Khatiwala, C., Law, R., Shepherd, B., Dorfman, S and Csete, M (2012) '3D Cell Bioprinting for Regenerative Medicine Research and Therapies', Gene Therapy and Regulation, 07(01), pp. 123-134. doi: 10.1142/S1568558611000301.

Kim, D. and Herr, A. E. (2013) 'Protein immobilization techniques for microfluidic assays', Biomicrofluidics, 7(4), pp. 1–47. doi: 10.1063/1.4816934.

Kim, D. N., Lee, Y. and Koh, W. G. (2009) 'Fabrication of microfluidic devices incorporating bead-based reaction and microarray-based detection system for enzymatic assay', Sensors and Actuators, B: Chemical, 137(1), pp. 305–312. doi: 10.1016/j.snb.2008.12.042.

Kim, J., Baek, J., Kim, H., Lee, K. and Lee, S. (2006) 'Integration of enzyme immobilized single-walled carbon nanotubes mass into the microfluidic platform and its

application for the glucose-detection', Sensors and Actuators, A: Physical, 128(1), pp. 7–13. doi: 10.1016/j.sna.2005.12.039.

King, E. et al. (1997) 'Solvent-assisted microcontact molding: A convenient method for fabricating three-dimensional structures on surfaces of polymers', Advanced Materials, 9(8), pp. 651–654. doi: 10.1002/adma.19970090814.

Kiński, W., Nalepa, K., Miąskowski, W. and Pietkiewicz, P. (2016). Analysis of print quality selected 3d printers FDM technology. Mechanik, (7), pp.724-725. doi: 10.17814/mechanik.2016.7.143

Kirschenbaum, D. (1978). 'Molar absorptivity and A 1 cm 1% values for proteins at selected wavelengths of the ultraviolet and visible regions. XV'. Analytical Biochemistry, 87(1), pp.223-242.

Kitson, P., Rosnes, M., Sans, V., Dragone, V. and Cronin, L. (2012) 'Configurable 3D-Printed millifluidic and microfluidic "lab on a chip" reactionware devices', Lab on a Chip, 12(18), pp. 3267–3271. doi: 10.1039/c2lc40761b.

Kitson, P., Symes, M., Dragone, V. and Cronin, L. (2013) 'Combining 3D printing and liquid handling to produce user-friendly reactionware for chemical synthesis and purification', Chemical Science, 4(8), pp. 3099–3103. doi: 10.1039/c3sc51253c.

Kokkinis, D., Schaffner, M. and Studart, A. (2015) 'Multimaterial magnetically assisted 3D printing of composite materials', Acta Medica Okayama, 45(5), pp. 333–338. doi: 10.1038/ncomms9643.

Kouassi, G. K. (2011) 'Magnetic and gold-coated magnetic Iron oxide nanoparticles as detection tools: preparation, characterization, and biosensing applications', Current Nanoscience, 7, pp. 510–523. doi: 10.2174/157341311796196907.

Kulshreshtha, A., Singh, B. and Sharma, Y. (1988) 'Viscometric determination of

compatibility in PVC/ABS polyblends. Part III. Choice of a common solvent and its effect on results', 24(2), pp. 191–194.

Kurlyandskaya, G. and Levit, V. (2005). Magnetic Dynabeads® detection by sensitive element based on giant magnetoimpedance. Biosensors and Bioelectronics, 20(8), pp.1611-1616.

Kwok, D., Gietzelt, T., Grundke, K., Jacobasch, H. and Neumann, A. (1997) 'Contact Angle Measurements and Contact Angle Interpretation. 1. Contact Angle Measurements by Axisymmetric Drop Shape Analysis and a Goniometer Sessile Drop Technique', Langmuir, 13(10), pp. 2880–2894. doi: 10.1021/la9608021.

Le Duigou, A., Castro, M., Bevan, R. and Martin, N. (2016) '3D printing of wood fibre biocomposites: From mechanical to actuation functionality', Materials and Design. Elsevier Ltd, 96, pp. 106–114. doi: 10.1016/j.matdes.2016.02.018.

Lee, B. H., Abdullah, J. and Khan, Z. A. (2016) 'Optimization of rapid prototyping parameters for production of flexible ABS object', Journal of Materials Processing Technology, 169(1), pp. 54–61. doi: 10.1016/j.jmatprotec.2005.02.259.

Lee, J. and Lee, S. H. (2013) 'Lab on a chip for in situ diagnosis: From blood to point of care', Biomedical Engineering Letters, 3(2), pp. 59–66. doi: 10.1007/s13534-013-0094-y.

Lee, J. M., Zhang, M. and Yeong, W. Y. (2016) 'Characterization and evaluation of 3D printed microfluidic chip for cell processing', Microfluidics and Nanofluidics. Springer Berlin Heidelberg, 20(1), pp. 1–15. doi: 10.1007/s10404-015-1688-8.

Lee, J. Y., Ann, J. and Chua, C. K. (2017) 'Fundamentals and applications of 3D printing for novel materials', Applied Materials Today. Elsevier Ltd, 7, pp. 120–133. doi: 10.1016/j.apmt.2017.02.004.

Levato, R., Visser, J., Planell, J., Engel, E., Malda, J. and Mateos-Timoneda, M. (2014) 'Biofabrication of tissue constructs by 3D bioprinting of cell-laden microcarriers', Biofabrication. IOP Publishing, 6(3), pp 350-362. doi: 10.1088/1758-5082/6/3/035020.

Li, D., He, Q., Cui, Y., Duan, L. and Li, J. (2007) 'Immobilization of glucose oxidase onto gold nanoparticles with enhanced thermostability', Biochemical and Biophysical Research Communications, 355(2), pp. 488–493. doi: 10.1016/j.bbrc.2007.01.183.

Ligon, S. C., Liska, R., Stampfl, J., Gurr, M., Mülhaupt, R. (2017) 'Polymers for 3D Printing and Customized Additive Manufacturing', Chemical Reviews, 117(15), pp. 10212–10290. doi: 10.1021/acs.chemrev.7b00074.

Liu, R., Mi, S., Li, Y., Chen, C., Xie, Y., Chen, Q. and Chen, Z. (2016). Synthesis of monodispersed Fe3O4@C core/shell nanoparticles. Science China Chemistry, 59(4), pp.394-397. doi:10.1007/s11426-015-5551-2

Liu, Y., Chi, Y., Li, X., Wang, S. and Lin, S. (2013) 'Research Development on the Preparation of NiFe Magnetic Nanoparticles', Advanced Materials Research, 756, pp. 128–131. doi: 10.4028/www.scientific.net/AMR.391-392.381.

Livak-Dahl, E., Sinn, I. and Burns, M. (2011) 'Microfluidic Chemical Analysis Systems', Annual Review of Chemical and Biomolecular Engineering, 2(1), pp. 325–353. doi: 10.1146/annurev-chembioeng-061010-114215.

Locascio, L. E., Perso, C. E. and Lee, C. S. (1999) 'Measurement of electroosmotic flow in plastic imprinted microfluid devices and the effect of protein adsorption on flow rate', Journal of Chromatography A, 857(1–2), pp. 275–284. doi: 10.1016/S0021-9673(99)00774-8.

Macdonald, N., Cabot, J., Smejkal, P., Guijt, R., Paull, B. and Breadmore, M. (2017) 'Comparing Microfluidic Performance of Three-Dimensional (3D) Printing Platforms',

Analytical Chemistry, 89(7), pp. 3858–3866. doi: 10.1021/acs.analchem.7b00136.

Mao, H., Yang, T. and Cremer, P. S. (2002) 'Design and characterization of immobilized enzymes in microfluidic systems', Analytical Chemistry, 74(2), pp. 379–385. doi: 10.1021/ac010822u.

Mark, D., Haeberle, S., Roth, G., Stetten, F. and Zengerle, R. (2010) 'Microfluidic lab-on-a-chip platforms: Requirements, characteristics and applications', Chemical Society Reviews, 39(3), pp.1153-1176. pp. doi: 10.1007/978-90-481-9029-4-17.

Martynova, L., Locascio, L., Gaitan, M., Kramer, G., Christensen, R. and MacCrehan, W. (1997) 'Fabrication of Plastic Microfluid Channels by Imprinting Methods', Analytical Chemistry, 69(23), pp. 4783–4789. doi: 10.1021/ac970558y.

Masood, S. H. and Song, W. Q. (2004) 'Development of new metal/polymer materials for rapid tooling using Fused deposition modelling', Materials and Design, 25(7), pp. 587–594. doi: 10.1016/j.matdes.2004.02.009.

Mateo, C., Palomo, J., Fernandez-Lorente, G., Guisan, J. and Fernandez-Lafuente, R. (2007) 'Improvement of enzyme activity, stability and selectivity via immobilization techniques', Enzyme and Microbial Technology, 40(6), pp. 1451–1463. doi: 10.1016/j.enzmictec.2007.01.018.

Mehesz, A., Brown, J., Hajdu, Z., Beaver, W., da Silva, J., Visconti, R., Markwald, R. and Mironov, V. (2011) 'Scalable robotic biofabrication of tissue spheroids', Biofabrication, 3(2). pp. 25-29. doi: 10.1088/1758-5082/3/2/025002.

Mirasoli, M., Guardigli, M., Michelini, E. and Roda, A. (2014) 'Recent advancements in chemical luminescence-based lab-on-chip and microfluidic platforms for bioanalysis', Journal of Pharmaceutical and Biomedical Analysis. 87(1), pp.36-52.doi: 10.1016/j.jpba.2013.07.008.

Mohamad, N., Marzuki, N., Buang, N., Huyop, F. and Wahab, R. (2015) 'An overview of technologies for immobilization of enzymes and surface analysis techniques for immobilized enzymes', Biotechnology and Biotechnological Equipment, 29(2), pp. 205–220. doi:10.1080/13102818.2015.1008192.

Mohamed, O. A., Masood, S. H. and Bhowmik, J. L. (2016) 'Analytical modelling and optimization of the temperature-dependent dynamic mechanical properties of fused deposition fabricated parts made of PC-ABS', Materials, 9(11), pp 895-899. doi: 10.3390/ma9110895.

Monti, M. (2016). Bioprinting in Regenerative Medicine. European Journal of Histochemistry, 60(1), pp.26-27. doi:10.4081/ejh.2016.2627

Moore, J., McCuiston, A., Mittendorf, I., Ottway, R. and Johnson, R. (2011) 'Behavior of capillary valves in centrifugal microfluidic devices prepared by three-dimensional printing', Microfluidics and Nanofluidics, 10(4), pp. 877–888. doi: 10.1007/s10404-010-0721-1.

Moraes Silva, S., Tavallaie, R., Sandiford, L., Tilley, R. and Gooding, J. (2016) 'Gold coated magnetic nanoparticles: From preparation to surface modification for analytical and biomedical applications', Chemical Communications, 52(48), pp. 7528–7540. doi: 10.1039/c6cc03225g.

Morgan, A., Hidalgo San Jose, L., Jamieson, W., Wymant, J., Song, B., Stephens, P., Barrow, D. and Castell, O. (2016) 'Simple and versatile 3D printed microfluidics using fused filament fabrication', PLoS ONE, 11(4), pp. 1–17. doi: 10.1371/journal.pone.0152023.

Mulakkal, M., Trask, R., Ting, V. and Seddon, A. (2018). Responsive cellulose-hydrogel composite ink for 4D printing. Materials & Design, 160, pp.108-118. doi:10.1016/j.matdes.2018.09.009

Munaz, A., Vadivelu, R., St. John, J., Barton, M., Kamble, H. and Nguyen, N. (2016) 'Three-dimensional printing of biological matters', Journal of Science: Advanced Materials and Devices. Elsevier Ltd, 1(1), pp. 1–17. doi: 10.1016/j.jsamd.2016.04.001.

Murphy, S. and Atala, A. (2014). 3D bioprinting of tissues and organs. Nature Biotechnology, 32(8), pp.773-785. doi: 10.1038/nbt.2958

Murphy, C., Thompson, L., Alkilany, A., Sisco, P., Boulos, S., Sivapalan, S., Yang, J., Chernak, D. and Huang, J. (2010) 'The many faces of gold nanorods', Journal of Physical Chemistry Letters, 1(19), pp. 2867–2875. doi: 10.1021/jz100992x.

Murphy, S. V. and Atala, A. (2014) '3D bioprinting of tissues and organs', Nature Biotechnology. 32(8), pp. 773–785. doi: 10.1038/nbt.2958.

Nakanishi, K., Sakiyama, T. and Imamura, K. (2001) 'On the adsorption of proteins on solid surfaces, a common but very complicated phenomenon', Journal of Bioscience and Bioengineering, 91(3), pp. 233–244. doi: 10.1016/S1389-1723(01)80127-4.

Nge, P. N., Rogers, C. I. and Woolley, A. T. (2013) 'Advances in microfluidic materials, functions, integration, and applications', Chemical Reviews, 113(4), pp. 2550–2583. doi: 10.1021/cr300337x.

Nitzsche, B., Ruhnow, F. and Diez, S. (2008) 'Quantum-dot-assisted characterization of microtubule rotations during cargo transport', Nature Nanotechnology, 3(9), pp. 552–556. doi: 10.1038/nnano.2008.216.

Norde, W. (1986) 'Adsorption of proteins from solution at the solid-liquid interface', Advances in Colloid and Interface Science, 25(3), pp. 267–340. doi: 10.1016/0001-8686(86)80012-4.

Oberpenning, F., Meng, J., Yoo, J. and Atala, A. (1999) 'De Novo Reconstitution of a Functional Mammalian Urinary Bladder by Tissue Engineering', Nature biotechnology,

2(17), pp. 149–155. doi: 10.1063/1.4898632

Okafor, O., Weilhard, A., Fernandes, J., Karjalainen, E., Goodridge, R. and Sans, V. (2017) 'Advanced reactor engineering with 3D printing for the continuous-flow synthesis of silver nanoparticles', Reaction Chemistry and Engineering, 2(2), pp. 129–136. doi: 10.1039/c6re00210b.

Okamoto, T., Suzuki, T. and Yamamoto, N. (2000) 'Microarray fabrication with covalent attachment of DNA using Bubble Jet technology', Nature Biotechnology, 18(4), pp. 438–441. doi: 10.1038/74507.

Okwuosa, T., Soares, C., Gollwitzer, V., Habashy, R., Timmins, P. and Alhnan, M. (2018) 'On demand manufacturing of patient-specific liquid capsules via co-ordinated 3D printing and liquid dispensing', European Journal of Pharmaceutical Sciences. 118, pp.134-143. doi: 10.1016/j.ejps.2018.03.010.

O'Neill, P., Ben Azouz, A., Vázquez, M., Liu, J., Marczak, S., Slouka, Z., Chang, H., Diamond, D. and Brabazon, D. (2014) 'Advances in three-dimensional rapid prototyping of microfluidic devices for biological applications', Biomicrofluidics, 8(5), pp.102-112. doi: 10.1063/1.4898632.

Openpcr.org. (2018). OpenPCR - the $499 Open Source PCR Machine / Thermal Cycler. [online] Available at: https://openpcr.org [Accessed 20 Apr. 2018].

Owens, C., Marga, F., Forgacs, G. and Heesch, C (2013) 'Biofabrication and testing of a fully cellular nerve graft', Biofabrication, 5(4), pp.45-47. doi: 10.1088/1758-5082/5/4/045007.

Ozbolat, I. T. and Hospodiuk, M. (2016) 'Current advances and future perspectives in extrusion-based bioprinting', Biomaterials. Elsevier, 76, pp. 321–343. doi: 10.1016/j.biomaterials.2015.10.076.

Parsa, S., Gupta, M., Loizeau, F. and Cheung, K. (2010) 'Effects of surfactant and gentle agitation on inkjet dispensing of living cells', Biofabrication, 2(2), pp.25-29. doi: 10.1088/1758-5082/2/2/025003.

Pati, F., Jang, J., Ha, D., Won Kim, S., Rhie, J., Shim, J., Kim, D. and Cho, D. (2014) 'Printing three-dimensional tissue analogues with decellularized extracellular matrix bioink', Nature Communications. 5(1), pp. 1–11. doi: 10.1038/ncomms4935.

Patrick, W., Nielsen, A., Keating, S., Levy, T., Wang, C., Rivera, J., Mondragón-Palomino, O., Carr, P., Voigt, C., Oxman, N. and Kong, D. (2015) 'DNA assembly in 3D printed fluidics', PLoS ONE, 10(12), pp. 1–18. doi: 10.1371/journal.pone.0143636.

Paul C.H. Li (2010) Fundamentals of Microfluidics and Lab on a Chip for Biological Analysis and Discovery. Volume I, 2nd ed. Boca Raton: CRC Press. pp.22-36

Peng, T. and Yan, F. (2018). Dual-objective Analysis for Desktop FDM Printers: Energy Consumption and Surface Roughness. Procedia CIRP, 69, pp.106-111. 10.1016/j.procir.2017.11.084

Petruccioli, M., Federici, F., Bucke, C. and Keshavarz, T. (1999) 'Enhancement of glucose oxidase production by Penicillium variabile P16', Enzyme and Microbial Technology, 24(7), pp. 397–401. doi: 10.1016/S0141-0229(98)00142-2.

Pinto, E., Faustino, V., Rodrigues, R., Pinho, D., Garcia, V., Miranda, J. and Lima, R. (2015) 'A rapid and low-cost nonlithographic method to fabricate biomedical microdevices for blood flow analysis', Micromachines, 6(1), pp. 121–135. doi: 10.3390/mi6010121.

Pisaruka, J. and Dymond, M. K. (2016) 'A low volume 3D-printed temperature-controllable cuvette for UV visible spectroscopy', Analytical Biochemistry. Elsevier Inc, 510, pp. 52–55. doi: 10.1016/j.ab.2016.07.019.

Pranzo, D., Larizza, P., Filippini, D. and Percoco, G. (2018) ‘Extrusion-Based 3D Printing of Microfluidic Devices for Chemical and Biomedical Applications: A Topical Review’, Micromachines, 9(8), pp. 374-141. doi: 10.3390/mi9080374.

Prendergast, M. E., Solorzano, R. D. and Cabrera, D. (2016) ‘Bioinks for biofabrication: current state and future perspectives’, Journal of 3D Printing in Medicine, 1, p. 3dp–2016–0002. doi: 10.2217/3dp-2016-0002.

Prentner, S., Allen, D., Larcombe, L., Marson, S., Jenkins, K. and Saumer, M. (2010) ‘Effects of channel surface finish on blood flow in microfluidic devices’, Microsystem Technologies, 16(7), pp. 1091–1096. doi: 10.1007/s00542-009-1004-1.

Qian, H., Pretzer, L., Velazquez, J., Zhao, Z. and Wong, M. (2013) ‘Gold nanoparticles for cleaning contaminated water’, Journal of Chemical Technology and Biotechnology, 88(5), pp. 735–741. doi: 10.1002/jctb.4030.

Qiu, K., Haghiashtiani, G. and McAlpine, M. (2018) ‘3D Printed Organ Models for Surgical Applications’, Annual Review of Analytical Chemistry, 11(1), pp.287-306. doi: 10.1146/annurev-anchem-061417-125935.

Ramsden, J. J. (1995) ‘Puzzles and paradoxes in protein adsorption’, Chemical Society Reviews, 24(1), pp. 73-83. doi: 10.1039/CS9952400073.

Rengier, F., Mehndiratta, A., von Tengg-Kobligk, H., Zechmann, C., Unterhinninghofen, R., Kauczor, H. and Giesel, F. (2010) ‘3D printing based on imaging data: Review of medical applications’, International Journal of Computer Assisted Radiology and Surgery, 5(4), pp. 335–341. doi: 10.1007/s11548-010-0476-x.

Rhee, S. G. et al. (2010) ‘Methods for detection and measurement of hydrogen peroxide inside and outside of cells’, Molecules and Cells, 29(6), pp. 539–549. doi: 10.1007/s10059-010-0082-3.

Rim, T. (2014) Biosensors Based on Nanomaterials and Nanodevices [Book Review]. IEEE Nanotechnology Magazine, 8(3), pp.38-38.

Rocchitta, G., Spanu, A., Babudieri, S., Latte, G., Madeddu, G., Galleri, G., Nuvoli, S., Bagella, P., Demartis, M., Fiore, V., Manetti, R. and Serra, P. (2016) 'Enzyme biosensors for biomedical applications: Strategies for safeguarding analytical performances in biological fluids', Sensors, 16(6), p.780-785. doi: 10.3390/s16060780.

Rocha-Gaso, M., Villarreal-Gómez, L., Beyssen, D., Sarry, F., Reyna, M. and Ibarra-Cerdeña, C. (2017) 'Biosensors to diagnose Chagas disease: A brief review', Sensors, 17(11), pp. 1–12. doi: 10.3390/s17112629.

Rodrigues, J. V. and Gomes, C. M. (2010) 'Enhanced superoxide and hydrogen peroxide detection in biological assays', Free Radical Biology and Medicine, 49(1), pp. 61–66. doi: 10.1016/j.freeradbiomed.2010.03.014.

Rosales-Leal, J., Rodríguez-Valverde, M., Mazzaglia, G., Ramón-Torregrosa, P., Díaz-Rodríguez, L., García-Martínez, O., Vallecillo-Capilla, M., Ruiz, C. and Cabrerizo-Vílchez, M. (2010) 'Effect of roughness, wettability and morphology of engineered titanium surfaces on osteoblast-like cell adhesion', Colloids and Surfaces A: Physicochemical and Engineering Aspects, 365(3), pp. 222–229. doi: 10.1016/j.colsurfa.2009.12.017.

Rossi, L. M., Quach, A. D. and Rosenzweig, Z. (2004) 'Glucose oxidase-magnetite nanoparticle bioconjugate for glucose sensing', Analytical and Bioanalytical Chemistry, 380(4), pp. 606–613. doi: 10.1007/s00216-004-2770-3.

Rusmini, F., Zhong, Z. and Feijen, J. (2007) 'Protein Immobilization Strategies for Protein Biochips', Biomacromolecules, 8(6), pp.1775-1789. doi: 10.1021/bm061197b

Sackmann, E. K., Fulton, A. L. and Beebe, D. J. (2014) 'The present and future role of

microfluidics in biomedical research', Nature. Nature Publishing Group, 507(7491), pp. 181–189. doi: 10.1038/nature13118.

Saha, K., Agasti, S., Kim, C., Li, X. and Rotello, V. (2012) 'Gold Nanoparticles in Chemical and Biological Sensing', Chemical reviews, 112(5), pp. 2739–2779. doi: 10.1021/cr2001178.

Salentijn, G., Oomen, P., Grajewski, M. and Verpoorte, E (2017) 'Fused Deposition Modeling 3D Printing for (Bio)analytical Device Fabrication: Procedures, Materials, and Applications', Analytical Chemistry, 89(13), pp. 7053–7061. doi: 10.1021/acs.analchem.7b00828.

Salentijn, G. I. J., Hamidon, N. N. and Verpoorte, E. (2016) 'Solvent-dependent on/off valving using selectively permeable barriers in paper microfluidics', Lab on a Chip. 16(6), pp. 1013–1021. doi: 10.1039/c5lc01355k.

Scholz Carmen (2017) Polymers for Biomedicine: Synthesis, Characterization, and Applications. Volume I, 2nd ed. John Wiley & Sons, Inc., pp.1-29. doi: 10.1002/9781118967904

Schubert, C., Van Langeveld, M. C. and Donoso, L. A. (2014) 'Innovations in 3D printing: A 3D overview from optics to organs', British Journal of Ophthalmology, 98(2), pp. 159–161. doi: 10.1136/bjophthalmol-2013-304446.

Scrimshaw, N. and Murray, E. (1988). The acceptability of milk and milk products in populations with a high prevalence of lactose intolerance. The American Journal of Clinical Nutrition, 48(4), pp.1142-1159. doi:10.1093/ajcn/48.4.1142

Serra, T., Planell, J. A. and Navarro, M. (2013) 'High-resolution PLA-based composite scaffolds via 3-D printing technology', Acta Biomaterialia. Acta Materialia Inc., 9(3), pp. 5521–5530. doi: 10.1016/j.actbio.2012.10.041.

Setti, L., Fraleonimorgera, A., Mencarelli, I., Filippini, A., Ballarin, B. and Dibiase, M. (2007) 'An HRP-based amperometric biosensor fabricated by thermal inkjet printing', Sensors and Actuators, B: Chemical, 126(1), pp. 252–257. doi: 10.1016/j.snb.2006.12.015.

Setti, L., Fraleoni-Morgera, A., Ballarin, B., Filippini, A., Frascaro, D. and Piana, C. (2005) 'An amperometric glucose biosensor prototype fabricated by thermal inkjet printing', Biosensors and Bioelectronics, 20(10), pp.2019-2026. doi: 10.1016/j.bios.2004.09.022

Shafiee, A. and Atala, A. (2016) 'Printing Technologies for Medical Applications', Trends in Molecular Medicine, 22(3), pp. 254–265. doi: 10.1016/j.molmed.2016.01.003.

Shallan, A., Smejkal, P., Corban, M., Guijt, R. and Breadmore, M. (2014) 'Cost-effective three-dimensional printing of visibly transparent microchips within minutes', Analytical Chemistry, 86(6), pp. 3124–3130. doi: 10.1021/ac4041857.

Shankles, P., Millet, L., Aufrecht, J. and Retterer, S. (2018) 'Accessing microfluidics through feature-based design software for 3D printing', PloS one, 13(3), pp. 192-195. doi: 10.1371/journal.pone.0192752.

Sharafeldin, M., Jones, A. and Rusling, J. (2018). 3D-Printed Biosensor Arrays for Medical Diagnostics. Micromachines, 9(8), p.394.doi: 10.3390/mi9080394

Shieh, H. F. and Jennings, R. W. (2017) 'Three-dimensional printing of external airway splints for tracheomalacia', Journal of Thoracic Disease, 9(3), pp. 414–416. doi: 10.21037/jtd.2017.02.53.

Skardal, A. (2018) 'Perspective: "Universal" bioink technology for advancing extrusion bioprinting-based biomanufacturing', Bioprinting, 11(1), pp. 10–14. doi:

10.1016/j.bprint. 2018.e00026.

Sood, A. K., Ohdar, R. K. and Mahapatra, S. S. (2009) 'Improving dimensional accuracy of Fused Deposition Modelling processed part using grey Taguchi method', Materials and Design. Elsevier Ltd, 30(10), pp. 4243–4252. doi: 10.1016/j.matdes.2009.04.030.

Sood, A. K., Ohdar, R. K. and Mahapatra, S. S. (2010) 'Parametric appraisal of fused deposition modelling process using the grey Taguchi method', Proceedings of the Institution of Mechanical Engineers, Part B: Journal of Engineering Manufacture, 224(1), pp. 135–145. doi: 10.1243/09544054JEM1565.

Srinivasan, V., Pamula, V. K. and Fair, R. B. (2004) 'Droplet-based microfluidic lab-on-a-chip for glucose detection', Analytica Chimica Acta, 507(1), pp. 145–150. doi: 10.1016/j.aca.2003.12.030.

Stachowiak, J., Richmond, D., Li, T., Brochard-Wyart, F. and Fletcher, D. (2009) 'Inkjet formation of unilamellar lipid vesicles for cell-like encapsulation', Lab on a Chip, 9(14), pp. 2003–2009. doi: 10.1039/b904984c.

Stanciu, L., Won, Y., Ganesana, M. and Andreescu, S. (2009) 'Magnetic Particle-Based Hybrid Platforms for Bioanalytical Sensors', Sensors, 9(4), pp. 2976–2999. doi: 10.3390/s90402976.

Stanton, M. M., Samitier, J. and Sánchez, S. (2015) 'Bioprinting of 3D hydrogels', Lab on a Chip. 15(15), pp. 3111–3115. doi: 10.1039/c5lc90069g.

Stone, H. A., Stroock, A. D. and Ajdari, A. (2004) 'Engineering Flows in Small Devices: Microfluidics Toward a Lab-on-a-Chip', Annual Review of Fluid Mechanics, 36(1), pp. 381–411. doi: 10.1146/annurev.fluid.36.050802.122124.

Streets, A. M. and Huang, Y. (2013) 'Chip in a lab: Microfluidics for next generation

life science research', Biomicrofluidics, 7(1), pp. 261-271. doi: 10.1063/1.4789751.

Sun, Y. Y., Zhao, S. and Ren, Q. X. (2012) 'Glucose Biosensor Based on Immobilization of Glucose Oxidase on Silica Nanoparticles Modified Au Electrode', Advanced Materials Research, 503(1), pp. 424–427. doi: 10.4028/www.scientific.net/AMR.503-504.424.

Tanikella, N., Wittbrodt, B. and Pearce, J. (2017). Tensile strength of commercial polymer materials for fused filament fabrication 3D printing. Additive Manufacturing, 15, pp.40-47.doi: 10.1016/j.addma.2017.03.005

Thakur, M. and Ragavan, K. (2012). Biosensors in food processing. Journal of Food Science and Technology, 50(4), pp.625-641.doi: 10.1007/s13197-012-0783-z

Thingiverse.com. (2012). Universal Paste Extruder for 3D printers by RichRap. [online] Available at: https://www.thingiverse.com/thing:20733 [Accessed 17 Sep. 2016].

Thermo Scientific Pierce protein assay technical handbook. (2009). [South Bend, Ind.]: Thermo Scientific.

Thomas, M. and Ando, D. (1997). Ultraviolet and visible spectroscopy. Chichester: John Wiley & Sons.

Thomas, D. J., Tehrani, Z. and Redfearn, B. (2016) '3-D printed composite microfluidic pump for wearable biomedical applications', Additive Manufacturing. Elsevier B.V., 9, pp. 30–38. doi: 10.1016/j.addma.2015.12.004.

Tintoré, M. et al. (2015) 'Gold-coated superparamagnetic nanoparticles for single methyl discrimination in DNA aptamers', International Journal of Molecular Sciences, 16(11), pp. 27625–27639. doi: 10.3390/ijms161126046.

Tothill, A., Partridge, M., James, S. and Tatam, R. (2017) 'Fabrication and optimisation

of a fused filament 3D-printed microfluidic platform', Journal of Micromechanics and Microengineering. 27(3), pp. 35-38. doi: 10.1088/1361-6439/aa5ae3.

Tsuda, S., Jaffery, H., Doran, D., Hezwani, M., Robbins, P., Yoshida, M. and Cronin, L. (2015) 'Customizable 3D printed "Plug and Play" millifluidic devices for programmable fluidics', PLoS ONE, 10(11), pp. 1–13. doi: 10.1371/journal.pone.0141640.

Vadgama, P. (2005). Surfaces and Interfaces for Biomaterials. Volume I, Woodhead Publishing, pp.45-48. doi: 10.1016/B978-1-85573-930-7.50034-0

Vega, V., Clements, J., Lam, T., Abad, A., Fritz, B., Ula, N. and Es-Said, O. (2010). The Effect of Layer Orientation on the Mechanical Properties and Microstructure of a Polymer. Journal of Materials Engineering and Performance, 20(6), pp.978-988. doi: 10.1007/s11665-010-9740-z

Ventola, C. L. (2014) 'Medical Applications for 3D Printing: Current and Projected Uses', P&T: a peer-reviewed journal for formulary management, 39(10), pp. 704–711. doi: 10.1016/j.infsof.2008.09.005.

Vigneshvar, S., Sudhakumari, C., Senthilkumaran, B. and Prakash, H. (2016) 'Recent Advances in Biosensor Technology for Potential Applications – An Overview', Frontiers in Bioengineering and Biotechnology, 4(1), pp. 1–9. doi: 10.3389/fbioe.2016.00011.

Villalpando, L., Eiliat, H. and Urbanic, R. J. (2014) 'An optimization approach for components built by fused deposition modeling with parametric internal structures', Procedia CIRP. Elsevier B.V., 17, pp. 800–805. doi: 10.1016/j.procir.2014.02.050.

Wang, H., Wang, X., Zhang, X., Qin, X., Zhao, Z., Miao, Z., Huang, N. and Chen, Q. (2009) 'A novel glucose biosensor based on the immobilization of glucose oxidase onto

gold nanoparticles-modified Pb nanowires', Biosensors and Bioelectronics, 25(1), pp. 142–146. doi: 10.1016/j.bios.2009.06.022.

Wang, J. (2008) 'Electrochemical glucose biosensors', Electrochemical Sensors, Biosensors and their Biomedical Applications, 16(2), pp. 57–69. doi: 10.1016/B978-012373738-0.50005-2.

Wang, Z., Lee, S., Cheng, H., Yoo, J. and Atala, A. (2018) '3D bioprinted functional and contractile cardiac tissue constructs', Acta Biomaterialia. Acta Materialia Inc., 70, pp. 48–56. doi: 10.1016/j.actbio.2018.02.007.

Weng, Z., Wang, J., Senthil, T. and Wu, L. (2016) 'Mechanical and thermal properties of ABS/montmorillonite nanocomposites for fused deposition modeling 3D printing', Materials and Design. Elsevier Ltd, 102, pp. 276–283. doi: 10.1016/j.matdes.2016.04.045.

Waheed, S., Cabot, J., Macdonald, N., Lewis, T., Guijt, R., Paull, B. and Breadmore, M. (2016). 3D printed microfluidic devices: enablers and barriers. Lab on a Chip, 16(11), pp.1993-2013.doi: 10.1039/c6lc00284f

Wijnen, B., Hunt, E., Anzalone, G. and Pearce, J. (2014) 'Open-source syringe pump library', PLoS ONE, 9(9), pp. 1–8. doi: 10.1371/journal.pone.0107216.

Wilson, J. (2005). Milk Intolerance: Lactose Intolerance and Cow's Milk Protein Allergy. Newborn and Infant Nursing Reviews, 5(4), pp.203-207. doi:10.1053/j.nainr.2005.08.004

Wilson R and Turner, A. P. F. (1992) 'Glucose oxidase: an ideal enzyme', Biosensors and Bioelectronic, 7(1), pp. 165–185. doi: 10.1016/0956-5663(92)87013-F.

Wilson, W. C. and Boland, T. (2003) 'Cell and organ printing 1: Protein and cell printers', Anatomical Record - Part A Discoveries in Molecular, Cellular, and

Evolutionary Biology, 272(2), pp. 491–496. doi: 10.1002/ar.a.10057.

Wong, L. S., Khan, F. and Micklefield, J. (2009) 'Selective Covalent Protein Immobilization: Strategies and Applications', Chemical Reviews, 109(9), pp.4025-4053. doi: 10.1021/cr8004668

Xiaofei, W., Ruiyi, L. and Zaijun, L. (2014) 'Synthesis of gold nanoclusters/glucose oxidase/graphene oxide multifunctional catalyst with surprisingly enhanced activity and stability and its application for glucose detection', RSC Advances, 4(20), pp. 9935–9941. doi: 10.1039/c3ra47553k.

Xu, T., Jin, J., Gregory, C., Hickman, J. and Boland, T. (2005) 'Inkjet printing of viable mammalian cells', Biomaterials, 26(1), pp. 93–99. doi: 10.1016/j.biomaterials.2004.04.011.

Yamanaka, K., Vestergaard, M. C. and Tamiya, E. (2016) 'Printable electrochemical biosensors: A focus on screen-printed electrodes and their application', Sensors, 16(10), pp. 1–16. doi: 10.3390/s16101761.

Yang, H. (2017) 'A glucose biosensor based on horseradish peroxidase and glucose oxidase co-entrapped in carbon nanotubes modified electrode', International Journal of Electrochemical Science, 12(6), pp. 4958–4969. doi: 10.20964/2017.06.05.

Yang, T., Jung, S., Mao, H. and Cremer, P. (2001) 'Fabrication of phospholipid bilayer-coated microchannels for on-chip immunoassays', Analytical Chemistry, 73(2), pp. 165–169. doi: 10.1021/ac000997o.

Yang, Z., Lei, J., Sun, X., Lei, C., Zhou, Y. and Liu, Y. (2015) 'A Dynabeads-labeled immunoassay based on a fluxgate biosensor for the detection of biomarkers', Analytical Methods. 7(6), pp. 2391–2398. doi: 10.1039/c4ay02727b.

Yazdi, A., Popma, A., Wong, W., Nguyen, T., Pan, Y. and Xu, J. (2016) '3D printing:

an emerging tool for novel microfluidics and lab-on-a-chip applications', Microfluidics and Nanofluidics. 20(3), pp. 1–18. doi: 10.1007/s10404-016-1715-4.

Yu, Y., Moncal, K., Li, J., Peng, W., Rivero, I., Martin, J. and Ozbolat, I. (2016) 'Three-dimensional bioprinting using self-Assembling scalable scaffold-free "tissue strands" as a new bioink', Scientific Reports, 6(1), pp. 1–11. doi: 10.1038/srep28714.

Yun, Y., Lee, B., Choi, J., Kim, S., Yoo, B., Kim, Y., Park, K and Cho, Y. (2011) 'A Glucose Sensor Fabricated by Piezoelectric Inkjet Printing of Conducting Polymers and Bienzymes', Analytical Sciences, 27(4), pp. 375-378. doi: 10.2116/analsci.27.375.

Zhang, Q., Xu, J. J. and Chen, H. Y. (2006) 'Patterning microbeads inside poly(dimethylsiloxane) microfluidic channels and its application for immobilized microfluidic enzyme reactors', Electrophoresis, 27(24), pp. 4943–4951. doi: 10.1002/elps.200600024.

Zhang, S., Wang, N., Yu, H., Niu, Y. and Sun, C. (2005) 'Covalent attachment of glucose oxidase to an Au electrode modified with gold nanoparticles for use as glucose biosensor', Bioelectrochemistry, 67(1), pp. 15–22. doi: 10.1016/j.bioelechem.2004.12.002.

Zhang, Y. and Chou, K. (2008) 'A parametric study of part distortions in fused deposition modelling using three-dimensional finite element analysis', Proceedings of the Institution of Mechanical Engineers, Part B: Journal of Engineering Manufacture, 222(8), pp. 959–967. doi: 10.1243/09544054JEM990.

Zhang, Y., Myung, S., You, C., Zhu, Z. and Rollin, J. (2011) 'Toward low-cost biomanufacturing through in vitro synthetic biology: Bottom-up design', Journal of Materials Chemistry, 21(47), pp. 18877–18886. doi: 10.1039/c1jm12078f.

Zhou, Y. (2017) 'The recent development and applications of fluidic channels by 3D

printing', Journal of Biomedical Science. 24(1), pp. 1–22. doi: 10.1186/s12929-017-0384-2.

APPENDIX

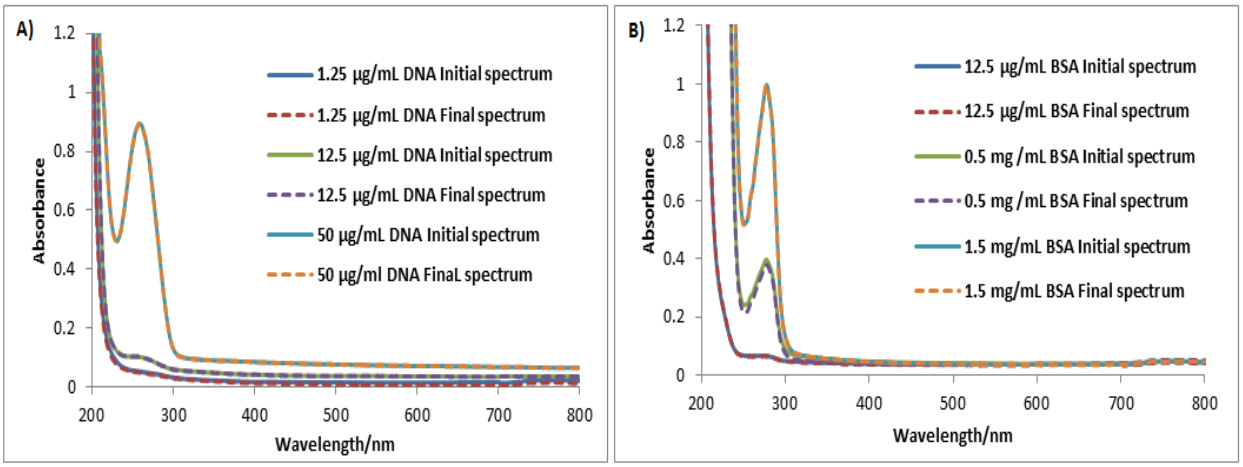

Figure 3.23 | **Initial and final spectrum measurement for DNA [A] and BSA [B] solutions at concentrations of [1.25 µg/mL, 12.5 µg/mL and 50 µg/mL] and [12.5 µg/mL, 0.5 mg/mL and 1.5 mg/mL];** A-B shows overlap of initial and final absorption spectra for DNA [A] and BSA [B] for ABS thermoplastic cuboids printed at 10% infill density. Since the spectrum graph for rest of the other thermoplastic cuboids, assessed (refer to section 3.7) in this report where exactly identical to this graph. Only spectrum data for ABS filament are presented here as example.

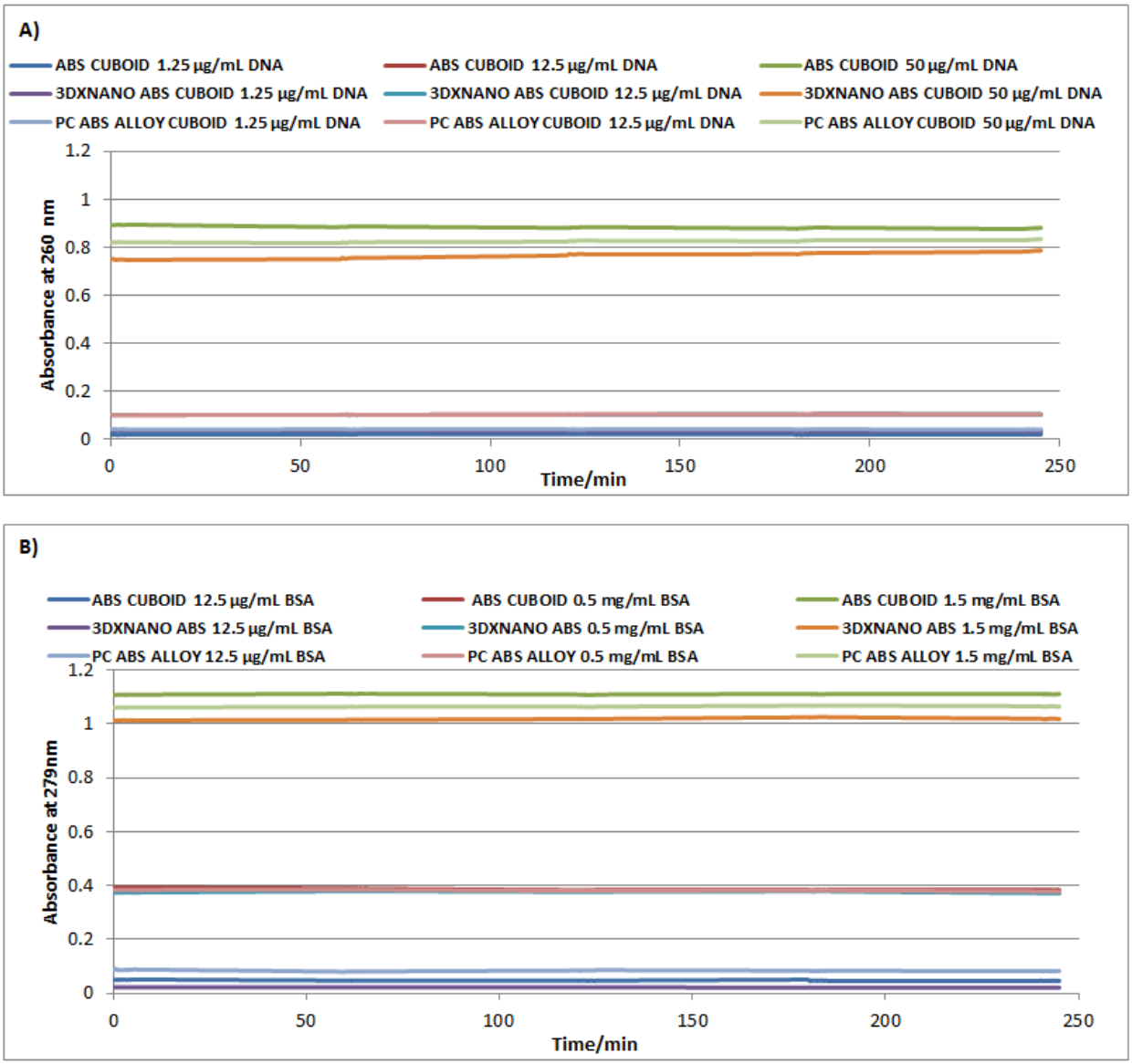

Figure 3.24| **Absorption time course measurements for DNA [A] and BSA [B] solutions at concentrations of [1.25 µg/mL, 12.5 µg/mL and 50 µg/mL] and [12.5 µg/mL, 0.5 mg/mL and 1.5 mg/mL]**; DNA and BSA solutions absorbance were measured at 260 nm and 279 nm. Cuboids were printed at 10% infill density. Since the graph for rest of the other thermoplastic cuboids, assessed (refer to section 3.7) in this report where mostly identical to this graph. These graphs are presented here as an example.

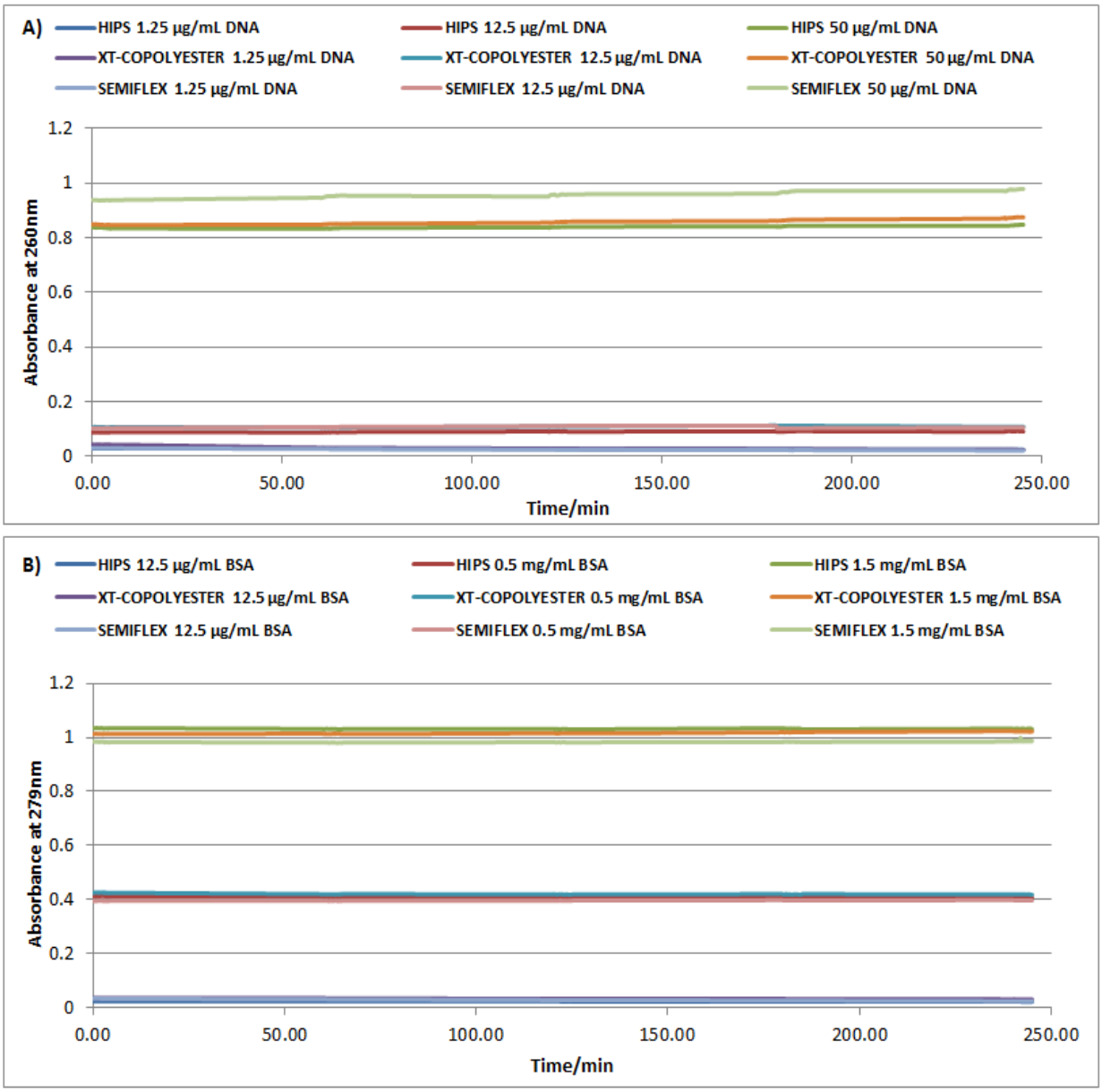

Figure 3.25 | **Absorption time course measurements for DNA [A] and BSA [B] solutions at concentrations of [1.25 µg/mL, 12.5 µg/mL and 50 µg/mL] and [12.5 µg/mL, 0.5 mg/mL and 1.5 mg/mL]**; DNA and BSA solutions absorbance were measured at 260 nm and 279 nm. Cuboids were printed at 10% infill density. Since the graph for rest of the other thermoplastic cuboids, assessed (refer to section 3.7) in this report where mostly identical to this graph. These graphs are presented here as an example.

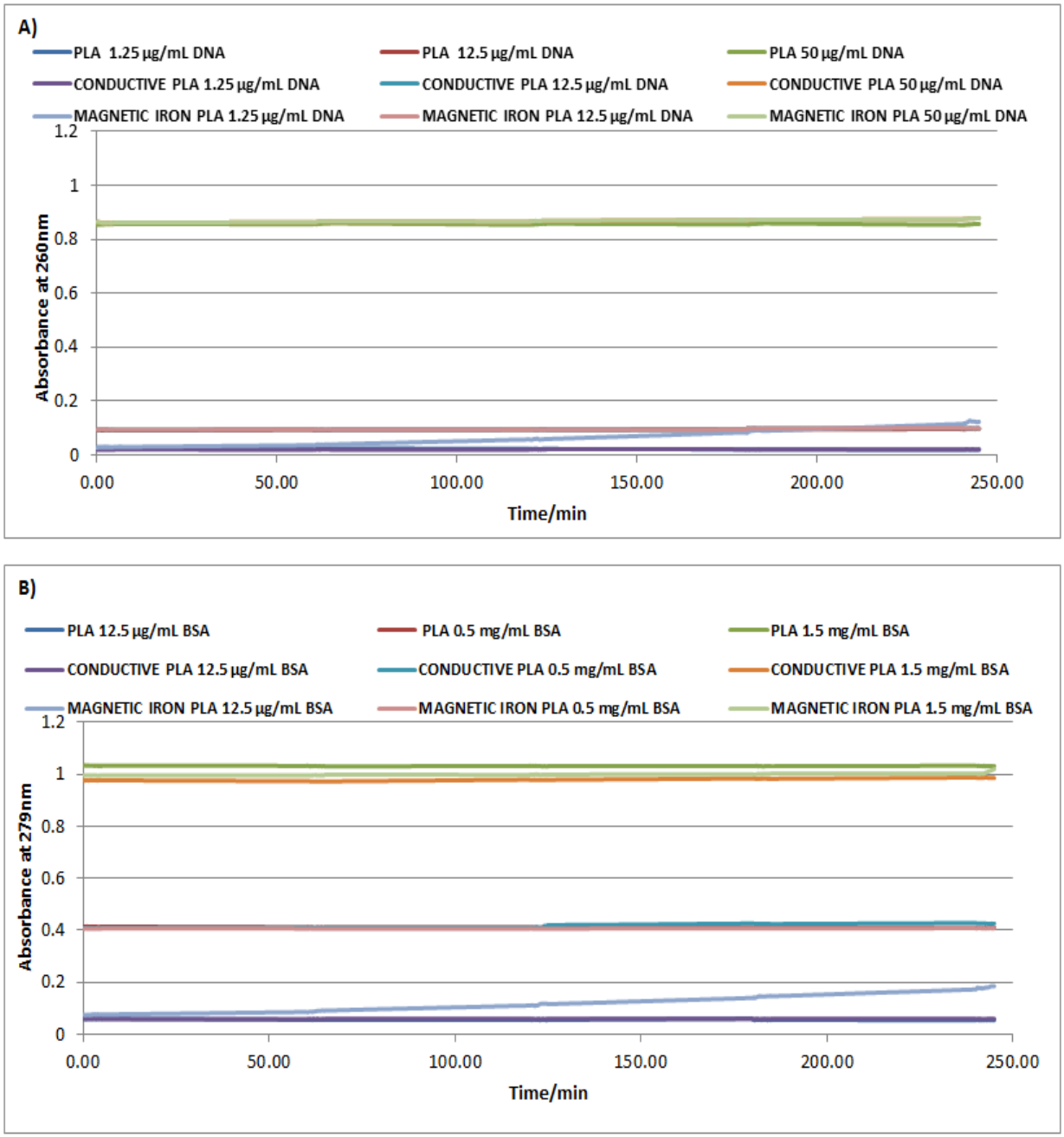

Figure 3.26 | **Absorption time course measurements for DNA [A] and BSA [B] solutions at concentrations of [1.25 µg/mL, 12.5 µg/mL and 50 µg/mL] and [12.5 µg/mL, 0.5 mg/mL and 1.5 mg/mL]**; DNA and BSA solutions absorbance were measured at 260 nm and 279 nm. Cuboids were printed at 10% infill density. Since the graph for rest of the other thermoplastic cuboids, assessed (refer to section 3.7) in this report where mostly identical to this graph. These graphs are presented here as an example.

Attached CD

The CD provided with this thesis contains the CAD design, as well as STL files of all FDM 3D printing models used in this thesis. All the CAD and STL files are termed according to Figure number of 3D models as presented in the thesis.